New generation fast Silicon detectors for timing and particle Identification

High Energy Physics and applications

©2022

Tommaso Isidori

Submitted to the graduate degree program in Department of Physics and Astronomy and the Graduate Faculty of the University of Kansas in partial fulfillment of the requirements for the degree of Doctor of Physics.

Committee members

Dr. Christophe Royon, Chairperson

Dr. Nicola Minafra, Co-Supervisor

Dr. John P. Ralston

Dr. Christopher Rogan

Dr. Daniel Tapia Takaki

Dr. Caroline A. Jewers, Graduate Studies Representative

Date defended: March 31, 2022

The Dissertation Committee for Tommaso Isidori certifies
that this is the approved version of the following dissertation :

New generation fast Silicon detectors for timing and particle Identification
High Energy Physics and applications

Dr. Christophe Royon, Chairperson

Date approved: March 31, 2022

Abstract

The High Energy Physics (HEP) community is working towards the upgrade of existing research facilities, as well as paving the way for the construction of state-of-the-art particle colliders. The increased rate of collisions per bunch crossing poses a great challenge in preserving the reconstruction capabilities of the experiments. This situation has constituted a breeding ground for the development of particle detectors specialized in reconstructing the time coordinate of events with great accuracy. This thesis presents the results obtained from the characterization and optimization of Low Gain Avalanche Detectors (LGADs) designed for the End-Cap Timing Layer (ETL) of the Compact Muon Solenoid (CMS) experiment. Together with the Barrel Timing Layer (BTL), the ETL will be part of the new MIP Timing Detector (MTD) of CMS and will require the installation of radiation resistant detectors capable of maintaining great timing resolution until the end of their expected life-cycle. During the tests performed at the Fermilab facilities, the performance of the detectors were investigated as a function of the irradiation received. The work of analysis pursued put on display the timing capabilities of these devices, showing a uniform response and total efficiency of the tested LGADs. The time resolution of the detectors was found to be consistent with the nominal specification required from the MTD, with values ranging from 30 ps for non irradiated sensors, to about 50 ps for sensors irradiated to a fluence of 10^{15} n_{eq}. The timing technology of new generations has been extended well beyond the interests of particle physics experiments and embraces a number of different commercial and technical applications. In addition to the studies of LGADs for HEP experiments, this thesis describes the original contributions to two projects that employ the use of timing detectors, fast electronics, and reconstruction techniques. A description of the results obtained from an LGAD-based detector for beam monitoring of a medical linac, used for cancer treatments and diagnostics, is presented. This work exploits the synergies between HEP experiments and medical physics for addressing the demand for fast dosimetric devices. The tests performed in collaboration with the University College of Dublin (UCD), and the Saint Luke's Hospital of Dublin, Ireland, proved unprecedented single particle

resolution capabilities in radiation dense environments. The data analysis show the detector's linear behavior in charged particles counting up to about 100 MHz, with a time resolution of about 50 ps. This information was used to characterize the beam temporal profile. It also allowed for the first ever reconstruction of a medical linac pulse sub-structure, revealing a characteristic oscillation frequency of about 3.2 GHz. The last section of this thesis presents the Advanced enerGetic Ion eLectron tElescope (AGILE) project. AGILE exploits the capabilities of fast read-out electronics, and sampling techniques typically employed for the development of timing detectors to perform real-time on-board particle identification in space. The project aims in discriminating and identifying the contribution of ions (form H-Fe) in a wide range of energies (1-100 MeV/nuc) employing novel Pulse Shape Discrimination (PSD) techniques, with the sole use of silicon sensors. A prototype of the detector was designed, assembled, and tested using radiation sources at the KU facilities. The studies of the main key features for particle identification are consistent with the simulated performance, showing an overall energy resolution between 5.1% and 3.5%. The results are within the minimum standards required by AGILE for correct identification, of about 10%.

Dedicated to my Family.

Acknowledgements

I first want to thank my advisor, Prof. Christophe Royon, for his support during my research work at the University of Kansas. My collaboration with Christophe started in 2017, when He received me in his group as one of his Ph.D students. He gave me the opportunity to pursue my research on hardware topics that I love and thoroughly enjoy. Christophe encouraged me in presenting my results at conferences and workshops, which enriched me as a student and as a physicist.

I want to give a special thank to Prof. Daniel Tapia Takaki, who offered me a new, exciting position as a post-doc in the ALICE group, at KU. He directed and supervised me during the beginning of this new adventure, and provided me invaluable suggestions and help for concluding my Ph.D career.

Another very special thanks goes to Nicola Minafra, great friend, excellent physicist, and co-supervisor of my Ph.D program. Nicola has always striven to help me progressing in my professional career and, no matter at what time of the day (and night) he never failed to answer my many and frustrating questions. I hope our professional collaboration and friendship will last for many years to come.

I want to thank all the members of my thesis committee for providing me their feedback and for reading the thesis I'm presenting.

I want to thank the U.S. National Science Foundation, and the University of Kansas for funding my research activities, for financing my research trips and my attendance to conferences. Your support allowed me to carry out my research project and achieved this important milestone in my career as a physicist.

I want to thank the direction and staff of the physics department at KU, that always provided us an optimal environment for pursuing our research goals. A huge, personal thanks goes to Kristin Renells, Joel Sauerwein, Kayla Wegley, which had to deal with my constant barrage of bureaucratic questions and doubts.

A big thank you to the many past and present colleagues and friends of the research group at

KU: Cristian Baldenegro Barrera, Hussein Al-Ghoul, Timothy Raben, Laurent Forthomme, Nicola Minafra, Alexander Novikov, Georgios Krintiras, Guillaume Biagi, Federico Deganutti, William Doumerg, Florian Gautier, Gauthier Legras, Maxime Massa, Cole Lindsey, Zachary Warner, Justin Williams, Saray Arteaga Escatel, and Luis Alcerro.

I want to thank the colleagues from UCD and the Saint Luke's Hospital of Dublin: Patrick McCavana, Brendan McClean, Ronan McNulty, Naomi Raab, and Luke Rock. Our collaboration led to interesting and important results that played a big role for the drafting of this document.

I would like to thank my colleagues from the US-CMS group that enabled my contribution to the CMS MTD project. Thanks to the KU group: Prof. Christopher Rogan, Nicola Minafra, Andres Abreu, Zach Flowers, Jack King, Margaret Lazarovits. Thank you to all of the collaborators from FERMILAB and institutions across the USA that shared long days and nights at the test beams with us!

Thanks to all of the colleagues from the NASA AGILE collaboration: Christophe Royon, William d'Assignies, Florian Gautier, Ashely Greeley, Shri G. Kanekal, Nicola Minafra, Alexander Novikov, Eric Oberla, Quintin Schiller, and Rob Young. I owe a special thanks to Sasha and Galya for all of our coffees, meals, beers, and conversation together. Thank you for all of the time spent together!

I want to thank my closest friends that made this adventure unforgettable. Thank you to Calvin, Bryce, Cristian, Pavel, Michell, Federico, Svetla, Ana, Zach, Alyssa, Cole, Justin, Sasha, Galya, Nick, Marcela, Tim, Hussein. Thank you to all my friends in Europe: Paolo, Mattia, Davide D., Giacomo, Davide V., Dario, Riccardo, Andrea, Simone, Giulio, Barbara, Francesco, Stefano, Luca, Matteo, Elena, Nicola... Far too many to list all of them in here. I'm so extremely grateful for having all of you in my life, welcoming me every time I'm back home. A huge thank you to everyone from the Dojo Mukei Siena, with whom I shared some of the best years of my life.

Thank you to my second family over here, in Lawrence, Kansas: the Rivers Brazilian Jiu Jitsu academy. Thank you to Trevor, Heidi, and Matt to welcome me with open arms and thank you to all the people that orbited around the gym in the last few years. Thank you for all the time on the mats, the laughter, the learning, and all the incredible connections and bonds.

Finally, I want to express my gratitude and deepest love to my family. The one back home: Donatella, Valentina, Marco, Vanda, Antonio, Francesco, Grazia, Marta, Marco, Giovanni e Bernardo, Michele, Mauro, Davide. I love all of you more than anything. You made me who I am and you

thought me what I know. I could not be more grateful to have such a wonderful group of people around me. Much love and appreciation goes to my family here, in Kansas. Thank you to Janice, Jess, Amanda, Weston, Hayden, Hadley, Linda, Bob, Anita for all the love and support. Lastly, a huge thanks goes to Hanna Fontes, who had to put up with me for these last years. Thank you for all the love you gave me, thank you for the patience and understanding. I cannot wait to see where the future is going to lead us.

Cheers to new adventures.

Contents

List of Figures

List of Tables

Introduction

During the last decades a great amount of work has been done to improve the capabilities of particle colliders: cutting edge hardware technology employed in the development of detectors and accelerating components has evolved together with modern data collection and reconstruction techniques. Since the statistical validity of measurements scales proportionally to the number of independent collected events, the study of rare phenomena requires physicists to constantly look for more sophisticated ways to study signal events. This is obtained by fine-tuning the energy of the colliding bunches, increasing the rate of collisions and adjusting the spatial density of particles inside the bunches or in the targets. Unfortunately, this process also amplifies the rate of unwanted events (*backgrounds*) causing a differential growth that often favors the collection of more ordinary products. In light of future detector upgrades and of the construction of colliders of new generation, this dilemma has been thoroughly studied: how can we increase the number of interesting events recorded without getting overwhelmed by the background-like byproduct? Collecting data in radiation dense environment poses a technological challenge that calls for the design of fast and precise detectors to track decaying products, spatially locate their collision vertices, and identifying particles while maintaining the acquisition efficiency.

For these reasons, the particle physics community has focused on improving particle detectors and their timing performance. This has required dedicated R&D work that has led to the design of novel devices. Many research institutes and national laboratories affiliated to the European Organization for Nuclear Research (CERN) have been collaborating for the development of prototypes of timing detectors for High Energy Physics (HEP) experiments. In particular, this thesis covers the description of the new timing layer expected to be installed in the Compact Muon Solenoid (CMS) experiment at the Large Hadron Collider (LHC) in 2026. As the upgraded LHC will start colliding particles at increased rate (High-Lumi LHC during run 4, expected for 2027), this new addition to the experiment will enable CMS to explore a wide variety of physics programs beyond what has been done so far. Simulation studies and test campaigns highlighted

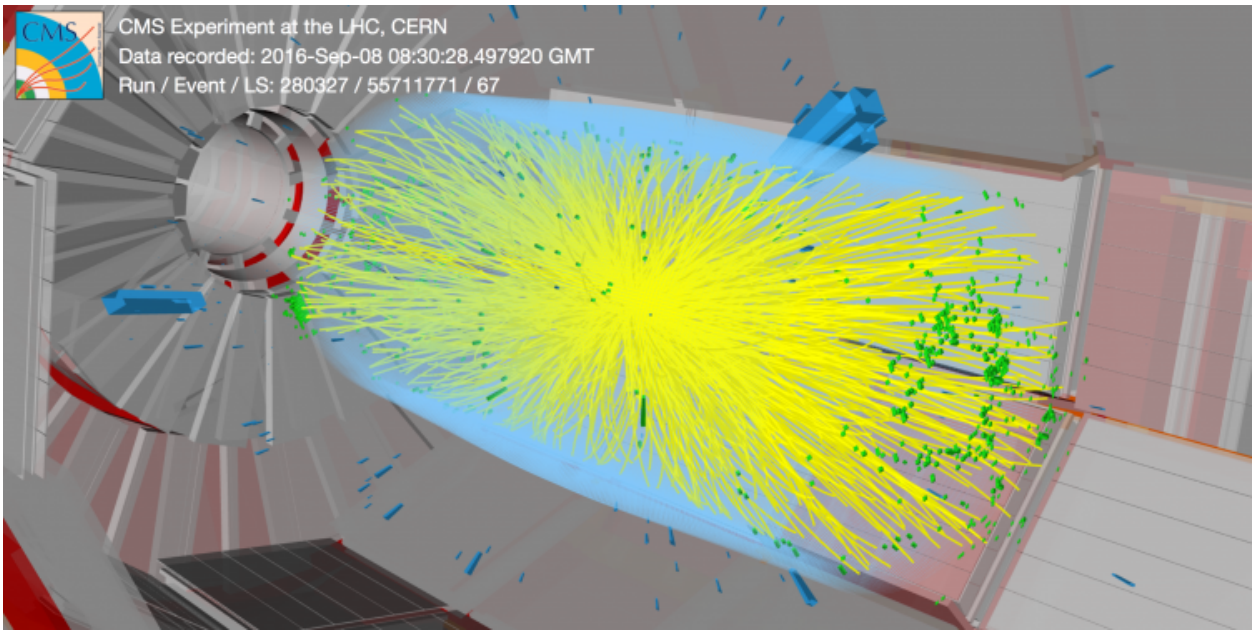

Figure 1: The image (1), shows an event display of protons bunches colliding inside the CMS experiment at the Large Hadron Collider (described in chapter 2). The density of yellow lines, representing the tracks of charged particles passing through the detectors. It illustrates the challenge of selecting signal events and rejecting background events.

the effectiveness of solid-state detectors of new generation for fast and accurate measurements. The growing demand coming from particle physics experiments, and the potential for novel technological applications has motivated a number of silicon foundries around the world into the design and production of more technologically advanced devices. Considerable effort has been put in the studies of the structure of silicon semiconductors and their response to incident radiation. This led to the production of thinner sensors with quicker charge collection times and finer granularity. Particular attention was devoted to the improvement of the weaknesses that previously characterized these detectors, such as the quick decrease of their performance as a function of the absorbed radiation. Producers have been implementing experimental techniques (addition of carbon atoms, modifying the doping, and intrinsic gain, structural improvement) to achieve a substantial increase in the average minimum displacement energies, therefore improving the overall radiation resistance. New detectors have demonstrated to be capable of performing after absorbed doses in the range $10^{14} - 10^{15}\,\mathrm{n}_{eq}$. This corresponds to to an integrated luminosity of $3000\,\mathrm{fb}^{-1}$ at the CMS experiment.

Before describing how novel timing detectors can help in mitigating the problems listed above,

We first give an introduction on the topics of fast and precise timing measurements. *Precise* timing detectors are used for accurately reconstructing the time coordinate of incident particles. Measuring the relative time needed to reach the detector (i.e. the time between the initial collision and the detection time) it is possible to extract information on the distance covered by the particle during its path; the measurement's precision is defined by the resolution of the timestamps. Combining this quantity to the spatial tracking information provides a four-dimensional reconstruction of the particle transport inside the experiment. This can be of crucial importance when investigating multiple overlapping hadronic collisions (a phenomenon called *Pile-Up*). In particular, the operation of the CMS experiment during High Luminosity runs of the LHC will be challenged in matching the decay products to their correct primary interaction vertex within the proton bunches. This can be achieved by factorizing the contribution of the timing information, as the sole tracking reconstruction would not suffice. Fig. 2 depicts a primary vertex detection using the timing information. The use of precise timing detectors is not only limited to the research environment, it extends to numerous technical and commercial applications: variation of these devices are mass produced by companies and employed in the fabrication of precise sensing apparatus (LIDARs, motion and distance sensors).

Further complications arise when the particle fluences are too large for the detectors to properly respond to individual energy deposit. The integration time of the sensor and read-out electronics could be too slow for individually processing consecutive incident particles. In this case the generated signals contain the sum of multiple consecutive interactions. While this represents the operating principle of many integrating detectors, this feature leads to the loss of single particle resolution. We refer to a detector being *fast* whenever capable of narrowing the acquisition time of individual measurements to perform single quanta detection, and maintain a linear response when subjected to large fluxes of particles. This technique often sacrifices the reconstruction precision of particles timestamp, instead drastically reducing the system's overall dead time. Irradiation facilities, as well as medical cancer treatment centers have displayed increasing interest in the capabilities of fast detectors: the possibility of studying the features of individual energy deposits, or just precisely measuring the particles occupancy makes them suitable for beam monitoring and dosimetric studies.

In the production of timing detectors, the semiconductor sensors have to be paired with per-

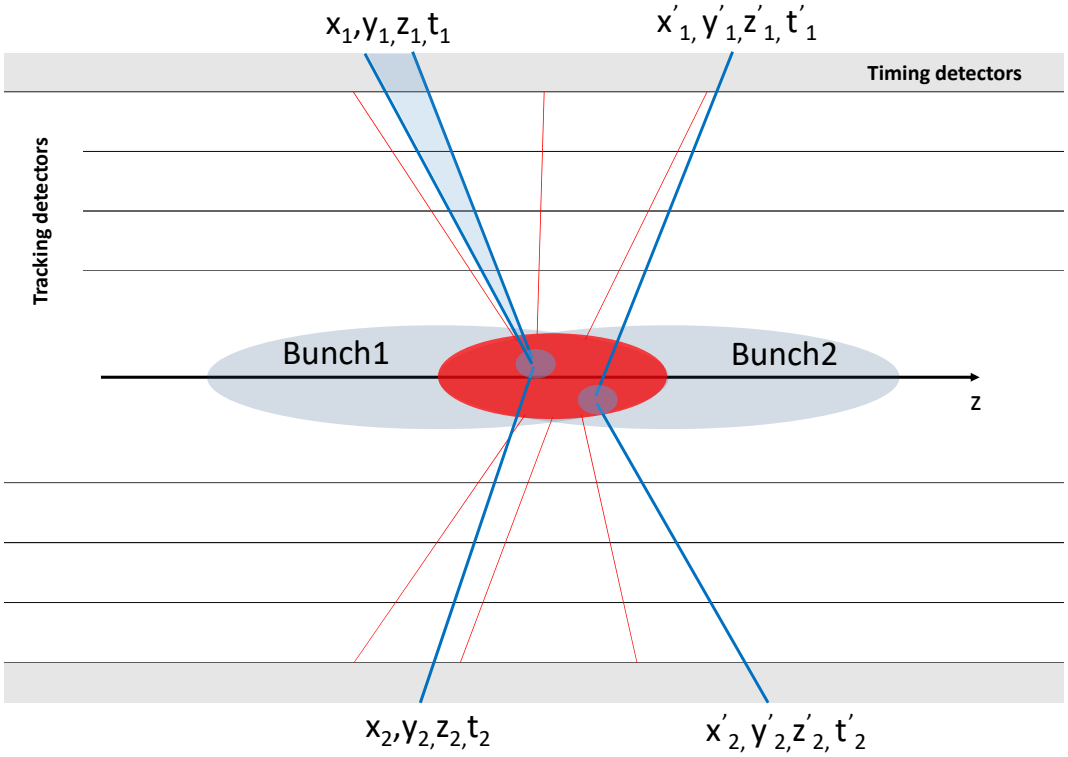

Figure 2: The figure sketches the section of two dense hadron bunches colliding at an interaction point. While the sole tracking information might not provide a measurement accurate enough to match the detected particles to the primary interaction vertices (represented with the red lines and the red area), the addition of the timing layer (in gray) allows to operate a background rejection and associate decay products (in blue) to the correct interactions within the bunch crossing.

forming read-out electronics, often tailor-made for preserving all the signals crucial information (e.g. shape, rise time). These detectors often rely on the use of powerful sampling devices, which record and digitize the outputs without introducing significant distortions; the collected signals can then be post-processed and analyzed using customized software. Typical reconstruction frameworks employ methods for correcting artifacts introduced during the shaping and digitizing process and finally produce cleaner, and revised data sets. An analysis algorithms is then used for the characterization of the detectors (rise time, amplitude distributions), and for the extraction of crucial physical quantities (time of flights, fluence). For this work, we have explored the possibility to use the signal-like features for obtaining experimental signatures for particle identification.

This thesis centers around the R&D work, design and construction of fast semiconductor particle detectors for timing measurements, and applications. The various research topics presented

embrace different fields of physics, although similarly describing the implementation and optimization of such novel detectors originally envisioned for HEP experiments.

Chapter 1 provides an introduction on timing measurements and operating principles of particle timing detectors. After a brief section regarding particles interacting with matter, the reader is introduced to crucial concepts that serve as a precursor for content that will be expanded in later sections.

In Chapter 2 we present the results produced during a series of test campaigns (2017-2020) at the Fermilab beamline testing facilities for the performance evaluation of the Low Gain Avalanche Detectors (LGADs) expected to be installed in the new Mip Timing Layer at the CMS apparatus. After a detailed description of the experiment, the chapter introduces the new challenges CMS will face with the data acquisition system during the High-Luminosity LHC (HL-LHC) period. This section details the detector upgrade as well as the prospects of the physics program. The corresponding test-beam and lab-tests performed during the course of this work were important for KU's participation to the MTD Technical Report (TDR) of the CMS Collaboration.

The knowledge and experience obtained working on timing measurements with LGADs has resulted in new applications. Chapter 3 presents the description of a detector developed at KU for the characterization of a high-rate medical linear accelerator used for cancer treatment and diagnostics. This work was published by Physics in Medicine & Biology (48) and it represents the first practical example of the use of LGADs for beam monitoring with single particle resolution. It constitutes a benchmark of the synergy between timing detectors and medical dosimetry. In addition to providing fundamental notions on the principles of dosimetry and standard medical detecting technologies, this chapter describes the Saint Luke's hospital testing facilities and reports the results obtained with the KU timing prototype device.

In Chapter 4 we describe the R&D work that led to the design and development of a compact, low-power detector for real-time particle identification in space. The Advanced enerGetic Ion eLectron tElescope (AGILE) detector is the result of a combined effort from the KU group and NASA Goddard Space Center. This collaboration has brought together the respective groups expertise in fast detectors and spaceborne experiments. Although rooted in different physics goals, this project shares many similarities with the experiments previously described. In particular, this NASA-funded project uses the powerful performance of fast read-out electronics. AGILE relies

on fast signal shaping and sampling techniques for processing and recording incident particles. It aims at extracting unique experimental features of the signal.

Finally, a last section is dedicated to the summary and conclusions of the work presented, as well as future prospects of the projects reported in this document.

Chapter 1

Particle detection with fast solid state sensors

A great improvement in semiconductor technology has rapidly pushed the frontier of timing detectors, attracting the interest of the particle physics community. These timing sensors are optimal candidates for particle detection for future HEP experiments. This technology will help improving the experiments reconstruction efficiency, and achieve a better background rejection at high collision rates. In addition, these detectors display excellent radiation hardness, enabling research projects exposed to high levels of radiation. Their enhanced features also appealed to tech companies, which have manifested strong interests in their use for the design of commercially available sensors.

This chapter introduces the basic concepts of particle detection and interaction of radiation with matter. It also describes the development steps needed for the construction of solid state detectors, giving particular attention to the studies of timing measurements. A large fraction of this thesis centers around the use of silicon detector and, in particular, Low Gain Avalanche Detectors (LGADs). Their main features will be described in the following sections.

1.1 Timing measurement

Among the tasks of experimental physicists, one of the most fundamentals is verifying the validity of the theoretical frameworks describing the known and yet undiscovered phenomena. When constructing an experiment, the community aims for the design of devices, or 'detectors', for gathering data to support, or discredit the theoretical models. Detectors represent the core hardware concept of particle physics experiments. These devices record the passage of particles, converting low-level quantities such as charge, and current induced signals into higher-level information. Calibration, and characterization procedures are required to correlate the output data to the features of the detected objects. This serves to unfold properties from the measured quantities that

could not otherwise be directly observed. Some detectors can operate efficiently for certain measurements, while at the same time representing an impracticable option for others. Sets of specialized sub-detectors are optimized to study individual features of the particles physics properties and, when combined, they work in synergy for reconstructing a more comprehensive view of the physics phenomena.

The use of novel particle timing detectors is a common denominator of the projects described in this thesis. These sensors enhance the capabilities to precisely reconstruct the time coordinates of particles time of arrival. This technology is a result of many years of previous experience in the design of particle detectors and combine the use of performing sensors, such as LGADs, fast read-out electronics, and fine sampling of the signals. As for any particle detector, timing sensors seek to produce signals characterized by large amplitudes, while attempting to reduce the various noise contributions. For achieving excellent time resolution, a good Signal-to-Noise Ratio (SNR) has to be complemented by a fast rise-time of the pulses. Collecting the timestamp of incident particles with great accuracy is a technique used in particle physics.

The time employed by a particle to cross two sections of a detector (or two different detectors) is called *Time Of Flight* (TOF). This quantity links the uncertainty of the reconstruction of a spatial coordinate (distance between the detectors) to that of a time coordinate: different particles cross a system of detectors with different TOF. This strategy is used to measure their mass difference for identification purposes. One can use:

$$\Delta T = L\left(\frac{1}{v_1} - \frac{1}{v_2}\right) \simeq \frac{Lc}{2p^2}(m_1^2 - m_2^2), \tag{1.1}$$

where v_1 and v_2 are the particle velocities, and m_1 and m_2 their masses. The second part of the equation represents the relativistic approximation, where p, the particles momentum is much larger than mc. In Fig. 1.1 an example of particle identification with TOF is shown. As the luminosity of particle colliders increases, the experiments are challenged to cope with unprecedented collision rates resulting in high-pile up events (see Fig. 2). In this thesis we investigate the possibility of using timing detectors for discriminating signal from background events in the context of the future upgrade of the Compact Muon Solenoid (CMS) at the Large Hadron Collider (LHC). As each particle is characterized by a different decay time, timing detectors can be used to precisely match the

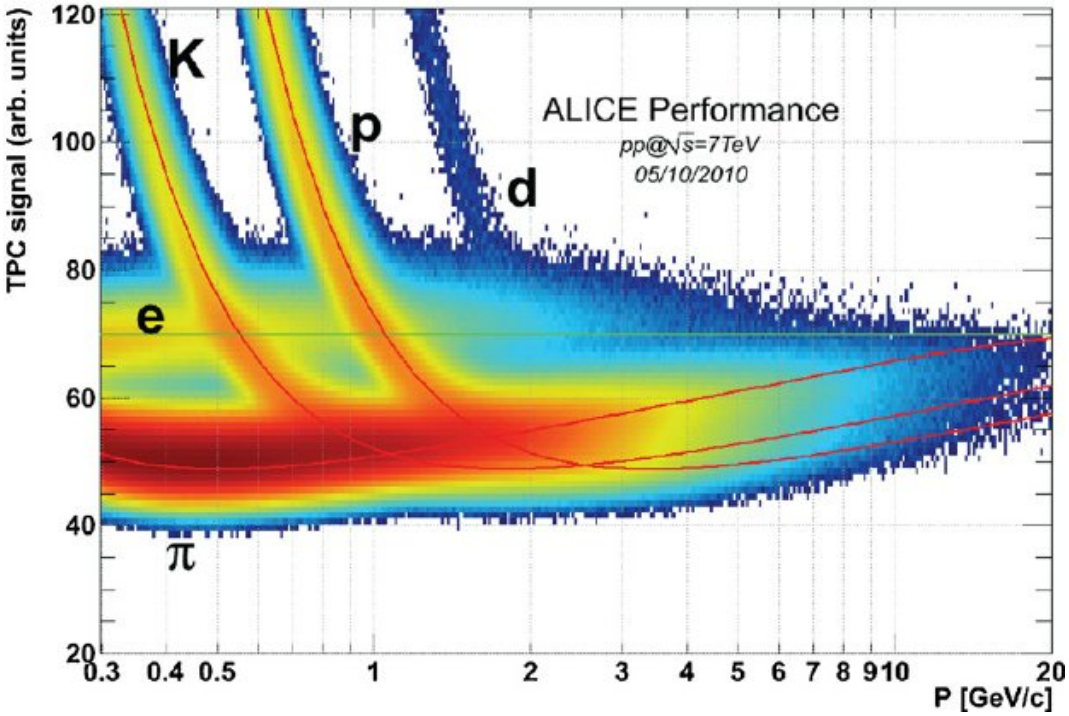

Figure 1.1: At the ALICE experiment, TOF measurements performed with a Time Projection Chamber is used for discriminating the particles identity (2).

timestamp of particle decays to the primary vertex of interaction. The timestamp measurement is naturally coupled to the spatial reconstruction of the interaction. Since the particle velocities are close to that of the speed of light, the resolution of the measurement can be approximated using the following expression:

$$\sigma_z = \frac{1}{N}\sqrt{\sigma_{t_1}^2 + \sigma_{t_2}^2 + ... + \sigma_{t_n}^2}c, \tag{1.2}$$

Where N is the number of events or independent measurements performed and $\sigma_{t_i}^2$ the uncertainty of each time measurement. Chapter 2 provides a description of the work done in the context of the timing detectors for the CMS project.

The use of timing detectors is not exclusive to measurements that require outstanding time precision. The performance of these sensors have found applications for the design of fast particle detectors. With *fast* we indicate detector concepts conceived to resolve the passage of consecutive particles with single pulse resolution. This can be achieved reducing the detector's integration time, often sacrificing some of its time resolution. In this case, the sensors are read out by fast amplification circuits, shaping the pulses to be contained within a few ns. Reducing the dead-

time between acquisitions offers the possibility of studying single-particle incidences up to high rate of detection. This class of detectors is of optimal use for applications in radiation-dense environments. Chapter 3 presents a concrete example where a LGAD is used to monitor an intense medical source with single-particle resolution up to high detection rates (more than 100 MHz).

The following sections will discuss the quantities that most influence the resolution of particle timing detectors, focusing on the features of solid state devices.

1.1.1 Contributing factors to the time resolution

The resolution of a timing detectors is not only affected by the choice of a well constructed sensor. The full detection system can be modeled as a current source connected in parallel to a capacitance, and read out by a pre-amplification stage (see Fig. 1.2). A particle crossing the detector produces a signal, which is simulated by the charge integrated over the model capacitance. The amplification stage shapes the pulses, amplifying the total input charge. The device used to record the data sets a threshold value on the signal (in Volts). The time at which the rising edge (or falling edge) of the signal crosses the threshold provides the timestamp of the incident particle. The contribution of each of this components is added for obtaining the overall resolution of the time measurement (49). It can be expressed as:

$$\sigma_t^2 = \sigma_{jitter}^2 + \sigma_{TimeWalk}^2 + \sigma_{Local\,ionization}^2 + \sigma_{TDC}^2 + \sigma_{Distortion}^2. \tag{1.3}$$

Equation 1.3 σ_{jitter}^2 includes the read-out electronics contribution, while $\sigma_{TimeWalk}^2$ and $\sigma_{Local\,ionization}^2$ come from intrinsic uncertainties of the energy depositions. The signal distortions due to non homogeneous electric fields inside the sensors is factorized inside $\sigma_{Distortion}^2$. Lastly σ_{TDC}^2 contains the uncertainty introduced in the digitization of the pulses. The total uncertainty is mostly affected by the distortions of the signals shape, which constitute the effective limit to the measurement.

The next sections will attempt a description of each contribution to the total uncertainty, and the strategies often employed for their mitigation.

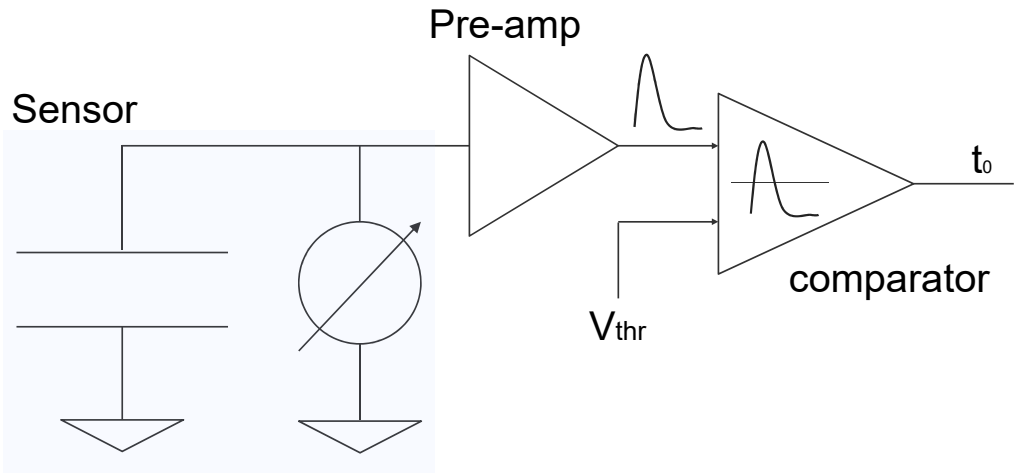

Figure 1.2: Diagram representation of a particle timing detector. The contribution of the sensor is modeled by the parallel configuration of a current source, and a capacitor. The charge collected is then processed by a pre-amplifier, which amplifies and shapes the current. The signal is then compared to a threshold for the extraction of the signal's timestamp.

1.1.2 Contribution of the read-out electronics

The contribution of the read-out electronics to the total timing precision of a detector is factorized inside the jitter term of the equation, σ_{jitter}. The jitter can be expressed as:

$$\sigma_{jitter} = \frac{\sqrt{N_{el}^2 + N_{SN}^2}}{dV/dt}, \tag{1.4}$$

where dV/dt is the slew-rate of the signal and Nel is the electronic noise introduced by the read-out.

The numerator of the jitter contains a portion that derives from the intrinsic *shot noise* of the sensor N_{SN}. This term is a consequence of the discreteness of the electron charge and derives from the time-dependent fluctuations in the current produced by the electric charges motion in the junction of a semiconductor. The shot-noise spectral density increases quadratically with the leakage currents of the sensor (50) at lower frequencies, and linearly at higher frequencies. Gen-

erally, in sensors with no gain, the shot-noise represents a negligible part of the total fluctuations, and can be mitigated with the choice of a proper operation point. For sensors with gain, a more detailed description will follow in section 1.3.2. In detector with no gain this contribution is much less relevant than the Landau fluctuation, as described in section 1.1.3.

By neglecting the shot-noise term, Eq. 1.4 can be rewritten as:

$$\sigma_{jitter} \simeq \frac{N_{el}}{dV/dt}. \tag{1.5}$$

From Eq. 1.5 one can notice that a reduction of the the jitter is achieved by balancing low electronic noise with fast rising signals. A fast slew-rate of the rising pulses leads to a well defined threshold crossing in the comparator. For obtaining large slew-rates, the pre-amplification stage of the read-out necessitates high-bandwidth components. Unfortunately, the electronics noise levels are related to the frequency through the proportionality:

$$N_{el} \propto \sqrt{BW} \propto \frac{1}{\sqrt{t_{rise}}}, \tag{1.6}$$

where BW indicates the pre-amplifier bandwidth. At the same time, the slope of the rising signal is intrinsically proportional to the inverse of the time required to reach the pulse's maximum. Their relation can be expressed through:

$$\frac{dV}{dt} \propto V_{max} BW \simeq \frac{V_{max}}{t_{rise}}, \tag{1.7}$$

where V_{max} is the amplitude of the signal's output by the amplification stage. Finally, the jitter can be formulated using the following expression:

$$\sigma_{jitter} \simeq \frac{N_{el}}{dV/dt} \simeq \frac{N_{el} C_{det}}{Q_{tot}} t_{rise} \quad . \tag{1.8}$$

Using its definition, V_{max} was expressed as the ratio between the total charge collected over the capacitance of the detector; Eq. 1.8 validates our first assumptions, highlighting the parameters to optimize for reducing the total jitter. To reduce this contribution, the design of a read-out has to provide large signals affected by low electronic noise, and steep rise-times. In addition, the

capacitance of the sensor plays an important role in the optimization. Analyzing Eq. 1.8 one can observe $\frac{Q_{tot}}{e_n C_{det}}$ being the SNR of the detector. It is important noticing that this is an approximation, and requires assuming a constant slew-rate dV/dt. Under this approximation, the jitter becomes:

$$\sigma_{jitter} \simeq \frac{N_{el}}{dV/dt} \simeq \frac{t_{rise}}{SNR}. \tag{1.9}$$

This approximation loses its validity in the case of irradiated sensors, where the shape of the signals is distorted (further discussed in section 1.3.3). This operational definition is often used for characterizing the design of the read-out electronics for precise timing detectors. This process is a result of a fine balance between the discussed parameters, that optimizes the signals slew-rate and the noise levels.

In practice, this requires an attentive design of the amplification and shaping circuit. The bandwidth of the electronic components should be chosen to prevent distortion of the signals rise-time, while at the same time, minimize the noise spectrum. The input capacitance, and impedance of the read-out has to be adapted to the senors properties: the input time constant of the pre-amplification stage is designed not to limit the rising and integration time of the pulses.

1.1.3 Intrinsic noise contribution of the sensor

One intrinsic limit to time precision comes from the fluctuations of the particles energy deposition. The uniformity of the signals is affected by the density of ionization processes that change for each event. The resulting difference in charge depositions (local and total) contributes to the variation of the signals amplitude and to its shape irregularities.

1.1.3.1 Total ionization: the Time Walk effect

Derived by the fluctuations in the total charge depositions, the time walk ($\sigma_{TimeWalk}$) represents one of the main contributors to the degradation of the time resolution. This effect indicates the time difference in crossing a static threshold for signals with different amplitudes. The delay in time between simultaneous pulses at different magnitude can be observed in Fig. 1.3. Although this effect can be minimized by choosing an optimized threshold and improving the signal rise-time, this factor has to be corrected off-line, with the implementation of dedicated algorithms.

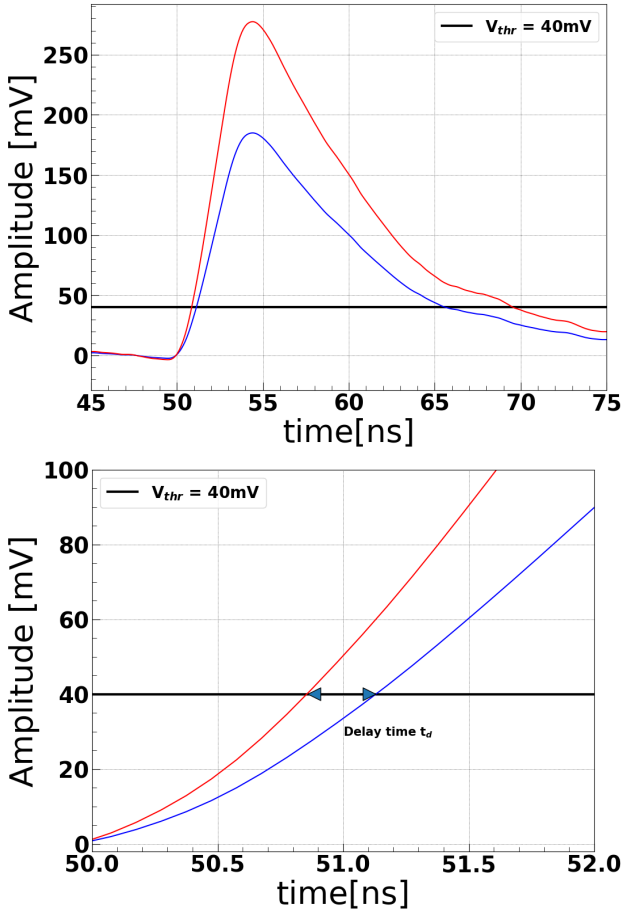

Figure 1.3: The plot shows how simultaneous pulses crossing a static threshold, and describes the amplitude dependence on the reconstruction of the crossing time; the trigger of the comparator fires when the amplitude of a pulse exceeds the set value.

Section 1.1.4 provides more details about the used algorithms.

1.1.3.2 Local ionization: the Landau fluctuations

An irreducible noise contribution to the time measurement is represented by the fluctuations of the energy deposit in the detector. This effects results in localized ionization phenomena causing non-uniformity in the collection of the charge. The shape variations generated in the spectra are called *Landau noise*, representing the intrinsic limit in the time resolution of semiconductors. An example of charge deposit distribution inside a silicon sensor is displayed in Fig. 1.4. The Landau noise cannot be reduced through the bias voltage, and its effect scales inversely with the sensors thickness. This last property is of crucial importance when selecting the size of the silicon detectors: the energy distribution fluctuations may represent the largest timing uncertainty

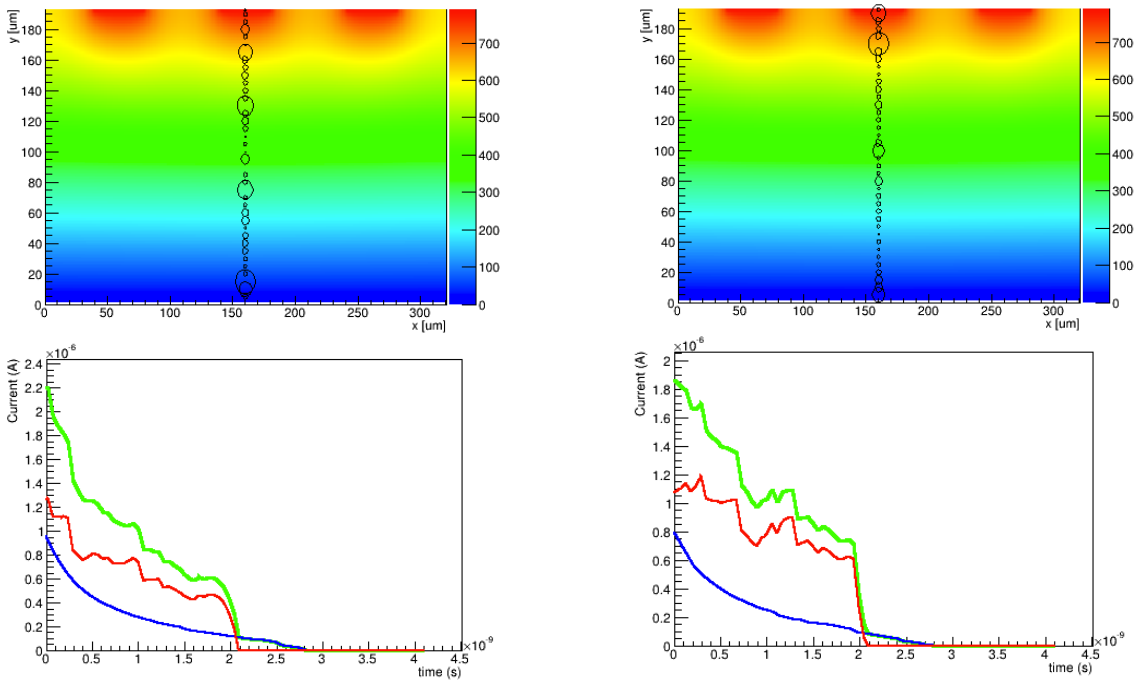

Figure 1.4: In the top panels, the cross section of a silicon sensor displays the local energy distributions along the track of a MIP (3). The current of holes (in blue) of the electrons (in red), and the total current (in green) are displayed in the bottom panels. The non-uniform shape of the currents is due to the Landau-like structure of the ionization process.

when using thinner sensors. $\sigma_{Local\,Ionization}$ comes from the nature of the ionization process inside the silicon bulk and it constitutes the ultimate intrinsic limit to the uniformity of the signal rise-time. The Landau noise affects sensors with and without gain. However, in later sections We will present how LGADs mitigate this contribution, and achieve excellent resolution using thin silicon substrates.

1.1.3.3 Distortions and non-uniformity

The charge carriers drift inside a semiconductor with a maximum velocity determined by the external bias, which is limited by the saturation velocity in the medium (see section 1.2.2). The current signal induced on the detectors electrodes is proportional to the carriers velocity. For achieving a good uniformity on the signals rise time distribution, the drift velocity of the charges has to be kept constant. According to the Shockley-Ramo theorem (51), the induced current is

proportional to the weighting field E_w[1]. Although the field should not vary with the position of the incident radiation, the detectors can experience a reduction of the intensity around its edges of the implants inside the bulk.

However, the effect is limited manufacturing the implant layers with sizes comparable to the pitch of the sensor. While this can be a delicate parameter in the production of other types of detectors, the intrinsic thickness of the LGAD sensors drastically reduces the contribution of this effect. For example, the sensors used by the ETL project (described in section 2.2.3) are pads of $1.3 \times 1.3\,\mathrm{mm}^2$size, with a thickness of 50μm. In this configuration the sensor effectively emulates the behaviour of a parallel plate capacitor, and allows to neglect this contribution. In addition, the uniform motion of the charges inside the silicon can be ensured setting the detector bias to voltages large enough to saturate the drift velocity. This value depends on the condition of detector operation (such as the temperature), and the absorbed fluence.

1.1.4 Digitization and data processing

Section 1.1.3 and 1.1.2 describe the contributions of the sensor and read-out electronics to the uncertainty affecting the time reconstruction. The best mitigation is achieved optimizing the quantities playing a role in the final calculation. For recording and analyzing the detector response, the waveforms have to be digitized and post-processed. This requires the use of suitable electronic devices and reconstruction algorithms.

Ideally, finely sampling the pulses represents the preferred data collection technique. The use of fast Analog-to-Digital Converter (ADC) provided of good resolution allows for the best offline reconstruction of the signals in the time domain. The high-bandwidth and sampling rate characteristic of such devices ensures to preserve the shape of the analog waveforms output from the read-out. This is of crucial importance for the purpose of precise timing measurements: distortions in the shape of the pulses can degrade the rise-time and increase the jitter. Commercially available oscilloscopes are optimal options for testing purposes: these device can offer great sampling rate and bandwidth performance, as well as the possibility of visually monitoring the waveforms. Modern oscilloscopes are provided of operative systems to run native or custom ac-

[1]The weighting field is the component of the external field pointing in the direction of the charges motion. This definition requires the assumption that a single electrode in the system is raised to unit potential, while the others in the system are grounded.

quisition software and stored data locally or remotely. However, digitizing, recording, and storing an oscilloscope active channels can be a time and memory consuming procedure. At high rates, the capabilities of these devices are limited by the rearm time of the acquisition system. Moreover, the applications of these instruments are capped by the cost and technical complications of scaling such technology to larger numbers of input channels.

For these reasons, timing measurements in physics experiments are often performed by discriminators, followed by Time-to-Digital Converters (TDCs). In these acquisition chains, discriminators are devices producing a standardized digital output for each input pulse crossing a set thresholds, while TDCs generate digital signals embedding information on the time of an occurrence. For example, a TDC can provide the timestamps of the leading and trailing edges of a discriminator output signal. Although this doesn't allow accessing further information of the initial analog waveforms, TDCs are the most common instruments for reconstructing the particles time of arrival in HEP experiments. In Eq. 1.3 the TDC contribution to the uncertainty of a timing measurement is reported in This factor depends on the minimum resolution of the TDC; an estimation can be obtained assuming a uniform resolution on each bin of the device. Using the definition of variance for a flat, uniform distribution ($\sigma^2 = \frac{1}{12}(b-a)^2$), one can express it as:

$$\sigma_{TDC} = \frac{1}{\sqrt{12}}(Binwidth) \quad , \tag{1.10}$$

where the $Binwidth$ indicates the minimum resolution of the TDC.

From the recorded data it is possible to compute the time of arrival. However, every stage of the data collection (from the sensor to the sampler), adds contributions to the noise spectrum. Some of these contamination can be mitigated using propering filtering and smoothing procedures:

- *lower frequency fluctuations* can be removed subtracting the average of samples in the sideband areas of the recorded pulse. The RMS of the baseline profile will be subjected to a shift and consequently be centered around zero.

- *Higher frequency fluctuations* smear the data distribution, directly affecting the slew-rate and, in turn, the jitter. It requires the data to be processed with low-pass filters. While many n-th

orders filtering options are offered by computing libraries, custom made filters are often obtained with the convolution of individual pulses with fast decreasing functions. A common example is the convolution of the signals with functions in the form of $\frac{sin(x}{x}$. One of the filter methods chosen for this work of thesis was a sinc-filter of the form (52):

$$sinc(t) = C\frac{sin(2\pi ft)}{2\pi ft}, \tag{1.11}$$

where C is a normalization constant, and f is the filter's cut-off frequency. The choice of this parameter depends on the detector response, and its application. The filtered signals can still be affected by distortion affecting the definition of important signal features.

- Additional *data smoothing* can be implemented using moving averages, which step can be decided accordingly to the sampled points. These filtering procedures have to be carefully optimized for avoiding losing information on the parameters of the distributions. A severe smoothing could smear data points around the maximum or near the threshold crossing.

An example of the implementation of the filtering and smoothing procedures is displayed in Fig. 1.5. For this example, an LGAD was used to detect the passage of $\sim$0.55 MeV electrons. The generated pulses were reconstructed and processed through the three stages of data filtering described using a custom-made analysis framework.

Finally, the definition of a crossing time has to take into account the effects of the time walk (introduced in section 1.1.3) due to the use of a static threshold. Two off-line methods are reported in this section.

1.1.4.1 Constant Fraction discriminator (CFD)

dynamically selects the threshold to define the time crossing of a pulse. This effect is better explained using a signal, and an attenuated copy of itself. The attenuation factor is indicated as f. Both signals are input to a comparator. The main signal is delayed, with respect to the attenuated one, which works as the comparator threshold. A scheme is provided in Fig. 1.6. Assuming, for

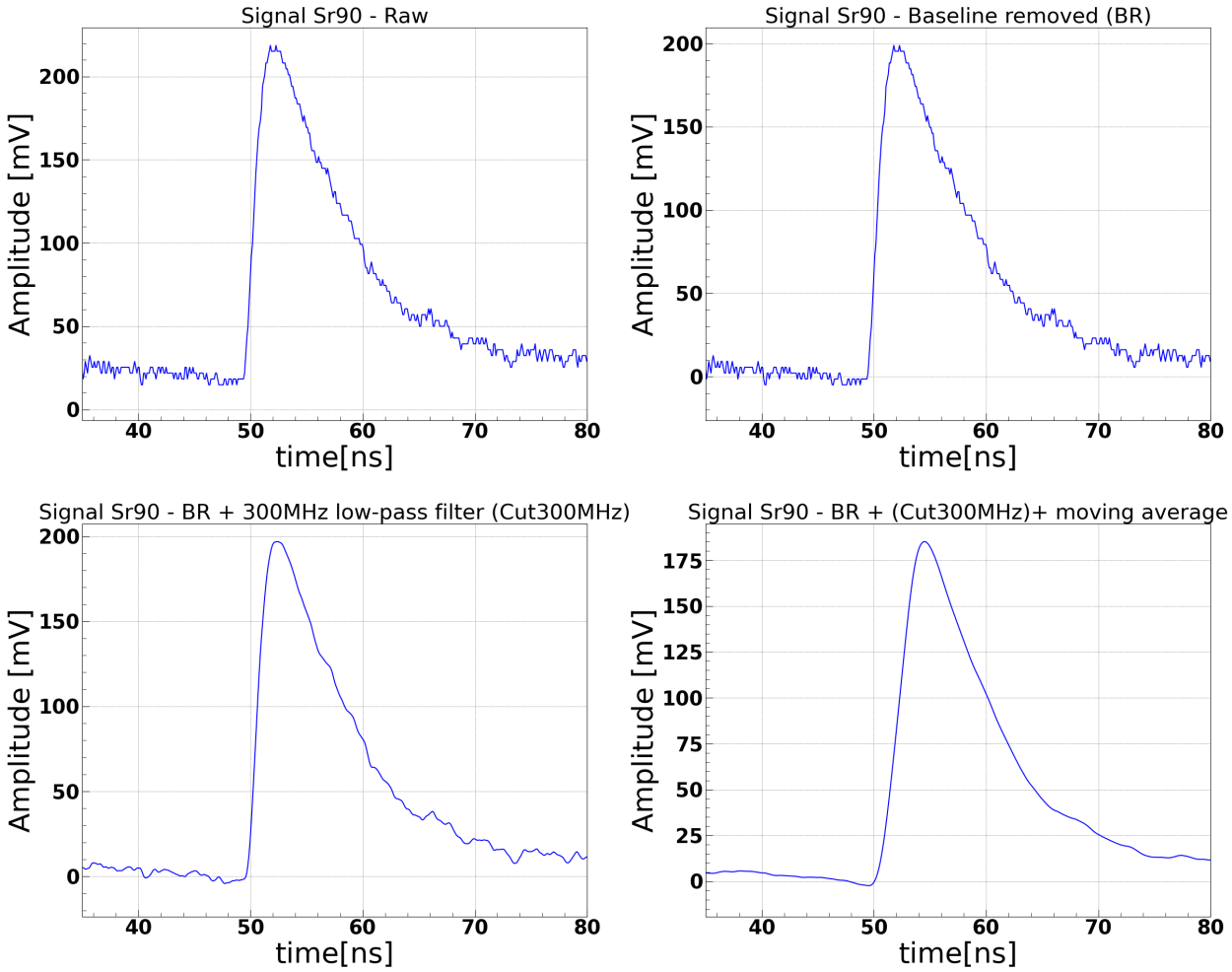

Figure 1.5: Pulse generated by electrons crossing a LGAD. Each panel of the image shows a step of the data processing. The raw data is displayed in the top left panel. Firstly the DC offset is removed and the signal's baseline shifted to 0 V (Top left panel). Then a low-pass filter with a cut-off frequency of 300 MHz is applied (bottom right panel). A moving average using 10 samples per step is used for a final data smoothing (bottom right panel).

simplicity a linear leading edge of the signal one defines:

$$V(t) = \begin{cases} V_0 \frac{t}{t_{rise}} & for \quad t \leq t_{rise} \\ V_0 & fort \geq t_{rise} \end{cases} \tag{1.12}$$

The signal applied to the input can be therefore expressed as:

$$V(t) = \frac{t - t_{delay}}{t_{rise}} V_0, \tag{1.13}$$

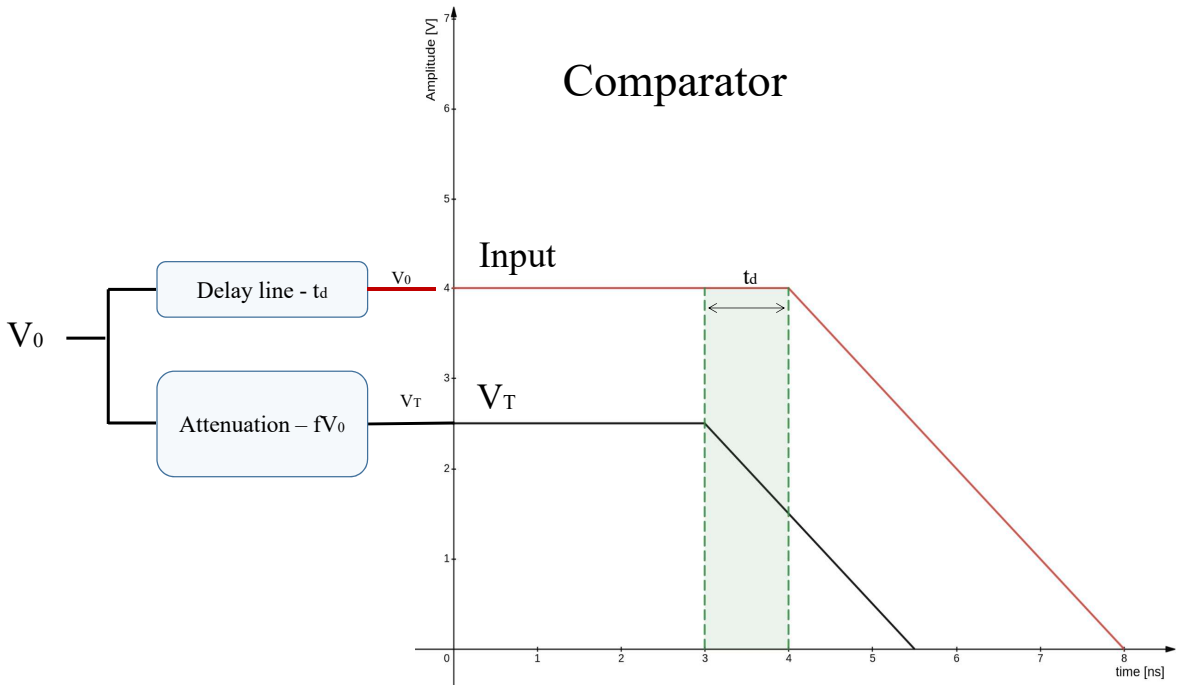

Figure 1.6: Schematic design of a CFD: the same signal is split into two lines. The first one is attenuated and used as the comparator threshold. The second one is delayed, for waiting the threshold to rise to its maximum.

Where t_{delay} is defined as the difference between the real crossing time and the one reconstructed by the system. It is possible to use f so that $V(t) = \frac{t-t_{delay}}{t_{rise}} V_0 f$. One can define the time when the comparator fires as:

$$t = f t_{rise} + t_{delay} \qquad for \quad t_{delay} > t_{rise}. \tag{1.14}$$

Setting t_{delay} such as the two initial pulses overlap, it is possible to rewrite the threshold V_T as:

$$V_T = f \frac{t}{t_{rise}} V_0. \tag{1.15}$$

We can write the equality:

$$f \frac{t}{t_{rise}} V_0 = \frac{t - t_{delay}}{t_{rise}} V_0 \,. \tag{1.16}$$

Therefore, it is possible to finally write the crossing time independently from the signal amplitude:

$$t = \frac{t_{delay}}{1-f}. \tag{1.17}$$

However, for non-linear rising edges, the choice of the correct fraction depends on the shape of the rise-time of the pulse. The fraction f is experimentally selected to maximize the slew-rate at the crossing point so that the jitter is minimum. Computationally, the choice of f usually results from a scan of the optimal fractions of the signal amplitudes.

1.1.4.2 Time Over Threshold (TOT)

Conversely to the previous case, this method does not require the identification of the pulse's amplitude, rather its width. Like before, the analytical form of this quantity usually fails in describing complicated structures. However, it can be attempted to provide a generalized definition. This method attempts to find a correlation between the real crossing time, and the time difference between the signal's trailing and leading edge to fire the trigger of a comparator. Two independent measurements are performed. The leading edge crosses a static threshold at time t_{LE}, and the trailing edge at t_{TE}. We can define a function $\phi(t_{tot})$ such that $t_{cross} = t_{th} + \phi(t_{tot})$. In this equation t_{cross} represents the real crossing time, and $t_{tot} = t_{TE} - t_{LE}$. The best fit to the relationship between the individual quantities and the TOT, provides the function to use for the correction. Figure. 1.7 shows an example of the use of TOT for the extraction of the crossing time of an LGAD signal. This algorithm is often used when correcting data collected with TDCs, where it evaluates the TOT between the leading and trailing edges of discriminated pulses. The correction function is then expressed through correlation between the TOT and the leading or trailing edges reconstructed time. Both described methods are widely used in particle physics, displaying great capabilities in the minimization of the time-walk. The analysis presented during the rest of the thesis employs the use of the CFD method for extracting the crossing time from sampled data. However, parts of the discussion presented in chapter 2 recall the use of TDCs and TOT corrections.

This section provided the basic knowledge for a comprehensive understanding of how timing measurements are performed. The listed contributions affecting the precision of the measurement are valid for any type of detector based on semiconductor technology. However, the rest of this

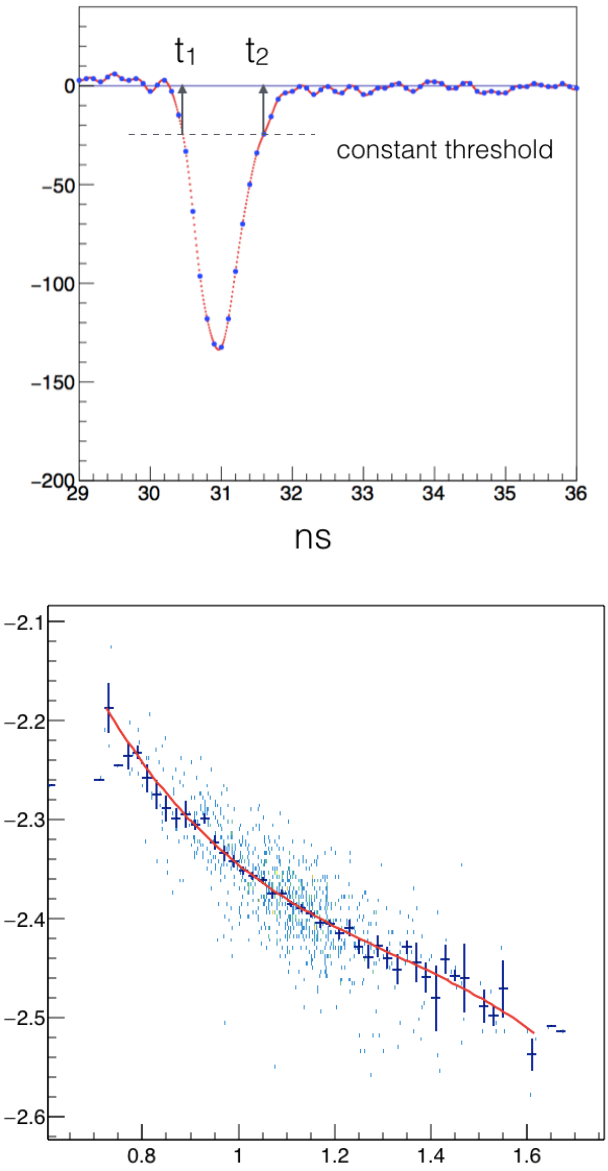

Figure 1.7: Top panel: Measurement of the leading and trailing edge crossing time of an LGAD pulse. Bottom panel: Correlation between the Leading Edge (LE) crossing time, and the TOT information.

document will focus on the use of silicon devices, in particular of LGADs. The next part of this chapter will describe the structure, and features of semiconductors, as well of their use for particle detection.

1.2 Silicon detectors

Silicon is the main semiconductor used in the production of particle detectors, commercial sensors, and electronic components. Its production process is well understood, as well as its electrical properties. It stands out among all semiconductors thanks to its great versatility, and availability. It is characterized by a low ionization energy, high carriers mobility and, in latest productions, a great radiation tolerance. This section introduces the reader to the concept of charged particle detection, describing the properties of semiconductor devices. After an introduction on the structure of semiconductors, the discussion focuses on particle interacting with matter. At last, the reader will be introduced to the principle of operations of silicon particle detectors.

1.2.1 Electronic band structure

The electrons residing in the atomic shells occupy discrete levels of energy, according to the Pauli exclusion principle. Multiple atoms are brought together to form a crystal's lattice. The electromagnetic forces acting on the electrons cause the formation of new levels, or ' bands', characterized by a continuous spectrum of energy. Inside the crystal, the atomic orbitals overlap with the ones from neighboring atoms. The valence electrons, the ones in the outer shells, are the ones mostly contributing to the chemical bondings.

The electrons occupies energy levels starting from the ones at lowest energies. The energy difference between the highest and lowest occupied states of a system of non-interacting fermions (this nomenclature is better explained in section 2) is called Fermi energy[2]; it can be defined when the temperature of the quantum system is at the absolute zero, and it helps defining the concept of valence, and conduction bands. The first available energy band exceeding the Fermi energy is called *conduction band*. The first band below the Fermi level filled by the fermions is called *valence band*.

The width of each of these bands depends on the width of the overlapped orbitals. The range of energies not populated by the atomic electrons are referred to as 'band gaps', and contribute to the electrical properties of the material. Fig. 1.8 describes the three different configurations of a solid. In the leftmost case, the sketch describes a conductor (or metal). This is the scenario where

[2]The Fermi energy can be defined for quantum systems of non-interacting fermions when T = 0 K.

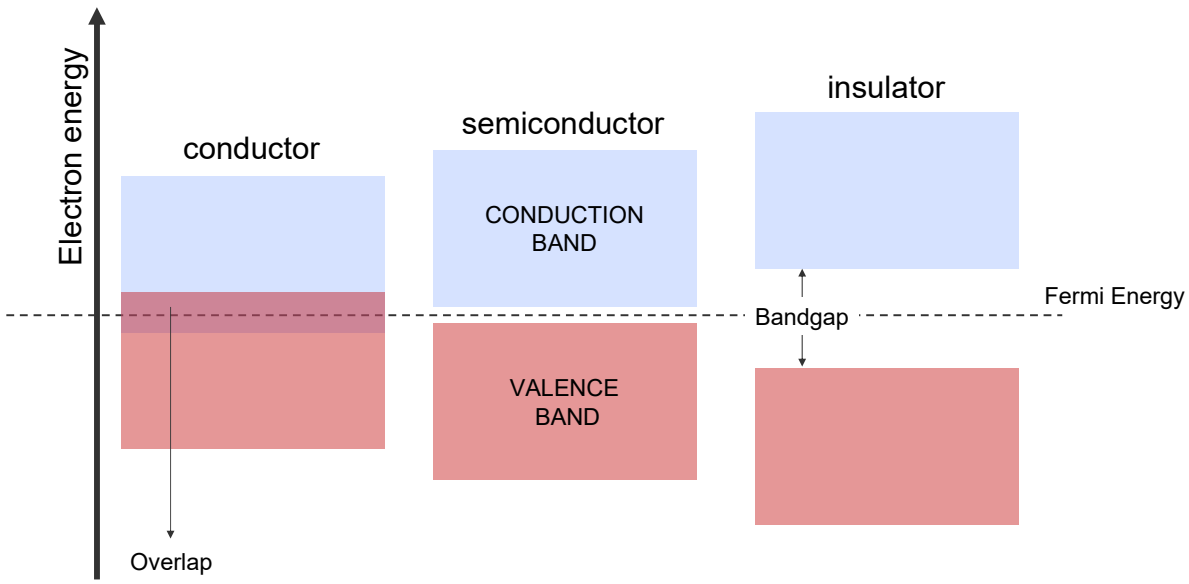

Figure 1.8: Simplified sketch of the electrical band structure for insulators, conductors, and semiconductors.

the bandgap is small or non-existent. The valence and conduction bands can overlap and a significant amount of electrons can transition to conduction with no need of thermal excitation. The rightmost case of Fig. 1.8 describes the behaviour of insulators. In this case, the electrons motion is limited by the tight bounds between the atoms in the crystal. They are characterized by larger band-gaps and require large thermal energy for an electron to jump into the conduction band. Lastly, the central part of Fig. 1.8 illustrates the structure of semiconductors. These are characterized by bandgaps width between the ones of conductors and insulators. While at absolute zero temperature no electron can occupy the conduction band, small thermal fluctuations (e.g. room temperature) can provide enough energy for electrons to migrate to the conduction band.

Silicon is the most known semiconductor of the periodic table for its employment in technological applications. In its atomic structure, 4 electrons are loosely bound to its outermost orbitals. Of these, two belongs to the p-shell and 2 belong to the s-shell. When bringing two atoms of

silicon together, the 8 valence electrons contribute to the reaction creating two bands in correspondence of the two sub-shells (s, and p). These two bands are the conduction (higher energy), and the valence (lower energy) bands (53). The gap between the silicon bands is of 1.12 eV. Semiconductors are widely used in the production of electronic devices, thanks to their two regimes of operation: conduction, and insulation. When an electric field is applied to the bulk of a semiconductor, charges can flow between the two bands, creating moderate currents. However, the electrical properties of semiconductors can be modified by the addition of impurities in the crystal lattice. The next section 1.2.2 will discuss the characteristics of *doped* semiconductors, and the technological advantages of controlling the charge flow inside their structure.

1.2.2 Electrical properties of semiconductors

Other band configurations can be achieved ' doping' the structure of a semiconductor. A doped semiconductor is a semiconductor where specific concentrations of impurity atoms have been added for modifying the electron or holes density in its substrate[3]. These impurities are added for donating or accepting extra electrons to the crystal lattice. We refer as *n-type* to materials presenting a majority of negative charge concentration. That can be achieved adding states that are closer to the conduction band (or *donors*), increasing the probability of ' donating' loosely bound electrons to the conduction band. For example, adding arsenic impurities (5 valence electrons) in a silicon substrate (4 valence electrons) creates a single loosely bound electron caused by the covalent bonds of the two elements.

Conversely, in a *p-type* semiconductor the majority of the carriers are positive charges. In this case, the impurities add levels closer in energy to the valence band. These *acceptors* create a vacancy resulting from the covalent bonds (for examples boron, which has three valence electrons) that is filled by one of the electrons. This process generates a positively charge *hole* in the valence band. The two types of doping configurations determine the shape of the final electrons and holes currents, as the carriers motion differs in the two cases. Section 4.4.1 reports studies on the compared performance of detector based on n and p-type semiconductors.

Inside semiconductors, the constant scattering of electrons with the elements of the lattice (e.g. atoms, impurities) generates a thermal motion of the charges. Although the total net displacement

[3]We refer as *substrate* to the bulk of the semiconductor material.

is null, electrons move in every direction with a mean free time defined as $\bar{t}$. When an external electric field is applied to the semiconductor, electrons and holes start gaining momentum, drifting in opposite directions. The *drift velocity* is a property of the material, and depends on the applied field. It can be expressed as:

$$v_d = -\left(\frac{q\bar{t}}{m}\right)E\,, \tag{1.18}$$

Where m is the effective mass[4] of the electron. The term $\left(\frac{q\bar{t}}{m}\right)$ is called mobility and varies between holes, and electrons ($\mu_{e,h}$). Due to the higher effective mass, the mobility of the holes is lower than the electrons one (54). Experimentally, the drift velocity is known to saturate when, increasing the external field, the charges are subjected to increasing scattering collisions. The maximum achievable velocity by electrons (and holes) in a certain material is called *saturation velocity* (52). Including its contribution, the drifting velocity can be expressed as:

$$v_d = -\left(\frac{\mu E}{1+\frac{\mu E}{v_s}}\right)E. \tag{1.19}$$

The mean free time of consecutive collisions can be affected by the interaction with impurities inside the crystal. In this scenario, the moving charges can undergo Coulomb interaction with a dopant impurity (55). Table 1.1 reports a summary of the most important electrical characteristics of silicon. The features listed are some of the quantities that will be addressed in later chapters for describing the results obtained using silicon detectors. We will describe how free charges are generated through ionization processes in the semiconductor; given a fixed amount of energy deposited in the sensor, the magnitude of the currents moving through the substrate is determined by the minimum energy for creating free electrons-holes pairs $E_{e/h}$. The carriers drift determines the currents shape, and duration. The discussion about the carriers mobility, and drifting velocity provides an insight of the capabilities of fast silicon sensors. Together with the material permittivity ε_r (proportional to the sensor's capacitance), these features decide the overall response of the material to incident radiation.

In conclusion, the manufacturing quality of the sensor determines the final electrical properties of the detector. These are the foundation for the development of a performing semiconductor

[4]The effective mass of an electron inside a semiconductor can be defined as the mass that contributes to its interaction with other identical particles belonging to the thermal distribution.

Silicon electrical properties

E_g	Band Gap (eV)	1.12
E_b	Breakdown field ($\frac{\mathrm{V}}{\mathrm{cm}}$)	3×10^5
ρ_{el}	Resistivity ($\Omega\,\mathrm{cm}$)	2.3×10^5
ρ	Density ($\frac{\mathrm{g}}{\mathrm{cm}^3}$)	2.33
$E_{e/h}$	Energy to create e/h pair (eV)	3.6
E_{MIP}	Most probable energy released by MIP ($\frac{\mathrm{MeV}}{\mathrm{cm}}$)	3.21
$E_{e/h}$	Most probable number of e/h pair created by MIP ($\frac{\mathrm{N}}{\mu\mathrm{m}}$)	89
μ_e	Electron mobility ($\frac{\mathrm{cm}^2}{\mathrm{Vs}}$)	1350
μ_h	Holes mobility ($\frac{\mathrm{cm}^2}{\mathrm{Vs}}$)	480
v_e	e saturation velocity ($\frac{\mathrm{cm}}{\mathrm{s}}$)	$\sim 10^7$
v_h	h saturation velocity ($\frac{\mathrm{cm}}{\mathrm{s}}$)	$\sim 7.5\,10^6$
ε_r	Relative permittivity	11.9
T_d	Displacement threshold energy (eV)	36

Table 1.1: List of the main electrical properties of silicon. Table modified from Ref. (46)

particle detector.

1.2.3 Charged particles interacting with matter

The energy deposited by a particle along its track inside a material can be studied for reconstructing information about the nature of the particle itself. An example can be found in discussions reported in chapter 4, where the distribution of energy loss in silicon detectors is used as a key identification factor for particles and ions. When a charged particle crosses a medium, it loses energy along its path. This process occurs through the interaction with the material, which can happen due to multiple effects. The type of medium, as well as the energy of the incident particle determines the type of interaction.

The energy exchanged by charged particles through solid medium is usually characterized by the ionization of the material's atoms[5], excitation of the bound electrons, and the generation of free charge carriers. Given the density of the material, the amount of energy lost per unit of space is modeled by the Bethe-Bloch equation, given in Eq. 1.20. The equation describes a particle with an initial velocity v, energy E, and charge z. The material is characterized by an atomic number Z, and atomic weight A (56). The material can be described as an electron gas with density ρ, and

[5]The process where the energy of incident particles is sufficient to strip electrons from the atoms outer shells.

ionization potential I.

$$-\langle\frac{dE}{dx}\rangle = 4\pi N_a r_e^2 m_e c^2 \rho \frac{Z}{A}\frac{z^2}{\beta^2}\left[\frac{1}{2}\ln\left(\frac{2m_e c^2\beta^2\gamma^2 T_{max}}{I}\right) - \beta^2 - \frac{\delta}{2}\right]. \tag{1.20}$$

In Eq. 1.20, $\beta = \frac{v}{c}$ is the ratio between the particle velocity and the speed of light, $\gamma = \frac{1}{\sqrt{1-\beta^2}}$ is the Lorentz relativistic factor. Additionally, $N_a = 6.022{\cdot}10^{23}\, mol^{-1}$ represents the Avogadro number, or the number of atoms per gram atom. $m_e = 0.511 MeV$ is the electron mass, and $r_e = \frac{1}{4\pi\varepsilon_0}\cdot\frac{e^2}{m_e c^2}$ its classical radius. Eq. 1.20 represents the relativistic extension of the classical Bethe equation. It describes the energy loss when the incident particle relativistic $\beta \to 1$. For example, the maximum kinetic energy that can be transferred to a free electron during a single collision inside the material is $T_{max} = \frac{2m_e p^2}{m_0^2 + m_e^2 + 2m_e E/c^2}$. However, when the mass of the incident particle exceeds the one of the electron $m_0 \gg m_e \implies T_{max} \approx 2m_e c^2\beta^2\gamma^2$. The last part of the equation, depending on δ, describes the density effects. With the increasing of the incident particle's energy, the dominant term of the equations becomes the one depending on the distant-collisions contributions ($ln\,\beta\gamma$). Due to the polarization of the material, the extension of the field is truncated, killing the resultant logarithmic rise. The stopping power as a function of the particle $\beta\gamma$ is displayed in Fig. 1.9. Eq. 1.20 is an approximation derived by perturbative quantum mechanics calculations, which model the absorbing material as an electron gas.

Although it neglects a number of effects (e.g bremmstrahlung, pair production, nuclear collisions), the equation represents an accurate operative tool. It used for the prediction of energy loss of charged particles in a regime of energy that spans nine orders of magnitude (see Fig. 1.9). The equation is particularly useful for describing the stopping power for particles with $\beta\gamma \simeq 3$, corresponding to the curve's global minimum. Particles around the minimum, are called Minimum Ionizing Particles (MIP) and are characterized by rather similar energy loss rates of $-\frac{dE}{dx} \simeq 2\frac{MeV}{g\,cm^{-2}}$, depending only on the material density. It has to be noted that the Bethe-Bloch equation approximates the stopping power for thin absorbers, where few collisions occur, and the total energy loss has a large variance.

For this reason, the Bethe-Bloch is not well defined when describing the energy losses of individual particles. Is is instead used for bulk deposit of radiation (e.g. dosimetry). For a generalization to absorbers of moderate thickness, the energy loss probability distribution is better described

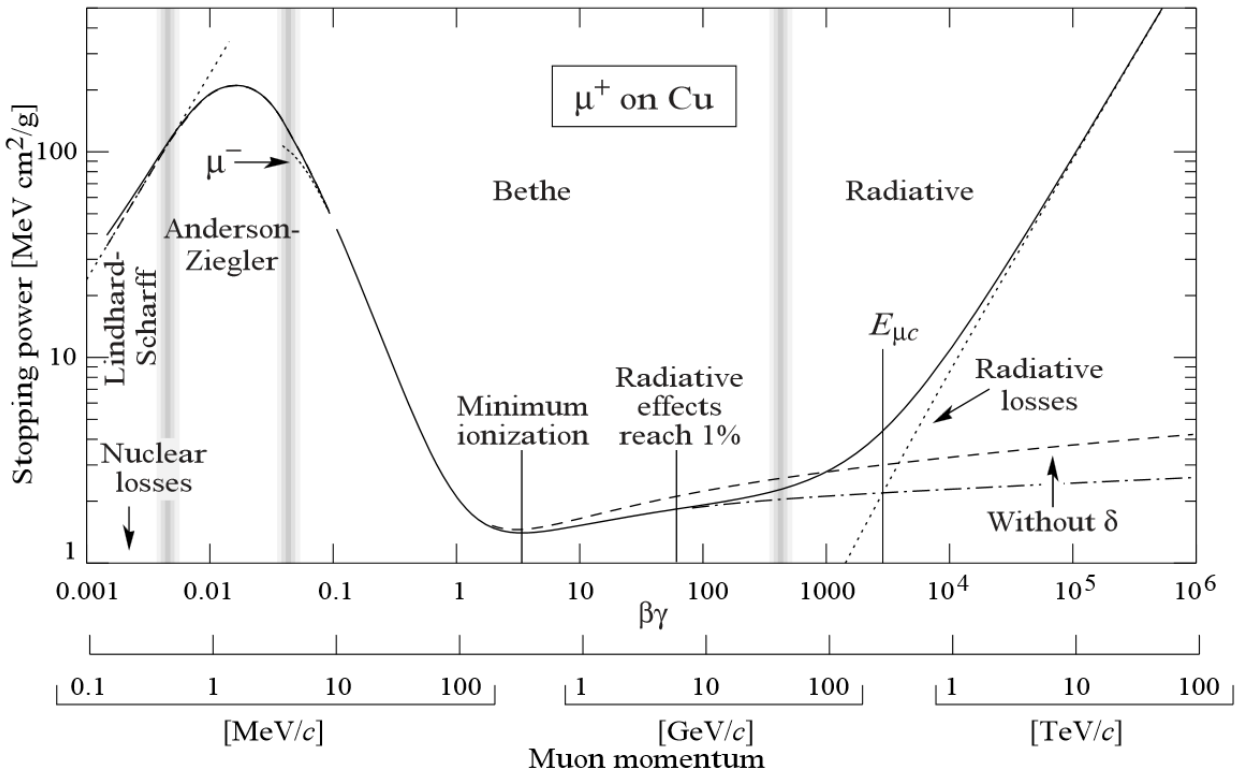

Figure 1.9: Energy loss $-\langle\frac{dE}{dx}\rangle$ in copper as a function of the $\beta\gamma$ of positive muons (4)

by the non-symmetric Landau-Vavilov distribution (56). The Most Probable Value (MPV) of the energy loss can be found solving $L(\lambda) = \frac{1}{2\pi}e^{-\frac{1}{2}(\lambda+e^{-\lambda})}$, where $\xi = 4\pi N_a r_e^2 m_e c^2 \rho \frac{Z}{A}\frac{z^2}{\beta^2}x$. In this context, $\lambda = \frac{\Delta E - \Delta E_p}{\xi}$, where ΔE_p represents the MPV. The energy loss distribution can be rewritten as:

$$\Delta E_p = \xi\left[\ln\left(\frac{2m_e c^2\beta^2\gamma^2 c^2}{I^2}\right) + \ln\frac{\xi}{I} + 0.2 - \beta^2 - \delta\right]. \tag{1.21}$$

Eq. 1.21 is of fundamental importance for modeling the fluctuations of the energy loss of charged particles crossing a detector of thickness x. As opposed to the Bethe-Bloch formula, the Landau distribution takes into account the fluctuation of large energy transfers by single collisions. This extends the tails of the distribution, resulting in a highly-skewed shape of the energy loss. When describing detectors used in HEP experiments (for example in chapter 2), Eq. 1.21 can be computed for extracting the MPV of MIPs passing through a thin silicon layer. Using a MPV energy released in silicon by MIP of 3.21, extracted from table 1.1, and a sensor of thickness of thickness 50 μm,

one can calculate:

$$\Delta E_p(Si,50) \simeq 3.21 \frac{MeV}{cm} \times 50 \simeq 16\,KeV \tag{1.22}$$

Eq. 1.22 describes the energy deposit of a MIP crossing 50 μm of silicon. This configuration describes a common scenario in particle physics experiments where incident energetic particles are detected with the use of thin silicon detectors. This process happens when the energy losses ionize the medium creating free carriers moving through the sensor. The generated charge can be collected and studied. This conversion is at the basis of particle detection with semiconductors and is used throughout this thesis for timing and particle identification purposes.

For understanding how the energy loss can be converted in a measurable physical quantity, we first need to get a grasp on the principle of operation of particle detectors. This thesis will focus on the description of the functionalities of detectors based on semiconductor technology.

1.2.4 Principle of operation

When semiconductor materials of opposite type are brought together, one can form a new structure called ' junction'. The gradient deriving from the contact of regions with excess of holes, and excess of electrons creates a movement between the charges (diffusion). In this scenario, holes are attracted by the negative area, while electrons flow towards the positive region. The recombination of the carriers crossing the junction creates a potential difference, which remains locally stable thanks to the ionization process of the acceptors and donors. Thanks to this newly produced static charge, the potential increases and then reaches the equilibrium, preventing further flowing of the carriers. The new stable region does not contain free charges and it is known as ' depletion region'. This process is schematized in Fig. 1.10.

The potential (or built-in potential VB_i) for achieving the equilibrium in the charge flows is a property of the materials, and only depends on the doping concentrations and temperature. The VB_i of silicon is about 0.7 V. The width of the depletion region can be calculated solving the Poisson's equation as discussed in (57). One obtains:

$$W = \sqrt{\frac{2\varepsilon_0}{q}\left(\frac{N_A + N_D}{N_A N_D}\right)\Delta V} \quad ; \tag{1.23}$$

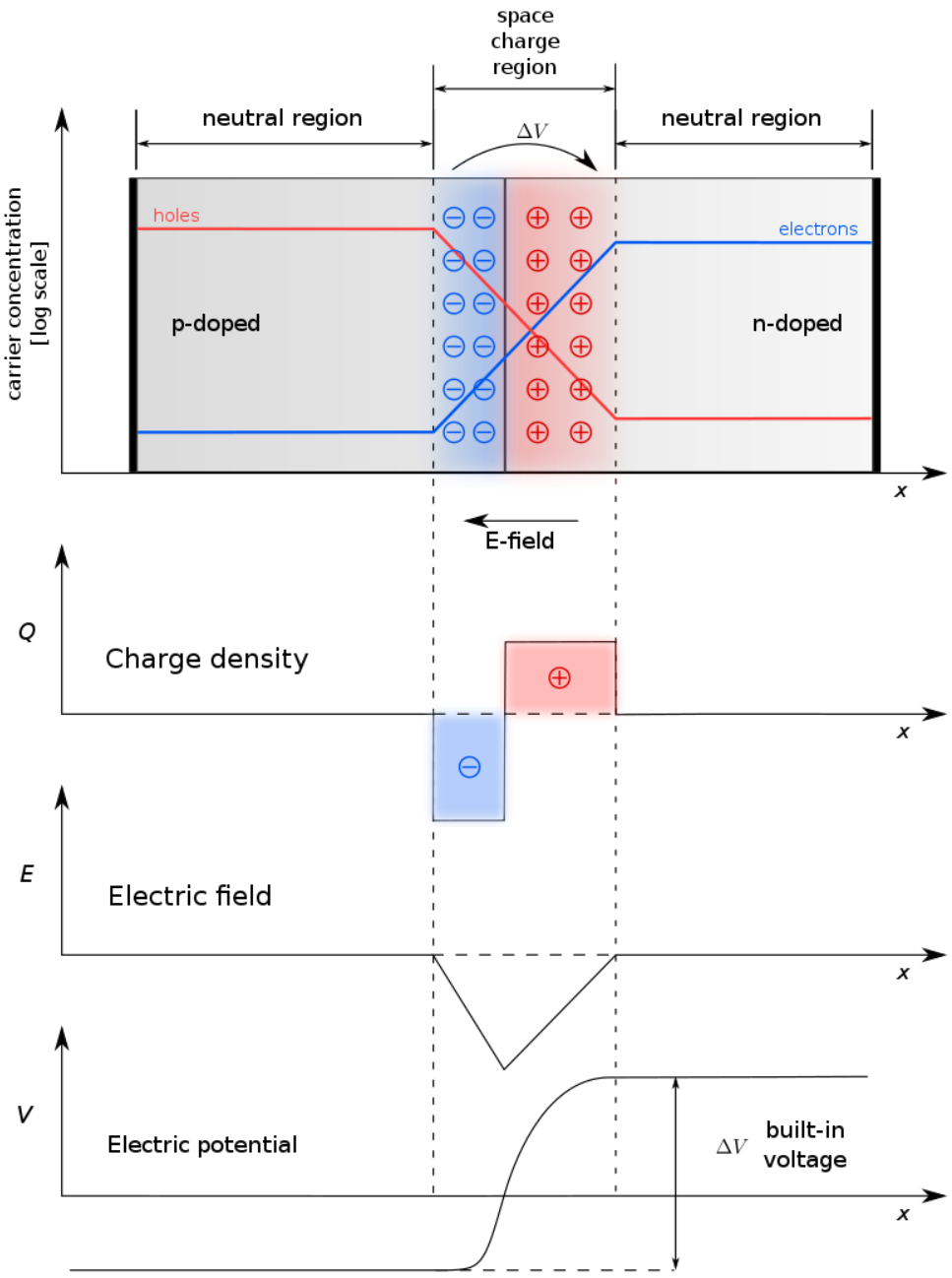

Figure 1.10: Sketch of a p-n junction with no externally applied voltage, from Ref. (5). Underneath the junction, one can observe the charge distribution, the electric field, and voltage as a function of the junction's depth. These quality affect the motion of charge carrier, in turn determining the produced currents.

were N_A and N_D are the density of the acceptors and donors concentrations, ε_0 is the dielectric constant, and q is the unit charge. $\Delta V = VB_i - V_{ext}$ is the the potential difference between the built-in potential and any external applied bias.

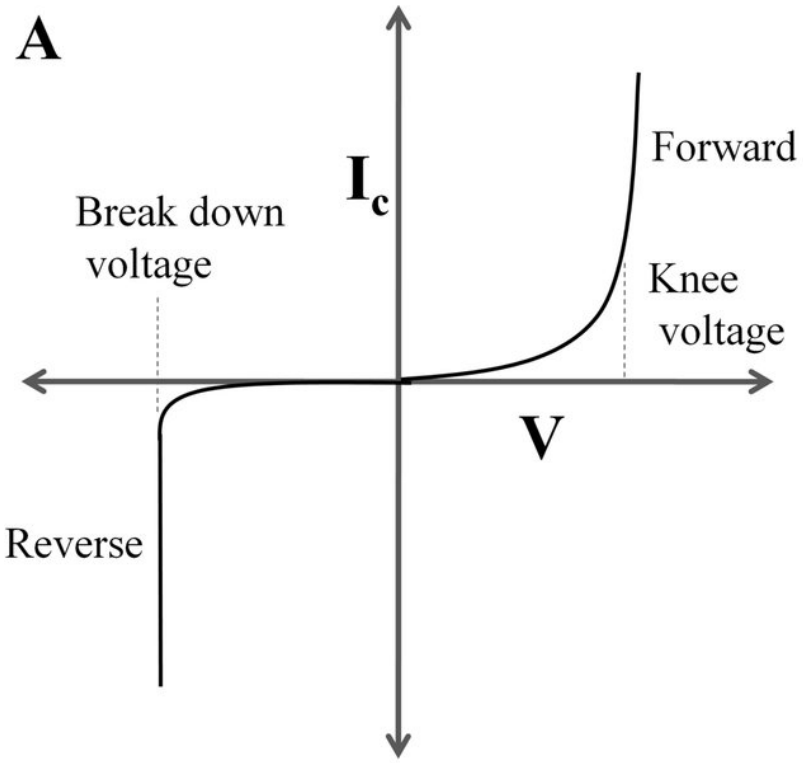

Figure 1.11: Typical IV curve of a diode (6). In the plot one can spot the reverse-bias, and forward-bias region.

Depending on the sign of the applied bias, the width of the depletion region can be modified. When a positive voltage is applied to the n-type region, and a negative to the p-type, the junction become *forward biased* and the depletion region shrinks. Charges can flow through the system, if the depletion region's width becomes null. When the positive voltage is applied to the p-type material and vice versa, the junction becomes *reverse biased* and the width of the depletion region consequently increases. Increasing the depletion region width, the number of free charges flowing through the junction decreases, and, for ideal systems, the total current gets very close to zero. However, the silicon wafers production process introduces impurities that modify the junction depletion region. This can affect its actual size within one of the devices side (p-doped or n-doped).

In real devices, the current flowing through a reverse biased junction is referred to as *leakage current*, and constitutes the intrinsic noise of the sensor. Figure 1.11 describes the operation of a typical p-n junction subjected to an external bias (forward and reverse). From Fig. 1.11 one can also notice that, when reverse biased, the current flowing across the junction slowly increases up until

a potential called breakdown. After this point, the current increases exponentially. This scenario is particularly interesting, as silicon particle detectors usually use silicon p-n structures operated in reverse biased condition. The energy deposit caused by incident particles (see section 1.2.3) generates free pairs of electrons and holes inside the silicon bulk. The threshold energy for this to happen is decided by the material ionization energy (I $\simeq$3.6 eV). The bias provided to the detector is usually set to reach full depletion. In other words, this ensures to generate an electric field across the whole structure of the silicon sensor. In this way, the electron-hole pairs drift in opposite direction inside the detector, reaching the electrodes, and generating a transient current along their path.

This current (which can be calculated through the Shockley-Ramo theorem (58)) is induced on the electrodes, and can be amplified and read out. This quantity provides an information on the collected charge and, for fully efficient detectors, it can be related to the charge produced by the passage of incident particles. In reality, the percentage of collected charge is affected by the impurities in the semiconductor structure which can limit the Charge Collection Efficiency (CCE). We can define the CCE as the ratio between the generated, and the collected charge. It can be expressed as:

$$CCE = \frac{N_{eh}(collected)}{N_{eh}(generated)} \quad , \tag{1.24}$$

where $N_{eh}(collected)$ and $N_{eh}(generated)$ are the number of electron-hole pairs generated and collected. Given the density of the material, one can find this number computing:

$$N_{eh}(generated) = \frac{dE}{dx}\frac{x}{E_{e,h}}. \tag{1.25}$$

Where E_{eh} is the threshold energy required for creating free charge pairs (see table 1.1). x is the incident particle range. For a MIP crossing 50 μm of silicon, N_{eh} $\sim$4500.

Another important quantity that is considered for detector applications (see chapter 2 and chapter 4) is the shape of the current, and its time of total collection. These quantities depend on the carriers mobility, saturation velocities, as well as the operation point of the detector. The versatility of solid state detectors results on a large number of applications in particle experiments. These detectors can be used in the reconstruction of the position, of the energy, as well as the time

of arrival of charged particles. LGADs are silicon detectors of particular interest for the production of timing, radiation resistant detectors. The magnitude of the drifting field in their substrate is enhanced controlling the doping concentrations in the junction. The next section describes the conceptual design of LGADs, highlighting their main features and limitations.

1.3 Low Gain Avalanche Diodes

A new class of silicon detectors has been developed for improving the timing capabilities of Avalanche PhotoDiodes (APDs), and Silicon PhotoMultipliers (SiPMs) traditionally used for particle detection. These devices work exploiting the phenomenon of *impact ionization*: increasing the external electric field, the charge carriers can gain enough energy to create secondary free charges, producing an avalanche process. The ratio between the initial produced charge and the ones contributing to the induced current is called *gain*, and it is indicated as G. For APD typical gains are greater than 100, while for SiPM are of the order of 10^6. The avalanche effect can be achieved controlling the concentrations in the silicon substrate. Controlling the doping implant profiles of standard APDs, one can design new detectors, optimized for the production of fast signals. In LGADs the concentration of doping atoms closer to the junction produces electric fields similar to ones of APDs. However, the charge multiplications is limited by gain levels usually set around 20. This allows for the production of signals characterized by extremely fast rise-time (sub-ns) when detecting MIPs (which energy loss is equally distributed along their track). The intrinsic lower gain, and the shape of the electric field of LGADs allow for the construction of finely segmented, and thin devices. Therefore, the total signal is comparable to the ones of traditional pin diodes, while the sensor thickness can be drastically reduced to produce faster signals. The promising features of LGADs have been thoroughly studied by particle physics Collaborations. 50 μm thick devices have shown to be capable of time resolution better than 30 ps (59). Their timing capabilities have been put to use for the design of fast detectors: their size, and granularity makes for optimal sensors for numerous research and commercial applications. Most recently, the stringent demands imposed by HEP experiments have pushed vendors in designing LGADs capable of operating in radiation dense environments. Chapter 2 reports the extraordinary performance of small LGAD pixels ($1.3\times1.3\,mm^2$), irradiated up to high fluences ($1.5\times10^{15} n_{eq}$).

This section will provide an introduction to the LGAD technology and design, highlighting some of the required properties of these detectors. Later, another section will be dedicated to addressing the degrading of their performance as a function of the absorbed radiation.

1.3.1 Conceptual design of LGADs

The first conceptual design of an LGAD was formulated by the Centro Nacional de Microelectronica (CNM) (8; 49), with the purpose of creating sensors capable of preserving their performance when heavily irradiated. In this concept, inherited by more conventional APDs, the multiplication gain of the sensor was limited by the doping structure. The lower overall gain helps mitigating the thermal noise, however preserving the magnitude of the signals. Moreover, this results in the production of linear multiplication avalanches, which can preserve information on the initial energy deposit.

The bulk of LGADs consist of a substrate composed of highly-restive p-type silicon (with concentrations of n_p of about $2\times10^{19}\,\mathrm{cm}^{-3}$). A p+ anode complete the sensor structure. Figure. 1.12 compares the design of a LGAD to the one of a traditional pin diode with no gain layer. The structure of the LGAD usually uses n implants inside a p substrate (although a discussion about the use of p-in-n structures can be found in (60)).

The gain is obtained diffusing a deep p-type layer (about $5\,\mu$m inside the bulk) underneath a shallow n+ electrode (about $1\,\mu$m). In typical LGADs, the peak doping concentrations can reach about $10^{19}\,\mathrm{cm}^{-3}$ in the n-type cathode, and $10^{16}\,\mathrm{cm}^{-3}$ in the gain layer (55; 8). The concentrations in the p-layer modifies the electric field within the multiplication region, and adjusts the overall gain. Due to the multiplication processes, this area could be affected by early breakdown when subjected to higher bias. For creating secondary charges in a linear regime, the sensor has to generate a field of $300\,\mathrm{V/cm}$. This value cannot be achieved by applying an external bias as that sensor would operate in a breakdown regime. In LGADs the local electric field is enhanced by the doping concentration in the gain layer.Eventual breakdowns affecting the perimeter of the cathode are mitigated with a larger diffusion of the n+ electrode. However, in most LGAD designs, the fringes of the high fields are regulated via the insertion of additional deep n+ doping regions. These are known as the Junction Terminating Extensions (JTE), and play a major role when segmenting the

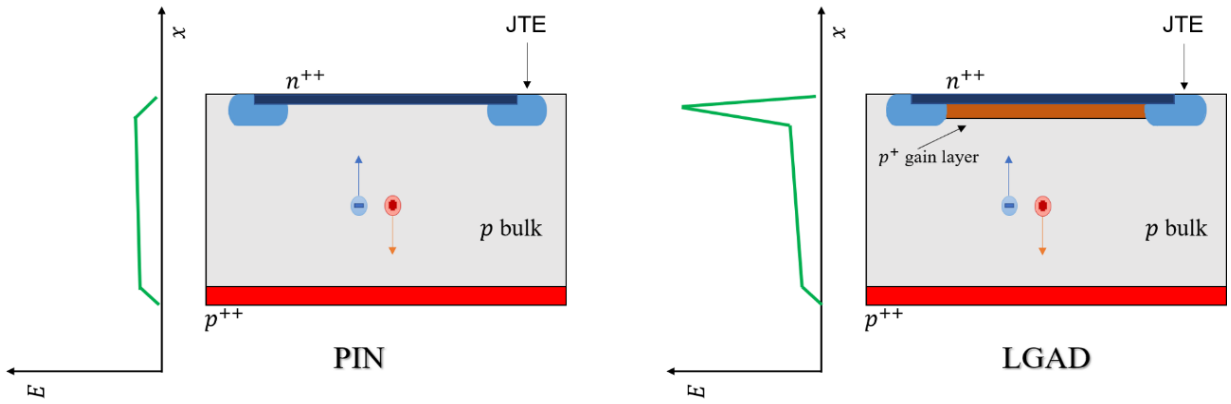

Figure 1.12: Comparison between a traditional silicon pin diode (on the left), and a LGAD (on the right), extracted from Ref. (7). The adjacent plots show that the local electric field inside a pin diode is uniform across the sensor's depth. The spike in the LGAD electric field is caused by the added gain layer.

sensor in adjacent pixels. The field profile of an LGAD provided of JTE is displayed in Fig. 1.13.

All these features make LGADs unique devices for particle timing detection. The multiplication process occurring in their gain layer are controlled by the density of impurities, limiting the avalanche processes to a localized area in the substrate. The high electric field profile of the n+/p junction allows for the use of lower bias voltages without a reduction of the signal amplitude. Lower external fields lead to a reduction of the thermal noise, therefore to an increment of the SNR. The introduction of a gain layer also works in favor of producing of thinner devices. The multiplication of the produced charges balances the loss of the signal caused by the reduction of the ionization region. On the other hand, a lower distance to cover ensures a faster time of charge collection. Next section provides some technical details about these detector performance, and their intrinsic limits.

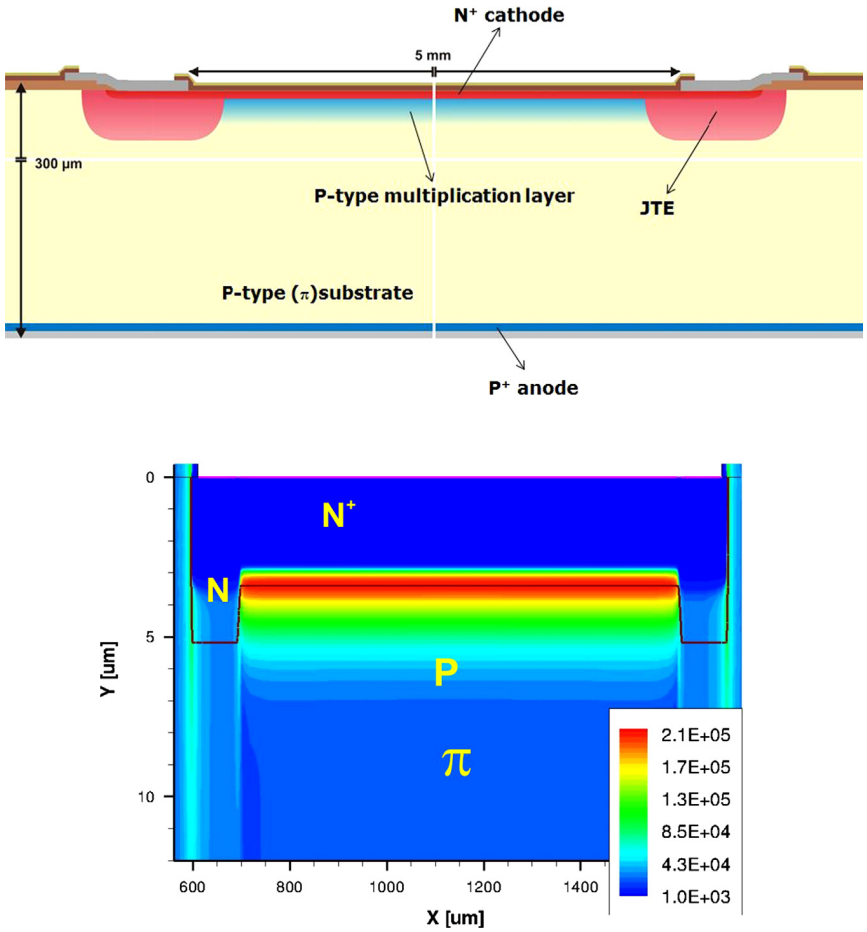

Figure 1.13: Structure of an LGAD comprising JTE to limit the breakdown effects at the edge of the n+/p junction. In the bottom panel, the simulated shape of the electric field inside the detector (8).

1.3.2 Performance of LGADs

The previous section described the structure of the electric field inside LGADs substrates. The added gain layer locally increases the field, and the multiplication process starts when E = 300 V/cm. At this potential, the relationship between the local fields and the charge multiplication can be expressed as:

$$N(l) = N_0 e^{\alpha(E)l} \quad ; \tag{1.26}$$

l represents the path length inside the LGAD's high-field, $\alpha(E)$ is a multiplication function, strongly dependent on the local field (18; 60). N_0 is the number of initial carriers, generated during the primary ionization process. The generated avalanches (electrons and holes) move towards opposite

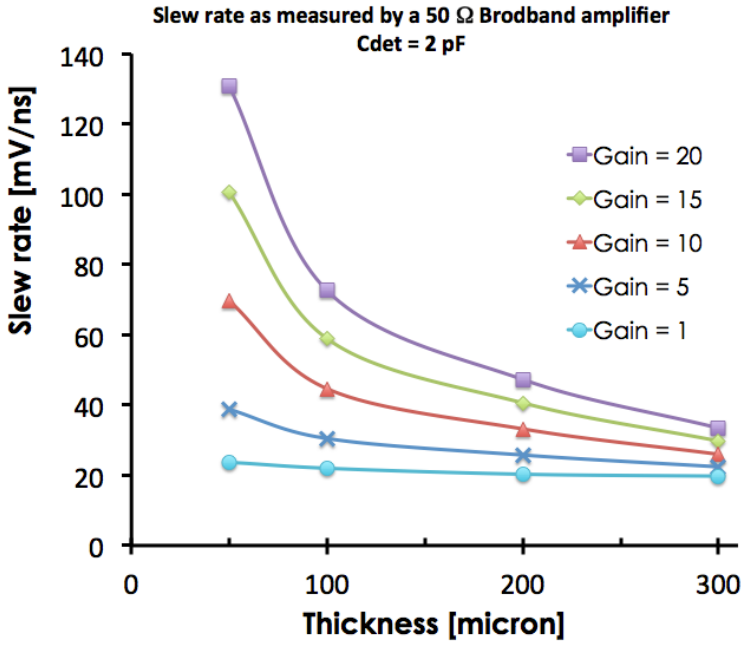

Figure 1.14: Slew-rate as a function of the detector's thickness for different level of internal gain (9). A thickness of 300 μm leads to great improvement (factor 2-3) for a 2 pF detector with G=20.

electrodes, inducing a current signal along their path. The collection time, and slew rate, can be reduced with the choice of a thin sensor. However, for thinner sensors the effects of Landau fluctuations in the energy deposit become increasingly problematic (this effect is described in 1.1.3). Fortunately, in LGADs the introduction of the gain layer mitigates the effects of the Landau fluctuations on the timing resolution. Calculations reported in (9) demonstrate the inverse proportionality of the current induced by secondary charges as a function of the sensors thickness:

$$\frac{di_{gain}}{dt} \propto q\, vs\, \frac{G}{d}. \tag{1.27}$$

In the equation, q is the unitary charge, v_s is the carriers saturation velocity (introduced in section 1.2.2), G is the gain, and d indicates the detectors thickness. Figure 1.14 summarizes the results obtained from simulations of LGADs rise-times as a function of the sensor's thickness. The results demonstrate that, although the Landau contributions dominate the intrinsic noise in thin detectors, the introduction of a gain layer mitigates the degradation of their rise-time distribution.

While, in section 1.1.3 the contribution of the shot-noise was neglected for sensors with no

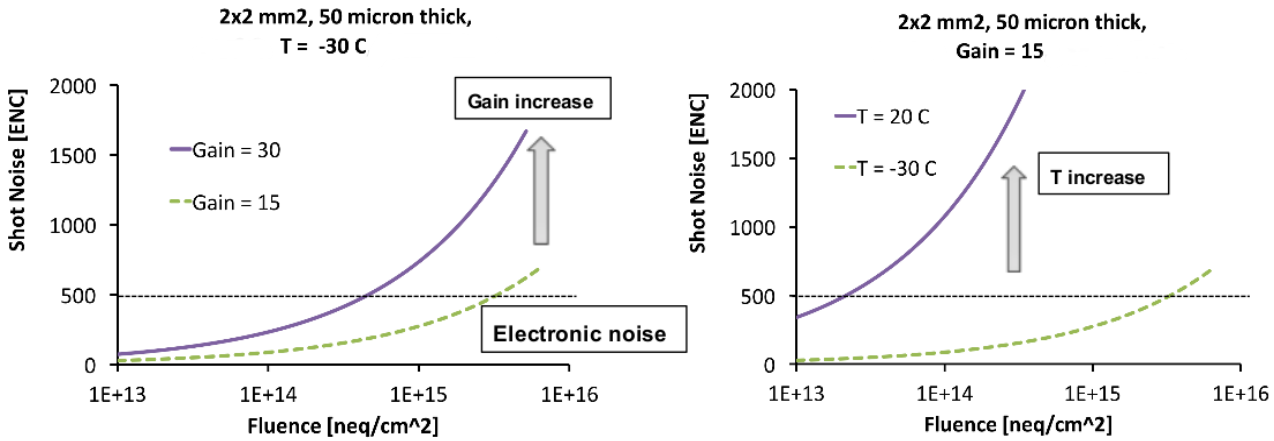

Figure 1.15: The plot reports studies of the shot-noise contribution as a function of the radiation absorbed by the sensor (10). One can notice that the gain level has to be limited for keeping the contribution of the shot-noise under the electronics noise floor. In the plot on the right, the difference between the two values of temperature is dictated by the rising in the leakage currents at higher temperatures.

gain, this cannot be done when analyzing the noise profile of LGADs. Section 1.1.3 reports that the shot-noise increases with the increasing of the leakage currents. When the charge carriers produced by noise undergo the process of multiplication, the shot-noise is also enhanced. This phenomenon is called Excess Noise Factor (ENF), and it is a limiting factor of the detectors SNR. This term increases faster than the signal as the gain increases (61; 62). For LGADs, the shot-noise contribution has to be lower than the one introduced by the read-out electronics. This is done by adjusting the gain level of the sensor. This effect is of particular interest in irradiated sensors, where the contribution of the shot-noise can easily become the dominant factor. Figure 1.15 shows the simulation studies of the shot-noise as a function of the absorbed radiation fluence. From Fig. 1.15 we can also extract information about the temperature dependence of the gain. This is quantified by empirical models, which point to a slow decrease of the gain as a function of the temperature (62). The temperature affects directly the carriers mobility, as it modifies the mean

free path inside the semiconductor.

To conclude, LGADs offer excellent solution for designing thin, finely segmented performing timing detectors. Using low value of gains, these devices can operate as single particle detectors with excellent SNR, and stable time resolutions for MIP. LGADs have demonstrated a precision in the reconstruction of MIP crossing time of about $\sigma_t = 30\,\text{ps}$ for $2\,\text{mm}^2$ pixels (59). More results on the study of LGADs with highly energetic particle beams are reported in section 2.4. The original conceptual design of LGADs came for the demand of improved radiation resistance of silicon particle detectors. Although they have been perfected for producing optimized time response, this appealing feature still characterizes these sensors. Physicists identified LGADs as possible substitutes for traditional silicon detectors in radiation dense environments. Many R&D projects are currently moving towards the development of increasingly more radiation tolerant detectors for preventing, or reducing the expected signal degradation.

1.3.3 Radiation damages

The timing performance of LGADs are being evaluated under extreme radiation conditions as they are planned to be installed at HEP experiments at colliders. Their radiation hardness has been largely improved for sustaining the level of fluences expected for long periods of data acquisition. The radiation damages affecting LGADs are not the same expected for simple pin diode detectors. The features of their detectors design (such as their thickness, and gain) poses a set of unique problems.

In solid state detectors, the CCE (introduced in section 1.2.4) is known to decrease as a function of the collected radiation. Deposit exceeding the minimum displacement energy (see table 1.1) can generate defects in the silicon's crystal, in turn creating traps for the charge carriers. This effectively increases the collision rates of free charges moving in the semiconductor. In LGADs, the mean free path of the carriers is of about $50\,\mu\text{m}$ at an irradiation level of $1\times10^{15}\,\text{n}_{eq}/\text{cm}^2$. This corresponds to the typical size of their sensitive area (depletion region). From the simulated studies of Baldassari (11), one can observe that the rise-time of the signal does not display a strong dependency on the irradiation, for values lower than $1\times10^{15}\,\text{n}_{eq}/\text{cm}^2$. This effect can be observed in Fig. 1.16. The levels of radiation in Fig. 1.16 have been chosen to replicate the environment of

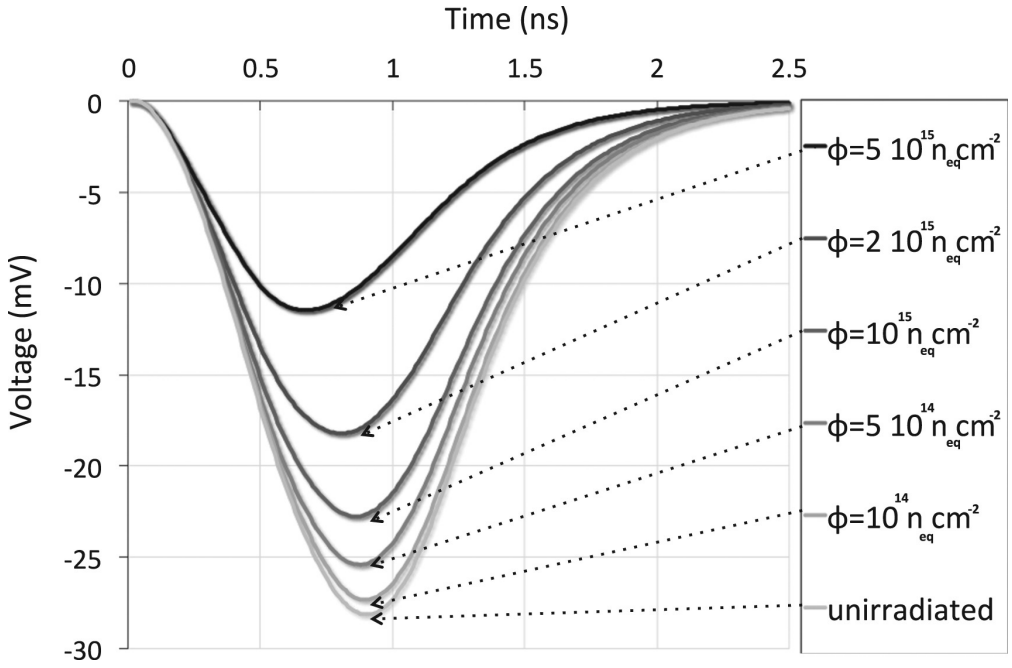

Figure 1.16: Results of simulation studies of the signals produced by irradiated LGADs, from Ref. (11). The rise-time does not experience significant distortions up to values of irradiation higher than 1×10^{15} n_{eq}/cm^2.

the future LHC operation (chapter 2 is dedicated to the description of the us of timing detectors at the LHC). In the same way, one can calculate the contributions affecting the SNR in irradiated sensors. The increase in leakage current is enhanced by the sensor's gain. In turn, these currents lead to increased power consumption and shot-noise (18). Optimizing the response of irradiated sensors, usually requires to operate these devices at lower temperatures (about -20 °C to -30 °C).

Another contribution can be identified in the modification of the concentrations of dopants in the silicon. This effect has been empirically demonstrated, but its causes are still under investigation. Absorbed fluences exceeding 10^{14} n_{eq}/cm^2 seem to lead to a decrease in the gain of LGADs. This can be attributed to an effective reduction of the p-type layer caused by increased trapping of the carriers. Another reason could be found in the inactivation of the doping impurities (63). New typologies of LGADs, tries to mitigate this phenomena including carbon impurities inside their gain layer, and substituting the existent doping materials (boron) with heavier ones (gallium). Figure. 1.17 reports studies of irradiation in LGADs with alternative doping schemes. LGADs of new generations are capable of sustaining large amount of absorbed doses with minimal performance losses, when compared to other silicon timing detectors. While designed to be intrinsically

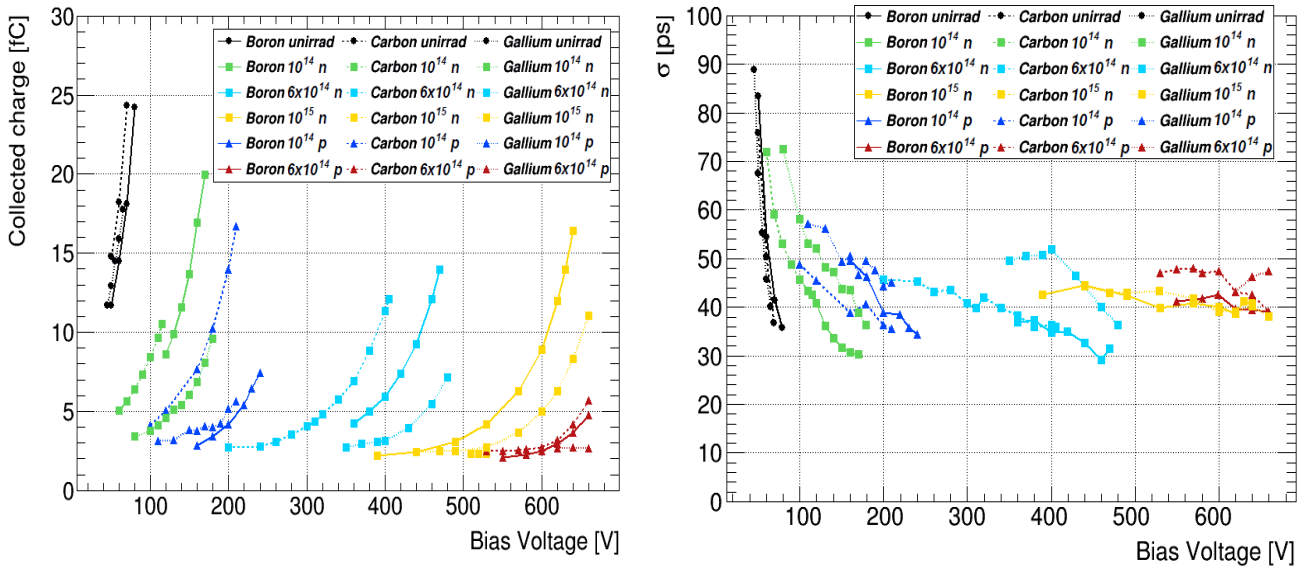

Figure 1.17: Collected charge (left), and time resolution (right) of irradiated CNM LGADs. The plots, extracted from Ref. (12), report the studies of gallium, and carbon-added LGADs, irradiated up to 10^{15} n_{eq}/cm^2.

radiation-hard, their capabilities have been improved via the addition of different impurities, and targeted modifications of their structure.

At present, these detectors have demonstrated an operational range that reaches absorbed doses greater than 10^{15} n_{eq}. When utilized with optimized working points, LGADs subjected to such values of irradiation produced surprising results, with measured time resolution of about 50 ps (in 1.3 mm$\times$1.3 mm sensors). Evaluating the time performances of irradiated detectors was one of the important measurements performed during the R&D work reported in this thesis. The results obtained during the characterization studies of irradiated LGADs are described in section 1.1.1.

1.4 Chapter summary

This chapter laid the foundation for understanding the functions of fast silicon detectors, by describing the performance of state-of-the-art devices. With this as the framework, a general intro-

duction on the topic of timing measurements was followed by a description on semiconductors and their use for particle timing detection. A good time resolution is determined by the combination of a quality sensor's design, an optimized read-out electronics, and effective signal digitizing and processing. These components directly affect the overall precision of the time reconstruction, adding to the total uncertainty.

From the studies of these sensors, one concludes that the main source of intrinsic noise comes from the non-homogeneous nature of the ionization processes. The energy deposit of incident particles is dictated by stochastic physics effects and generating non-uniform pulse profiles. This effect plays a role in degrading the slew-rate of the generated pulses. LGADs mitigate this problem using thin sensors with gain layers producing linear multiplication of the carriers. This configuration ensures a fast collection of the charges and reduces the amplitude loss due to shorter drift times. Fast rise-times, and large SNR lead to a more defined intersection with the threshold set by digitizing devices. The smearing of the crossing time of static threshold or jitter, is addressed in the design of the detectors read-out. The bandwidth of the electronic components should not restrict the detector's rise-time. At the same time it has top be selected for containing the noise levels. These precautions, together with performing digitizers and dedicated post-processing algorithms are the ingredients for developing timing detectors.

Chapter 2

Precise timing detectors for the CMS Mip Timing Layer

This chapter presents a brief description of the Large Hadron Collider (LHC) and an introduction to the Compact Muon Solenoid (CMS). Particular attention is devoted to the description of the CMS technical upgrades for the High-Lumi LHC (HL-LHC), scheduled to start by 2027. The increased luminosity will impose the use of new particle detectors and systems that can cope with the expected particle rates in the barrel and end-caps of the experiment. These two regions of the CMS apparatus will see the installation of a MIP Timing Layer (MTD), an additional layer of detection responsible for the reconstruction of the Time Of Flight (TOF) of final decay products. After a brief introduction to the proposed physics program, the present chapter provides the technical details of the detectors populating the timing layers. The following sections report the test results obtained during the prototyping phase of the Low Gain Avalanche Diodes (LGAD) produced for the End-Cap Timing Layer (ETL). The presented data was obtained during the test campaigns pursued at the FERMILAB facilities and the results of the LGADs performance were evaluated during the following analysis work. The R&D results are introduced by a section describing the characterization procedures at the laboratories at KU of a fast timing detectors used during the tests. The latest sections are dedicated to the description of the ETL modules electrical quality control procedures.

2.1 Particle physics at colliders

The Standard Model (SM) of particle physics represents the most successful framework for describing three out of the four fundamental forces in nature. This framework derives from Quantum Field Theory (QFT) calculations and successfully predicts events happening in the regime of small distances. In the models, particles are described as excitation of the quantum fields permeating the universe. The same fields produce force carriers, the quanta of energy exchanged during

particle interactions, also responsible for generating the observable matter and radiation. The model classifies particles based on the statistical distribution describing their occupancy of discrete energy states, and according to the forces defining their mutual interactions. The quantity, or quantum number, used for this classification is called *spin (S)*. The spin is an intrinsic property of a particle directly related to its angular momentum and varies as even or odd multiples of 1/2.

The distribution describing particles belonging to the first group follows the statistic of Bose-Einstein; these particles are indicated as *Bosons*. The fundamental[1] SM blocks belonging to this category include the gluons, called photons, the $W^{\pm}$ and Z bosons. These are the *gauge* bosons mediator of the forces: the $W^{\pm}$ and Z bosons mediate the weak interaction between subatomic particles and are responsible for the nuclear decay of radioactive atoms; the particles composing the nucleus are kept confined thanks to the action of gluons, who mediates the strong interaction between the partons. In the case of electromagnetic interactions, that mediation is performed by the exchange of spin-1, massless particles, the photons. Finally, the *Higgs* boson, the scalar boson (*spin S*-0) in the SM, completes the picture. Although its discovery was the latest addition to the model, the presence of the Higgs boson naturally derives from spontaneous symmetry breaking mechanism theorized in the 1960s. Through their interaction with the Higgs field, particles of the SM obtain their typical masses.

Particles with odd multiples of 1/2 spin follows instead the Fermi-Dirac and are classified as *Fermions*. *Quarks* and *Leptons* are the fundamental fermions of the SM. Leptons are fundamental fermions interacting through electromagnetic and weak force but not directly sensitive to strong interactions. Within the SM, pairs of charge-1 leptons (electrons, muons, tau leptons) and associated neutrinos (electron, muon, and tau neutrinos) are organized in three generation, and classified by a quantum number called *flavor*. Although the SM does not account for events violating the flavor conservation, it has been experimentally proven that neutrino flavor eigenstates do not correspond to the particles mass eigenstates. This results in a peculiar *oscillation* effect, where neutrinos of a given generation can fluctuates to different flavors while propagating through space. interact among each other forming *colorless*[2] bound states called *Hadrons* which can be organized

[1] describes particle without internal substructure. This experimental definition follows results probing matter to extremely short distances, around 10^{-20}.

[2] The term *color* refers to an additional quantum number used in quantum chromodynamics to describe properties of the strong interactions. The principle of color confinement dictates how free particles must present a null color charge. The three colors (and respective anticolors) described in the theory are chosen in analogy with primary colors and are:

in *baryons* when quarks are interacting in odd numbers, and *mesons* when in even.

Although the SM could look like a complete and reliable framework for describing all possible interactions of fundamental particles, there are many open questions still to be addressed. It is the duty of particle physicists to verify with increasing accuracy what can already be predicted by the model while, at the same time, investigating phenomena beyond the known SM (BSM). Historically, particle colliders have provided a perfect testing ground for probing the validity of the theory and looking into new physics events in a broad spectrum of energy regimes (keV - TeV). Accelerators can be used in a variety of different applications, however research laboratories optimize particle accelerators for maximizing the production of interesting physics events. Particles are accelerated over linear or circular tracks in order to reach the desired energy and collided at designated interaction points. The final decay products of particle interactions are then collected by the detecting apparatus of physics experiments.

Accelerators can operate using leptons (e.g. electrons, positrons), hadrons (e.g. protons, antiprotons), light and heavy ions (e.g. He, Pb), or combinations of them. Many accelerators segment their streams of particles into equally spaced packets, or *bunches* travelling inside the beam lines. The collisions can happen between the two, if the accelerator is designed to revolve particle beams in opposite directions (therefore adding the energy of the colliding particles), or the beams can be directed to interact with a fixed target. It has to be noted that, in the process of accelerating hadrons, while the total energy provided can be controlled, there is no a priori knowledge of the energy carried by the fundamental quarks composing the hadrons. When the collision happens at high energies, the 'bullet' particle is energetic enough to probe the structure of the target, and the accelerator effectively acts as a powerful, subatomic telescope. In this scenario, the partons are the ones effectively interacting, while the contribution of the hadron's electromagnetic form factor is negligible. Hadronic accelerators exploit this for producing a broad spectrum of final states and facilitating the observation of previously unrevealed particles and resonances. The same phenomenon does not affect data collected at lepton colliders, as the energy of the fundamental particles can be controlled through the acceleration process. This type of accelerators is more suitable for precise physics measurement, where the quantities to be studied are understood and the collider features can be tuned for optimizing the yields.

red, green, and blue.

2.1.1 The Large Hadron Collider

The European Organization for Nuclear Research (CERN) hosts the largest and most powerful accelerator ever built, the Large Hadron Collider (LHC). Extending over a circumference of 26.7 km, the LHC is located near the French-Swiss border, at the outskirts of Geneva, Switzerland approximately 100 m underground (64). Inside the LHC 'bunches' populated with more than 10^{11} of protons are injected into two intersecting rings. Radiofrequency cavities accelerate the bunches in opposite directions over multiple stages, with the purpose of gradually reaching the desired energy. As the protons are accelerated, their trajectory is bent and kept on a main orbit using 1232 superconductive dipole electromagnets. Additional dipoles are used to modify the particles direction around the Interaction Points (IPs), where the two beam lines intersect and the protons are frontally collided. In order to maximize the number of interactions, the beams are focused 'squeezing' together the particles inside the bunches using pairs of crossed magnetic quadrupoles. The number of event produced per unit of time during the collisions can be expressed as:

$$\frac{dN_{events}}{dt} = \sigma, \tag{2.1}$$

where σ, the cross section, is related to the probability of having proton collisions, and , the instantaneous luminosity, depends only on the accelerator parameters. For circular synchrotrons (such as the LHC), the instantaneous luminosity is provided by the formula:

$$\mathscr{L} = \frac{k_b N_1 N_2 f_{rev} \gamma}{4\pi \varepsilon_n \beta^*} F, \tag{2.2}$$

where N_1 and N_2 correspond to the number of particles populating each colliding bunch, k_b is the total number of bunches, f_{rev} is the revolution frequency, and γ is the Lorentz boost factor. The denominator contains parameters solely constrained by the optics of the accelerator: β^* and ε_n, the normalized transverse beams emittance, and the amplitude function, respectively. The crossing angle at which the bunches meet at the interaction points is represented by the F term in the equation; effectively reducing the total number of collisions. The LHC was designed to collide protons accelerated to energy of 14 TeV with an instantaneous luminosity of $= 10^{34} cm^2 s^{-1}$. The acceleration chain required for achieving these parameters can be summarized as follows:

- In the first stage, of ions of hydrogen gas are stripped of their electrons thus obtaining bunches of protons. These are pumped inside the LINAC (65) and accelerated over its linear track to reach an energy of 160 MeV.

- From there, the protons are injected inside the first circular accelerator, the Proton Synchrotron Booster (PSB) (66), where they are accelerated to 2 GeV and prepared for their injection inside the Proton Synchrotron (PS) (67).

- In the PS protons reach 26 GeV, enough energy to be injected inside the orbit of the Super Proton Synchrotron (SPS) (68) where they are accelerated up to 450 GeV, about 99.9% of the speed of light (c).

- Finally the SPS injects the bunches to the LHC, where the particles are evenly divided between the two beam lines, driving the protons in opposite directions. Inside the accelerator revolve 2,808 bunches, each containing 115 billion protons, with a revolution frequency of 40 MHz (hence a bunch spacing of 25 ns). The LHC uses RF cavities (400 MHz) designed to resonate with the the revolution frequency of the particles to gradually increase their momentum. It requires approximately 20 minutes for the protons in the beam pipes to achieve their final energy of 6.5 TeV.

Fig. 2.1 provides a detailed sketch of the LHC accelerator complex and highlights the four IP indicating the name of the corresponding experiments: ALICE , ATLAS, CMS, LHCb. In the early years of the LHC physics program, a great deal of effort was devoted in searching for the Higgs boson. After achieving enough statistical evidence to announce its discovery in 2012 (69), the LHC and the various experiments have been subjected to a series of major hardware and software upgrades, increasing the experimental capabilities to search for beyond the standard model (BSM) events.

At present, the LHC is expected to resume its data acquisition which will last until the end of 2022, the so-called Run 3 phase. The previous paragraphs describe the LHC functionality at its maximum achievable collision rate and energy, yet the accelerator is capable of colliding proton beams in different running conditions. During 'special runs' lower number of collision events arise form the crossing bunches, thus reducing the number of pile-up (PU) events, and favoring

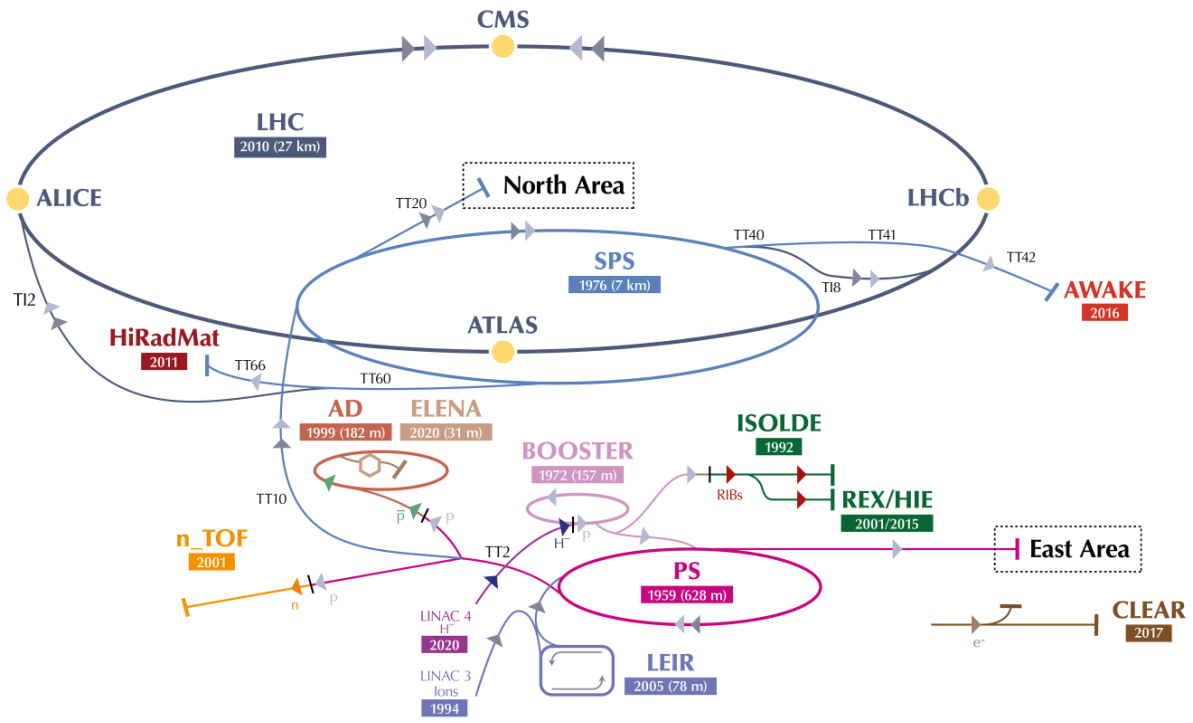

Figure 2.1: Schematic representation of the parts composing the CERN accelerator complex (13). The arrows direction follow the trajectory of the particles circulating inside the beam lines.

high-precision measurements. Additional operational modes of the LHC complex include the acceleration of heavy-ion nuclei, mostly Pb, stripped off their electrons and collided at relativistic energies against other heavy nuclei or protons. This modality allows to reach high energy densities and temperatures for dedicated studies of hidden properties of strong nuclear interactions, including studies of the Quark Gluon Plasma.

2.1.2 The CMS detector

Together with the 'A Toroidal LHC ApparatuS' (ATLAS), the Compact Muon Solenoid (CMS) is one of the two general purpose detectors[3] present at the LHC. To maximise the acceptance and cover the majority of the 4π solid angle, CMS is structured in a set of concentric layers of detection to create a cylindrical symmetry around the interaction point 5 (IP5). In CMS, the inner detection layers are enclosed by a superconductive solenoid magnet which bends the trajectory of

[3]We define 'general purpose detectors' those experiments designed to inclusively reconstruct the majority of the possible decay channels of the heavy particles generated during the collisions.

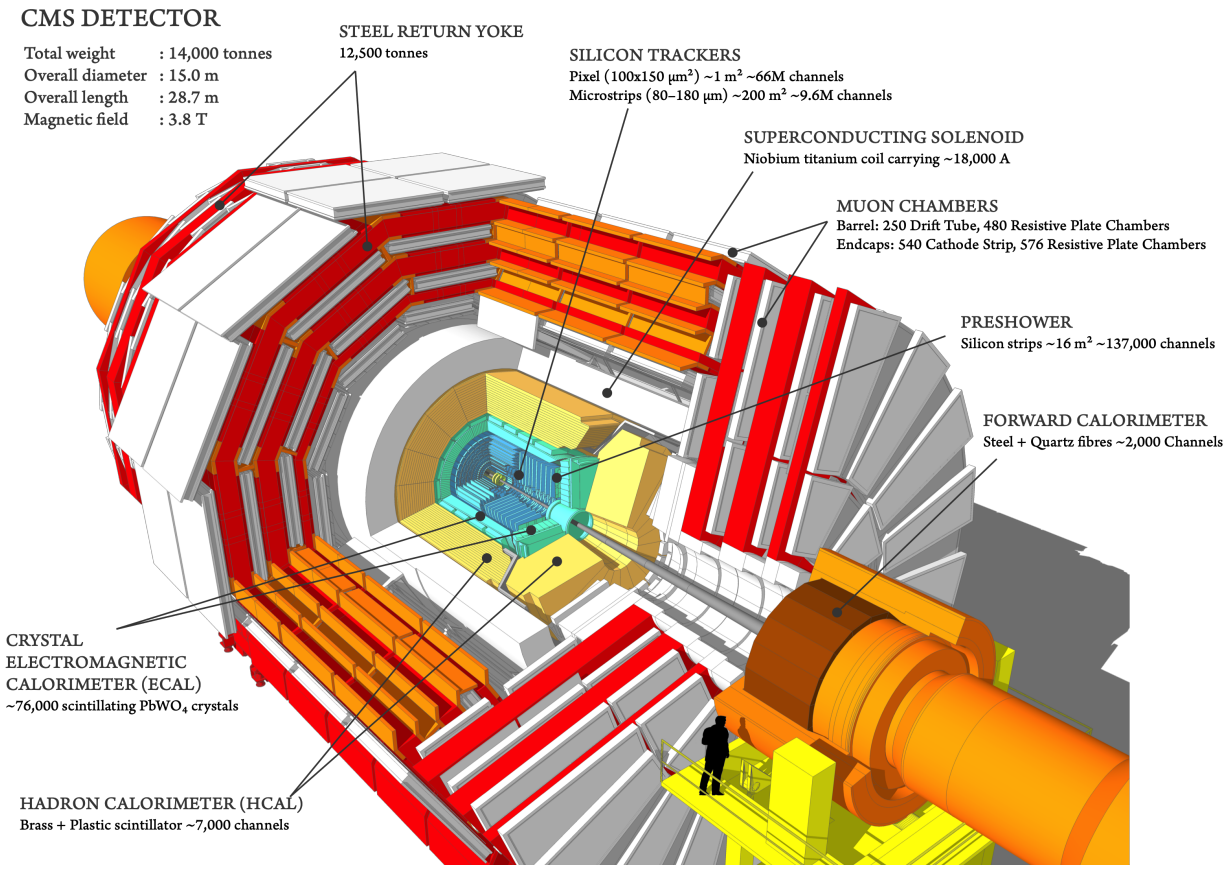

Figure 2.2: CMS experiments cutaway diagram (14). The parameters displayed in the legend refer to the detector status during Run-2.

charged particles. Outside the solenoid, the muon chambers reconstruct the tracks of the penetrating objects escaping the main detecting apparatus. The cylinder of CMS is positioned around the interaction point (Central Barrel) and closed on the forward regions by circular supports hosting additional particle detectors (End-caps). The design of the CMS apparatus is shown in Fig. 2.2.

The reference frame of the collisions in the experiment, also known as the laboratory frame, is based on an arbitrarily selected reference system centered on the nominal IP geometrical location. Pointing towards the French Jura mountains, the z-coordinate of the system moves along the beamline while the y and y axis define the transverse plane. The x-axis lays horizontally on this plane, facing the center of the LHC circumference. The y-axis points vertically upward. The polar angle θ is defined as the the angle between the y and the z axis, and the azimuthal angle (ϕ) is measured from the x-axis in the x-y plane. These coordinates are needed to build the kinematic parameters of the collision products such as the Pseudorapidity, defined as η = -ln tan($\theta/2$)

and the rapidity $y = \frac{1}{2} \ln \left(\frac{E+p_L}{E-p_L} \right)$ where p_L indicates the longitudinal component of the particle's momentum. In order to understand the benefits and complications coming from the hardware upgrades scheduled for the High-Luminosity LHC (HL-LHC), a description of CMS sub-detectors is provided below.

2.1.2.1 Superconducting solenoid

At the core of the CMS central barrel, the superconductive solenoid produces a magnetic field of 3.8 T, 100 times stronger than that of planet Earth. Such an intense magnetic field is needed to contain within the barrel the tracks of charged particles produced on the x-y pane (their z-coordinates results mostly unaffected), bending their trajectory according to the Lorentz force. This provides an invaluable tool for particle identification as well as a direct measurement of the particle momenta. However, the design and integration of detection layers has to be carefully pondered to avoid issues due to mechanical deformations. The solenoid coils are structured in four layers of niobium-titanium superconducting strands kept in vacuum and therefore thermally isolated from the surrounding environment. While providing the main structure of the CMS experiment, the iron structure surrounding the coils, called the yoke, provides a conductive layer for the return of the magnetic field's lines. The latter is composed of five dodecagonal three-layered barrel wheels enclosed by four end-cap disks at each end. The 620 mm thick steel blocks comprised in the structure also serve as absorber plates for the muon detectors (70).

2.1.2.2 The inner silicon tracker

Comprising of concentric layers and sealed on the side by additional detecting components, the silicon inner tracker is the closest detection system to the IP and it extends in a cylindrical volume of 5.8 m in length and 2.5 m in diameter, covering a range in pseudorapidty of $\eta < 2.5$. In its innermost region, the tracker employs the use of silicon pixels to provide highly accurate vertex reconstruction using three-dimensional interpolation of signals generating over its concentric layers. After the upgrades operated in 2016-2017, the original detector, consisting of three barrel layers with radii of 44 mm, 73 mm, and 102 mm and two end-cap disks at distances of 345 mm and 465 mm from IP5, have been replaced to comply with the more stringent requests imposed by

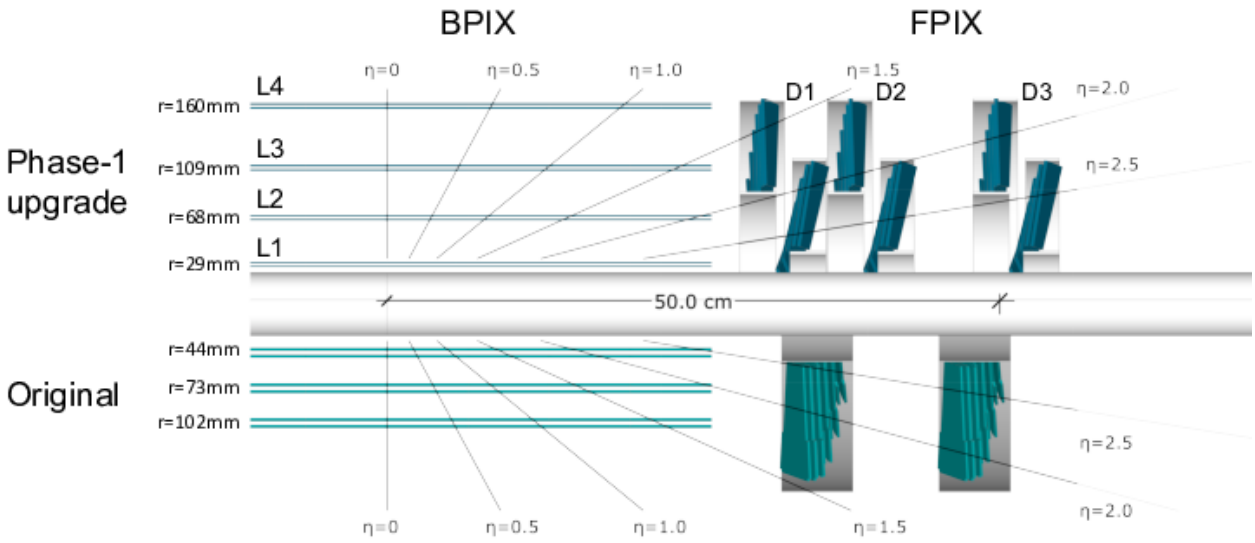

Figure 2.3: The upgraded inner tracking system of CMS is compared with the the original one. (15)

the increased LHC luminosity. The newer CMS Phase-1 pixel detector includes 1856 segmented silicon modules: 1184 modules compose the barrel pixel detector (BPIX) and 672 are used for the forward disks (FPIX). The modules are read-out by 16 Readout Chips (ROCs) with upgraded bandwidth and data loss reduction at higher collision rates, bringing the operational data rates from 160 Mbit/s to 320 Mbit/s. Figure. 2.3 displays a section of the layered barrel structure (L1-L4) with radii of 29 mm, 68 mm, 109 mm, and 160 mm as well as the forward disks (D1-D3) located at distance 291 mm, 396 mm, and 516 mm from the IP. In the figure, the CMS-phase 1 pixel detector is compared with the original one.

The upgraded detector, designed to sustain higher dose-rates (up to $3.6 \times 10^{15}\,\mathrm{n}_{eq}/\mathrm{cm}^2$ after collecting an integrated luminosity of $500\,\mathrm{fb}^{-1}$) improved the track resolution for non-isolated clusters up to 1.5% in and 20 in the transverse, and 40 in the longitudinal directions. Around the pixel detector, the strip tracker employs silicon strip modules parted into subsystems, and

extending out to a radius of 110 cm from the IP. The Tracker Inner Barrel (TIB) and the Tracker Inner Discs (TID) cover r $<$ 55cm and $|z|<$ 118cm utilizing four layers of strips closed by three discs at each end. In the outermost region, the Tracker Outer Barrel (TOB) includes six barrel layers covering r $>$ 55cm and $|z| <$ 118 cm. The Tracker EndCaps (TEC) is structured in nine discs to cover the region of $124 < |z| < 282$cm.

2.1.2.3 The Electromagnetic Calorimeter

Outside the silicon tracker layers, one can find the CMS Electromagnetic CALorimeter (ECAL) designed for the detection of photons and electrons. It consists of 75 848 lead tungstate ($PbWO_4$) crystals covering intervals of pseudorapidities of $\eta < 1.48$ in the barrel region (EB) (where the blocks are arranged in 36 supermodules), and $\eta < 3.0$ in correspondence of the two end-caps (assembled in a 5×5 pattern). Inside the scintillating metallic crystals, electrons and photons dissipates their initial energy via bremmstrahlung and pairs production. The absorber material is carefully selected to balance fast response time, small radiation length ($X_0 = 0.89cm$) (71), and an excellent radiation tolerance. Moreover, the $PbWO_4$ crystals cross-section is optimized to contain the typical transverse size of the EM showers (Moliere radius). In the barrel region, the scintillation light produced by the energy of the EM showers contained in the crystals travels toward the Avalanche photodiodes (APD) for the final energy reading while the showers produced in the end-caps are reconstructed by vacuum phototriodes (VPTs). To maintain the expected efficiency, the fully assembled blocks are maintained at a temperature of 18° C and the crystals transparency is monitored using the reflection of laser pulses. Additional part of the CMS ECAL are the silicon sensors interleaved with a total of $3X_0$ of Lead composing the preshower detector, installed in front of the end-caps detectors ($1.6 < |\eta| < 2.5$). These are needed for proper identification of neutral pions in the end-caps, discriminating electrons from MIPs, and improves the photon and electron spatial location. A section of the CMS ECAL structure is depicted in Fig. 2.4. In the barrel region, the energy resolution of the ECAL reaches remarkable results of about 0.4% for energies of 100 GeV or above, and displays a rise to about 1% for unconverted or late-converting photons with energies spanning tens of GeV. A resolution of about 1.3% up to a pseudorapidity of $\eta = 1$, and about 2.5% at $\eta = 1.4$ is found in the remaining cases. The end-cap ECAL region displays a

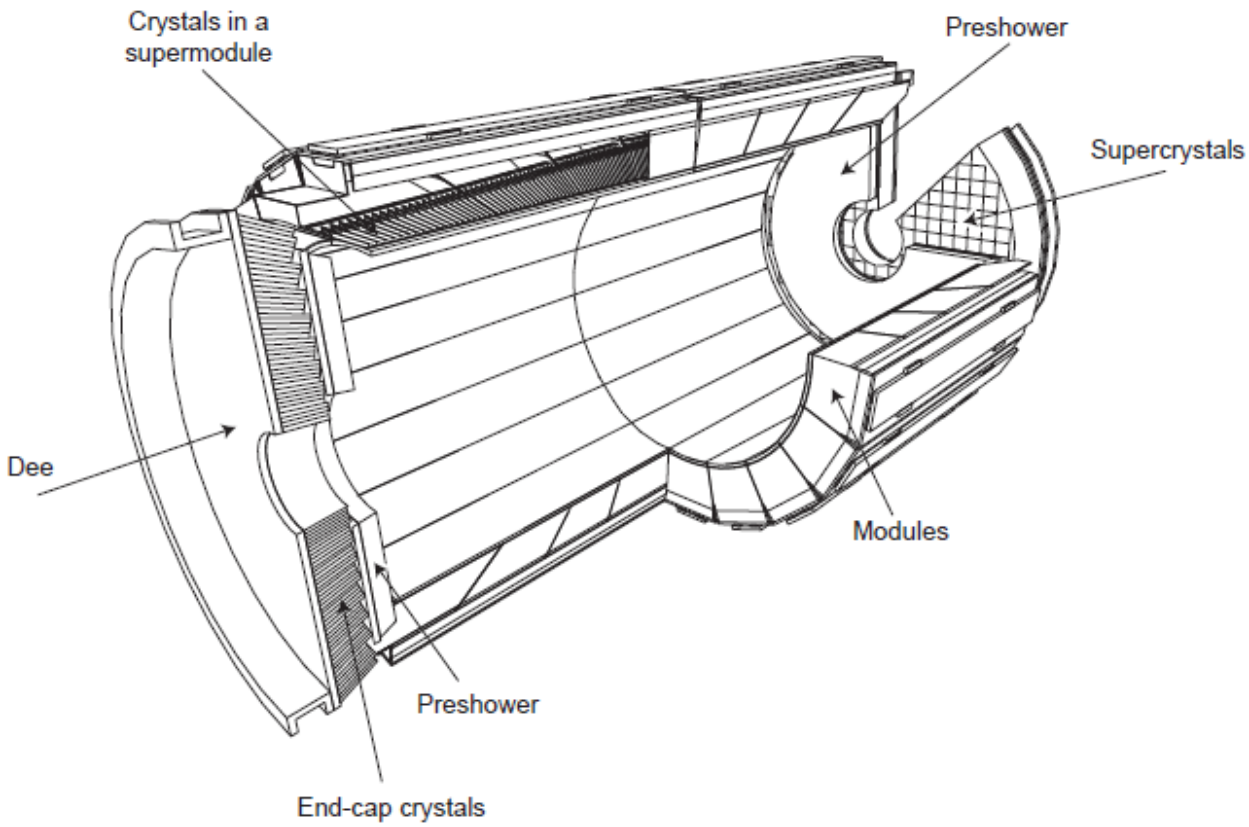

Figure 2.4: A schematic depiction of the CMS ECAL, pinpointing the position of its sub-detectors(16).

resolution of unconverted or late-converting photons of about 2.5%, and between 3 and 4% in the remaining cases.

2.1.2.4 The Hadronic Calorimeter

To reconstruct the energy, the position and the arrival time of hadrons, the CMS apparatus incorporates sets of dense absorbing layers interleaved with scintillating material. The Hadronic CALorimeter (HCAL) extends both inside and outside of the solenoidal coil of the experiment as it includes barrel (HB) and end-caps (HE) sub-detectors, as well as an outer barrel (HO) and forward (HF) components located at the fringe of the magnetic return flux. The full HCAL structure is sketched in Fig. 2.5. Built as two sections with cylindrical symmetry, the central part of the HCAL, the HB, covers an interval of $\eta < 1.48$, mapping the ECAL crystals arrays to form calorimeter towers; the latter projects radially outwards with respect to the IP, and the total combined energy deposition reconstructed by the two detectors provides an estimation of the energy

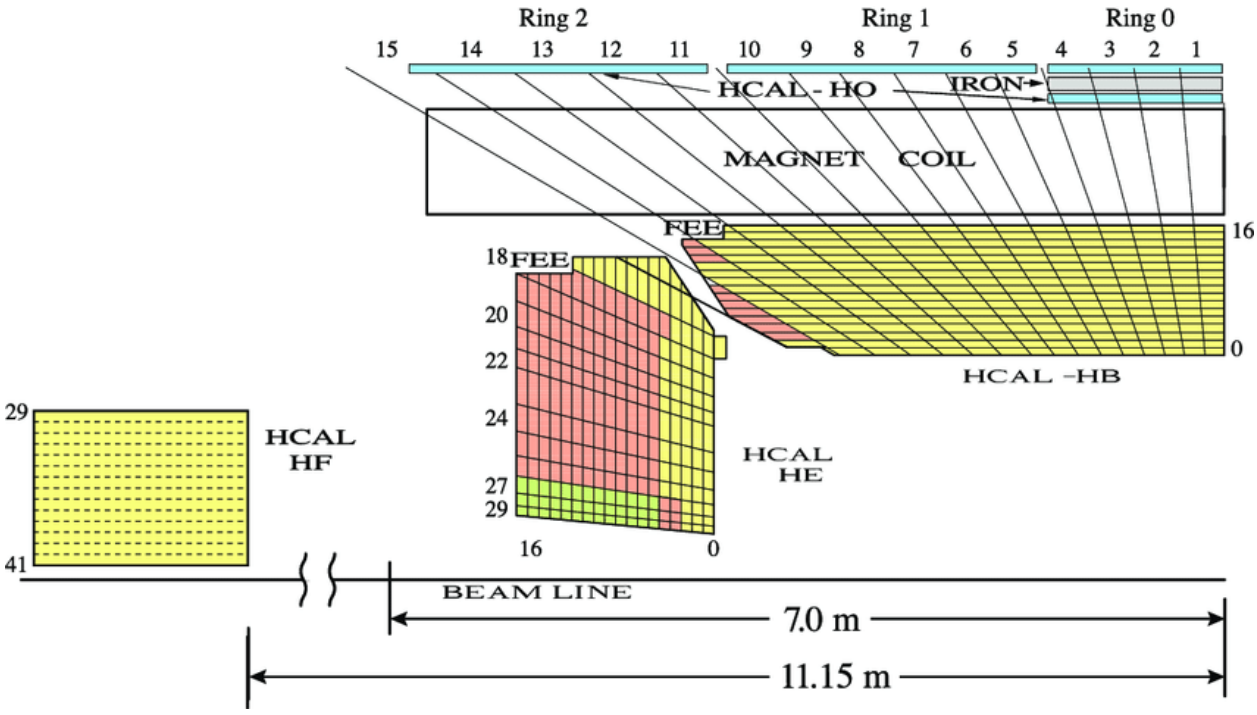

Figure 2.5: Lateral (r-z plane) section of the CMS HCAL detectors. With the color scheme, the authors (17) intend to highlight the different layers of sub-systems forming consecutive depth segments.

carried by the hadronic jet. Each of the 16 projective towers composing the half barrel is parted in 17 layers of plastic scintillators and absorbing material, and the produced signals are collected by pixelated hybrid photodiodes installed at the end of each section. Typically, the total energy resolution is about 15–20% at 30 GeV, 10% at 100 GeV, and 5% at 1 TeV.

2.1.2.5 Muon Chambers

Since muons are not expected to strongly interact with matter and are less subjected to radiative losses due to their mass larger than the electrons one, their trajectory is often undisturbed by the layers composing the structure of CMS. Muons are usually invisible to the experiment's calorimeters and their characteristic signature consists in the sole trajectory inside the silicon tracker. CMS relies on a set of additional detectors for identifying and reconstructing the particles four-momenta. The 'muon chambers' are situated outside of the solenoidal magnet and in the forward regions; this sub-system employs the use of three types of detecting technologies: Drift Tubes (DT), Cathode Strip Chambers (CSC) , and Gas Electron Multipliers (GEMs). The layout of

one of CMS quadrants highlights the muon chambers setups. The DT modules are located radially outside the barrel region, each of them covers an area of $2 \times 2.5\,\mathrm{m}^2$ and consists of 12 aluminum layers and 60 gas filled tubes. Incident muons produce free carriers inside the gas detectors and their collection provides information about the muon coordinates: the tubes are grouped such that the inner layers provide information over the z-coordinate while the outer layers reconstruct the transverse (x and y) coordinates. The region of the end caps is instead covered by the CSCs. These detector use a gas filled volume to intercept the muons and drift the resulting charge avalanches to induce signals in the read-out. The latter consists of crossed anode wires and cathode strips which, respectively, provide a position for the electrons and ions clusters generated by the particles passage. The two point reconstruction is operated over six consecutive layers of detection for an accurate trajectory matching with the information provided by the silicon tracker. In both regions, namely the barrel and the end-caps, one can find sets of GEM and Resistive Plate Chambers (RPC) detectors. The avalanche clusters generated by the passage of muons drift towards the read-out planes (portioned in conductive strips), inducing highly localized signals characterized by fast rise-times. CMS employs the outstanding spatial and temporal resolution of these devices for reconstructing the muon momenta and to provide reliable trigger options.

While the CMS experiment is fully equipped to reconstruct the majority of events coming from the hadronic collisions, the finite data acquisition rate, read-out bandwidth, and data storage limits the possible output stream. At the same time, the physics program of CMS focuses on very rare events, and the more ordinary collisions are mainly used as control sample and for detector calibration purposes. Indeed, the so-called 'minimum bias'events originate from long-range interactions and populate the data buffers, hiding the more rare processes. A trigger system based on a dual tier architecture is responsible for selecting the events of interest while rejecting background events. The custom made processors in the CMS first trigger level (L1) are use to compute fast measurements over a simplified set of information. From the merging of single hits in the calorimeters to the tracking of the muon system, L1 operates with a selection rate limited to about 100kHz. After a typical latency of $3\,\mu$s, the gathered information are propagated to the higher level of decision layers. The farm of processors comprising the High-Level Trigger (HLT) performs the last data reduction needed before the storage. This operation employs the use of an optimized version of the CMS full event reconstruction software in order to limit the output data-streams to

an event rate of about 1kHz.

2.1.3 The High-Luminosity upgrade of the LHC

During the last decade, the LHC has gone through a series of technological upgrades that helped the physics community achieving important scientific goals. With the increased collider's center-of-mass energy (up to 13 TeV) implemented during 2015, and the following reduction of the beams emittance finalized during the Long Shutdown 2 (LS2), the LHC greatly improved its sensitivity to BSM effects. A major upgrade of the machine's capability is planned for LS3. This phase will see a massive increase in the LHC luminosity, resulting from a better collimation of the colliding beams around the IPs and larger population of the bunches. Although the collider is expected to run providing a stable instantaneous luminosity between 5 and $7.5\times10^{34}\,\mathrm{cm}^{-2}\mathrm{s}^{-1}$, the new apparatus will be capable of delivering up to $2\times10^{35}\,\mathrm{cm}^{-2}\mathrm{s}^{-1}$.

In this scenario, the accelerator will provide the CMS and ATLAS experiments an additional integrated luminosity of about $2500\,\mathrm{fb}^{-1}$ over a span of 10 years. This regime of operation will benefit a vast variety of physics programs (72); it will open the possibility to study extremely rare processes, and increase the sensitivity on BSM phenomena. Unfortunately, this comes at the price of a dramatic increase in the number of collisions per bunch crossing, which is expected to reach $\sim$200 at maximum luminosity (around four times the current peak PU). Only a few of these particle interactions can be used for searching new physics phenomena, as most of the collisions are 'soft' (or 'peripheral') and happen at scales much lower than TeV. The sea of collisions products is therefore dominated by PU events entering the detectors acceptance and recorded as mismeasured or misidentified tracks. Additionally, radiation coming from such a high PU adds to the energy within the calorimeters, complicating the reconstruction of isolated leptons and photons.

The amount of radiation to sustain, as well as the processing rate needed for data collection, pushed the LHC experiments to work towards the improvement of its detectors capabilities. During LS3, CMS will undergo a series of major upgrades to comply with these unprecedented requirements (73; 74). The excellent efficiency, resolution, and background rejection performance of the experiment will be maintained introducing several modifications to the detector hardware and reconstruction techniques (75; 76; 77).

2.2 The MTD for the CMS Upgrade

In light of the post-LS3 upgraded luminosity of the LHC 2.1.3, the CMS Collaboration is striving for preserving the excellent detector's performance. In 2017, a CMS Technical Proposal (47) details the modifications the experiments will have to undergo to pursue the new data acquisitions. Among the planned upgrades, CMS proposed the installation of a new layer of detection that will employ modern state-of-the-art timing technologies: the MIP Timing Layer (MTD). This system will aim to provide precise timestamp for MIPs, matching charged tracks to the correct interaction vertices within the bunch crossing. In this way, the experiment can strongly suppress the out-of-time PU coming from individual particle interactions occurring at different times[4]. The time at which one of the collision occurred can be reconstructed associating the tracks coming from a vertex to the timestamp of hits in the MTD. The MTD R&D program is divided into two sections. A portion of the timing detectors will cover the region of the CMS central barrel, and it is referred to as Barrel Timing Layer (BTL) group. The End-Cap Timing Layer (ETL) describes the set of detectors responsible for the timing reconstruction in the forward regions.

2.2.1 Impact on CMS operation at HL-LHC

Within CMS, the identification of particles relies on a global event reconstruction algorithms, the particle flow (PF) event reconstruction (78). The PF combines the information of all sub-detectors for establishing a list of candidate objects to associate to the reconstructed products. In CMS, the PU mitigation is performed by the PF, which utilizes statistical inference techniques for eliminating charged tracks inconsistent with the most probable vertex location and improving the reconstruction quality. While the high granularity of the tracking detecting apparatus will suffice for an efficient PU mitigation at current LHC capabilities, the HL-LHC higher line density[5] dN_v/dz of collision vertices substantially complicates the matching procedure. The PF algorithm associates primary vertices to decay products minimizing their relative distance of closest approach $|\Delta z(\text{track,PV})|$.

However, this sample is contaminated by tracks coming from displaced sources (secondary

[4]This effect is due to the longitudinal overlap of the bunches, which distribution has typical RMS ranging between 180-200 ps.

[5]Density of vertices per unit of space, calculated along the axis of the beams.

interactions, resolution tails, particles decaying in flight) which require the PF to set optimal cuts on the acquisition along the z-coordinate. Increasing dN_v/dz, the acquisition window can become larger than the one set by considering the tracking resolution alone: simulation results show how setting $|\Delta z(\text{track,PV})| < 1\,\text{mm}$ causes a non-negligible PU contamination for vertex linear densities greater than $1\,\text{mm}^{-1}$. At the peak scenarios expected for the HL-LHC, these densities substantially increase to around 1.2 mm^{-1} and $1.9\,\text{mm}^{-1}$, respectively for 140 and 200 PU interactions (assuming a bunch spread of about 4.5 cm RMS). This could greatly affect the CMS performance, degrading the efficiency and resolution of all measurements requiring isolated objects, or merged tracks (e.g. study of missing energy, jets).

With the installation of the MTD, the object reconstruction and identification strategy relies on a combined 4D information. Simulation results confirm that a satisfying PU mitigation is achieved considering time resolutions of around 30-40 ps expected at the beginning of the detectors life. A satisfying background rejection can be achieved with the 50-60 ps of resolution expected after the irradiation. For every track it will be possible to define a window $|\Delta t(\text{track,PV})| < N \times \sigma_t$, that depends on the detector resolution, and the number of independent measured timestamps. Figure 2.6 compares the performance of the vertex matching for a simulated high PU scenario, with and without the use of timing information. This noticeably reduces the overall contamination of incorrect vertex merging from 15% to 1% for collision with a PU = 200 (as displayed in Fig. 2.7). With the installation of the MTD, CMS will gain efficiency in the reconstruction of single, and multi-object final states, as well as an improvement in the reconstruction of missing momentum (p_t^{miss}). Overall, the efficiency gain, when compared to the constant background rates, amount to about 20%-30% over many different measurements. Table 2.1 summarizes the expected scientific impact of the MTD at the HL-LHC.

The HL-LHC aims on opening the possibility of measuring rare decay channels with unprecedented statistical accuracy. Rare decays of the Higgs boson constitute one of the main physics motivation for the installation of a more performing experimental apparatus. In particular, studies of di-Higgs production provide the only tool for a direct determination of the Higgs boson trilinear self-coupling (λHHH) (79; 80) and determining the shape of the Brout–Englert–Higgs potential. At the LHC, this measurement relies on the small cross section of the Vector Boson Fusion (VBF) process, and combines the information of five decay channels: bbbb, bb$\tau\tau$, bbWW

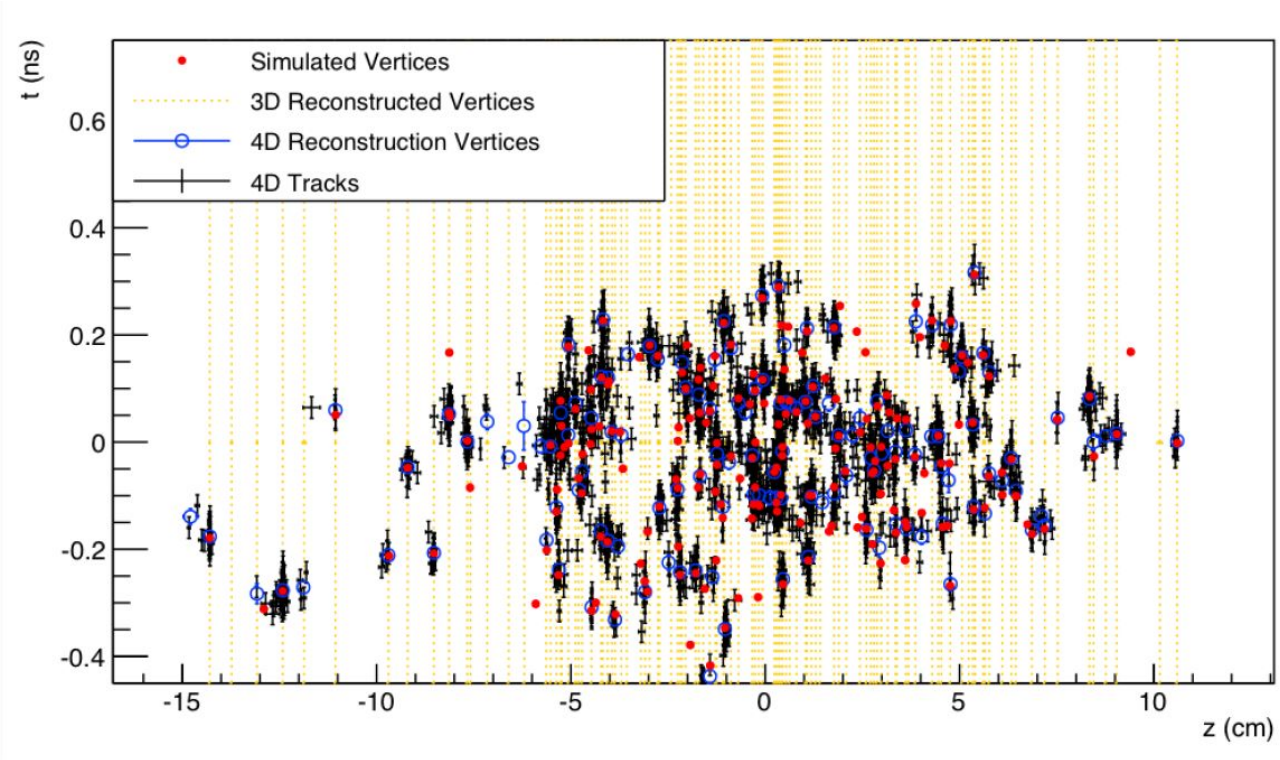

Figure 2.6: Vertices simulated (in red) for a PU = 200 scenario (18). The vertices position in time and space is represented with respect to the bunch crossing t_0, and z_0. It's clear how the sole 3D reconstruction (yellow dotted lines) does not contribute in detecting individual vertices within the bunch crossing (t_{RMS} ~180 ps, z_{RMS} ~4.6 cm). An accurate location is achieved by adding a MIP timing detector with about 30 ps of resolution (in blue and black).

final states	**Physics measurement**	**MTD impact**
H→ $\gamma\gamma$ H→4 leptons	+ 15–25% (stat) precision on cross section → Improve coupling meas.	Isolation and Vertex identification
VBF→H→ $\tau\tau$	+ 30% (stat) precision on cross section → Improve coupling meas.	Isolation VBF tagging, p_t^{miss}
HH	+ 20% gain in signal yield → Consolidate searches	Isolation b-tagging
EWK SUSY	+ 40% background reduction → 150 GeV increase in mass reach	MET b-tagging
Long-lived Particles	Reconstruction mass of the products → improve potential for discoveries	β_{LLP} from timing of displaced vertices

Table 2.1: Impact of the MTD installation on some of the main physics measurements for the HL-LHC. Table edited from Ref. (47).

(with WW → $l\nu l\nu$), bb$\gamma\gamma$ and bbZZ (with ZZ → $ll'll'$).

The increased luminosity of the HL-LHC will allow the collection of more significant sam-

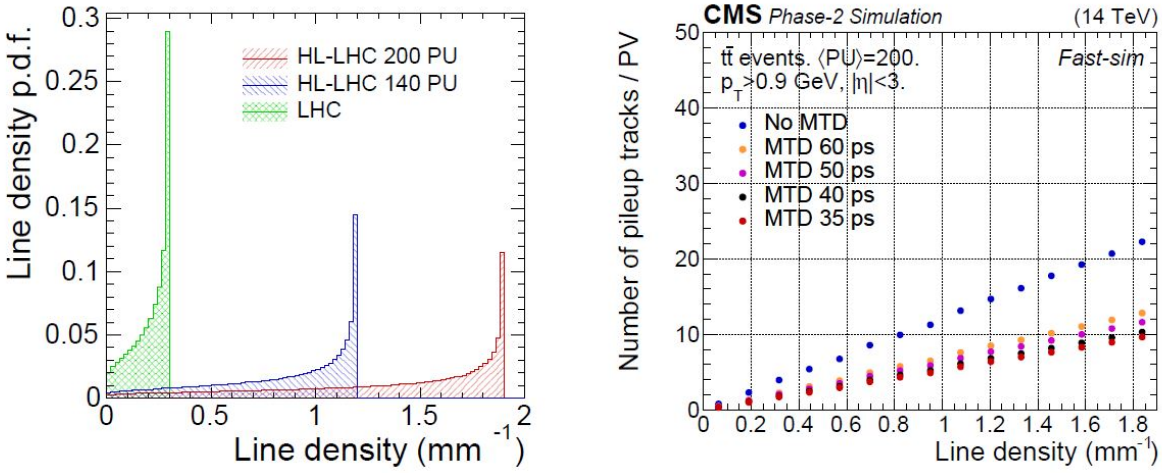

Figure 2.7: Left: the plot shows the probability density functions of the line densities along the z-axis. The three PU scenarios under analysis, 30, 140, and 200 correspond to densities respectively peaking at 0.3, 1.2, and 1.9 mm^{-1}. Right: the plot shows the reduction in the rate of misidentified tracks as a function of the density of event per square millimeter. The 3D (in blue) and 4D (in red) reconstruction are performed for a PU = 140,200. Both plots have been extracted from Ref. (18).

ples. However, the contamination of PU tracks adding spurious secondary vertices leads to a SNR degradation that increases with the rate of interactions. This results in b-jet tagging efficiency losses of about 10% at high PU. In this scenario the MTD helps mitigating the PU and enhancing the matching of candidate particles with the primary vertex with an improved b-jet identification efficiency. The b-jet tagging efficiency degradation is recovered by requiring the track to fall in a window of $3.5\sigma_t$ (with σ_t = 30 - 40 ps) of the candidate vertex. As a result, the contamination of secondary vertex matching is reduced by about 30%, and the separation capabilities of b-jets and jets from light-flavor quarks, is greatly enhanced.

The improved MTD b-jets tagging performance impacts the searches for di-Higgs production, with at least one of the two bosons decaying in $b\bar{b}$ quarks. These measurements will experience a reconstruction gain of around 4-6% in the case of a single Higgs decaying in b quarks, and a combined gain in the yield of the multi-object final state HH $\rightarrow b\bar{b}b\bar{b}$ of about 18% (including the ETL and BTL). Figure 2.8 (right) puts in display the signal's enhancement adding the timing information in the analysis of HH $\rightarrow b\bar{b}b\bar{b}$. Left panel of Fig. 2.8 shows the efficiency of the b-tagging procedure, as a function of the line density at the vertex candidate. Similarly, the signal where H $\rightarrow \tau\tau$ (or other leptonic channels) is enhanced due to the lepton isolation from charged tracks

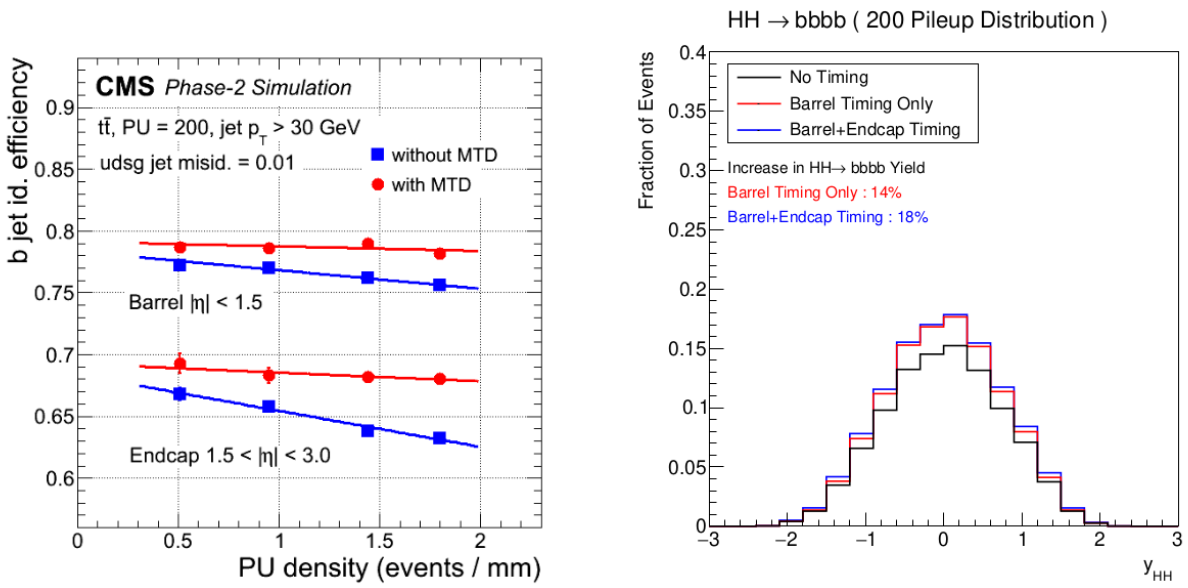

Figure 2.8: Left: b-tagging efficiency as a function of the line density (in a scenario of 200 PU interactions). Right: yield enhancements of the di-Higgs decaying in b quarks as a function of the Higgs rapidity (normalization operated on the no-MTD case). Plot extracted from Ref. (18).

capabilities, as well as the improved resolution over p_t^{miss}. Simulated scenario (19) at the HL-LHC reports a gain of around 10% over the missing momentum resolution, which translate in a 10% enhancement in the $\tau\tau$ invariant mass distribution (see Fig. 2.9) At the projected integrated luminosity of the HL-LHC (3000 fb^{-1}), the addition of the MTD improves the significance of di-Higgs measurements of more than 13%. An additional 26% (or 20%, when considering a more conservative scenario, where the detectors resolution σ_t = 50 ps) of integrated luminosity would be required for obtaining similar results without timing information, therefore justifying the installation of a new layer of detection.

2.2.2 The MTD

The two sections composing the CMS structure, the barrel, and the end-caps, operate under very different conditions. Consequently, the hardware requirements to be considered during the R&D of the ETL and the BTL greatly differ. Aside from dissimilarities in their mechanical constraints, the two zones are exposed to very diverse levels of radiation, as the dose collected in the end-caps exceeds up to 30 times the radiation affecting the barrel region. Furthermore, the features of the new sub-detectors have to be compatible with the current experimental apparatus, enabling new

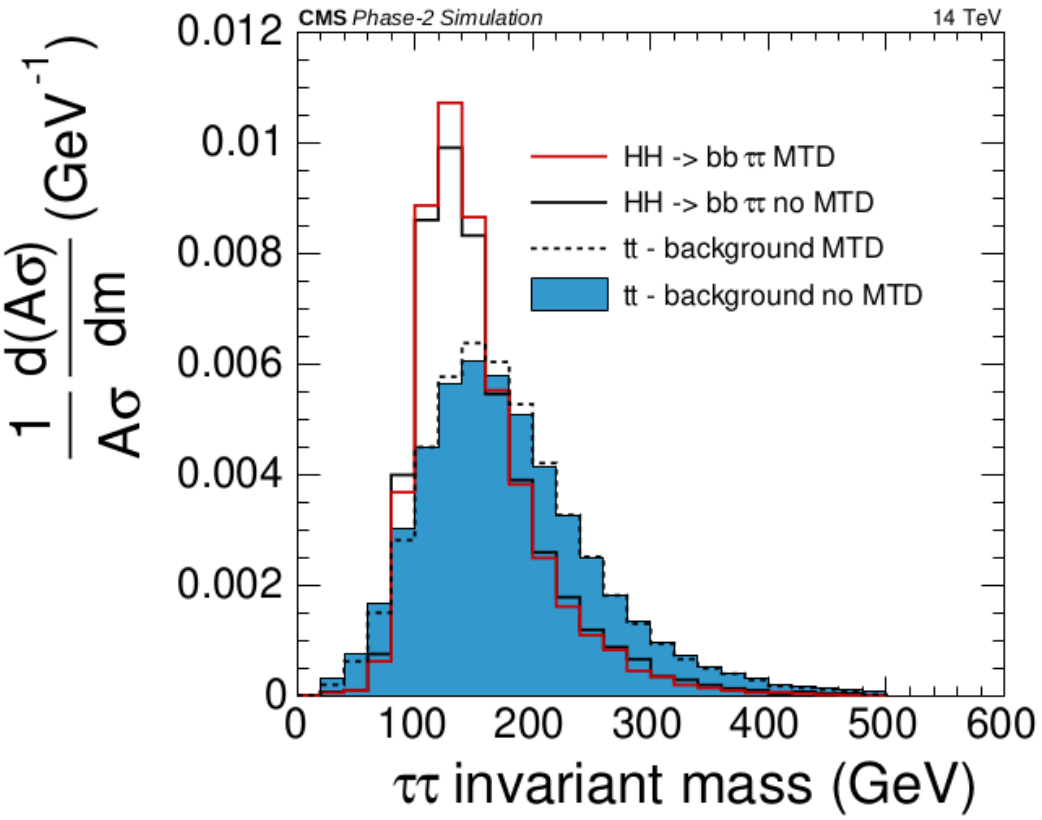

Figure 2.9: H $\rightarrow$ bb$\tau\tau$ studies: comparison between the reconstruction of the invariant mass of τ pairs with and without the use of the MTD (18; 19).

modalities of data collection while preserving the performance of the existent ones.

The region between the tracker and the calorimeters has been selected for the installation of the MTD. The new thin layer of detection will cover a pseudorapidity $|\eta| < 1.5$ in the barrel area, and up to $|\eta| = 3.0$ in the end-caps. The choice of the optimal sensor is constrained by the environmental differences of the two areas and is the results of extended R&D campaigns. For the BTL, the Collaboration has selected crystal scintillators read-out by SiPM. The SiPMs will be used to cover the barrel acceptance, and are required to sustain a total expected dose of around 3×10^{14} n_{eq}/cm^2. Their promising performance have already extensively been tested, and employed for the construction of physics experiments, and commercial applications. The SiPM production is fairly straightforward, and their quality relies on the experience of leading company providers around the world.

However, the radiation levels of the end-caps at the HL-LHC (up to 3×10^{15} n_{eq}/cm^2) largely

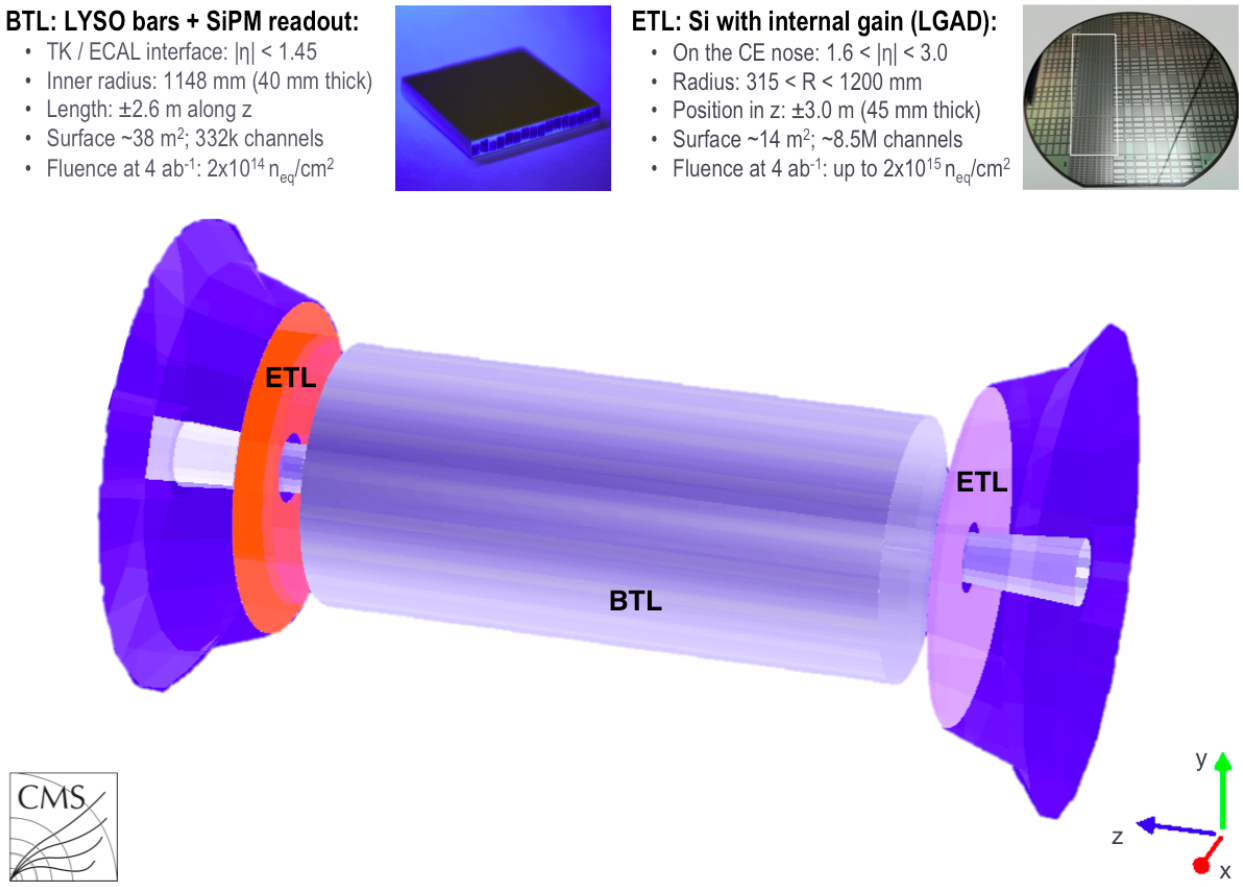

Figure 2.10: View of the timing layer. The BTL (in grey) and ETL (orange and violet disks) are simulated with the GEANT (20) framework and integrated inside the CMS apparatus.

exceeds the maximum tolerance of the SiPMs. LGADs have been selected as a solution for the ETL project. The less stringent installation schedule of the ETL allows the Collaboration to plan the performance evaluation of this technology yet unexplored by HEP experiments. Moreover, the higher production costs are compensated by the lower detection area to cover (around 2.5 times lower than the barrel region). The two detector systems require the development of incompatible front-end electronics, although synchronized by a common clock distribution. Their slow control, cooling and backend systems will also be shared. Figure 2.10 shows the complete geometrical MTD detector concept. The next section 2.2.3 describes the features of the ETL, focusing on the hardware requirements, and the detector design. A detailed description of the BTL can be found in Chapter 2 of the TDR (18).

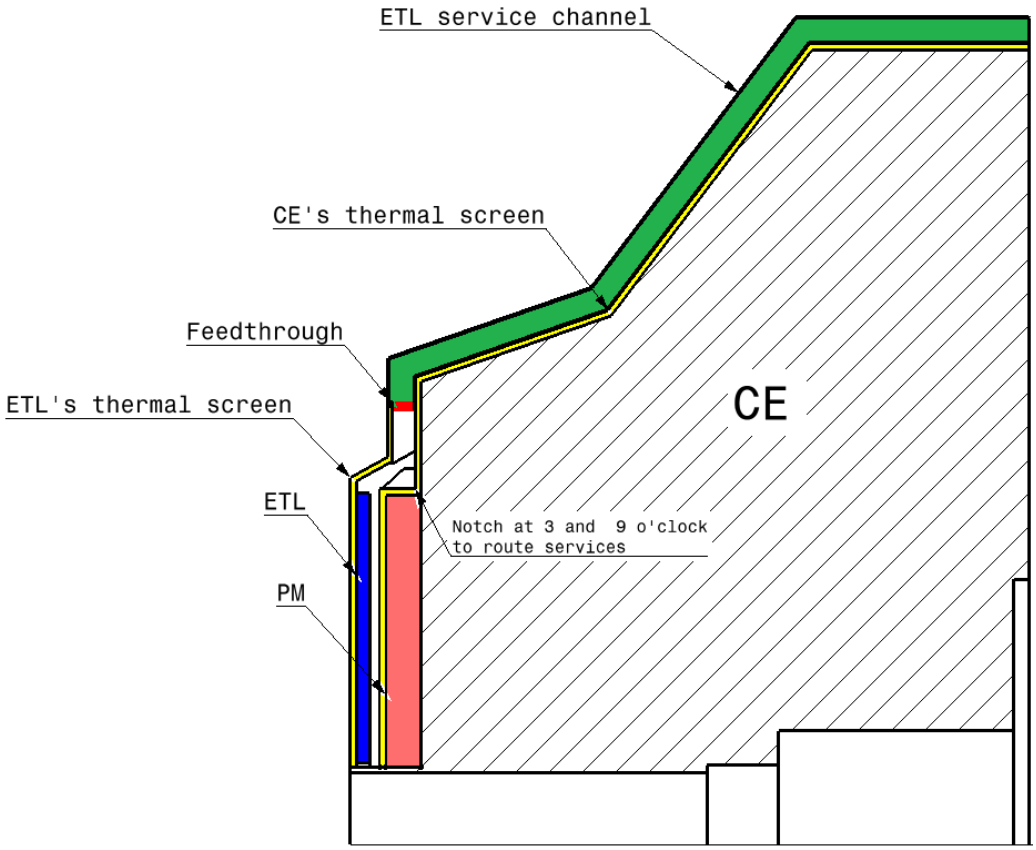

Figure 2.11: Side view of the ETL detectors placement inside CMS EC. The picture shows the thermally independent region allocated for the detectors (in blue) that will allow accessing the hardware during LHC Technical shutdowns.

2.2.3 End-Cap Timing Layer

Placed about 3 m away on both z sides of IP5, the ETL detectors extends radially from 315 < r < 1200 mm (or $1.6 < |\eta| < 3.0$), reaching a total coverage of 7.9 m^2 per side. The system hermetically closes the region between the calorimeters of the end-caps and the end of CMS tracker, enveloping the detectors in two sectioned disks (or *wedges*). The disks are thermally isolated and independent from the rest of the structure, and can be removed regardless of the presence of the beampipes. This concept allows easy maintenance of the hardware during LHC shutdown periods, without having to access the radioactive environment. Figure 2.11 shows the location of the ETL detectors inside the CMS apparatus.

A full detector stack is required to be contained in around 45 mm (in z), and comprises the sensors, the read-out, and the mechanical supports. In the proposed module design, each section

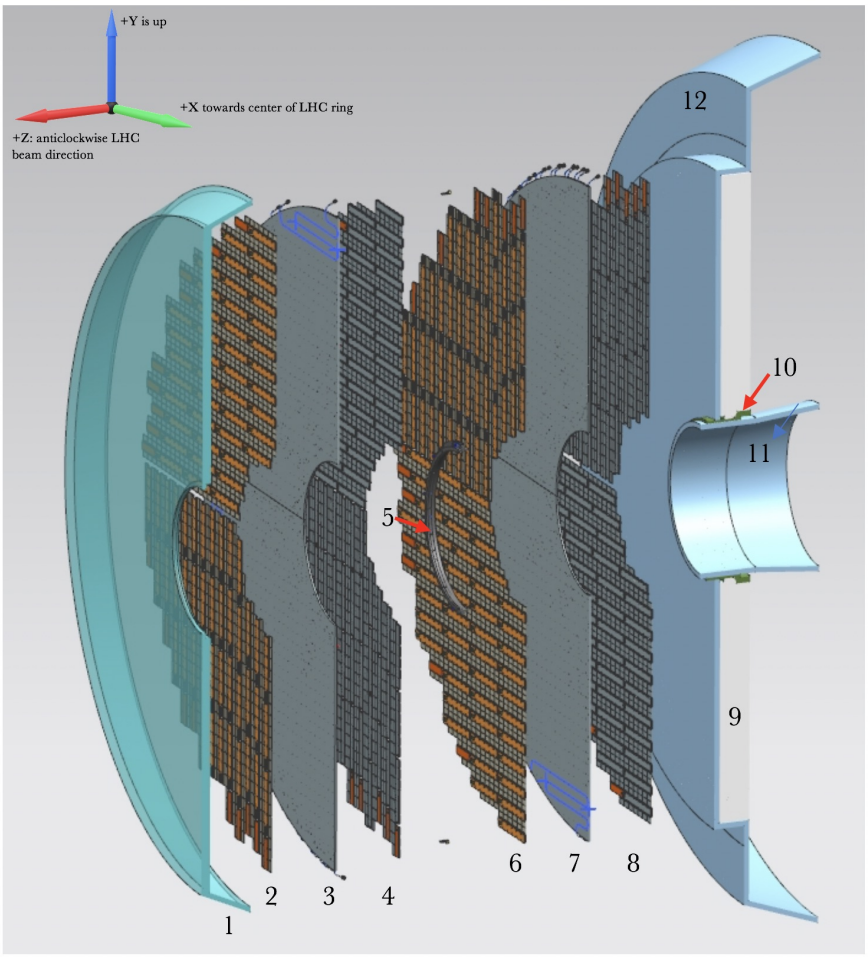

1: ETL Thermal Screen
2: Disk 1, Face 1
3: Disk 1 Support Plate
4: Disk 1, Face 2
5: ETL Mounting Bracket
6: Disk 2, Face 1
7: Disk 2 Support Plate
8: Disk 2, Face 2
9: HGCal Neutron Moderator
10: ETL Support Cone
11: Support cone insulation
12: HGCal Thermal Screen

Figure 2.12: Sectional view of one of the ETL detector units (18). The disk faces are populated with the pixels (in gray) and the service hybrids (in orange). The latter communicate with the read-out chips, while supplying them the power, and monitoring their functionality.

of the disks calls for an array of 13 $\times$ 32 square LGAD pads, each of 1.3 mm $\times$1.3 mm[6]. The total detection area per section is about 21 $\times$ 42mm^2. Two disks separated by 20 mm in z are installed in each EC, for a total of 4×10^6 pixels. The locations of the components in the adjacent disk are staggered, such that each face of the module covers the blind regions of the other one. This allows the reconstruction of two independent hits for each incident track, and ensures a more precise time reconstruction. Figure 2.12 displays a side vision of one of the ETL wedges.

To read out the sensors, a pair of 20 mm $\times$ 20 mm (hence processing a matrix of 16 $\times$ 16 pixels) custom-made ASICs, the end-cap Timing Readout Chips (ETROCs), is mounted in each

[6]The size of the pixels was selected for limiting the sensor's capacitance, in turn limiting their charge collection time, enhancing the SNR, although adding to the overall channel count.

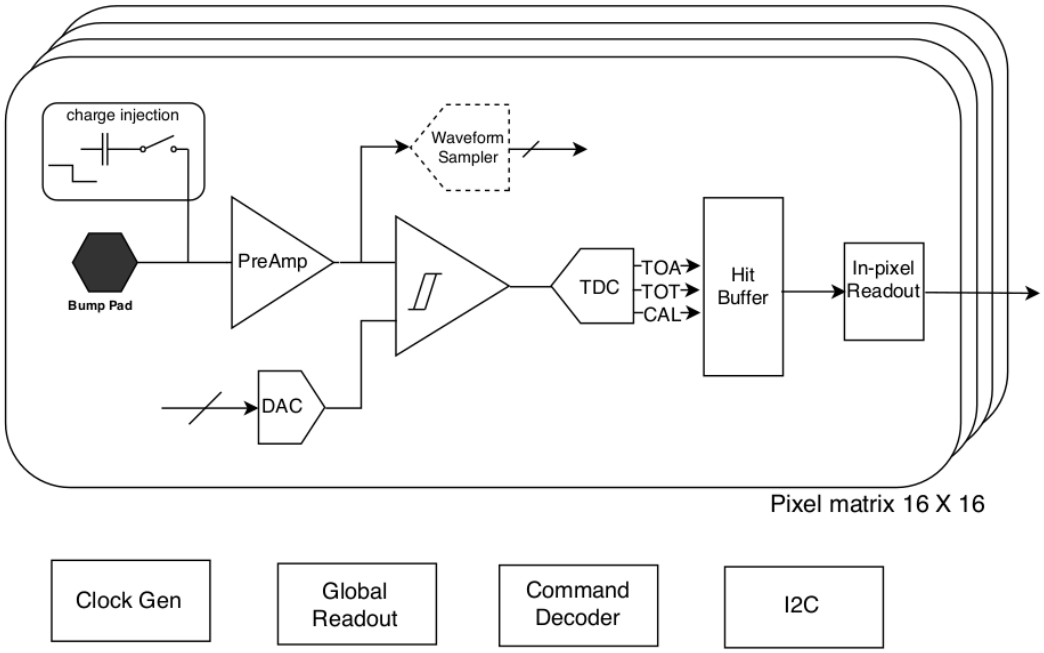

Figure 2.13: Sketch of the ETROC architecture extracted from Ref. (18). From the bump pad connected to the sensor, the signal is processed by the preamlification stage, and later the timing information in output by the TDC. For testing and calibration purposes, each ASIC is equipped with a charge injection circuit controlled by a DAC. As the absorbed radiation increases, a waveform sampling circuit allows for a more detailed monitoring of the pulses.

module. The architecture of the ETROC, sketched in Fig. 2.13), includes a pre-amplification stage, a discriminator, and a TDC. The collective performance of this chain has to ensure a final resolution per hit in ETL modules of 50 ps, or 35 ps for the two disks. To achieve it, the TDC uses a time-over-threshold information for correcting the distortions affecting the particles arrival time distributions. A rough of estimate of the total resolution has to include the LGAD contribution, measured to be about 30 ps, and the one of the TDC (less than 10 ps). The nominal 50 ps per disk requires an optimization of the jitter of the pre-amplifier and discriminator, which will have to be less than 40 ps. On-detector boards, the service hybrids, are responsible for reading the signals of the ETROCs. At the same time, the hybrids provide power for both the ETROCs and the LGADs, monitor the ASICs performance, and carries the instruction of the fast and slow controls.

For the scope of this thesis, the results reported in the next sections focus on the characterization of the LGAD sensors. Fundamental features such as their fill factor, and their spatial uniformity ensures the achievement of the performance required during the detector design. More importantly, their time resolution was evaluated over a vast range of accumulated dose, to mimic

the environmental conditions imposed by the ETL at the HL-LHC.

2.3 Characterization of LGADs at the KU laboratories

In addition to the tests in-loco at the FTBF (described in section 2.4), the KU team has provided support to the MTD project performing functionality tests and characterization of the ETL modules. To fulfill this task, the KU team has established a new timing laboratory for the installation of the required hardware. The laboratory at KU is equipped for investigating the capabilities of the individual sensors. Thanks to the group's expertise in the development of fast detectors, the read-out board designed at KU was selected to be employed for the LGADs characterization at the FTBF, and used to obtained the results discussed in section 2.4.

2.3.1 Experimental setup at KU

In order to finalize the MTD detector design, several procedures for quality control and performance evaluation of the produced detectors have to be followed. The KU team contributed to the acquisition and installation of new equipment for performing specialized characterization, and optimization tests on fast detectors. The laboratory facilities are provided with more conventional instruments dedicated to generic electrical tests, as well as more complex systems for automatizing measurements to be performed on mass produced components.

An optical table is dedicated to host the setup for collecting and analysing the response of the custom-made read-out boards produced at KU. The PCBs are mounted on motorized moving supports that spans the x-y directions with a minimum achievable incremental movement of around 0.8 μm (81). These configurable steppers motors can be controlled using a LabView (82) software that coordinates their movement with an external acquisition systems.

The bias voltage can be provided using two complementary devices. A Keithley 2410 SourceMeter (83) operates in the range of $\pm$200 mV to $\pm$1 kV, and current range of $\pm$1 μA to $\pm$1 A. In the same way, a four channels CAEN DT5533E (84) can bias the sensors with an output range that goes up to 4 kV with 3 mA. A Rode & Schwartz HMP4040 (85) programmable power supply (0 to 32 V and 0 to 10 A , 384 W) is used to provide the low voltages to the amplification stages on the read-out boards. The detectors can be tested with different radiation sources. For the studies of charged

particle interaction, an ^{241}Am producing α-particles with energies 5.486 MeV (85%), 5.443 MeV (13%), and 5.388 MeV (2%), and a ^{90}Sr with a continuous spectrum up to 2.3 MeV were used. The two can be kept on top of the detector under analysis using rigid supports connected to the table. For the production of neutral particles, the table also hosts a 1080 nm picosecond laser, generating 50 ps wide pulses with a peak power greater than 100 mW.

The waveform output by the detectors are then collected by a Teledyne-Lercroy Waverunner 640zi (86), a fast sampler capable of digitizing pulses with 4 GHz of analog bandwidth, and a maximum sampling rate of 40 GS/s. Alternatively, the acquisition can be performed using a SAMpler for PICosecond time pick-off (SAMPIC) ASIC (23), conceived by the collaboration between IRFU/SEDI, Saclay and LAL, Orsay. This device, originally designed for reading out the TOF forward detectors of the ATLAS experiment, is a fast sampler with picosecond precision and high rate capabilities. Input signals can be continuously sampled (up to 10 GS/s) using a series of 64 network capacitors controlled by delay lines. Signal amplitudes exceeding a set threshold trigger the digital conversion that uses a Wiilkinson Analog-to-Digital Converter (ADC). The ADC resolution depends on the acquisition modality: the SAMPIC can perform fast acquisition with less than 200 ns dead-time between samples using an 8-bit conversion. The voltage ramp of the Wilkinson ADC can reach a resolution of 11-bits although increasing the conversion time to about 1.6 μs. The intrinsic RMS noise of the SAMPIC chip ranges from about 1 mV (when used with the full ADC capabilities), and increases of about 15% when used in fast conversion mode. A software developed on Windows can be used for interfacing with the instrument: an acquisition module is constituted by a mother board hosting the FPGA for managing the digital I/O of up to two mezzanine boards. The software allows the calibration of the SAMPIC chips on the mezzanines, the data collection, and basic data analysis.

Since KU was selected for cooperating in the quality control of the ETL detectors modules, the laboratory has been also equipped with a SPS-2800 motorized probe station for the test of samples, with thermal testing capabilities. The environmental enclosure contains a triaxial thermal chuck capable of holding up to 8 in $\times$ 8 in wafers, and providing external bias. Using the cooling connections routed inside the chuck, the temperature can be modified from -25 °C to +85 °C. The included motorized stage translates the chuck in the XYZ axis with a resolution of 65 μm. The position and status of the samples can be observed with a wide zoom magnification ranging be-

tween 3.5× and 90×, with the use of the stereo zoom microscope installed in the enclosure.

Temperature studies on sensors and electronics can also be performed independently from the probe station, as the samples can be installed inside a T-50C thermal chamber produced by the Xi'An Lib Environmental Simulation Industry. This provides a range of temperature that spans from -50 °C to +100 °C; the operation modes are completely programmable and the temperature information and timestamp are stored locally wit the possibility to be retrieved off-line.

2.3.2 Characterization of the KU read-out board

A prototype of the read-out board developed at KU, and later utilized for characterizing LGADs during the ETL test-beam campaigns, was first developed and tested in 2017. Although its design has been since then slightly modified, the core of the amplification and shaping schematics presents the same overall structure of its successors (a later version of this board is described in section 3.3.3). This version uses a 16 mm × 13 mm gold HV pad were sensors can be glued and bonded to the near pre-amplification and ground connections. The HV pad distribute stable bias to the sensors up to more than 1 kV. The amplification chain is powered to 4.5 V through an independent low voltage line and is composed by two stages of transimpedence amplifiers based on bjt transistors technology. A picture of the KU 2 channels board can be found in Fig. 2.14.

When choosing the components for populating the board, simulation software (e.g. (43)) can be used to predict the optimized parameters to pair with the used sensor. To evaluate the detector performance, a LGAD sensor originally designed for the data collection at the PPS experiment (87) was glued to the board (the same detector design will be used in the test described in section 3.3). The CT-PPS sensor is subdivided in 32 pixels of different sizes, which provides a good testing ground for measuring the board capabilities when modifying the input impedance and capacitance of the system. A reconstruction of the pulse amplitude distribution can be obtained scanning the detector surface with the laser source setup (described in section 2.3.1). The resulting maps allows to reconstruct the spatial dependence of the signal intensity for individual pads. The senor specifications, as well as an example of the intensity graph are depicted in Fig. 2.15. The projection of the amplitude distribution over a single axis (as shown in Fig. 2.16) demonstrates a stable efficiency over most of the pixel length, and an abrupt drop close to the edges. This ensures

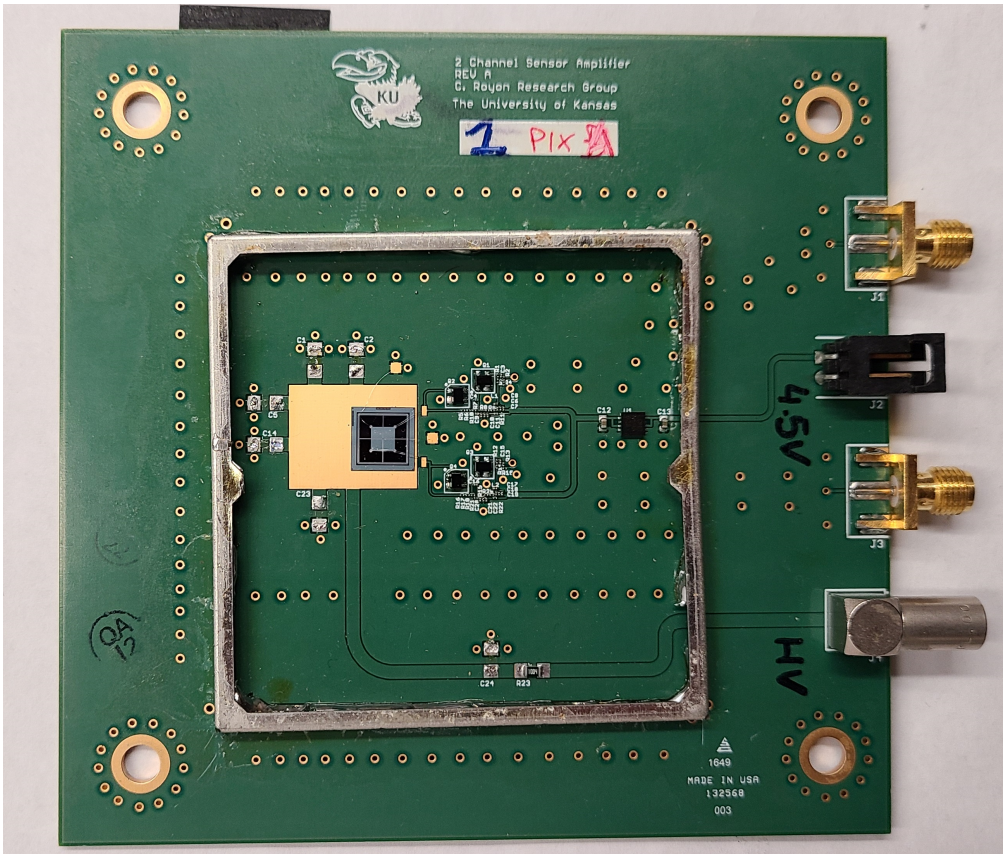

Figure 2.14: The KU read-out board hosting a 50 μm thick HPK LGAD. Next to the sensor, the two amplification chains are visible.

uniformity in the charge collection, and consequently on the time response of the detector. With this setup it is possible to study the inter-pad regions for measuring the no-gain distance between adjacent pixels. This quantity is of crucial importance when defining the fill factor of the detectors, namely the ratio between the sensor's active region and the total sensor's area, as shown in Fig. 2.36. The no-gain distance is computed using the 50% amplitude of the detector response. The plot is obtained using the laser spot to scan the area in between two adjacent pads of the CT-PPS sensor, biased at 100 V. It is important noticing that the presented measurements are not finalized to produce significant results for the characterization of the CT-PPS sensor. In this detector, each pad is in fact provided of metallized borders that intrinsically subdivide the drifting fields of the adjacent areas. These measurements are instead used as benchmark for the acquisition setup and proof of concept of the data reported during the next sections.

Using the laser pulse aimed between adjacent pads (as displayed in Fig. 2.18) it is also possible

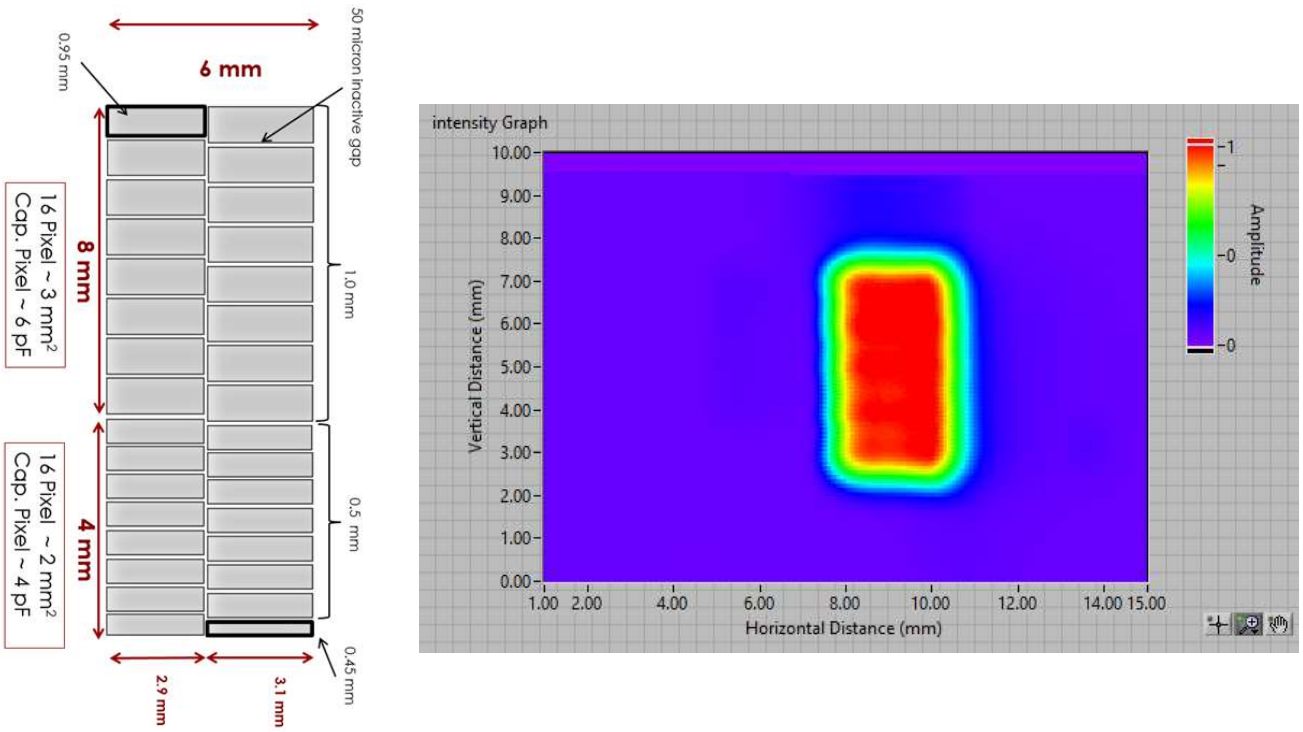

Figure 2.15: On the left, the image reports a sketch of the CT-PPS sensor used for characterization tests of KU read-out boards (21). On the right, the intensity graph of one of the detectors obtained during the laser scan (22). The area at lower intensity on the boundaries of the active area are comprehensive of the guard-ring, and the dead space between neighbor pixels.

to record the output waveforms and measure the difference in time between two signals. The two channels are output to the SAMPIC, which digitizes the pulses and provides the information for computing this quantity. The statistic measures of the resulting Gaussian distribution, shown in Fig. 2.19, displays a time resolution with this setup of around 10 ps. Since the energy deposit of monochromatic laser pulses is not affected by Landau fluctuations, this measurement provides a rough estimate of the maximum achievable resolution with the designed read-out.

The KU board utilized in the characterization tests at the FBTF was assembled according to simulated results for hosting a 20 pF sensor with:

- input impedance of 700

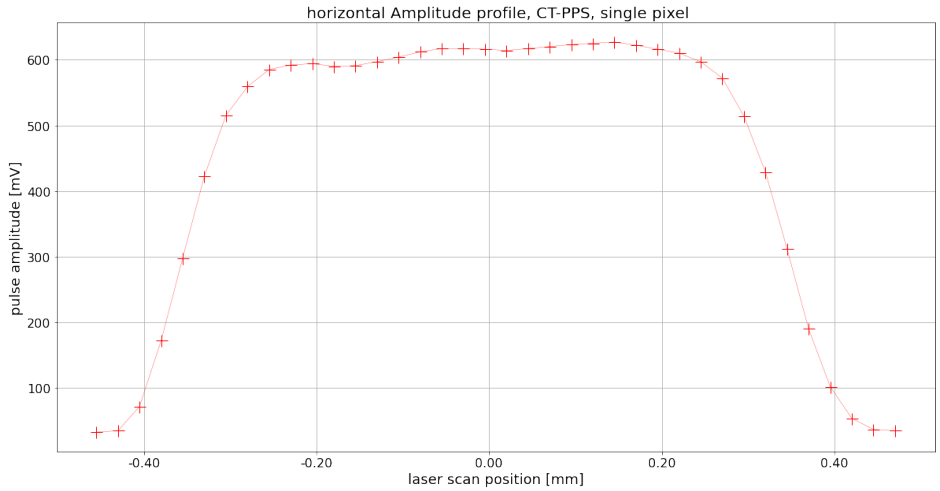

Figure 2.16: Profile of the amplitude distribution along the pixel's length. The charge distribution results to be uniform along the pixel's length with an expected drop around its boundaries.

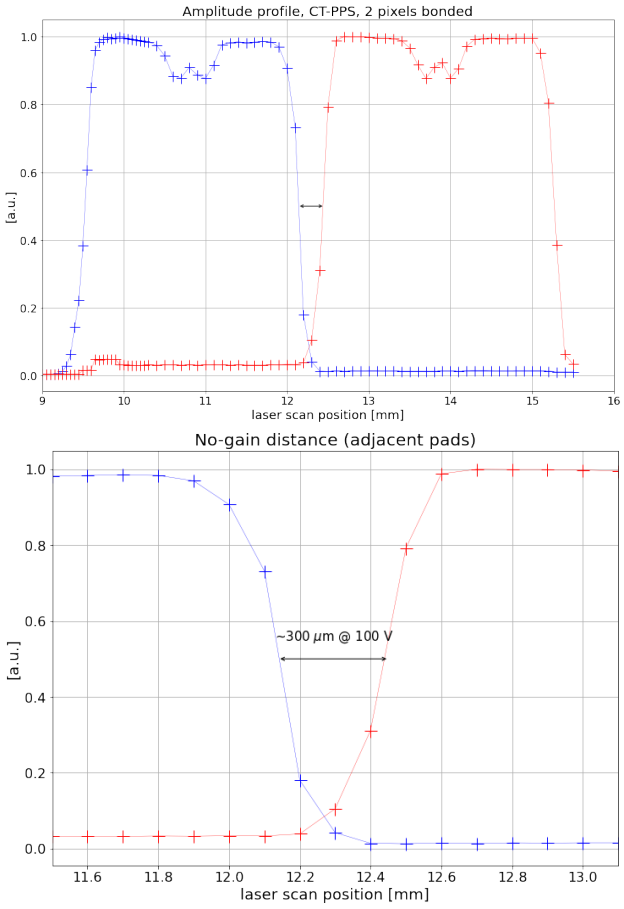

Figure 2.17: Studies of the no-gain regions of the CT-PPS detector biased at 100 V and performed with a laser scan. Although consecutive pads are equally spaced by 50 μm, the effective inactive area depends on the local gain uniformity.

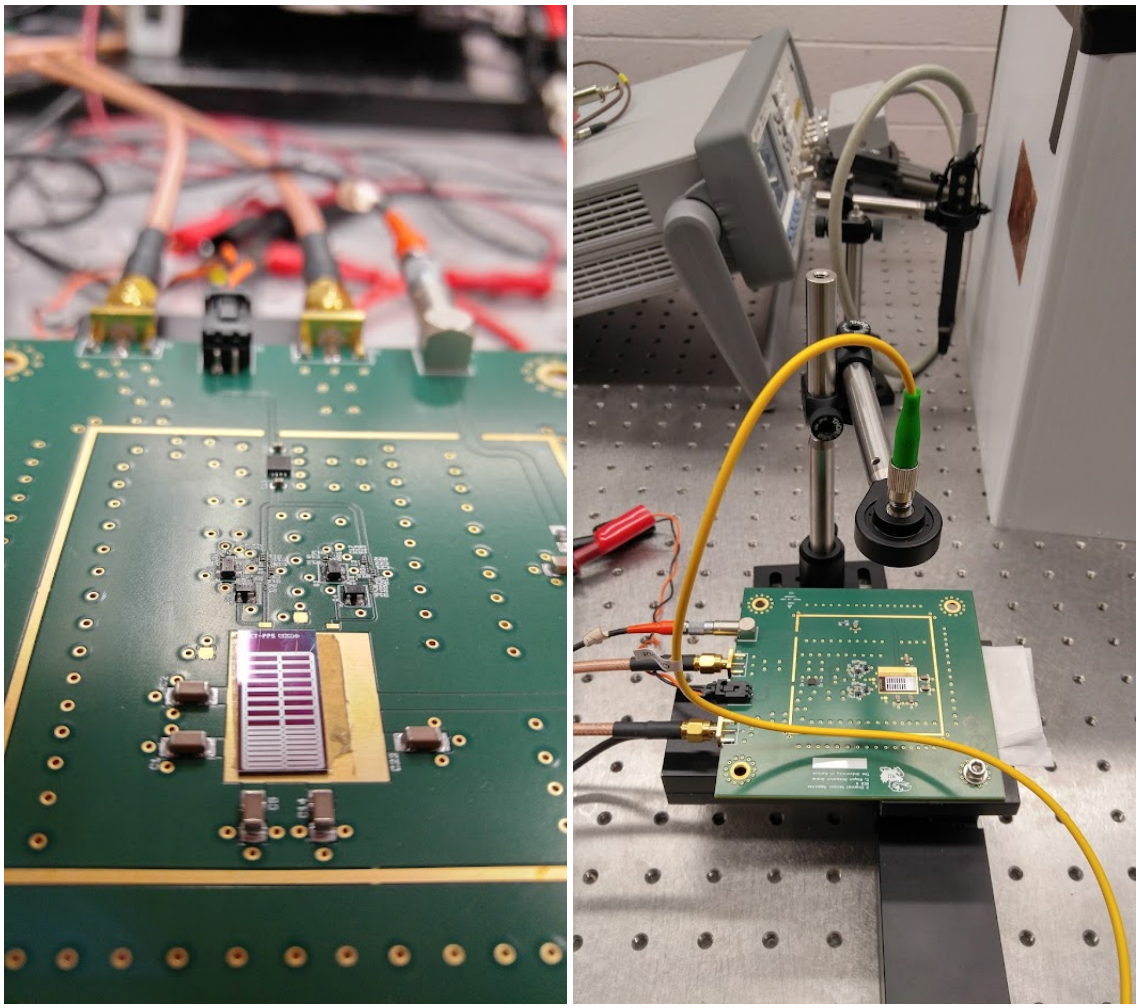

Figure 2.18: Left panel: The CT-PPS LGAD is bonded to the two-channels KU read-out board and mounted on the stepper motor. Right panel: the laser is aligned for aiming in targeting adjacent pixels. The two pixels provide independent measurements of the signal time of arrival, and their difference can be used for evaluating the detector resolution.

- output noise of around 4 mV
- gain in trasnimpedance configuration of about 50 mV/μA
- 3 dB bandwidth of 100 MHz
- power consumption of about 130 mW

Additional details can be found in Appendix C of the MTD TDR (77).

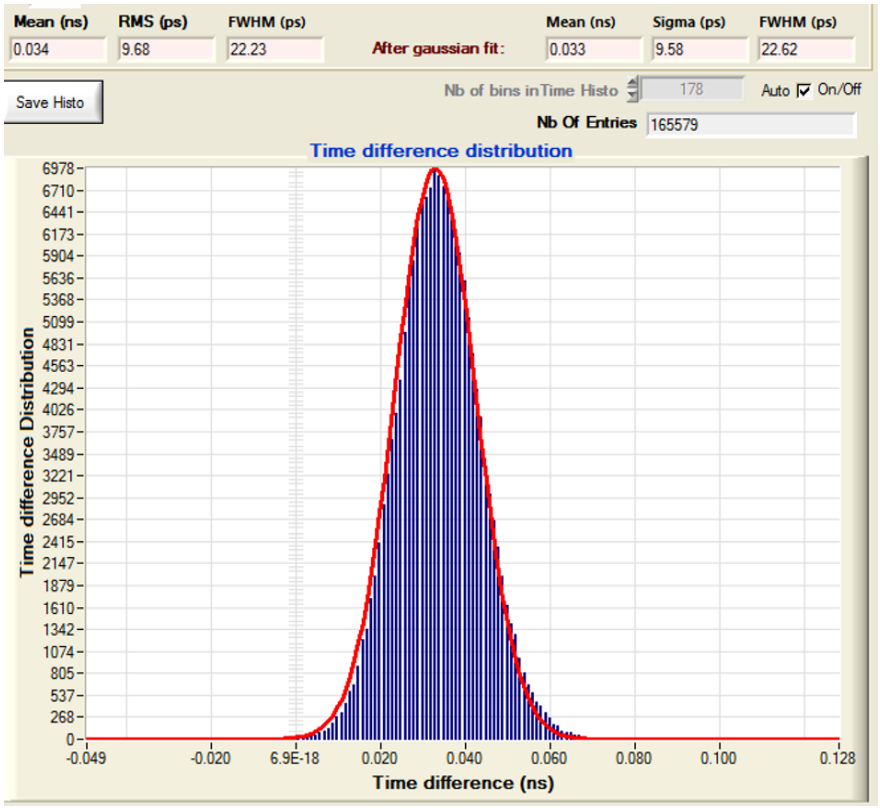

Figure 2.19: Time of arrival distribution measured aiming the laser between neighbor pixels on the CT-PPS sensor. The charge shared between the pixels generate two signals read out independently by the two channels of the KU board. The standard deviation of the ΔT Gaussian provides a final time resolution of 10 ps. The measurement was performed by acquiring the waveforms with a SAMPIC (23) fast sampler.

2.4 Irradiation studies of LGADs for the ETL project

Before the final production of the new timing detection layers, the CMS Collaboration scheduled a series of tests campaigns to assess the performance of the MTD individual components. Numerous institutes and laboratories collaborated to the R&D and design efforts, putting their expertise at the service of the detector design and development. During the last few years, the US-CMS groups have been playing a major role in the characterization of the sensors, as well as the optimization of the electronics acquisition chain. Starting in 2017, the project participants grouped around the testing facilities at Fermi National Accelerator Laboratory (Fermilab) (88). The hardware development work resulted in the MTD Technical Design Report. During this period, the KU CMS group has been involved in the characterization of the LGADs for the ETL final design, in the development of a framework for timing performance and spatial efficiency analysis, as well

			$3000\,\mathrm{fb}^{-1}$		$1.5 \times 3000\,\mathrm{fb}^{-1}$	
$\mid \eta \mid$	r (cm)	z (cm)	n_{eq}/cm^2	Dose (kGy)	n_{eq}/cm^2	Dose (kGy)
1.6	127	303	1.5×10^{14}	19	2.3×10^{14}	29
2.0	84	303	3.0×10^{14}	50	4.5×10^{14}	75
2.5	50	303	7.5×10^{15}	170	1.1×10^{15}	255
3.0	31.5	303	1.6×10^{15}	450	2.4×10^{15}	675

Table 2.2: The table (modified from table 1.3 in the MTD TDR (18)) describes the measured value of irradiation at different locations of the ETL detectors. The doses are quantified for an integrated luminosity of $3000\,\mathrm{fb}^{-1}$, with the addition of a safety margin of 1.5.

as in the integration of fast samplers in the testing setup.

The extensive R&D work pursued by the Collaboration focused on the optimization of the requested detector features, including: the sensors fill factor and signal uniformity, their gain and noise level, and their timing resolution. Most importantly, the tests were aimed at evaluating the detectors long term stability when subjected to high levels of beam radiation. This requires the investigation of different doping, and configurations. Three main vendors were considered for the production of the LGADs needed for the ETL: Fondazione Bruno Kessler (FBK) (89; 90), Hamamatsu Photonics (HPK) (91), and CNM. Different vendors provided LGADs designed with different doping, impurities, and gain layers, which offered the possibility of comparing their radiation resistance. A part of the production was first subjected to irradiation to dose expected for the HL-LHC. Table 2.2 presents a list of the doses at different locations of the ETL, for an integrated luminosity of $3000\,\mathrm{fb}^{-1}$, and considering a safety margin of 1.5.

2.4.1 Experimental apparatus at FNAL

Fermilab National Laboratory (FNAL) is a United States Department of Energy laboratory based outside the town of Batavia, Illinois. This particle physics laboratory hosts the Tevatron, a circular particle accelerator that started its operation in 1983 and remained active until 2011. The Tevatron was the second highest energy particle collider, next to the LHC (described in section 2.1.1), accelerating bunches of protons and antiprotons up to 1 TeV over a circumference of 6.28 Km. In addition to its use in neutrino experimental physics, part of the collider are currently used to provide stable beams to the Fermilab Test Beam Facilities (FTBF), a particle physics division to provide high-energy beams for detector R&D. The FTBF consists of two beamlines, MTest and

MCenter, where R&D collaborations can exploit a variety of particle types and a range of energies to test their hardware components. The tests were operated using bunches of 50k protons with an energy of 120 GeV, and frequency of 53 MHz. The Fermilab Main Injector cycle delivered single 4.2 s long spill per minute.

If required, the beam can also be targeted, in order to generate secondary pions, muons, or electron beams down to about 1 GeV. The US-CMS Collaboration assembled an experimental setup at the area for performing characterization tests using prototype LGAD sensors from HPK, FBK, and CNM, when irradiated up to the expected end-of-life neutron fluence. The detectors were hosted on custom-made fast read-out boards independently designed and produced at FNAL, at the University of Kansas (KU), and at the University of California Santa Cruz (UCSC). More information about their characteristics can be found in Appendix C of the MTD TDR (77).

The MTD detectors have been installed at the MTest area. In the experimental setup, the devices under tests (DUTs) are kept inside a cold box and mounted on motorized stages that can be controlled remotely. Downstream, the cold box additionally stores a Photek 240 micro-channel plate (MCP-PMT) detector which provides the time reference for the LGAD timing measurements. Its time precision was measured to be around 12 ps (92), as displayed in Fig. 2.20. Upstream the cold box, a precision telescope (93) comprising 7 planes of silicon strip detectors, tracks incident charged particles with a precision of 10 μm. Inside the coldbox, the aluminum plates used to hold the boards are provided with cooling loops routed inside their structure. The plates can cool down a total of 5 detectors down to the temperature of -25 °C. Inside the box structure, the DUTs alignment with the beam relies on the vertical and horizontal motion of the remotely controlled supports. The full experimental apparatus at the MTest area is sketched in Fig. 2.21.

For recording the signal waveforms, a combination of two Data Acquisition (DAQ) systems have been used. The detector and the MCP time reference were first sampled at 5 GS/s with a 12-bit ADC (0.25 mV of resolution), with the use of a CAEN V1742 digitizer board (94) based on a DRS4 chip. This system allows the acquisition of up to 32 channels and it was mostly used for the studies of sensor uniformity. For that reason, the digitizer board and the pixel tracker were triggered by a small scintillator connected to a photomultiplier tube (PMT) and placed upstream the cold-box. To achieve more accurate time measurements, the path of the analog output signals was split to be recorded by a Tektronix DPO7254 (95) oscilloscope (40 GS/s, analog bandwidth of

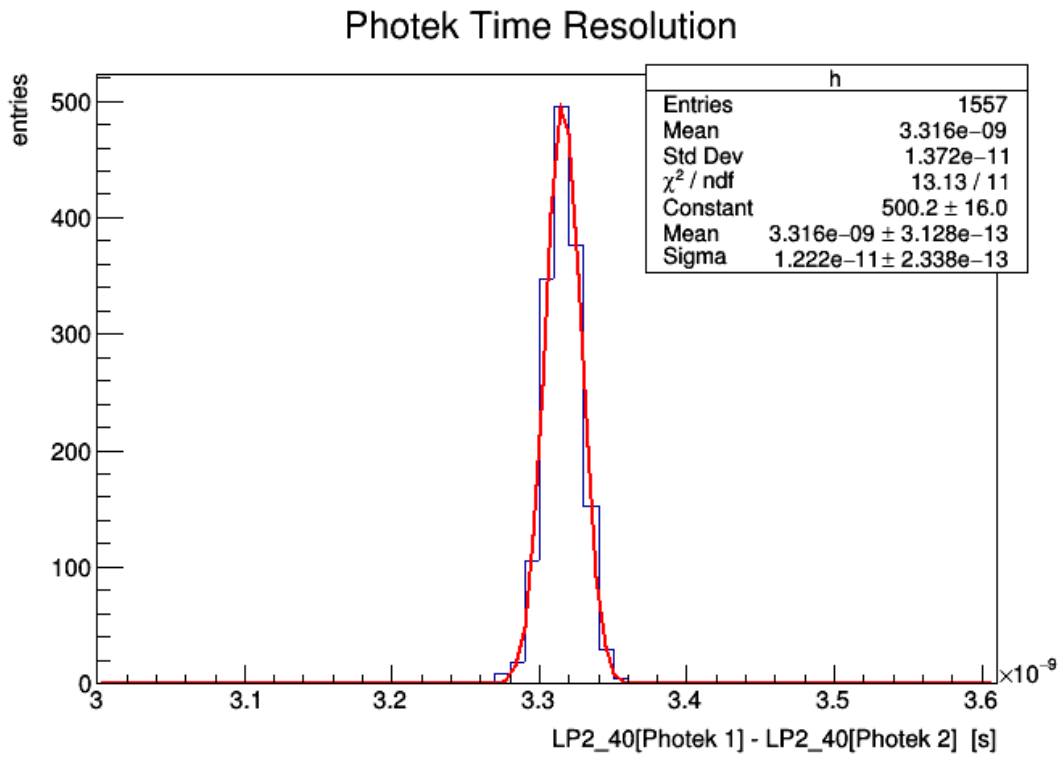

Figure 2.20: The time resolution of the Photek MCP used to as time reference for the DUTs was measured to be of about 12 ps.

2.5 GHz). Figure. 2.22 depicts the trigger logic for timing measurements, after the integration of the oscilloscope with the CMS testing apparatus. When the system is triggered, the tracker prompt the acquisition of the oscilloscope, which records the data collected by three DUTs and the time reference. The signals of the DUTs are split to also reach the input of the CAEN digitizer board. For selecting the detector to use for the acquisition, the signals are processed using a Multiplexer[7] card.

The integration of the timing system based on fast sampling constituted the original contribution to the test setup at FTBF; this led to the collection of the data presented during the next sections and allowed for a more precision time reconstruction during the analysis work.

[7]Device accepting several digital or analog inputs, and only forwarding a single one. The output signal is selected among the inputs through an independent control line.

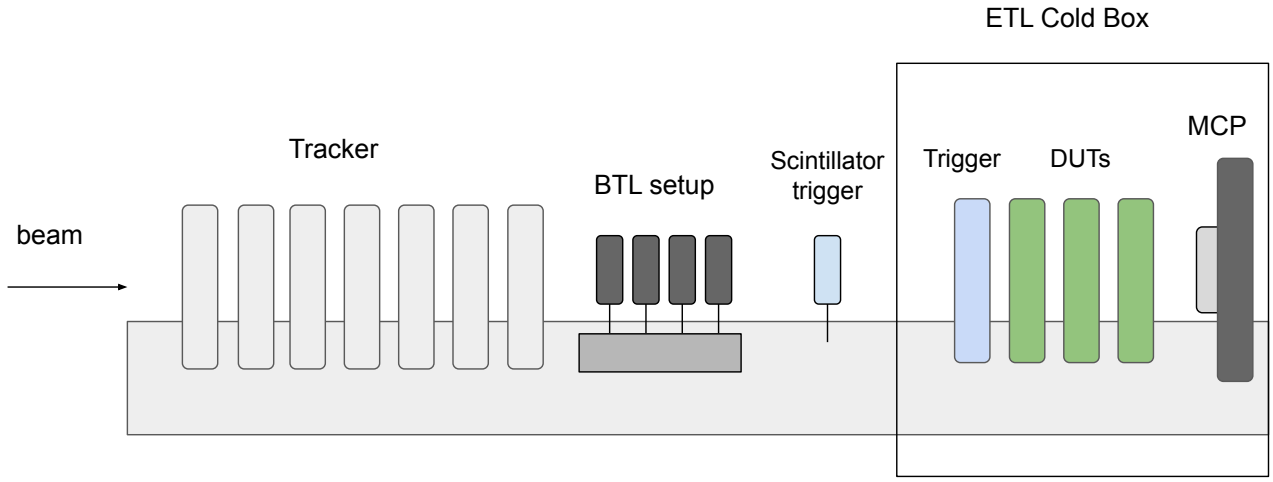

Figure 2.21: Acquisition apparatus at the MTest area. The upstream silicon strip tracker is used to evaluate the efficiency of the Devices Under Test (**DUTs**). The BTL setup and the scintillator trigger can be found downstream from the tracker. The ETL box contains the LGADs under test, as well as the MCP time reference and the acquisition trigger.

2.4.2 Data collection and analysis framework

The oscilloscope acquisition (see description in section 2.4.1) was triggered synchronously with the FTBF tracker, collecting the waveforms of the time reference (Photek MCP) and 3 DUT. A code developed in python uses pyvisa libraries to communicate with the sampler. Daemon software monitor the status of the systems controlled by the DAQ. The combined (oscilloscope + digitizer board) data collection is enabled when the oscilloscope is ready for an acquisition. The waveform generated are then saved in binary files and stored locally.

The data collection framework developed exploits the segmented memory acquisition option of the oscilloscope. Contrarily to the real-time option, this feature allows to subdivide the scope's acquisition memory into a collection of smaller memory segments. This enables the sampling of consecutive single-shot waveform at fast re-arm times without any information loss. In this configuration the oscilloscope takes advantage of the bunched structure of the beams and the

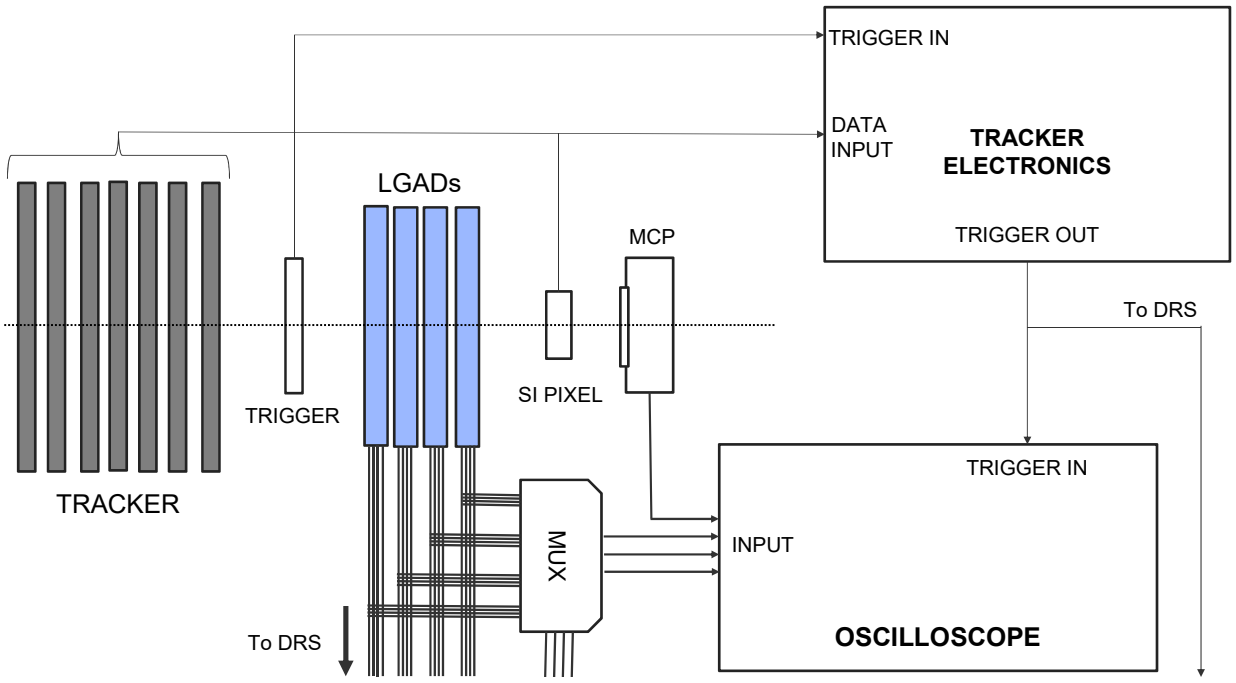

Figure 2.22: Connection maps of the acquisition system at the FTBF, comprising of the integrated oscilloscope.

bottleneck of the acquisition rate is dictated by the time needed for creating and saving the binary files. The segmented configuration allows to delay this phase to the interval between consecutive spills (lasting one minute). That allows to collect data within the spill with little dead time, and store the files locally whit no data-rate loss. This implementation improved the acquisition rate during test-runs from tens, to hundreds of Hz.

The waveform analysis was performed using an algorithm developed to be used during the data acquisition. The run table with all the information on the DUTs (e.g. position, bias voltage, number of channels, time of acquisition, detector status) was used to localize the data storage, and start the data conversion through a custom-made algorithm: a python code inputs the .csv files containing the run information and converts the raw waveforms of the oscilloscope in n-tuples (ROOT TTrees). The generated n-tuples are compatible with the standard of the test beam DAQ. The data analysis framework is depicted in Fig. 2.23 and is structure as follows:

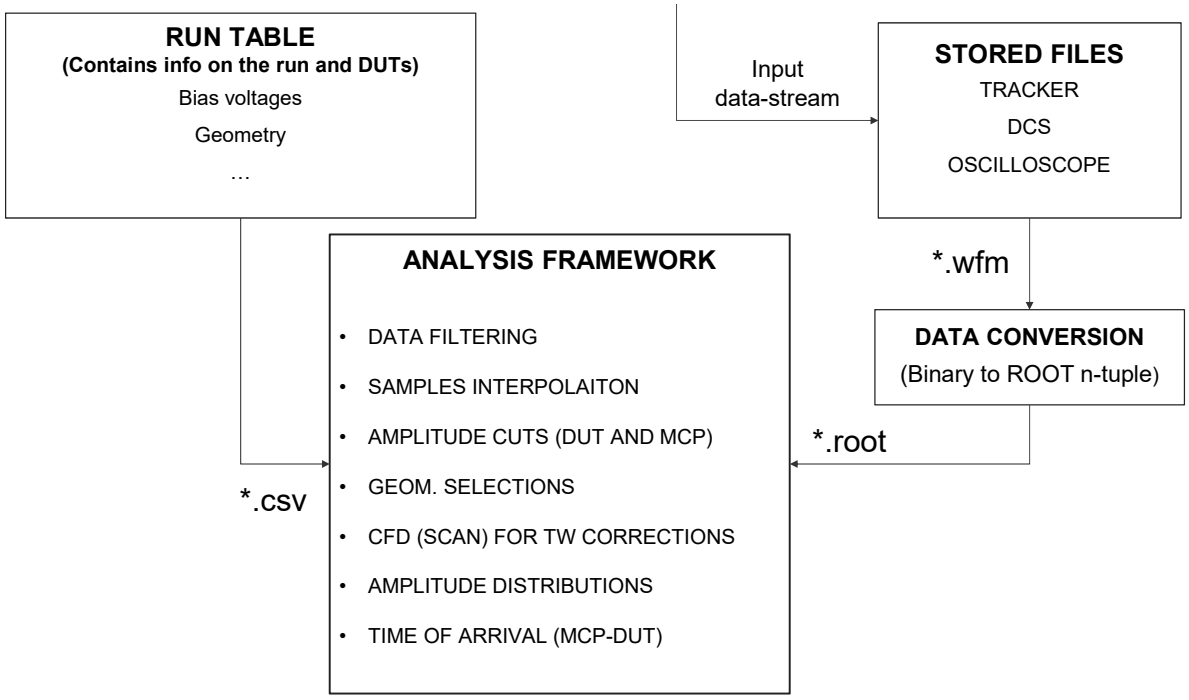

Figure 2.23: Diagram of the framework developed for analyzing the oscilloscope data. The data are stored and converted in ROOT n-tuples. The run table provides all of the information needed to apply the analysis cut during the data processing.

- **data filtering:** this process smooths out rapid fluctuations, reducing jitter effects, enabling a more precise identification of the signals timestamp. The cut-off frequency of the low-pass filter was chosen not to limit the pulses rise-time.

- **Amplitude selection:** We operate amplitude cuts for selecting the DUTs and reference signal regions. The cuts have to be performed according to the DUT features for removing contamination of coincidences triggered by noise. An additional selection helps getting rid of the regions displaying saturation of the amplifiers. The signal shape can be modeled as a Landau distribution (typical for MIP energy deposit) convoluted with a Gaussian coming from the resolution of the detector.

- **Geometrical selections:** the code uses the tracker information for applying geometrical selections for efficiency and uniformity studies. The projection of the tracks on the DUT pads

can be used for outlining the detectors geometry. The quantities reconstructed during the analysis can be studied as a function of the hit position and used for highlighting local phenomena in the sensors. During the tests, an additional pixel detector was integrated downstream of the ETL cold box to improve the reconstruction efficiency of the track location.

- **Data interpolation:** thanks to the excellent sampling rate of the oscilloscope, the sampled points in the waveforms can be interpolated with minor distortion. A spline interpolation is used for defining a crossing time and computing the time of arrival.

- **Time walk correction:** a custom-made CFD algorithm (introduced in section 1.1.3) initially finds the maximum of the pulses amplitude. A dynamic threshold is defined using a fraction of the measured maximum. The oscillation due to jitter affecting the crossing time are mitigated implementing a hysteresis cycle around the threshold cut. The optimization of the CFD parameters is obtained performing a scan of the selected amplitude fractions.

- **Amplitude distribution:** the maximum amplitude of the pulses is measured and stored. the resulting distribution is modeled using the convolution of a Gaussian (detector's resolution) and a Landau (energy loss of the incident particles). The average amplitude maximum can be extracted from its MPV.

- **Time of arrival measurement:** the algorithm computes the difference in time of arrival between the individual DUTs and the MCP reference. The standard deviation of Gaussian fit to the distribution provides the time resolution. The contribution of the MCP can be removed deconvolving its resolution.

2.4.3 Gain and noise

For maintaining the time resolution needed for the ETL, the selected LGADs have to preserve their optimal SNR for all the HL-LHC oeration time. In particular, the produced signals have to match an integrated charge of at least 5 fC. In the ETL LGADs this corresponds to multiplication process characterized by a a gain factor of 10. The collected charge increases when increasing the gain, and it depends on the sensors doping, and composition. For example, FBK sensors differ form HPK ones, as their breakdown voltage is lower.

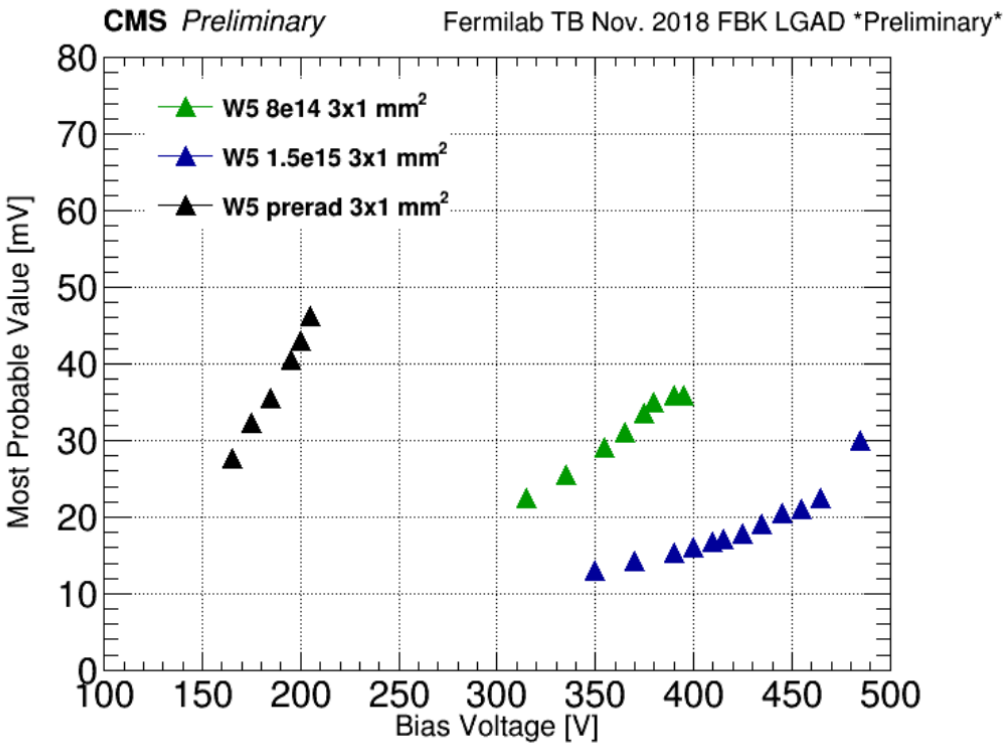

Figure 2.24: Most probable value of the amplitude distribution as a function of the bias applied to the FBK irradiated and non-irradiated (W5-prerad) sensors.

This quantity is defined by the sole characteristic of the sensor, and has to be tested prior to the installation on the amplification board. However, studies of the signal amplitude output by the read-out electronics provide relevant information about the detector stability and radiation tolerance. Individual DUTs amplitude distributions were plotted, and a fit to the data was performed to extract the signal region. Figure 2.24 shows the MPV of the amplitude distribution as a function of the bias applied to the sensor. The gain and charge collected can be roughly estimated assuming a linear behaviour of the signal amplitude as a function of the applied bias and full collection of the charges generated. In this way, the linear regression of the data points shown in Fig. 2.24 can be used to find the relation to the charge with Q = 0.246 MPV + 1.83 fC. The gain is then computed using G = $\frac{Q_{collected}}{Q_{generated}} \simeq \frac{Q}{0.5}$ fC. This formula derives from simulated data employed in (96): a MIP crossing through 50 of silicon generate a drifting charge of about 0.5 fC. The ratio between the collected charge undergoing the multiplication process and the generated charge provides an estimation of the gain. Figure 2.25 shows an attempt to measure the charge and gain information, starting from

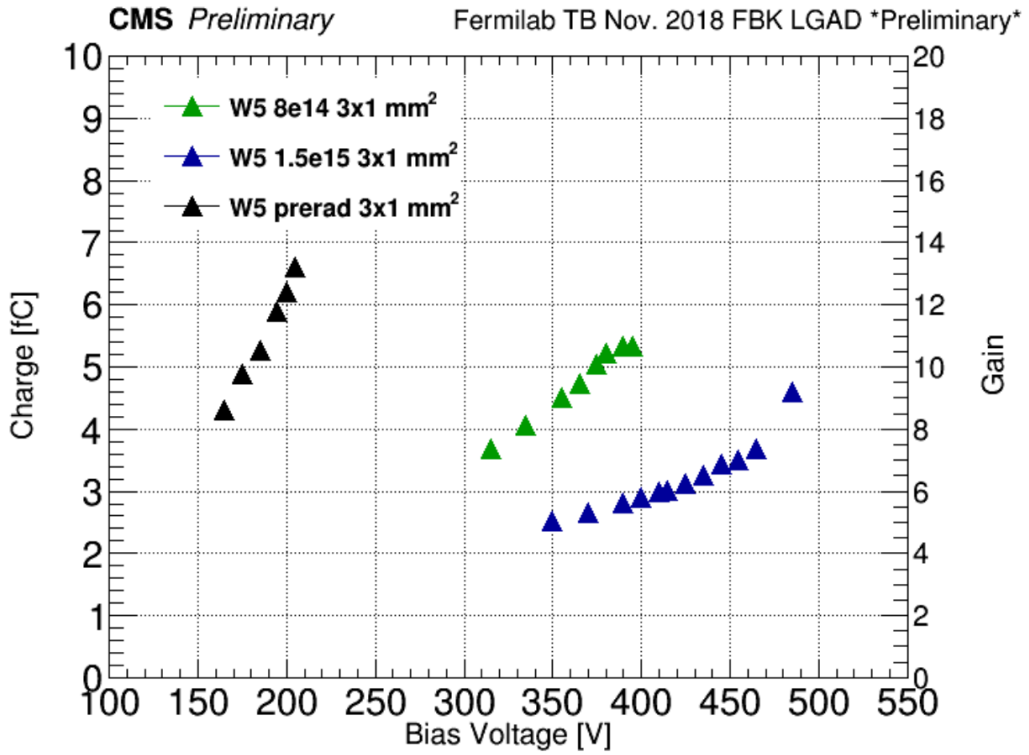

Figure 2.25: Starting from the signal amplitude, the analysis computes the charge, and gain of the detectors. The two quantities are reported as a function of the bias voltage applied to the FBK sensors.

the signals amplitude.

Concerning the noise of the LGADs, the Collaboration investigated two main contributions affecting the measurement: the shot noise, and the *popcorn noise*. Its effect can limit the operation of the sensor when biased at lower bias voltages than the ones needed for achieving the required gain. It is attributed to the fringes of the electric field at the edges of the LGADs p+ insertions (e.g. doping density, aggressive interpad regions). It is affected by the sensor's status (humidity, temperature), and it produces discharges between the pixels and the guard ring regions. Although these are rare events, the production of the final LGAD design requires an attentive analysis of the collected data. On the other end, the shot noise comes from the leakage current of the sensors and it can be mitigated operating at lower temperatures (the process is described in 1.3.2). A summary of the gain studies for all of the production was extracted from the MTD TDR. This is presented in Fig. 2.26. In the plots in Fig. 2.26 the dotted line represents the minimum requirement for obtaining a SNR sufficiently large to achieve the expected performance to operate during the HL-LHC.

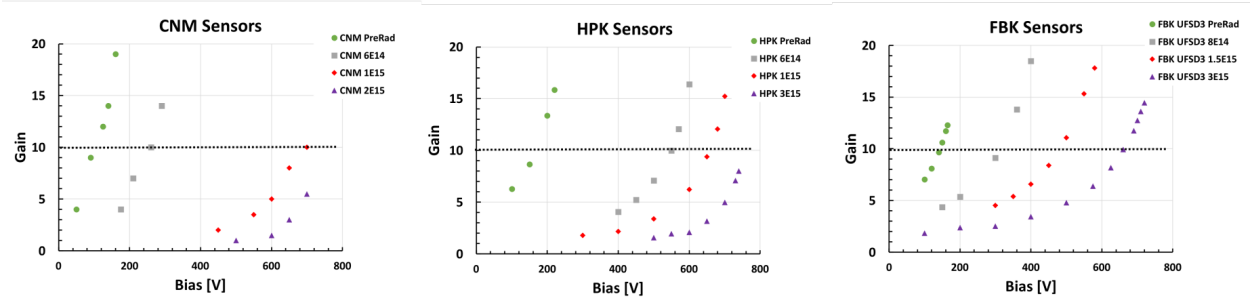

Figure 2.26: Gain as a function of the applied bias measured for a sample of LGADs for each vendor selected for the ETL. Plot extracted from the MTD TDR (18)

All the non-irradiated sensors reported (which are part of a much larger set of data collected during the ETL R&D campaign) are capable of reaching the desired region of gain.

Increasing the absorbed dose the multiplication layer of the sensors starts becoming less effective due to the phenomena discussed in section 1.3.3. As a product of increasing the bias voltage, the charge collection efficiency of the irradiated sensors is enhanced and their effective gain partially recovered. The R&D campaign is providing satisfactory results as most of the tested detectors meet the requirements imposed by the ETL TDR. These results are needed for the vendors to optimize the detectors production as the CMS Collaboration is moving towards a final design of the ETL. Newer detector batches are currently under development for exploring different doping configurations to achieve new frontiers of radiation tolerance.

2.4.4 Time resolution

One of the main results of the test beam campaigns scheduled by the US-CMS Collaboration is the time resolution as a function of the irradiation collected by the sensors. During the 2018 and 2019 test beam campaigns organized by the Collaboration, the KU CMS group has produced important results on the time resolution of the LGADs, focusing on the analysis of carbonated and non-carbonated FBK, and HPK sensors. The 50 μm thick LGADs provided by the vendors were bonded to the custom-made read-out board described in section 2.4.1 and installed inside the ETL cold box.

The limit to the intrinsic resolution of these devices is decided by the non-uniformity of the charge deposition of incident radiation, or Landau noise, already described in section 1.1.3. For 50 μm thick sensors, the intrinsic σ_t is around 25 ps. As reported in the studies described in

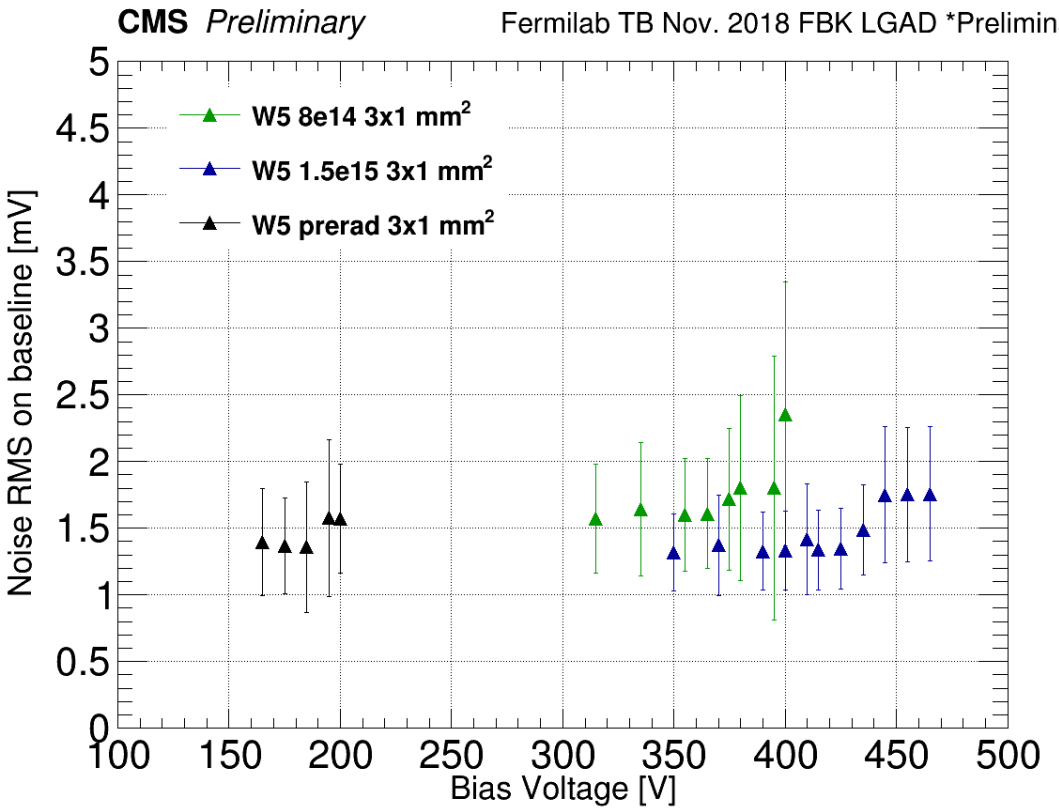

Figure 2.27: Distribution of the rms baseline noise as a function of the run number, collected during the test beam campaign of Nov 2018. The noise of the W5 series of sensor produce by FBK is reported for three levels of irradiation collected. The measured noise doesn't increase drastically with the dose collected by the sensors. That's of crucial importance for preserving their SNR as the gain layer becomes increasingly less effective.

Fig. 2.27, the selected read-out boards are characterized by low noise profile; the level of noise is not drastically affected by the radiation dose collected by the sensor. Maintaining the noise levels within few mV ensures to preserve the SNR of irradiated detectors and, in turn, their timing precision.

The time resolution studies require collecting the difference of time of arrival with respect to the time reference (Photek-MCP). As the resolution of the two detectors propagate into the final computation, the contribution of the reference is chosen to be negligible when compared to the DUTs. For that the reference was chosen to have a time resolution much better than the DUTs. Selecting a window of signal amplitude (for the DUTs and for the MCP), reduces the contamination of spurious events due to noise spikes, or saturation. The saturation region of the amplitude spectrum does not allow for a precise definition of the time of arrival, which relies on the identification

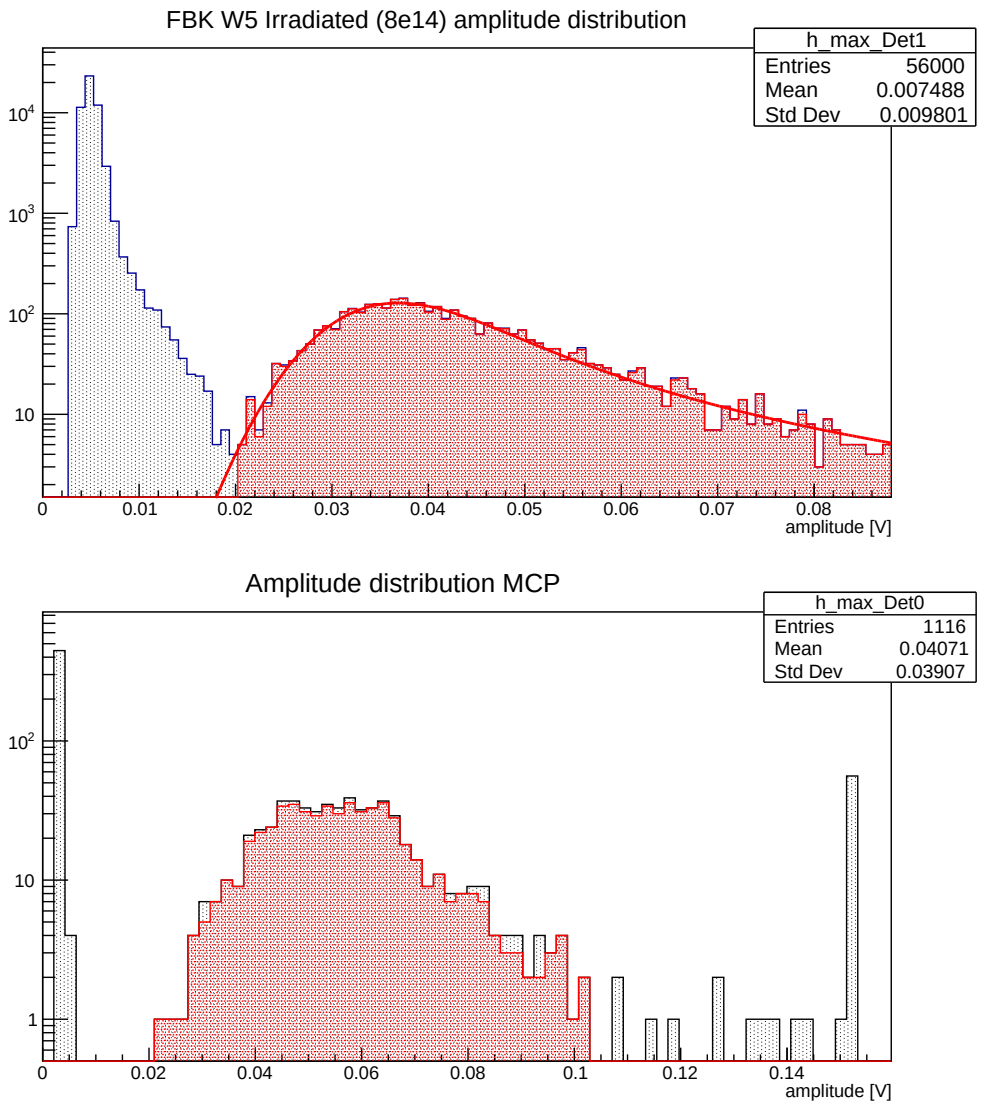

Figure 2.28: Amplitude selection (logarithmic scales) operated on one of the DUTs (top panel), and on the Photek MCP (bottom panel). The peaks at lower and higher amplitude, in the black regions, correspond to, respectively, electronic noise, and signal saturating the amplification chain.

of the signals amplitude. Additionally the tracker allowed to define of geometrical selections based on the particles occupancy on the DUTs (see section 2.4.5) for a stronger reduction of mismatched events (more details on the data analysis framework can be found in 2.4.2). An example of the amplitude selections can be found in Fig. 2.28. The sensors response has to be studied as a function of the collected dose and bias voltage. The gain increases with the applied voltage (see results in section 2.4.3). At the same time, the charge collection becomes faster reducing the time jitter affecting the measurements. Fig 2.29 displays the behaviour of the time resolution as a func-

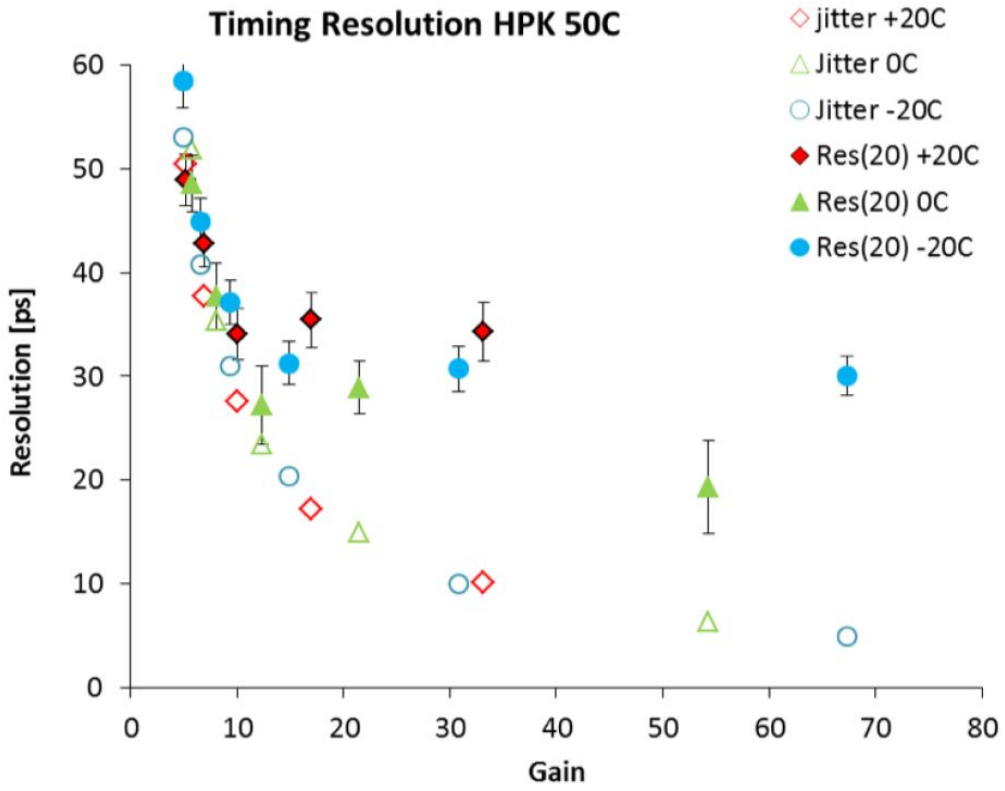

Figure 2.29: Time resolution studies as a function of the gain of HPK sensors (50 μm thick) (18). The data are collected at different sensors temperature, and the jitter (expressed as $\sigma_{jitter} \simeq \frac{SNR}{t_r}$) behaviour is also reported. Although the jitter contribution decreases with the gain, the time resolution flattens around 30 ps, when reaching the intrinsic resolution of the sensor (the topic is discussed in section 1.1.3 and section 1.3.2). The temperature variation play a role in increasing the gain, modifying the carriers mean free path in the silicon substrate.

tion of the sensors gain.

It has to be noted that, under the same bias voltage values, sensors cooled down to lower temperatures display better performance. This effect is due to the variation in the mean free path of the charge carriers inside the semiconductor, in turn affecting the sensors CCE, as well as its leakage currents. An example of early studies of the temperature analysis is illustrated in Fig. 2.30. These studies are of crucial importance for characterizing the noise behaviour of irradiated sensors. As already explained in section 1.3.2, as the absorbed dose rises, the shot-noise quickly becomes the main contributor to the signal degradation. As this effect increases with the sensors gain, the Collaboration aimed to study the best working point for the devices.

After the initial data smoothing, the implemented CFD corrects for the time-walk effects, and

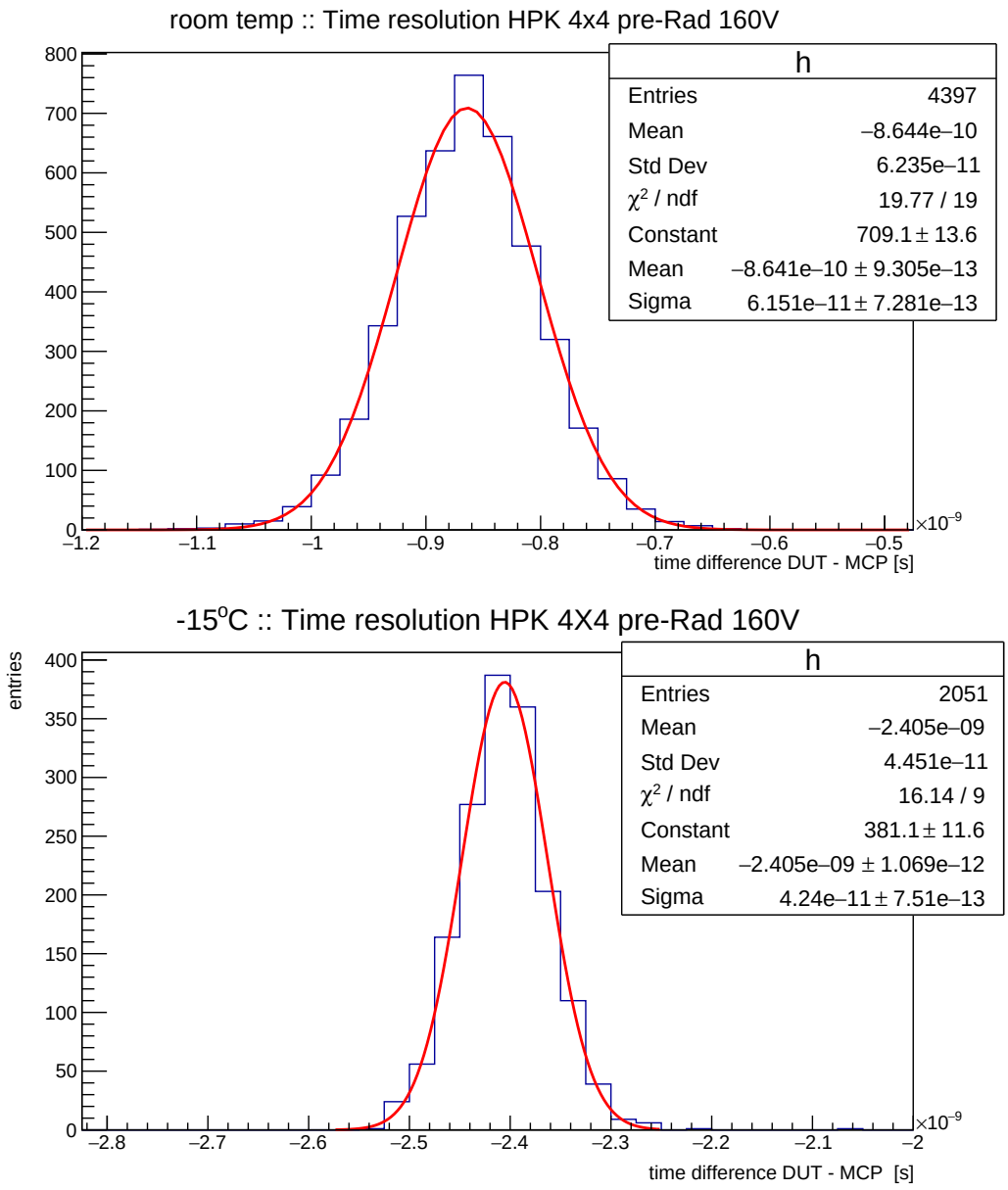

Figure 2.30: Comparison between early analyses of time resolution for the same sensor subjected to different temperatures. Decreasing the temperature (-15 °C) the performance noticeably improves. The results are in agreement with the expected behaviour of the multiplication processes in the LGADs: the overall gain is inversely proportional to the temperature.

reconstructs the arrival times. A scan is operated to evaluate the most effective CFD fraction. An example of its effect on the reconstructed resolution can be found in Fig. 2.31, flanked by an example of distribution of time difference between a DUT and the reference. Figure 2.32 shows the results obtained for the measurements of time resolutions on FBK sensors, as a function of the bias voltage applied to irradiated and non-irradiated detectors. The data points are displayed before

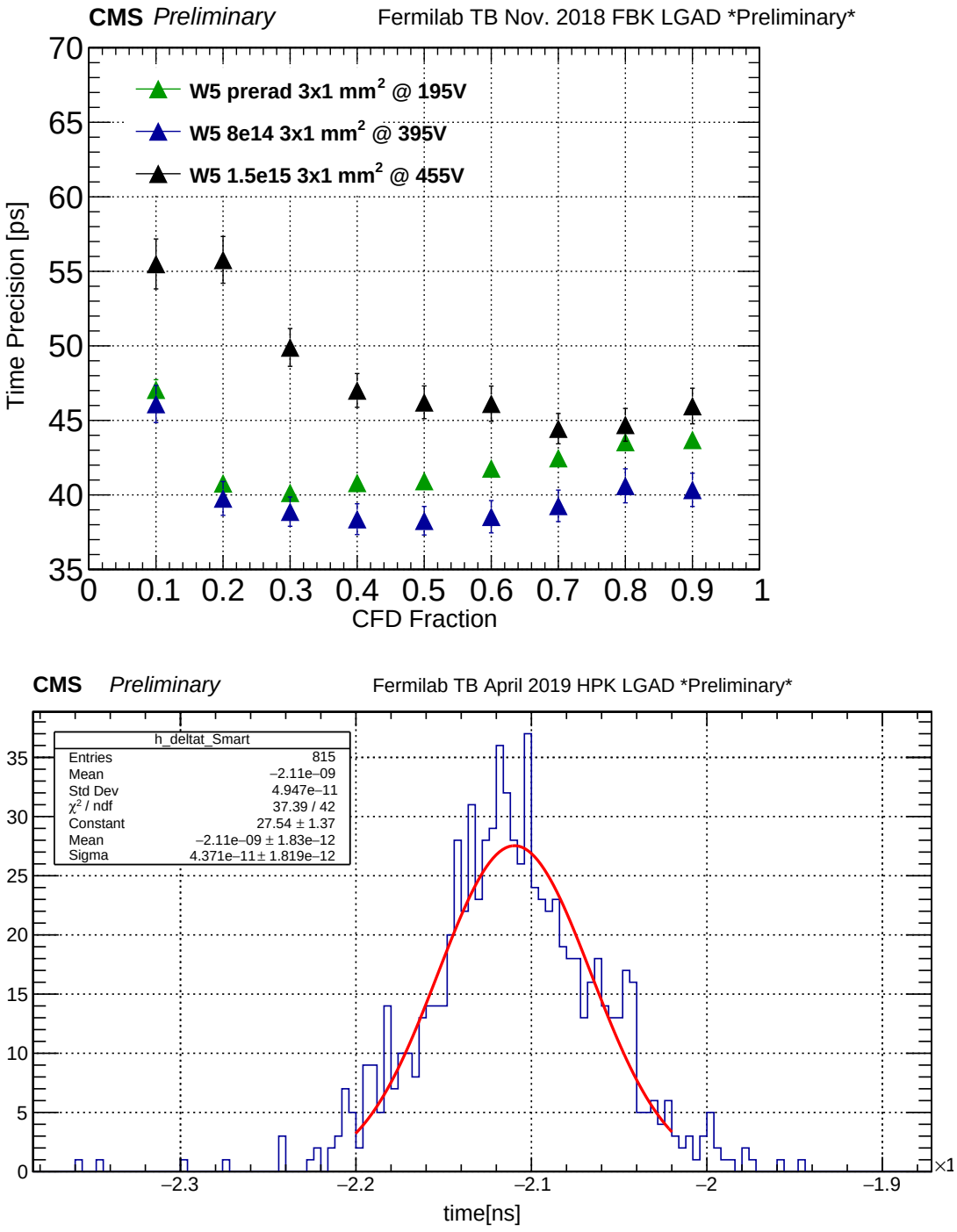

Figure 2.31: Top: Studies of the impact of the CFD fraction on the time resolution of carbonated sensors produced by FBK. Bottom: histogram of time of arrival difference between the reference and an irradiated HPK sensor. The standard deviation of the distribution provides a rough estimate of the DUT resolution of about 44 ps $\pm$ 2 ps, which meet the ETL installation requirements.

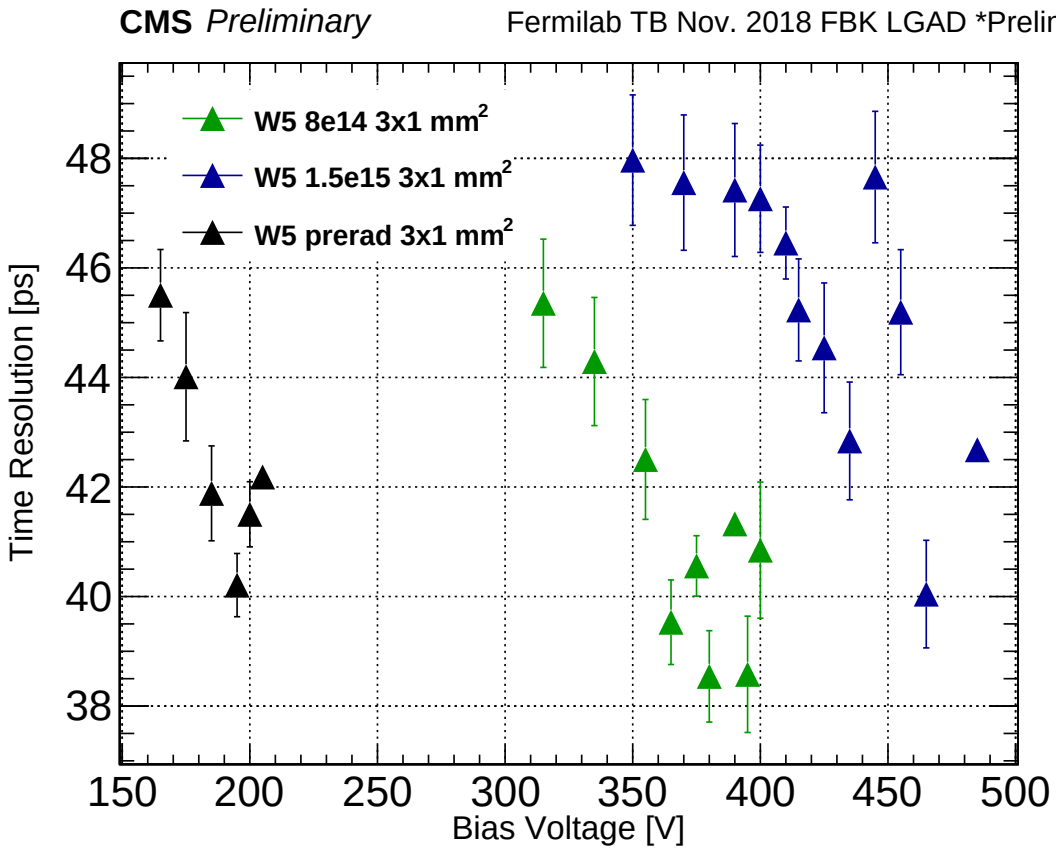

Figure 2.32: Summary of the results obtained during the time resolution studies on irradiated and non irradiated W5 sensors produced by FBK. The data point are computed using the standard deviation and relative uncertainty of the time of arrival difference between the DUT and the Photek-MCP time reference. The measured resolutions were found to be overall better than 50 ps, therefore meeting the the ETL requirements.

and after the deconvolution with the time reference resolution. The values and error bars are extracted from the statistics of the time of arrival Gaussian distributions. The analysis of Fig. 2.32 demonstrates that the sensors under analysis satisfy the nominal specifications required by the ETL. Even at the highest absorbed fluences (1.5×10^{15} n_{eq}) the sensors perform with a time resolution better than 50 ps. At higher voltages, one can note some outliers in the data distributions. These points correspond to a SNR loss due to electronic noise when operating closer to the nominal maximum stable bias of the board design.

In this computation we have omitted the jitter contribution introduced by the electronic noise of the ASIC used in the final design of the read-out. The results, together with the ones reported in Fig. 2.29 indicate that the required time resolution is obtained with a gain of around 10 (corre-

sponding to a collected signal of 5 fC), which can be achieved increasing the bias voltage during the detectors lifespan. This value of gain has been used to optimized the design of the ASIC, and of its maximum jitter.

At present, the R&D of the detectors time resolution is still ongoing. The reported analysis will be iterated prior to the final selection of the ETL sensors, for evaluating the performance of newer LGAD productions.

2.4.5 Fill factor, spatial uniformity, and hit efficiency

Tracks reconstructed by the 7 layers of tracking detector installed in the setup at the FTBF offer the possibility to precisely study the hit maps on the DUTs in the box. The addition of a pixel detector downstream, after the box, improves the tracking capabilities and in turn the measurements that rely on that, such as the efficiency and hit uniformity.

During the tests, We focused on analyzing data collected with HPK single and multi-pad sensors. The information provided by the track-reconstruction (which software package was developed for the test beam application) were read out using the signals of the 32 channel digitizer boards (described in section 2.21). The interpolation of the points along the track was matched to events on the DUTs pixels, while their geometrical position was monitored reading the remote controls of the stepper motors. Figure 2.33 is a reconstruction of the position in space of the LGADs as displayed by the DAQ during the alignment procedures. The detectors are aligned with the tracker, and the rotations with respect to the beam axis are corrected during the early stages of the analysis. This last procedure is needed for an accurate definition of geometrical selections to apply to the next analysis steps. This helps removing the contamination of particles escaping the DUTs acceptance. On the top panel of Fig 2.34, an occupancy map, corrected for the stage motion and rotation is displayed. The bottom panel reports the spatial distribution of the signal amplitudes. The studies performed on HPK sensors demonstrated a 2% spread in the pulse amplitude in non-irradiated sensors, corresponding to an optimal uniformity of the detector spatial response. Similar results were also obtained at higher collected fluences.

From the uniformity maps we can derive the reconstruction efficiency. In Fig. 2.35 the results of early studies of the local efficiency of a 4×4 HPK sensor are shown. During the tests, the

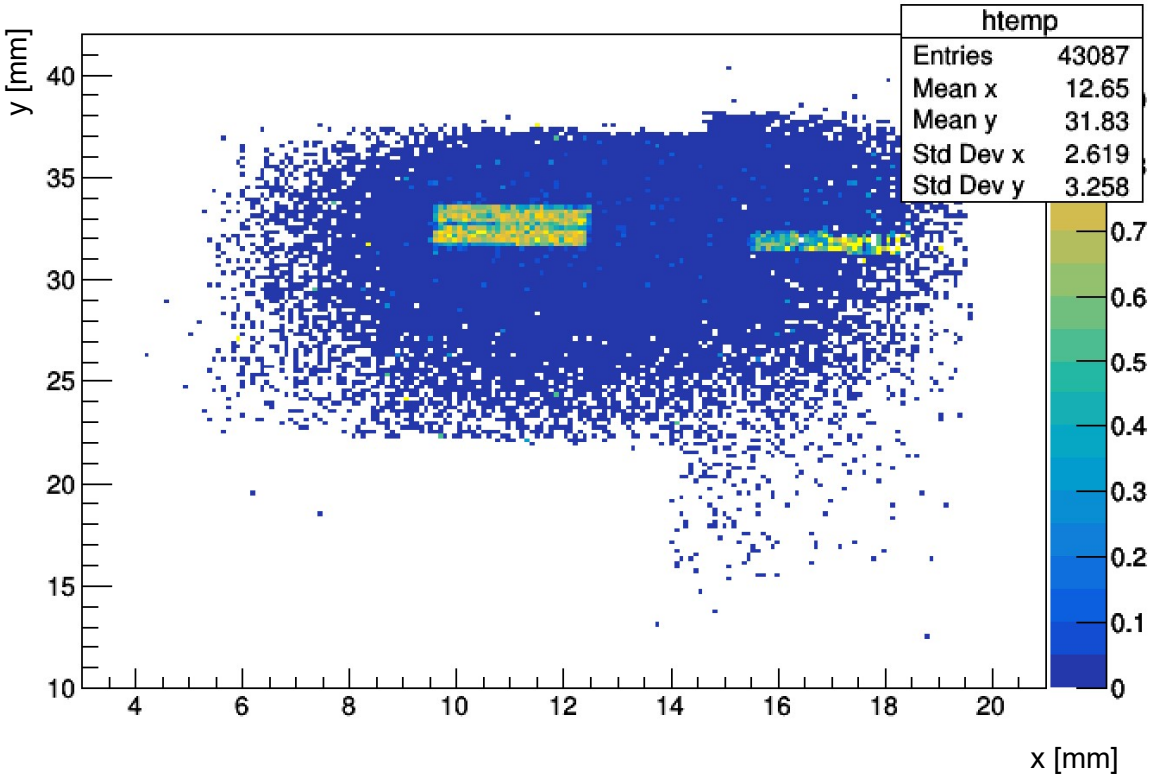

Figure 2.33: Inside the box, the detectors are relatively aligned to maximize the hit rate. The plot shows the hit occupancy map in space: the yellow shape represents the hits matched between the tracking reconstruction and the timing pixel detectors.

efficiency of the HPK sensors were found to be 100% for non-irradiated pixels, and up to radiation values of 6×10^{14} n_{eq} (18). In addition to the uniformity and efficiency studies, the same data can be used for rough estimations of the detectors fill factor. This quantity is usually measured in standard procedures, scanning with collimated laser spots the surface of the sensors (see section 2.3.2). The efficiency distribution of the surface smoothly decays while approaching the pixels edges. This region can be modeled using a step function (transition from the gain to the no-gain function) convoluted with a Gaussian representing the laser's beam spot. The edge of each of the pixels are not metallized, and the distance between the 50% amplitude of the curves for adjacent pixels is used to define the total no-gain zone. The same measurement can be replicated using the data obtained with proton beams. An example is provided in Fig. 2.36, where the no-gain region between adjacent pads of an HPK multi-pad sensor is measured to be about 87 μm.

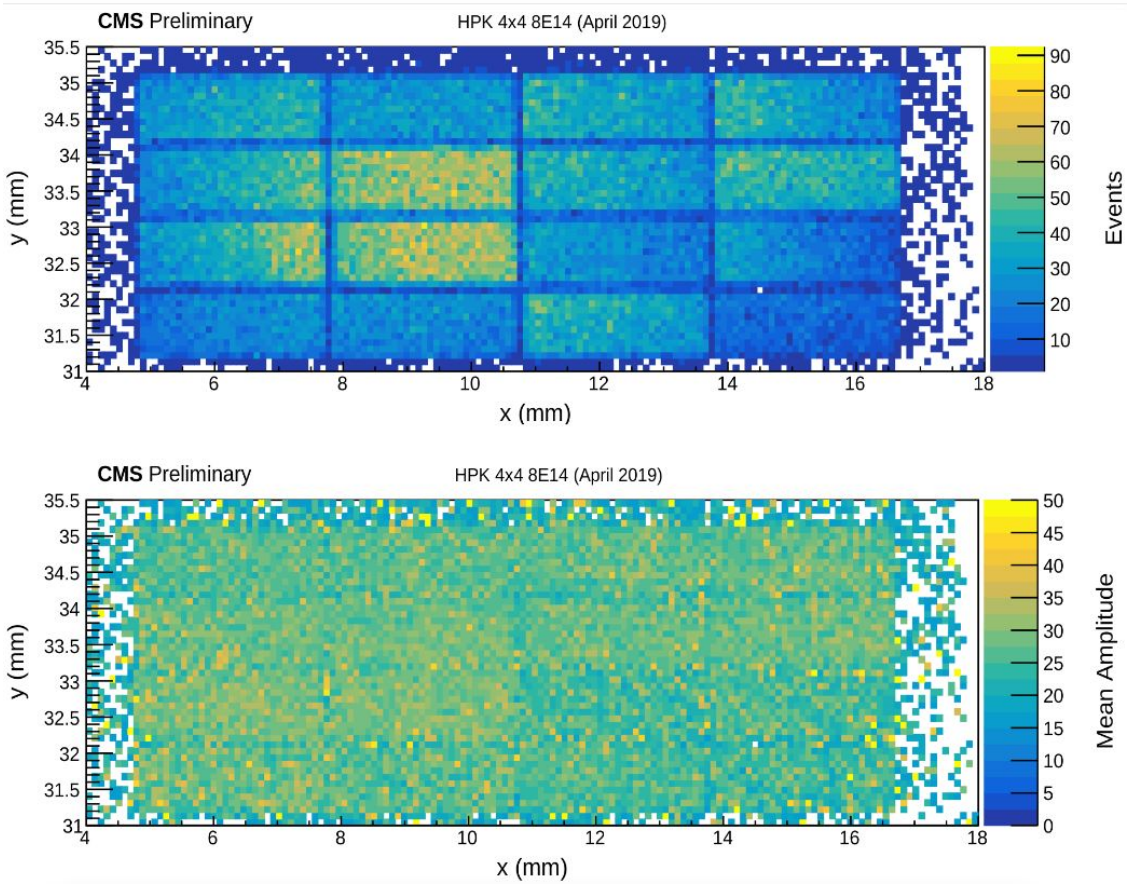

Figure 2.34: Top: hit map corrected for the translation and rotation of the moving supports. The planar view allows the definition of geometrical selections to be applied to the rest of the analysis (see section 2.4.4). Bottom: the amplitude distribution is displayed as a function of the hit position.

The FBK, HPK, and CNM vendors produce LGADs with different interpad designs, which can span between few tens micrometers to more than 100 μm. While the design of aggressive interpad design improve the fill factor, the detectors stability when applying higher biases can be impacted. Designs using smaller interpad distances have previously shown to be affected by early breakdowns and increased leakage currents. However, at the time of writing this thesis, the ETL is investigating the possibility to produce multi-pads LGAD sensors with 50μm interpad distances and regions between consecutive sensors (next to the last pixels of the row) of about 500 μm. Adding these contribution, the fill factor results to be of about 90%.

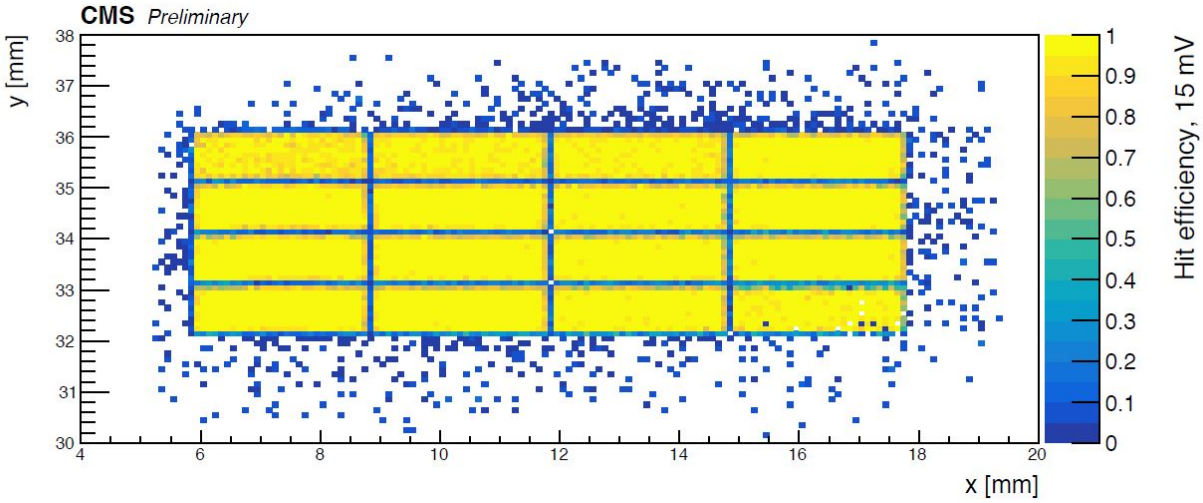

Figure 2.35: Studies of local efficiency of a 4×4 multi-pad sensor produced by HPK.

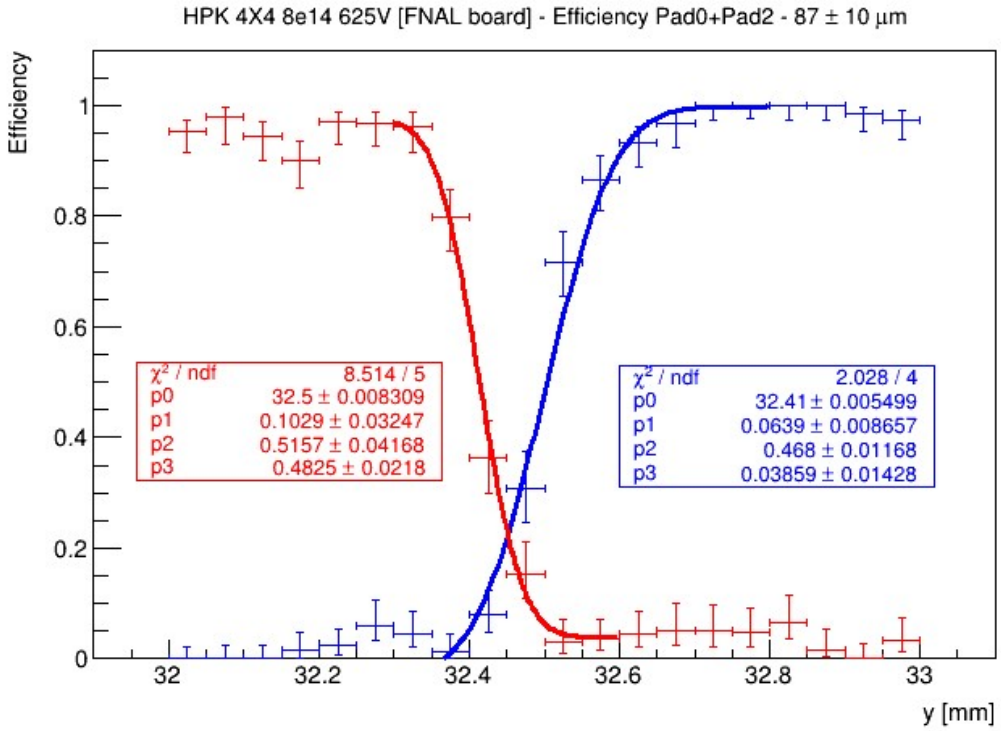

Figure 2.36: Efficiency as a function of the position on the surface of a HPK multi-pad detector. The plot illustrates the no-gain region between adjacent pixels to be about 87 μm at 625 V of bias voltage.

2.5 Quality control of the ETL modules

The KU CMS group is also contributing to the MTD project for the quality control studies of the detector modules of the ETL subdetector. These will contain the LGAD sensors and electronic read-out (ETROC chips) already described in section 2.2.3. In particular, the Collaboration has requested the production of dummies for testing the bump-bonding scheme to be used in the final products. These studies required the calibration of the probe station setup, as well as the development of a DAQ system, and user interface.

Each dummy unit hosts a set of passive electrical components on a planar silicon wafer, produced by Brookhaven National Lab (BNL) and CNM. The scheme of the populations is comprehensive of segmented aluminum traces for the dummy ETL sensors. A set of 30 serpentine resistors laid out in columns and connected together fully cover the individual ETROC metalization pads. For measuring the lines resistance, the end of each column is provided of a exposed testing pad. Moreover, every other column is connected to the next one with a low resistance trace, to allow the characterization of the full dummy measuring the resistance between the first and the last exposed pads. In Fig. 2.37 the design of the full wafer is flanked by details of the dummy ETROC (top right) and sensor's structure (bottom right). The dummies are designed for testing the quality of different bump-bonding schemes, and each end of the serpentine resistors are provided with metalization pads for hosting the solder balls. These are the conductive contacts that connect the sensors pads to the read-out channels. When bonding the dummy sensors to the dummy ETROCs the wafers allow for two preliminary designs to be tested:

- **single bump assembly:** in this design the pitch between connections is $1.3\,\text{mm} \times 1.3\,\text{mm}$, therefore of a single solder ball per metalization pad.
- **double bump assembly:** this configuration has half of the pitch of the single bump assembly, hence two bump bonds per metalization pad.

The description of the wafers layout can be found in (18) and observed in Fig 2.37. It is designed to contain five double bump ETROCs, six single bump ETROCs, two double bump dummy sensors, and three single bump dummy sensors. In either of the two configurations, single and double bump, when overlapping a dummy sensor with one of the ETROCs, the segmented aluminum

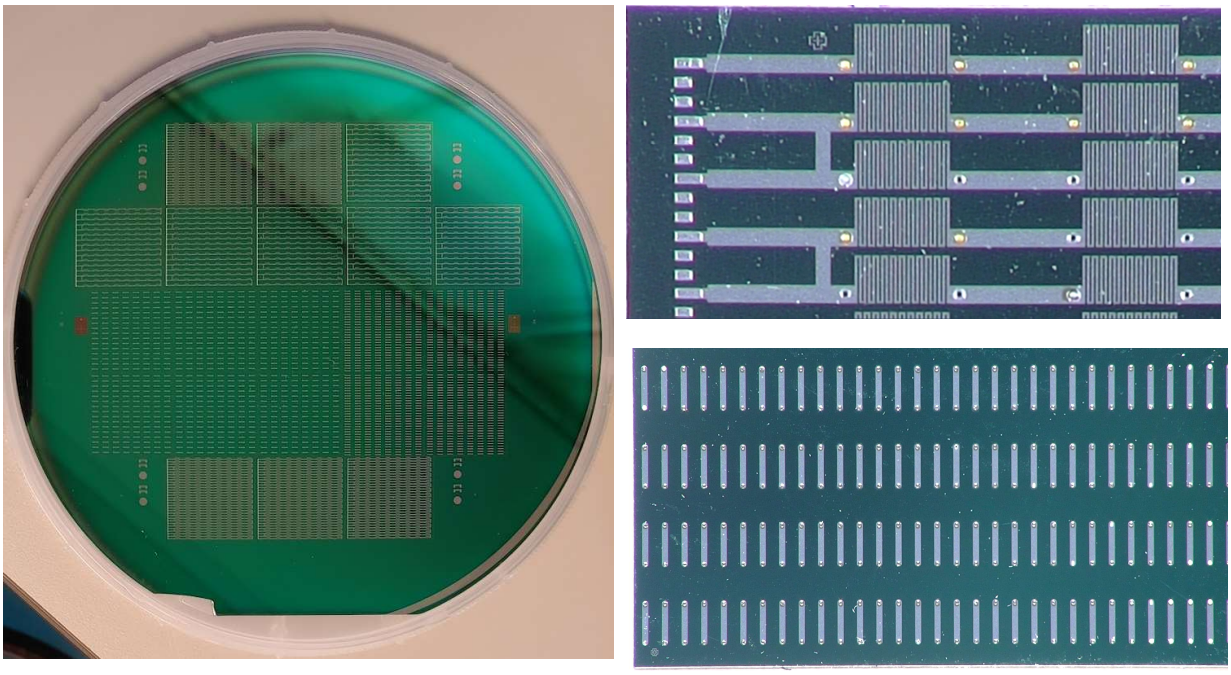

Figure 2.37: A picture of the wafer containing the ETL dummies is shown on the left. The serpentine structures comprehensive of the exposed testing pads used for the resistance measurements, are displayed in the top right panel. The picture on bottom right shows the conductive aluminum tracks simulating the pixel connections.

tracks of the first one are designed to short the exposed pads across the serpentine resistors.

The quality control of the bonding can be therefore evaluated measuring the resistance level of entire resistors columns. Figure 2.38 shows a 3D render of an assembled ETROC module, or 'assembly', where the dummy sensor is represented as a transparent layer. If any imperfection occurs in the contact between the two components (sensor and ETROC), the resistance of the affected serpentine adds to the one of the column, increasing the overall value. The test can be performed measuring the resistance across a single column (which nominal resistance is lower than 30 when no defects occurs), across a shorted path (which resistance should be lower than 5), or between any number of consecutive columns.

Before separating the various components for creating the individual assemblies, the wafers were used to develop the custom-made automatic measurement framework. During these tests

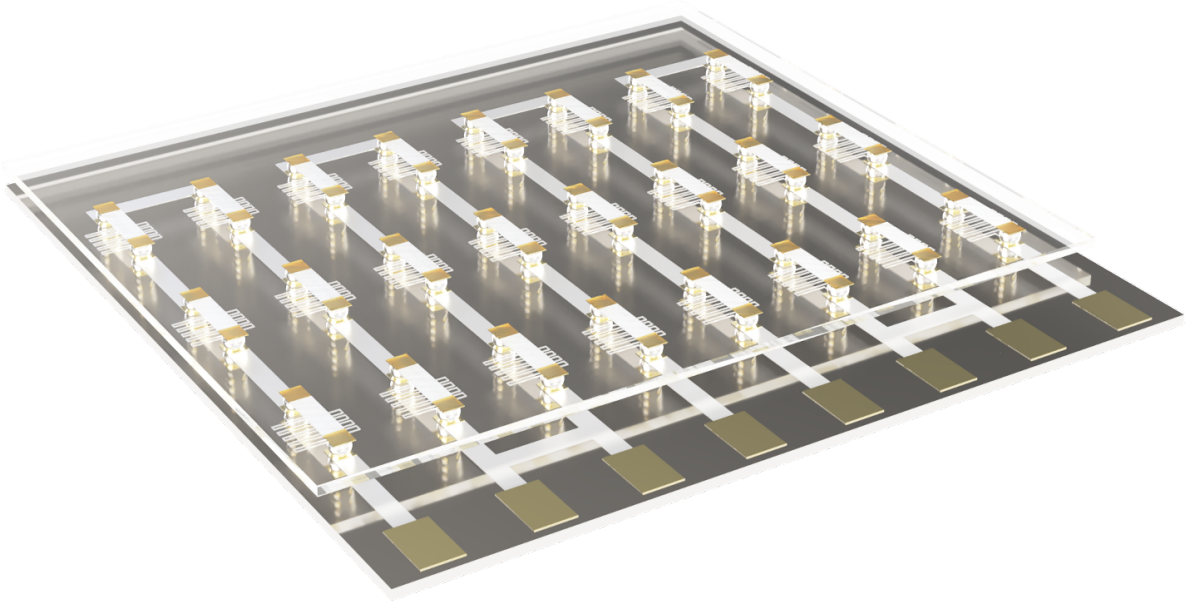

Figure 2.38: Rendering of an assembled module, comprising the dummy ETROC (provided of the columns of serpentine resistors), and the dummy sensor bump bonded on its top layer.

the wafers were positioned on the probe station's chuck. Due to the size of the exposed testing pads (100 μm $\times$ 300 μm), the columns resistance was measured using pairs of precise triax probes. Accurate resistance readings were operated through the use of a Keithley 2410 SourceMeter. A Python (97) framework based on PyVISA was developed to control the instrumentation. The custom-made measurements routine requests to manually collect a selection of points (at least 3) across the wafer's surface to measure the rotation, and translation of the wafer. Then, the code automatically searches for the testing points, reading the position of the exposed testing pads from a .json file.

The two probes are first aligned to the chosen reference points on the wafers (such as the edges if their structure) with the visual aid of the installed microscope. Once the alignment is achieved one can set the origin of the axis system. To compute the matrix needed for geometrical trans-

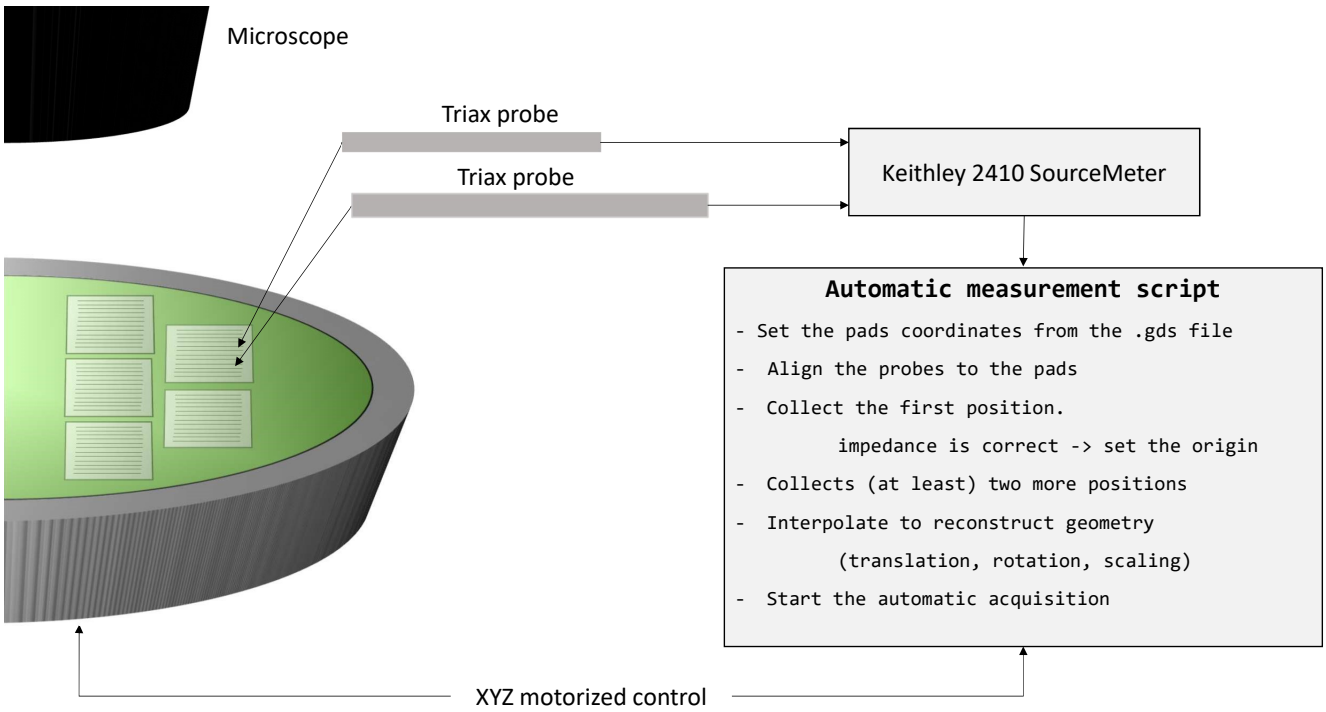

Figure 2.39: Sketch of the setup used during the preliminary characterization tests of the automatic framework for data collection. The fundamental steps of the code are reported inside the grey box.

formation, the system needs to record a total of at least three positions. The setup and DAQ are described in Fig. 2.39.

For building the ETROC assembly, eight wafers were diced, and their component bonded by private vendors (Micross components (98), and Barcelona Detector Technologies (Baretek) (99)). In Fig. 2.40 is reported one of the assemblies, mounted on the chuck of the probe station. The probes are aligned with the first test point for starting the automatic acquisition. The quality of the assembly is verified using the procedure already described. A measurement of resistance of the two tracks (the shorted ones, and the columns with the serpentines) is performed providing a difference of potential between the two probes, and reading the returning current. Each measurement is repeated for a range of voltages, and the average result is used to evaluate the resistance

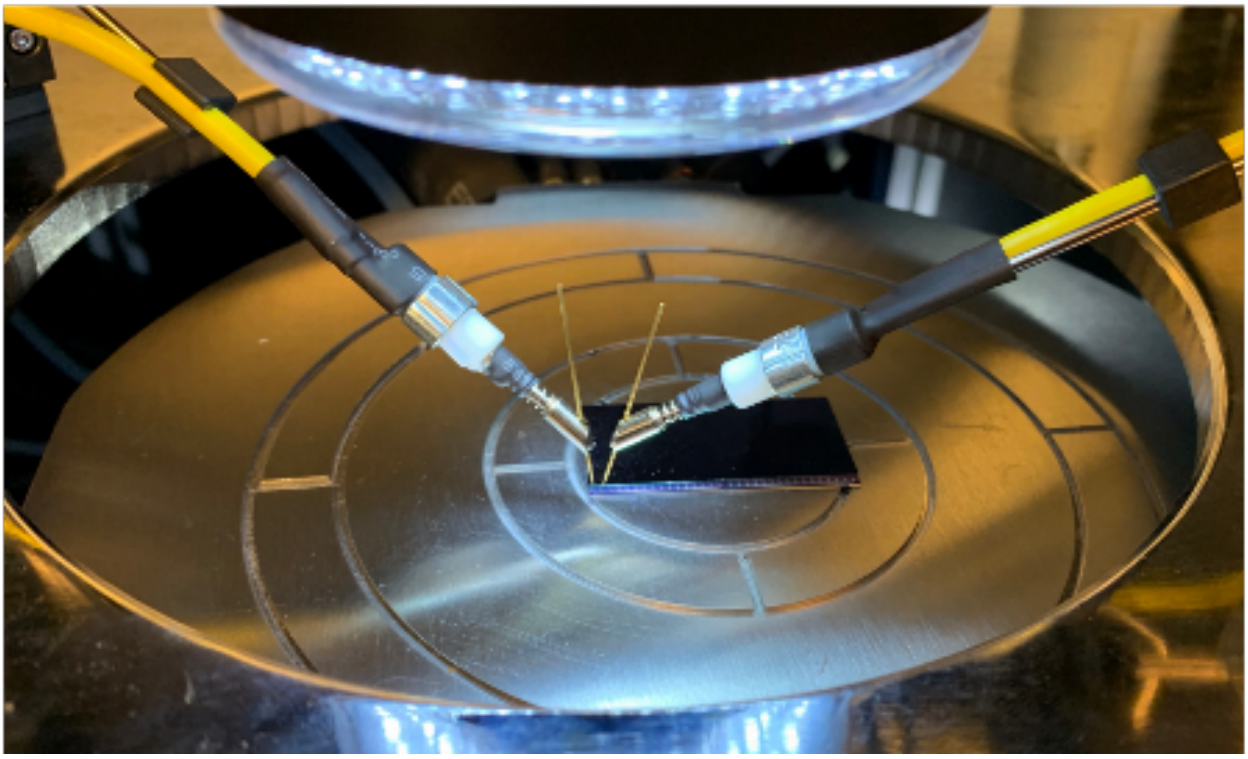

Figure 2.40: Assembly completed, and mounted on the probe station setup. The probes are aligned for starting the resistance measurement.

through a simple ohmic relationship. The test aim to spot eventual bypass of resistance in the column, which would indicate a lacking bump bonding connection. This would result in and effective increased values of resistance in the column.

Fig. 2.41 displays one example of the results obtained. The two rows of data points, centered around 30 , and 5 describe the resistance of, respectively, the shorted pass, and the serpentines. The points are staggered in the x axis, as each measurement requires the alignment of the probes with adjacent test points. The point distribution can be better understood observing the diagram in Fig. 2.38. in the plot, the points at $\sim$30 describe the resistance path of consecutive rows. If every solder ball is in place, the total resistance should skip individual serpentines and provide a reading of about 30 . The row of data points around 5 are measured over shorted path (placed in staggered position, with respect to the columns). The bottom panel of Fig. 2.38 shows a steep increase of the resistance column numbers between 30 and 50. This behavior signals imperfections in the bonding procedures. With the studies of the ETROC and sensors dummies, the KU CMS group is providing aid to the quality control campaigns for the ETL final modules production. In

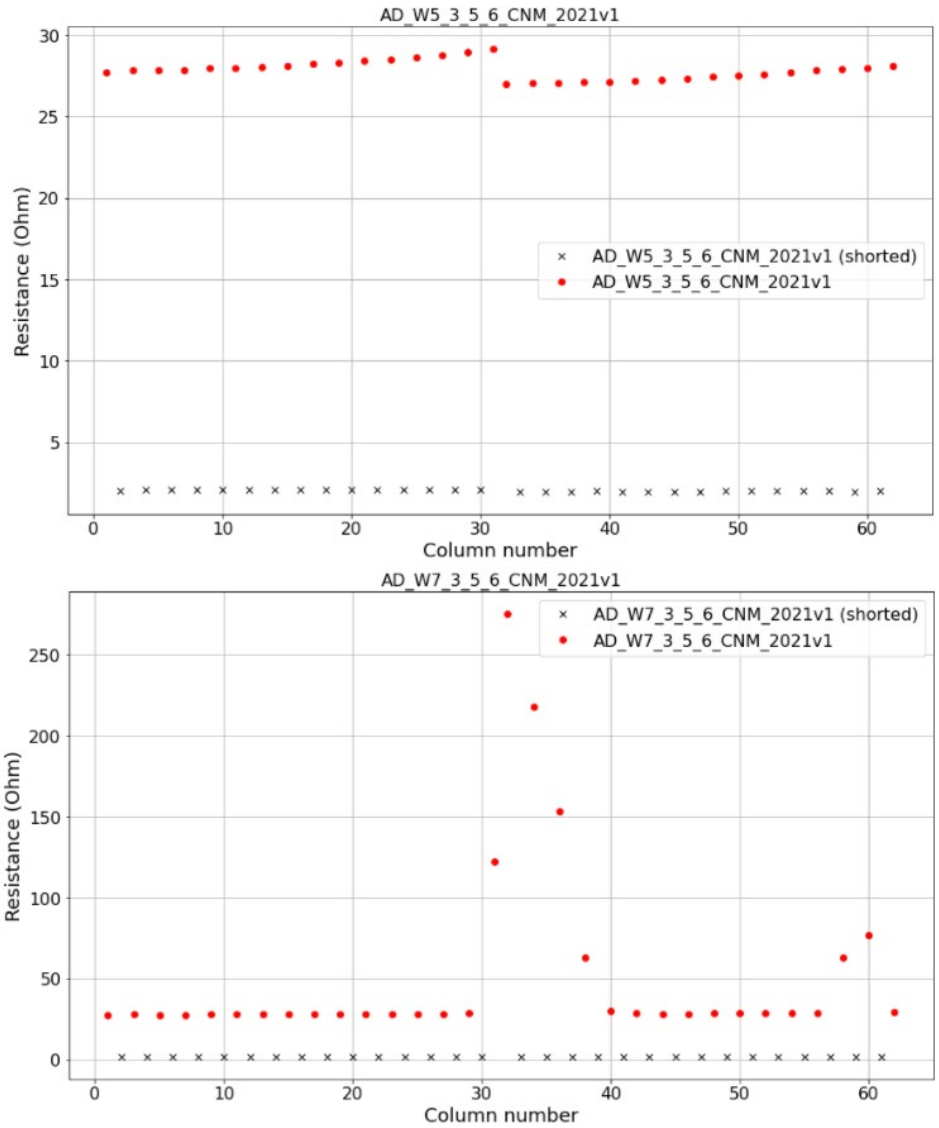

Figure 2.41: Two examples of results obtained with the automatic resistance measurement described in this section. The top panel reports the nominal behavior of an assembly in correct electrical contact: the two rows of dots and crosses correspond to the resistance as read from the assembly.

particular, the procedures described try to evaluate a fundamental technical step of the production chain, being the bump bonding standard connecting the sensors to the read-out. In addition, KU is offering further support through complementary mechanical, and thermal tests for proceeding in the final development of the components.

2.6 Chapter summary

In this chapter we presented the R&D work pursued by the KU CMS group in the characterization of the ETL detectors. In particular, this section reports the results obtained during the tests campaign organized by USMCS for the performance evaluation of irradiated LGAD sensors. During the tests, the work performed required the integration of a fast sampling system in the test beam setup at the FTBF facilities. That allowed for independent reconstruction of the timing performance of the detector. It also led to relevant measurements on the performance stability of irradiated LGADs. The fast read-out amplification concept mounted on the board developed at KU (and later discussed in chapter 3) was employed during the tests for hosting some of the DUTs.

The performance of the tested LGADs met the requirements for the ETL installation. The resolution of the detectors was found to be better than 50 ps for the dose expected to be absorbed by the sensors during the HL-LHC. That requires stability of the gain over the irradiaiton levels sampled. The performed studies reported a minimum gain greater than 10, corresponding to a charge collection of the 5 fC. From the simulated data, this represents the minimum requirements for obtained a sufficient signal amplitude for achieving the wanted time resolutions. Additionally, the detectors performance were measured as a function of the hit position in the single LGADs composing an array. The detectors were found to be fully efficient in MIP detection, with a uniform response over the their active area. The efficiency of the no-gain regions between adjacent pads were evaluated using the tracking information. The results of these studies provided an important feedback to the LGAD vendors for the productions of new sensor batches.

The KU CMS group continues collaborating with the MTD project, providing fundamental support in the quality control of the ETROC read-out modules. The work carried out during this thesis was instrumental in developing a state-of-the-art laboratory at the University, provided of dedicated machinery. The results obtained from this work have resulted in original contributions to the R&D work and detector design for the ETL project.

Chapter 3

Fast detectors for characterisation of medical beam profiles

Chapter 2 described the use of LGADs for the production of radiation resistant detectors capable of precise time reconstruction. As already introduced in chapter 1, LGADs of new generation have displayed promising performance in the fast integration of charged particle fluences. Completed by an intrinsic spatial resolution that can be lower than $1\,\mathrm{mm}^2$, LGADs seem suited to become leading detection devices for radiation monitoring and dosimetry in a variety of research fields.

In this chapter, a detailed description of the project on fast timing detectors using a medical linac, pursued in collaboration with the University College of Dublin (UCD) and the Saint Luke's Hospital (Dublin, Ireland) (100) is presented. Single particles were observed with a time resolution of 50 ps. When compared with the results obtained with the use of a standard medical ionising chamber, the LGAD device achieved a similar integrated response while having a spatial precision twenty times finer and a temporal precision over 100 million times better.

The timing detector performance opened the possibility to study the charge deposited by single linac pulses: its unprecedented resolving power allows to observe the structure of the 3.2 μs linac pulses and the 350 ps sub-pulses composing the machine spill's train. The results presented have been published on Physics in Medicine & Biology, in the paper entitled *'Performance of a low gain avalanche detector in a medical linac and characterisation of the beam profile'* (48).

3.1 Principles of radiation dosimetry

In this section an introduction to the fundamental notions of radiation dosimetry is provided, and the importance of particle detectors in medical applications is described. Although medicine and particle physics might seem distant fields of study, their research is strongly intertwined: progress on particle detection technologies has resulted in breakthroughs in the field of medical diagnosis and treatments.

The medical physics community is experiencing an increase in the demand of particle detectors capable of measuring particle fluence-rates with high spatial and timing resolution. Studies on the radiation resistance of silicon sensors of new generation are reported in chapter 2. While the final goal of these studies is represented by improvements in dosimetry techniques, medical facilities can additionally benefit from this booming experimental developments for a better characterization of particle beams used for medical treatments.

3.1.1 Quantities and units

With the term 'dosimetry' we indicate the study and determination of the energy deposited by direct and indirect ionization in organic and inorganic mediums (101). Dosimetry constitutes a fundamental part of radiation protection in exposed environments and operates in the monitoring of radiation source emission, exposure and contamination. It is often divided in two main fields, external and internal, differing in the way radiation is absorbed. The first one is a result of external exposure, which main contributions can be found from natural background radiation sources (^{222}Rd, ^{220}Rd, ^{40}K), terrestrial radiation and cosmic particles. An additional external source can be found from artificial radiation exposure, such as those from medical devices. Because of the impact in the life of people, its effects in diagnosis and treatment have to be carefully studied and compared with the achievable benefits.

Special dosimetric quantities, accounting for biological effectiveness and tissues and organ sensitivities, are used in the assessment of radiation exposures, relating the energy deposits to the radiation degradation (102). The particle fluence ϕ (Eq. 3.1 (left side)), $\frac{dN}{dA}$, measures the number of incident N particle over the surface A of a sphere (103; 104). This quantity is often used to describe monochromatic particle beams but can be extended to take into account eventual spread in energy (Eq. 3.1 (right side)).

$$\phi = \frac{dN}{dA} \longrightarrow \phi(E)_E = \frac{d\phi}{dE}(E). \tag{3.1}$$

For planar surfaces, or when this quantity is needed, this equation has to be modified to include a dependence on the beam's angle of incidence. If calculated over an interval of acquisition, ϕ measures the amount of particles crossing the surface per unit of time. The fluence-rate is described in

Eq. 3.2 and is measured in units of particles $m^{-2}\,s^{-1}$ (103; 104):

$$\dot{\phi} = \frac{d\phi}{dt} \quad . \tag{3.2}$$

Depending on the material stopping power (described in section 1.2.3), the incident radiation transfers energy to the volume crossed according to the type of ionization processes (101).

In the case of neutral particle beams (indirectly ionizing radiation), the energy is imparted in a two step process:

- indirectly ionizing radiation transfers kinetic energy to secondary charged particles. The amount of mean energy required in the process through the various photon interactions (e.g. photoelectric effect, Compton effect, pair production (105; 106; 107)) with the medium is called KERMA (Kinetic Energy Released per unit MAss) and is measured in units of J/km or Gray (Gy = $J{\cdot}kg^{-1}$).

- secondary charged particles transfer in turn some of their kinetic energy to the material, losing a portion of their initial energy in the form of radiative losses.

The non-stochastic quantity measuring the mean energy transferred to the material by the ionizing radiation is called the absorbed dose and It is expressed in units of Gy. The absorbed dose can be calculated as displayed in Eq. 3.3:

$$D = \frac{d\overline{E}}{dm}, \tag{3.3}$$

where m is the mass of the medium crossed, and $\overline{E}$ is the difference between the energy entering the volume and the one escaping it. The same equation can be used to describe directly ionizing radiation interacting with matter. In this case, the ratio between the energy loss by the charged particles colliding inside a volume V and the mass crossed is called CEMA (Converted Energy per unit MAss) expressed in Eq. 3.4. The unit describing the CEMA is J/kg or Gy (103; 108; 106).

$$C = \frac{dE_c}{dm}. \tag{3.4}$$

Assuming that all the secondary electrons generated are collected in the medium and that any radiative photon escapes the volume, it is possible to relate the absorbed dose to the incident

fluence of particle using the material's stopping-power S_{coll}. Eq. 3.3 can be therefore modified and re-written as:

$$D = \frac{S_{coll}}{\rho}\,\phi. \tag{3.5}$$

Due to the request of no radiative photons in the volume, the sole contribution of the charges colliding with the atomic orbital electrons of the material is taken into account in Eq. 3.6. Considering the spectrum of energy resulting from the distribution of electron energy loss in the medium, the previous equation can be expressed in its integral form:

$$D = \int_0^{E_{max}} \phi_E(E)\,\frac{S_{coll}}{\rho}(E)\,dE. \tag{3.6}$$

Finally, an additional operational quantity needed to understand the radiation dose delivered by clinical accelerators is the Monitor Unit (MU). MU measure the machine's output using ionization chambers (or *monitor chambers*) embedded in its structure. A count of 100 MU represents an absorbed dose of 1Gy (100 rad) delivered to a water-equivalent material, calculated at the point of maximum dose. In this operational definition, the isocenter[1] of the accelerating machine is positioned at the surface of the material, and the radiation field has a size of $10\,\text{cm}\times 10\,\text{cm}$.

This section provided some of the quantities that will be used during the description of the research work reported in this chapter. In the next sections We'll introduce some of the standard detector technologies used for radiation dosimeter.

3.1.2 Radiation dosimeters

In medical physics a device capable of measuring the quantities described in the previous section 3.1.1 is called dosimeter and, when combined with its read-out, is referred to as a dosimetry system. In order to output useful information, properly calibrated dosimeters work by processing physical properties that are functions of a measured dosimetric quantity. Although not all dosimeters can satisfy every users request, the quality of such devices is based off a few desirable characteristics, including the level of accuracy, linearity, dependence on the detected dose and rate, energy response, spatial and time resolution.

In particular, dosimeters that work measuring the integrated response are subjected to effects

[1] In dosimetry, the radiation isocenter locate the point through which the beam of radiation passes.

related to the dose collected per unit of time. While their response is supposed to remain constant for independent acquisitions, fast accumulation of charges modifies the provided output, therefore affecting the linear behaviour of the detector. Moreover, although dosimeters are calibrated using known monochromatic beams, their response could vary when operating in a different energy regime. Their energy resolution is often stable only for specific regions of interest and corrections are needed to study a wider spectrum. Most relevant for *in-vivo* dosimetry (109), these measurements can also vary as a function of the angle of incidence of the incoming radiation. Dosimeters with a directional dependence are the result of specific constructional details and physical size of the detector. In the case of medical applications, these devices are generally assembled in their original calibration geometry.

These qualities are strongly related to the dosimeter detection technology. The selection of a detector represents the first, yet important step, for working with a performing dosimetric tool which has to be selected accordingly to test requirements. For the purpose of introducing the main part of this work, two important technologies are now described.

3.1.2.1 Ionizing chambers

These gas detectors are one of the most used devices for dose measurements in radiotherapy and in diagnostic radiology. In these detectors the active volume (cavity) is filled with gas and encapsulated by a conductive wall that defines the shape and size of the instrument. The material required to build the outer surface is chosen to be as transparent as possible to the incident radiation. An electrode centered inside the gas filled volume attracts the free charges generated by the passage of an incident particle. To reduce the leakage currents and eventual sparks, the two electrodes are confined between an insulator layer. To further mitigate stray currents moving inside the cavity and grant a uniform drift field, ionizing chambers often employ the use of a guard electrode connected to ground, bypassing the collecting electrode.

Cylindrical ion chambers are often used in radiotherapy for calibration procedures. With typical active volumes between 0.1 and 1 cm^3, their chambers have internal length limited to 25 mm and characteristic diameters no greater than 7 mm. Around the cavity, the outer walls are built with typical densities lower than 0.1 g/cm^2. The basic design of a cylindrical ion chamber is

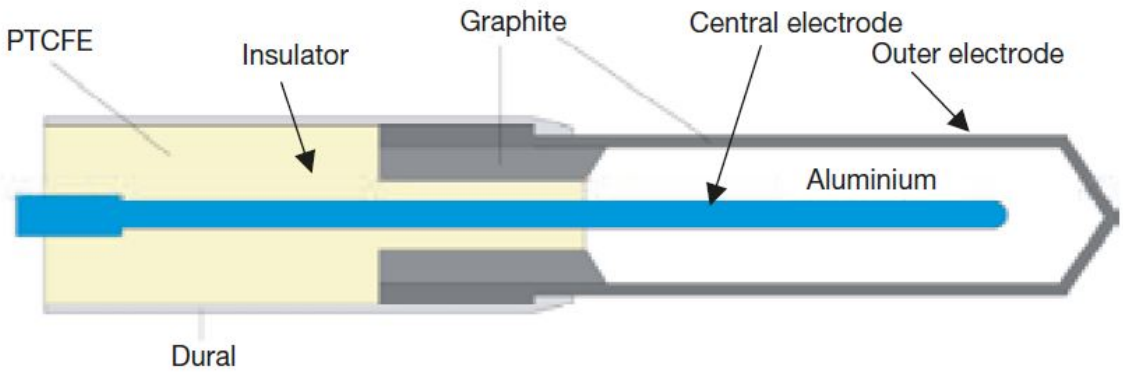

Figure 3.1: Simplified drawing of a cylindrical ©Farmer type ionization chamber (24; 25).

sketched in Fig. 3.1. Mostly used for dosimetry of electron beams with energies below 10 MeV, plane-parallel ionization chambers are constituted by an entry window and polarizing electrode on one side, and a collecting electrode in the opposite one. The latter is usually composed by a layer of graphite combined with a non-conductive material, forming the guard ring. In some cases, their sensitive volume can be adjusted to the incoming radiation profile and be directly embedded into a tissue equivalent phantom[2] to be used for absolute radiation dosimetry. These detectors are known as extrapolation chambers.

The information extracted by ionization chambers is read out by specialized devices capable of accurately measuring small currents (around fA) called electrometers. In Fig. 3.2 a schematic of their use in conjunction with the chamber is shown: the system works integrating the produced charge over a fixed time interval on the feedback capacitance and impedance of a high gain, negative feedback, operational amplifier.

3.1.2.2 Semiconductor dosimetry

In their simplest implementation, semiconductor dosimeters often exploit the properties of silicon pin diodes (introduced in section 1.2.4). Although not suited for energy calibration (as traditionally their efficiency can be affected by radiation damages) these compact, precise devices can be used for accurate reconstruction of the relative dose (110). To maintain linearity between charge and dose, diode dosimeters are usually operated in forward bias mode, as described in

[2]Phantoms are masses of material that emulate the typical densities of the human bodies. They are used for simulating the interaction of radiation with the human tissues and organs.

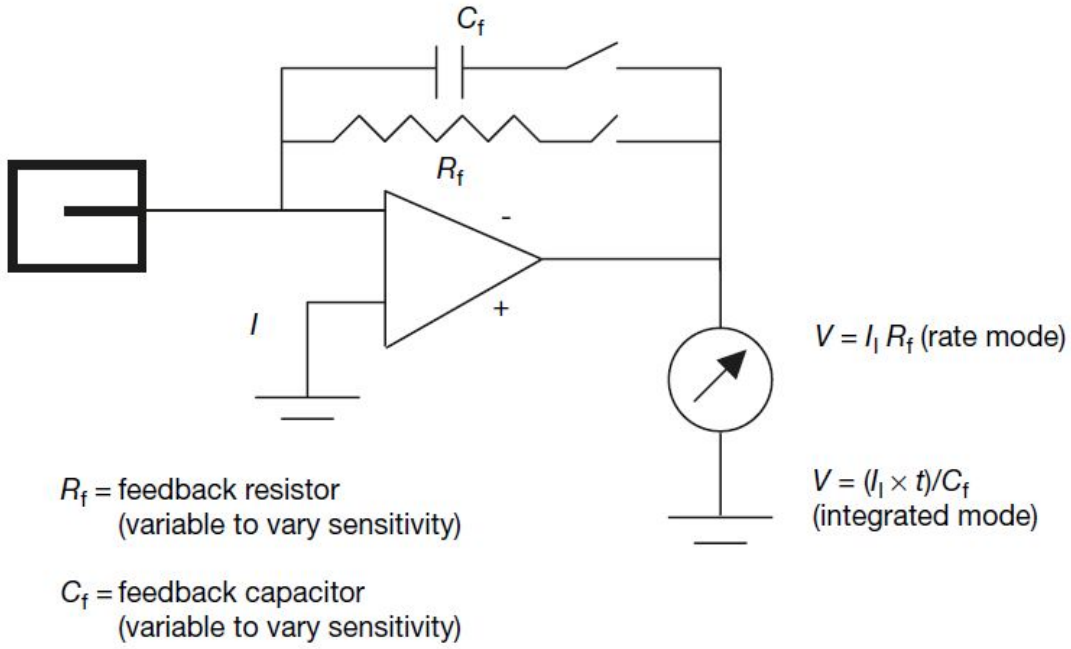

Figure 3.2: Schematic view of an electrometer integrating the charge produced in the active area of an ionization chamber (25).

section 1.2.4. Their intrinsic noise is mitigated by the absence of an external bias which drastically lowers the leakage currents. Thanks to their typical size (few mm^2) and their versatility, these devices are often used in small-field dosimety (111; 112) and in monitoring spatial distributions of dose as a function of position and depth. As opposed to the ionization chamber, radiation profiles distribution can be acquired directly and without any need for converting the dosimetric quantity. When used for in-vivo dosimetry, medical silicon diodes can be calibrated and enclosed in waterproof containers to maintain their operation stable. Unfortunately, these measurements require various correction factors to obtain useful results and the energy calibration procedures have to be repeated periodically as the diodes sensitivity to dose varies with the amount of collected radiation. Moreover, their response can be affected by several factors: temperature, dose-rate, angular and energy dependence.

Some of these problems are solved with the introduction of dosimeters based on metal-oxide semiconductor field effect transistors (MOSFET) which threshold voltage is intrinsically linear to the absorbed dose[3] (113; 114; 26). The linearity between the quantities can be spotted in Fig. 3.3.

[3]The trapped charge generated when ionizing radiation penetrates the transistor's oxide causes a variation of the threshold voltage.

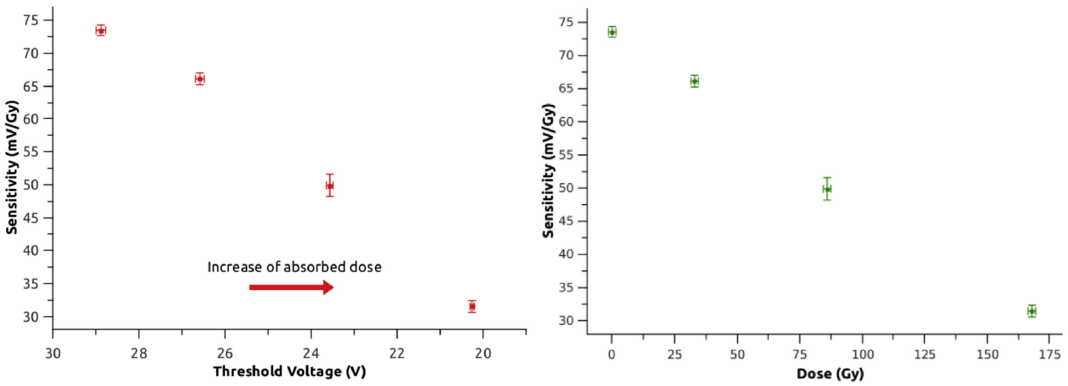

Figure 3.3: Results of the characterization of a dosimetric MOSFET using a 6MV LINAC (26). Left: sensitivity of the device expressed in mV/Gy as a function of its threshold voltage. Right: the same quantity is studied as a function of the collected dose.

These transistors display an excellent spatial resolution and introduce very little material budget in the detection apparatus, making them optimal devices for in-vivo relative measurements. The response of these devices can be instantaneous (measuring during the irradiation) or can be read out after the exposure. In the first case, the detector must be in an optimal condition as its response can be tainted by the effects of accumulated radiation. These detectors have been widely employed in the last decades for in-vivo and phantom dosimetry, as well as for the monitoring of intensity modulated radiotherapy (IMRT) machines (115).

Although mostly used for measuring relative dose distributions in high energy photon and electron beams, diamond detectors also fall into the classification of semiconductor dosimeters. Usually based on natural diamond or chemical vapor deposition (CVD) crystals sealed in a polystyrene housings (116; 117), these devices can be fabricated with small sensitive volumes of few mm^3 for optimizing their spatial resolution (118; 119). Their size and correspondent negligible angular dependence makes them good candidate for particle detection in high dose-rate environments. Due to charge accumulations, the response of diamond dosimeter can drift when subjected to intense dose gradients. To stabilize their response over time, these detectors are usually pre-irradiated to mitigate these localized polarization effects (118).

3.2 Accelerating machines for medical treatment

Since the discovery of X-rays by Roengten in 1895 (120; 121), radiation machines earned an important place in medical diagnosis and treatment procedures. Along with scientific discoveries and

breakthroughs in particle physics, nuclear physics and engineering, progress in medical accelerators have paved the way for the advent of modern techniques of radiation treatment.

Originally, the discovery of natural radiation became the driving force in the use of isotopes in the treatment of superficial cancer. The advent of new technology for X-rays manipulation and the increasing knowledge of unstable elements opened the doors to the possibility of attacking deeper tumor cells. The 1920s became the stage for crucial improvements in clinical machines, as physicists started understanding the different impact of fractioned or continuous dose delivered to patients. By 1928, the scientific community decided to address the question of radioprotection with the institution of the Internal Commission on Radiological Protection (ICRP) (122), where the recent discoveries in radiation damages where analyzed. The Commission also works on regulating the use of radiotherapy machines (123).

Through the decades, the fast evolution of clinical machines capabilities has been guided by the goal of obtaining higher photon and electron beam energies and intensities. Hadronic medical accelerators complete the picture: the use of heavy particles (protons, neutrons, pions) and the Bragg structure of their energy release inside organic tissues are currently under study. In some cases, hadronic medical accelerators are exploited during oncology treatments. To comply with these high intensities and particle rates, radiation therapy facilities have to be provided with the finest imaging and dosimetric technologies. Previously described detection devices are tested and manufactured to optimize the data collection, and to reduce the impact of collateral delivered dose.

In this section, the traditional radiation therapy methods, as well as modern promising techniques are discussed. An introduction of the achievable benefits and technical complications of accelerators of new generation will follow.

3.2.1 Linear accelerators for traditional radiotherapy

Often abbreviated with radiotherapy, radiation therapy refers to the branch of oncological medical procedures that employs ionizing radiation for cancer treatment: the malignant cells are killed or their spreading is kept under control bombarding the affected area with external (or brachial[4])

[4]Branch of radiotherapy specialized in treating patients via the placement of radioactive sources next to (or inside) the tumor (124). The versatility of its geometrical features and the control over the temporal patterns of dose delivered

radiation (127), which deposits energy along its path while travelling through the human tissue.

Historically, to produce these particle beams a variety of clinical radiation generators have been employed and their classification is marked by the maximum output energy. *Kilovoltage units*, developed up to about 1950, generated X-rays at peak voltages up to 300 kV and, although these machines started becoming obsolete less then a decade afterwards, they are still employed for superficial skin lesions. The achievable energy levels in the production of X-rays increased by almost an order of magnitude during the 1960s, when the capabilities of more performing resonant transformer units replaced older instruments, spanning an energy range of 500 to 1000 kV (106). This technology (called *SuperVoltage*) was then replaced by the advent of MegaVoltage clinical radiation generators, capable of delivering x-ray beams of energy 1 MV or greater. The increasing use of cobalt-60 units and, successively, the introduction of particle accelerators coming from the cross-pollination between the medical and high energy physics fields, represented the beginning of the modern era of radiotherapy.

Medical linacs allowed the exploration of new regimes of energies and penetration powers, exploiting high-frequency electromagnetic cavities for the acceleration of charged particles. The latter can be directly used for the treatment of superficial tumors or, alternatively, guided towards a Tungsten target to generate beams of collimated X-rays. The functioning of a linac, schematized in Fig. 3.4, can be summarized as follows.

- A power supply provides a DC current to the modulator, composed by a combination of a pulse generator network and a Thyratron, a vacuum tube filled with hydrogen that controls the current flow modifying the potential of a metallic grid between the anode and the cathode. Differently from a standard triod valve, the Thyratron uses the control over the potential on the grid to create glow discharges inside the tube and switch to its operational state. This change can be made to be really fast (few microseconds), and the Thyratron works as a fast controllable electronic switch allowing for the production of high-frequency, square current pulses.

- magnetrons and klystrons are microwave generators and amplifiers (128; 129). They are connected through a waveguide system to the complex of cavities composing the accelerator

makes it an invaluable medical tool for radiobiology (125; 126).

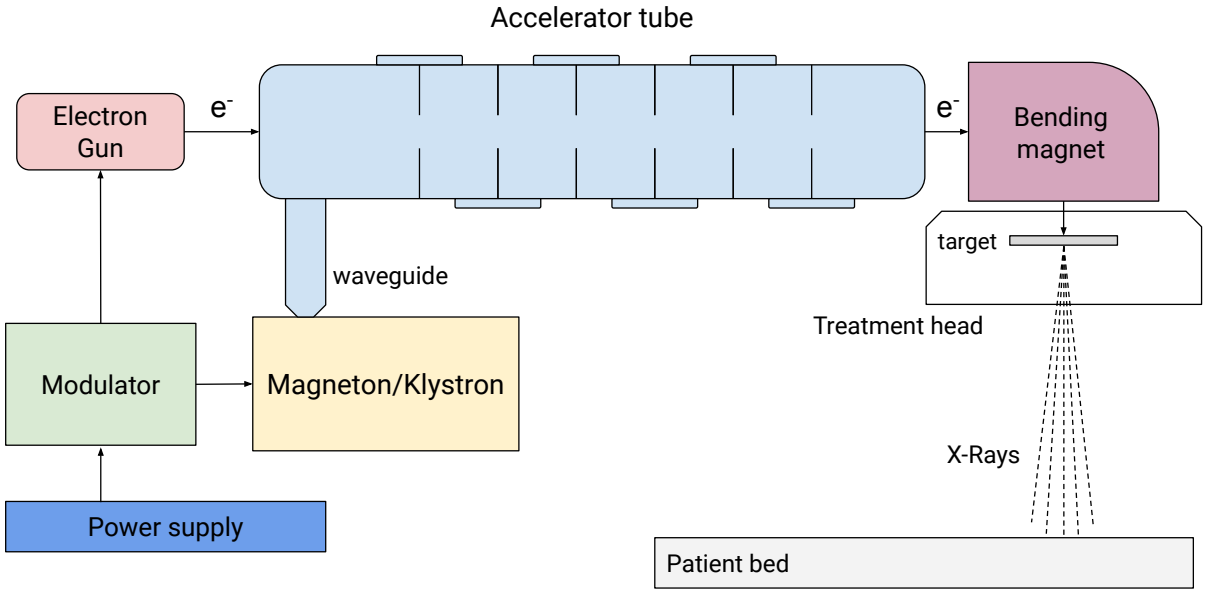

Figure 3.4: Scheme of a standard linear accelerator for radiotherapy treatments.

tube (101). The pulses controlling these components also drive the pulse injection of the electrons produced by the electron guns, forming the trains of the beam structure. The signal shape at every section of the accelerating machine is summarized in Fig. 3.5.

- Copper disks, or diaphragms, divide the main accelerator structure into sections subjected to high vacuum. Inside these copper tubes, the electrons gain momentum when interacting with the electromagnetic field of the microwaves. The accelerated charges are collimated to create a 'pencil beam' of about 3mm diameter and, if needed, collide with the Tungsten target to create X-rays. A system of bending magnets can be used in higher energetic linacs, when the main accelerator tubes would be too long to have a practical use in medical facilities. In linacs, it provides energies greater than 6 MeV. The trajectory of electrons is curved, and the beams are output with 90°or 270°with respect to their initial path.

- The collision with the Tungsten as well as the filtering and the collimation happen inside the treatment head. Composed by thick layers of dense material, this shielded housing contains additional items to characterize the beam. Inside the treatment head, the target is followed by a flattening filter, needed to reduce the momentum spread of the particle bunches. The beam is then collimated by a set of lead or Tungsten blocks (jaws). In addition to the jaws,

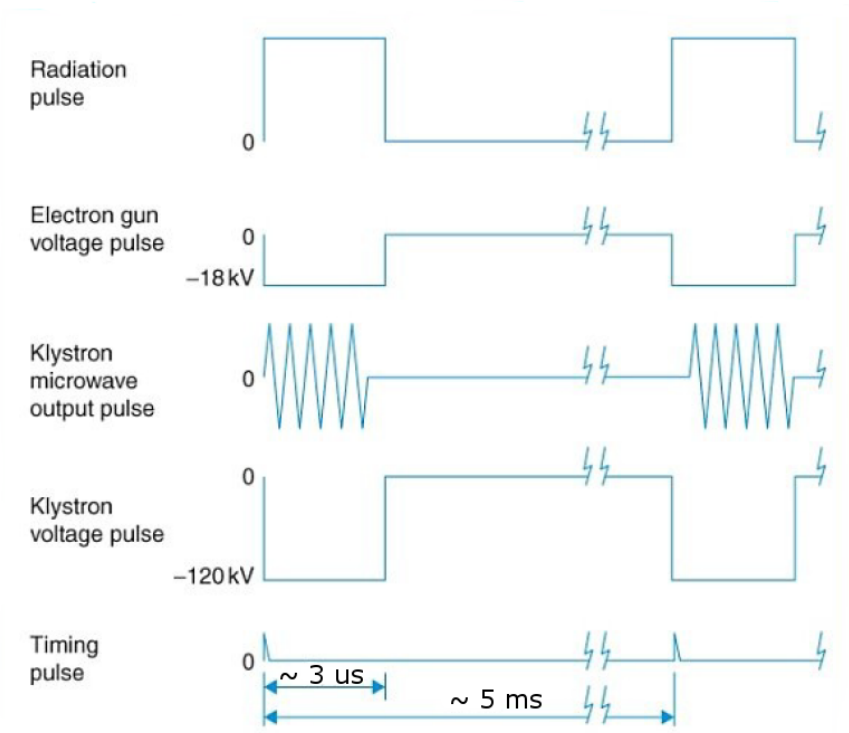

Figure 3.5: Diagram of the pulse shapes at every stage of acceleration of standard LINAC for radiotherapy. The figure is readapted from (27).

modern machines are provided with Multileaf Collimators which serve in dynamically shaping the beam and regulate the intensity over time (intensity modulated radiation therapy). To monitor the quality, they evaluate the dose delivered, and identify the beam's symmetry. The treatment head encloses also several flat parallel plate ion chambers to quantify the delivered dose (25).

The dynamics of radiothearpy treatment has been additionally facilitated by the introduction of rotating accelerating structures (gantries) which move the radiation source around the patient for exploiting better delivery angles. The gantry delivers dose focused toward an isocenter represented by the intersection between the collimator and the rotation axis.

Although few other technologies could be listed in this section (Betatron (130), Microtron (131)), their descriptions goes beyond the scope of this document.

3.2.2 FLASH radiotherapy

Although machines of new generation are capable of delivering focused and precise particle beams, the risk of damaging organs and tissue surrounding the tumor's volume constraints the maximum doses. Recent discoveries have resulted in the complex study of radio-biological effects. Such studies highlighted the benefits of single ultra-high dose-rate ($\geq 40\,\mathrm{Gy/s}$ against the $\geq 0.03\,\mathrm{Gy/s}$) in clinical treatments (132). This novel technique, called FLASH radiotherapy (FLASH-RT), provides an irradiation 400 times faster than conventional treatments, displaying a reduction of radiation-induced damages in healthy tissue without evident decrease in its clinical efficiency (133; 134).

This phenomenon was confirmed by studies in the 1960s reporting that, while the cancerous cells seems to be more affected by increased levels of radiation, the destructive effects of the improved instantaneous dose provided are not enhanced in the healthy human tissues. This differential behaviour is often attributed to:

1. **Oxygen depletion**: tissues that are deprived of oxygen display better radiation tolerance than well oxygenated tissues. The level of hypoxia can be explained by local oxygen consumption due to the rate of deposited energy, when the delivered dose is too fast to maintain a sufficient level of oxygenation (29).

2. **Immune modification**: due to the shorter treatment time, the response of the immune system is not as efficient and leads to less lymphocytes affected by the incident radiation (29). This phenomenon, backed up by studies of immune system activation in mice following FLASH-RT, is however to be completely understand.

Figure 3.6 shows the consecutive steps of radio-biological and chemical effects happening during radiation therapy, as a function of the irradiation time. Although previous studies observed the transient radiation-induced hypoxia, confirming the theory of local oxygen consumption being faster than the tissues oxygenation, the medical community still has to reach a consensus on the exact radio-biological mechanism explaining this differential effect.

Due the complex technical constraints to convert conventional machines to FLASH modality, only few FLASH-RT systems capable of high dose-rate delivery are currently available worldwide (some example can be found in (135; 136; 28)). An example of thee pulse structure output

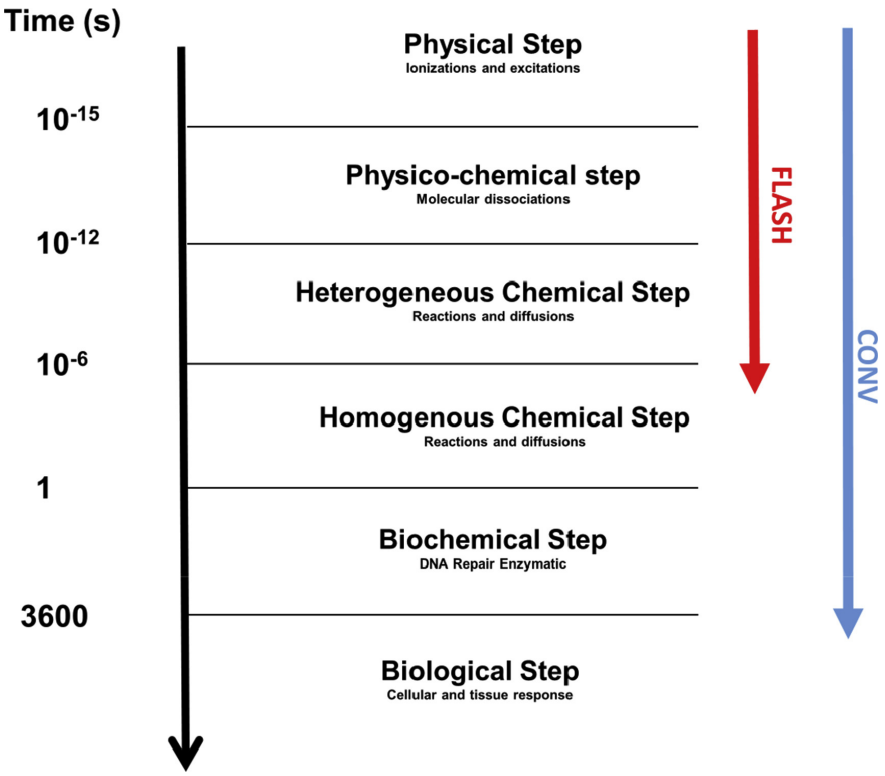

Figure 3.6: The image compares various physical, physicochemical, chemical, biochemical and biological events happening during conventional and FLASH radiotherapy (28). The stages of the cascade are highly dependent on the tissues oxygen concentration and are accessed at different exposure duration.

by a FLASH LINAC can be found in Fig. 3.7. At present, there are promising experimental results obtained with the use of electron sources and high-energies linear accelerator in research centers. In particular, the latter exploits the machine features for pushing the delivered dose and bunch repetition frequency (PRF) to extreme values (10^3 Gy/s up to 10^{10} Gy/s and > 10 MHz PRF, respectively), enabling unprecedented radio-biological and technical studies. The biological effectiveness of FLASH photon sources has already been verified, in vivo, using ultrahigh dose-rate x-ray beams generated at the European Synchrotron Research Facilities (ESRF, Grenoble, France) (137). A comprehensive overview of these machines and their features can be found in (138), while the necessity to identify their pulse structure and temporal parameters currently represent one of the crucial goals for FLASH-RT performance evaluation.

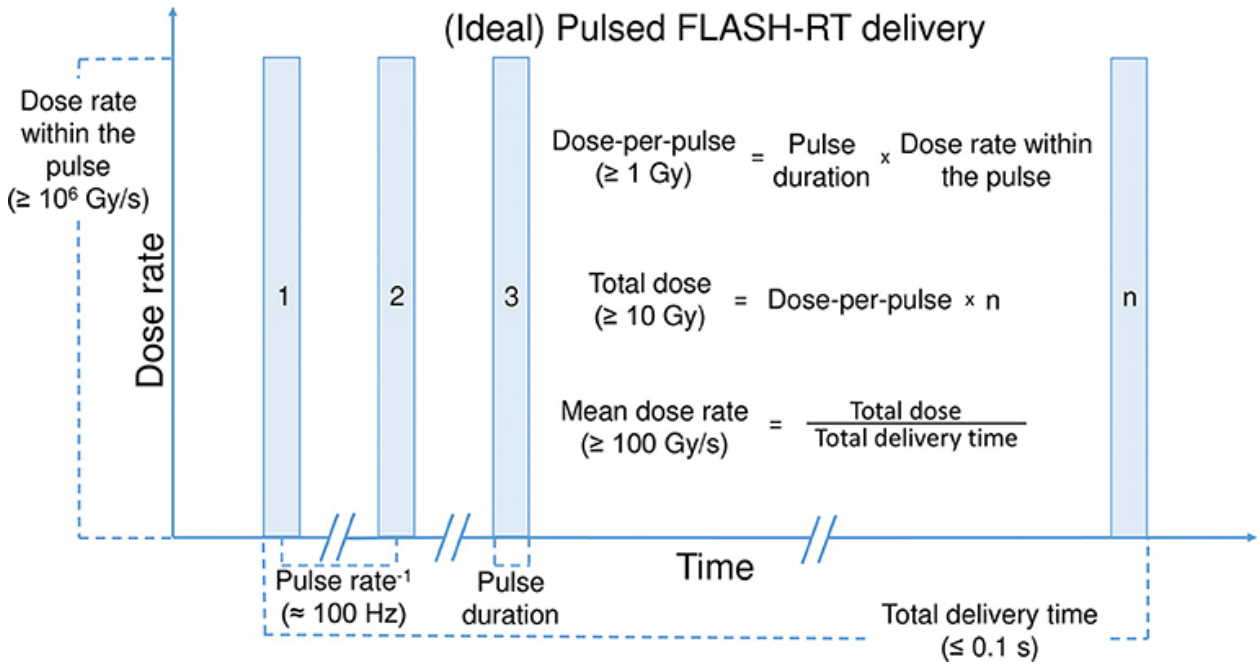

Figure 3.7: Ideal behavior of the dose-rate as a function of time output by a linear accelerator converted to FLASH modality (29).

3.2.3 Proton therapy

Accelerating facilities dedicated to medical irradiation using heavy particles (ions, protons, neutrons), employs their characteristic energy deposition for treating deep and superficial tumors. The peculiar shape of the *Bragg curve* illustrates how hadrons release to the medium the majority of their initial energy within the last portion of their range. This effect, called 'Bragg peak', is indeed of particular importance in radiotherapy, where the clustering of the energy loss can be employed for generating precisely focused particle beams. Contrary to lighter particles (and photons), proton therapy reduces the energy deposit along the particle trajectory and, being only constrained by the beam chromaticity, reduces the collateral effects of medical irradiation. Figure 3.8 compares the relative dose delivered by X-rays and protons as a function of the penetration depth. Despite these advantages, a crucial issue of proton therapy is the ability to stop the particles path within the targeted area. The same features that make the Bragg peak a great tool in radiotherapy, also represent an obstacle when decoupling effects not influencing conventional methods. Proton beams are much more sensitive to the crossed medium's density, which impacts the particles spread resulting in significant scattering inside the material. At the same time, an

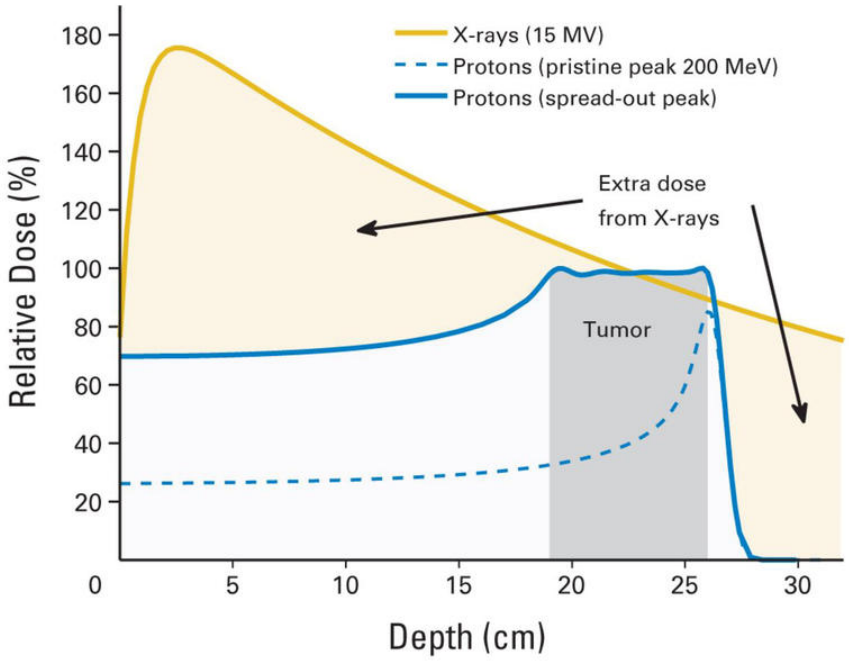

Figure 3.8: Comparison of the relative dose deposited by X-rays (in yellow) and protons (in blue) as a function of the penetration range in human tissue (30). The shaded region indicates the targeted area. Results obtained from simulations.

imprecise target coverage and the risk of overdosing the tumor surroundings are amplified when taking into account the organ motion over time, and the different tissues densities.

3.3 Beam monitoring of a medical LINAC

The motivation behind the collaboration between KU, the University College of Dublin, and the Saint Luke's Hospital (100) comes from the necessity of developing a new generation of detectors optimized for monitoring the intensities of high-rate medical facilities. This concept, already mentioned earlier in this chapter, is expanded in the following sections where We present the analysis of the set-up of the beam tests at the St. Luke's Hospital. This section gives an overview of the medical facility, detailing the property of the linear accelerator under analysis, and the ones of the detector provided by the KU group.

3.3.1 Research motivation

Earlier sections of this chapter (3.2, and 3.2) describe the importance of accurate dosimetric measurements for the monitoring of particle beams, and the evaluation of the dose delivered to the treated patients. Due to their ability of delivering highly localized radiation, medical accelerators of new generation need to be monitored with improved spatial resolution. Small-field dosimetry helps distinguishing between irradiation of the tumors and the surrounding healthy tissue. It is of particular importance in intensity-modulated radiation therapy or microbeam radiation therapies (139).

Recently, the medical field has witnessed a surge of interest in improving the time performance of monitoring devices, and precise reconstruction of dosimetric quantities in dynamic environments (whenever the target is in motion or the delivered dose varies in time). This requires detectors capable of coping with overwhelming fluence-rates. More stringent timing requirements came thanks to FLASH radiotherapy and the ability to deliver ultra-high radiation doses in nanoseconds (140; 141). The understanding of the underlying radiobiological mechanisms in FLASH treatments can be greatly assisted by new detectors with high temporal and spatial resolution.

Usually, standard monitoring procedures in clinical environments use ionisation chambers, devices characterized by a spatial precision of a few mm and response times of the order of a second (described in section 3.2). As reported in by several published studies performed using commercial devices (142; 143), the latter can be combined into 2D arrays and used to map the beam profile, although presenting limited spatial resolution and significant dead areas.

To maximize the spatial resolution, silicon diodes are preferred. With typical dimensions spanning from a few mm down to $50\,\mu$m, these detectors can achieve resolutions of up to about $5\,\mu$m (for a recent review, see (144)). In the same way, diodes can be combined to create 2D arrays with better resolution and granularity than ion-chamber arrays. Current examples can be found in the commercial SRS MapCHECK devices consisting of 1013 diodes covering an area of $7.7\times7.7\,\mathrm{cm}^2$ (145). The dated inheritance coming from their employment in high energy physics, highlights even better spatial precision and much greater granularity when using diode arrays with strips or pixel implants directly implemented in a single wafer of silicon. Their use in the

dense high-radiation environment of the Large Hadron Collider (LHC) (146; 77; 147) displays single particle resolution with an almost 100% efficiency, therefore making them the best candidates for many commercial activities (148; 149). Combining high spatial and temporal resolutions, these detectors have found several applications in dosimetry (examples can be found in (150; 151; 152; 153)). For example, the Medipix device (154) can deliver X-ray imaging as well as charged particle detection with near-photographic resolution. It is an array of 256x256 pixels, each 55 μm square represents a great example of their medical application.

Driven by the necessity of operating in the intense radiation environment of the LHC, recent advances in silicon wafers production helped improving their radiation resistance. The latter being the major drawback found in using these devices in clinical settings. It has been upgraded to withstand more than 1×10^{15} n_{eq} per cm^2 (about 200 kGy) (155; 156). The advent of modern clinical machines capable of delivering dose dynamically in complex systems where the gantry and MLC leaves move continuously during a treatment set the requirements for finer time resolution. The bottleneck of this measurement has generally been limited to collection times in the ms range, with typical acquisitions lasting around 0.25 s for scanned beam profiles and depth doses in water tanks. Silicon based 2D arrays were developed to analyse the delivered doses (i.e. Delta^4 diode phantom (157)), and with the use of a trigger pulse collecting individual pulse doses over tens of μs. The increasing interest in FLASH therapy has led to further investigations into the individual characteristic μs pulses. Examples can be found in recently developed scintillator fibres displaying sub-μs resolution for X-rays from a clinical LINAC (158). These devices use Cerenkov light produced in a fused silica cylinder to view the μs pulse in a FLASH beam. Additionally, diamond detectors have shown results proving ns resolution of X-ray pulses (159). While the signal collection time for typical silicon strips or pixels detectors is $\sim$10 ns (Timepix4 chip (160), for example allows a resolution on the pulses leading edge of 200 ps), LGADs of new generation proved to obtain some of the fastest time resolution achievable with silicon detectors. When read-out by specialised electronics, LGADs show a precision of the order of 30 ps.

During the test results reported in the next sections an LGAD, of dimensions 2.9 x 0.5 mm^2 was used to monitor an electron beam produced by an Elekta LINAC. This radiation-hard sensor was designed to measure the time of arrival (with a precision of 30 ps) of energetic protons at the LHC and previous tests proved its capabilities in measuring fluence rates of up to 100 million

Figure 3.9: Picture of the Elekta linear accelerator used during the tests.

particles per square millimeter per second. These promising results motivated the collaboration of KU and UCD to attempt the detection and identification of single electrons in the LINAC pulse and the investigation of its time-structure. Of great interest for radiobiologists as well as to machine engineers, is the comparison of the data with the ones acquired using the standard ionizing chamber. This comparison provides a better understanding of the temporal deposition of the dose and additional insights on the operation of a LINAC.

3.3.2 The Elekta LINAC

For these studies, the Saint Luke's Hospital of Dublin provided an Elekta Precise (Elekta AB, Sweden (161)) dual modality linear accelerator displayed in Fig. 3.9. The machine was capable of producing photon beams of energy 6 MV (potential for the accelerated electrons to reach energies of MeV) with dose rates up to 600 MU/min and electron beams with energies between 4 and 18 MeV and dose rates of 600 MU/min. The decommissioned LINAC has not been used for clinical use for the last several years, instead remaining an important tool for research purpose. It has been kept with a comprehensive maintenance, quality assurance program, and dose calibration. The accelerator can operate with a pulse repetition frequency of 400 Hz for photon beams and 200 Hz for electron beams. Each pulse is about 3.2 μs long and contains thousands of 30 ps sub-pulses

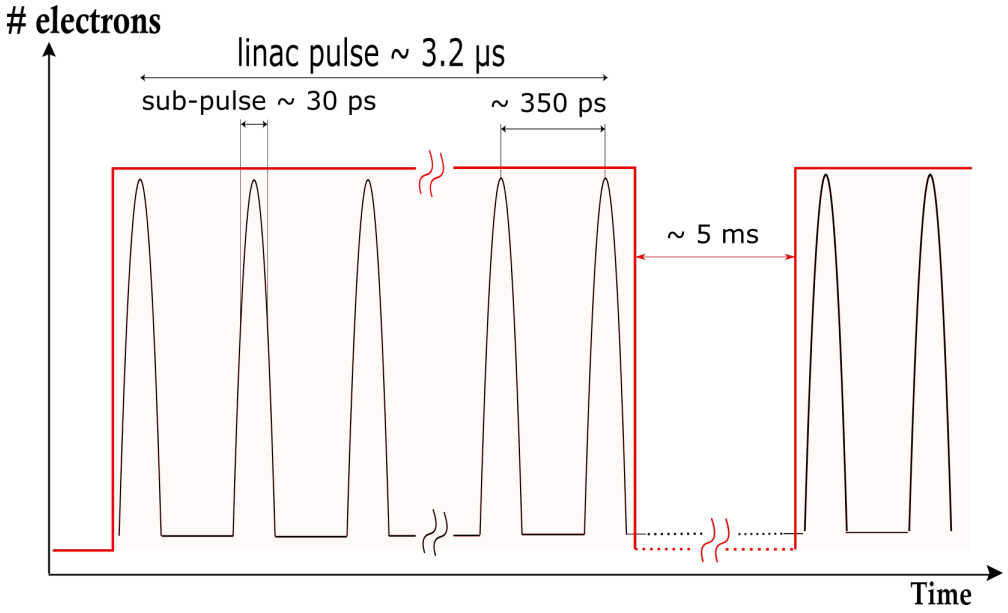

Figure 3.10: Nominal profile of the LINAC pulse.

separated by 350 ps resulting in a fine structure frequency of 2.858 GHz. The nominal schematic of the pulse is sketched in Fig. 3.10. The research accelerator was also equipped with a multileaf collimator (MLC), an electronic portal imaging device and a range of applicators for electron beam collimation. A PTW Semiflex Ionisation Chamber 31010, operated at +400 V, served to measured the provided dose. This detector is used to monitor the LINAC in standard medical procedures and it consists of two layers of material (0.55 mm PMMA and 0.15 mm graphite) encapsulating its sensitive volume (see table 3.1). The total active bulk, displayed in Fig. 3.11, is a cylinder of radius 2.75 mm and height 6.5 mm. To read-out the ionisation chamber, We used a dual channel

PTW Semiflex IonChamber 31010	
Active area	Cylinder radius 2.75 mm, height 6.5 mm
Material	0.55 mm PMMA, 0.15 mm graphite
Bias Voltage	+400 V
Resolution	10 fA
Measuring intervals	10 ms

Table 3.1: Table of the main techncial features of the PTW Semiflex ioninization chamber 31010.

PTW Tandem dual channel electrometer with 10 fA resolution and minimum measuring intervals of 10 ms. This parameter represents the bottleneck for the time required for every acquisition, while the dead time between consecutive measurements is determined by the time needed for the

Figure 3.11: Picture of the PTW Semiflex ioninization chamber 31010 encapsulated in the PMMA cylinder.

device's reset (typically several seconds).

3.3.3 The KU Low Gain Avalanche Detector

LGADs are rapidly becoming one of the most promising technologies available for fast and precise measurements of charged particles in high-rate environments. The rapid drift time of the free charges, and the contained avalanche process grants an intrinsic fast rise time and reduces the dead time between consecutive acquisitions. The thin multiplication layer amplifies the generated current with a typical gain in the range of 5-20 which is further amplified and shaped by the read-out electronics. In addition, the low dark currents characterizing LGADs are a consequence of the above mentioned properties and open the possibility to design of thin (of about tens of micrometers) sensors producing fast, low-noise signals. An extended description of the LGAD technology is provided in section 1.3.

The device used during the test is displayed in Fig. 3.12. It consists of a LGAD sensor mounted on a multipurpose read-out board, developed at KU. The sensor, originally designed to operate inside the CT-PPS experiments at the Large Hadron Collider (87), has a pattern of 32 available pads with decreasing sizes. The pad selected for the test had an active area of $2.9 \times 0.5\,\mathrm{mm}^2$. The left panel of Fig. 3.12 also displays the full read-out chain based on SMD discrete components hosted on the same PCB (96). This compact design allows to easily configure the board electronic properties for its use in different applications. The read-out consists of 8 identical two-stage trans-impedance amplifiers and a $20\text{x}20\,\mathrm{mm}^2$ pad that provides stable bias to the sensor up to about 500 V. To reduce the total input capacitance, the wire-bonded sensor is kept few millimeters away from the high speed SiGe transistors (to reduce eventual parasitic capacitance). A larger capac-

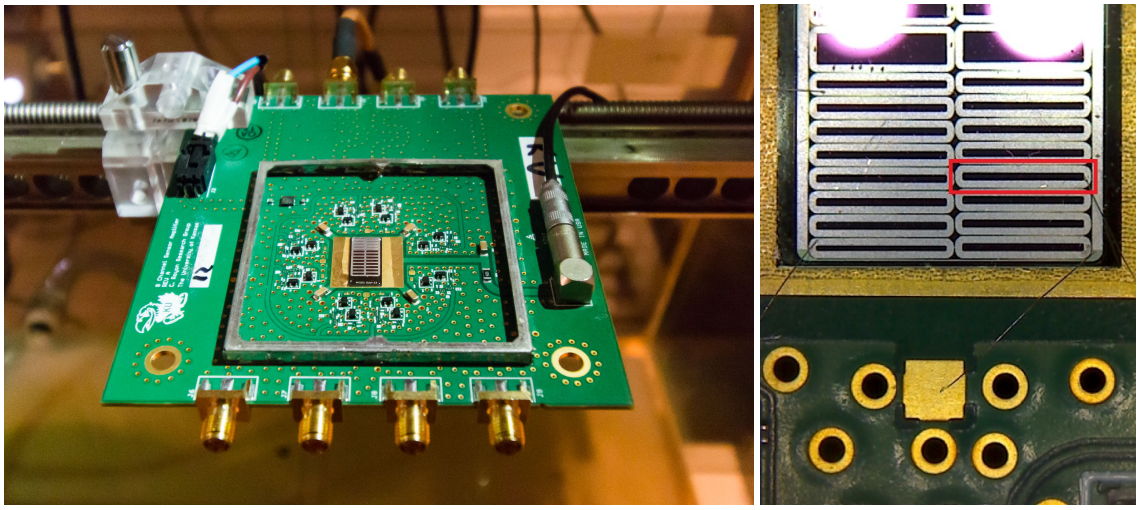

Figure 3.12: Left: The KU-board mounted on the horizontal rail of an empty PTW 3D scanning water tank provided by the hospital. Right: Magnification of the LGAD sensor aligned and glued to the HV pad of the KU-board. The red outline indicates the single pad used for these tests.

itance, combined with the typical large input impedance required for the amplification stages, would modify increase integration time of the system, impacting the output signal properties. Since the pre-amplifier on the KU-board reads out the current generated by the sensor through the RC made by the it on the capacitance of the sensor and the input impedance of the first stage, a higher input impedance would correspond to a better signal-to-noise ratio (SNR) with a slower signal. Using a high impedance requires longer times to collect the totality of the free charges drifting in the sensor to finally restore the baseline level. This presents a potential problem as subsequent signals could add to the charge already present in the sensor and the amplifier would be subjected to ealry saturations.

This compromise between higher SNR and lower sustainable rates represents a dilemma to be faced in the earlier stage of the detector design and strongly constraints the detector's range for practical applications. Using minimum ionizing particles, the detector showed typical rise times of the order of $\sim$600 ps, while the amplitude of the signal depends on the sensor properties (i.e. capacitance and gain). Similarly to the impedance, the choice of the sensor and its bias voltage represents another dilemma. As the device's gain depends on the applied electric field, while a bias voltage too low results in inefficiencies in the pulse shaping, a bias too large leads to generate too many free carriers at the passage of an incident particle. This can limit the the maximum rate of operation.

The detector's operating voltage was characterised during a previous test using a 180 GeV pion beam inside the LHC North Area Facility at CERN (96) where, for higher voltages (see Fig.13 in (96)), the results indicate a time precision better than 25 ps. In order to achieve a good compromise between SNR and fast response, during these studies the detector was operated at a bias voltage of 150 V with an expected time precision of about 50 ps.

3.3.4 The Measurements performed in the LINAC beam

After removing the Tungsten target needed for the generation of X-rays, the Elekta LINAC was setup to generate a pure 6 MeV electron beam. With the use of the primary collimator face-plate and no additional electron applicator[5], the field size was chosen to be 3x3 cm^2. With the use of a neodymium permanent magnet sitting 12 cm below the collimator face-plate, the electron beam trajectory was bent and spread along the horizontal axis.

The installation of the magnet not only served to select electrons within a range of momenta but it also isolated the charged from the neutral components of the beam, reducing the contamination coming from bremsstrahlung photons[6]. As depicted in Fig. 3.13, the KU detector was mounted on the horizontal rail of an empty PTW 3D scanning water tank. The detector position was controlled remotely. The detector, aligned vertically using the in-room positioning lasers and horizontally using the LINAC light-field crosshair, was used to scan the diverged beam and to collect particles as a function of the position relative to the main axis of the radiation source. The two stages of amplification in the read-out circuit produced signals with a total width in the range of $5 - 10$ ns (as depicted in Fig. 3.14). The signals were digitized using an Agilent DSO8104A Infiiium oscilloscope (163) with a bandwidth of 1 GHz and a sampling rate of 4 GSa/s. The full setup is sketched in Fig. 3.15. During the data acquisition, the detector collected 200 pulses for each position probed. A typical full spill of the machine recorded by the oscilloscope (in yellow) is shown in Fig. 3.16. To trigger the beginning of each acquisition, the collaboration decided to use the signal coming from the thyratron in the LINAC (in purple) corresponding to the electron injection inside the first acceleration stage of the machine. The details of the offline data analysis

[5]Set of metallic diaphragms used in most treatment machine to produce scattered radiation and modify the field size (162).

[6]This contribution is attributed to the neutral particles generated in the interaction between the output electrons and the column of air between the LINAC head and the detector.

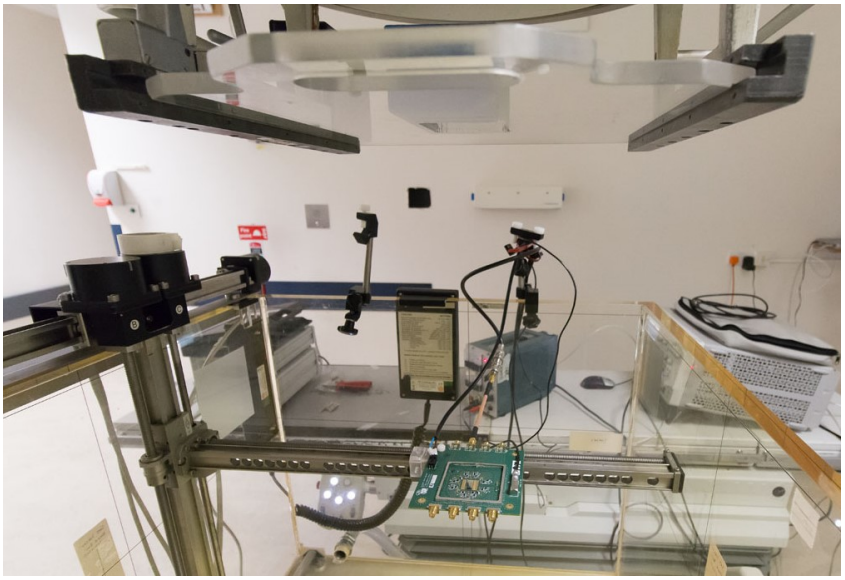

Figure 3.13: The KU board is mounted on the horizontal rail of the PTW 3D water tank and moved remotely to scan the beam profile.

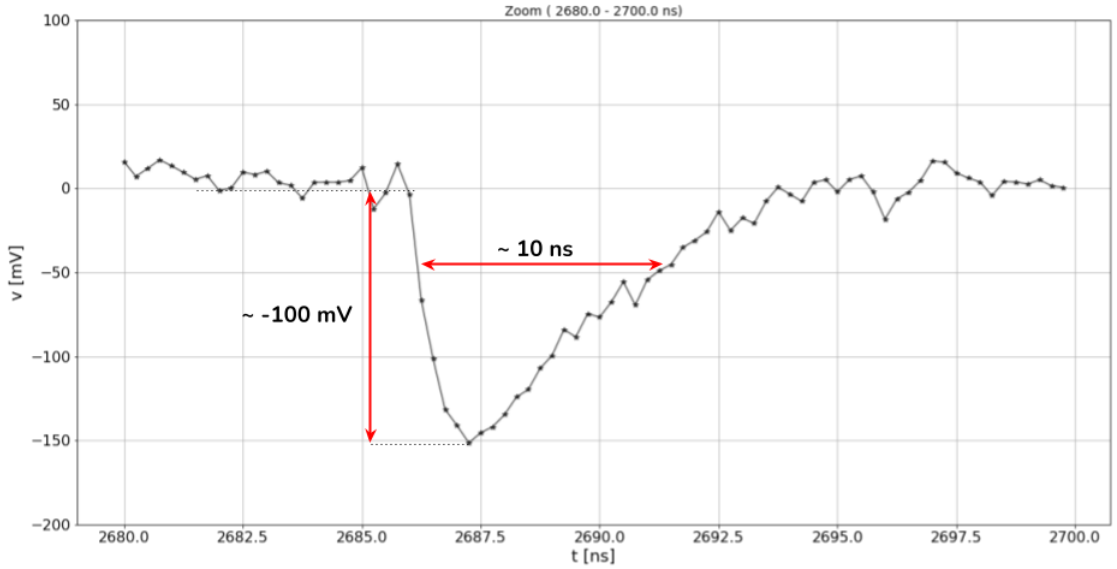

Figure 3.14: The picture reports the pulse output by the detector after the passage of an electron. In this configuration, the signals are typically ∼10 ns long with amplitudes spanning few hundreds of mV up to few V.

as well as the obtained results can be found in the next section 3.4 of this chapter.

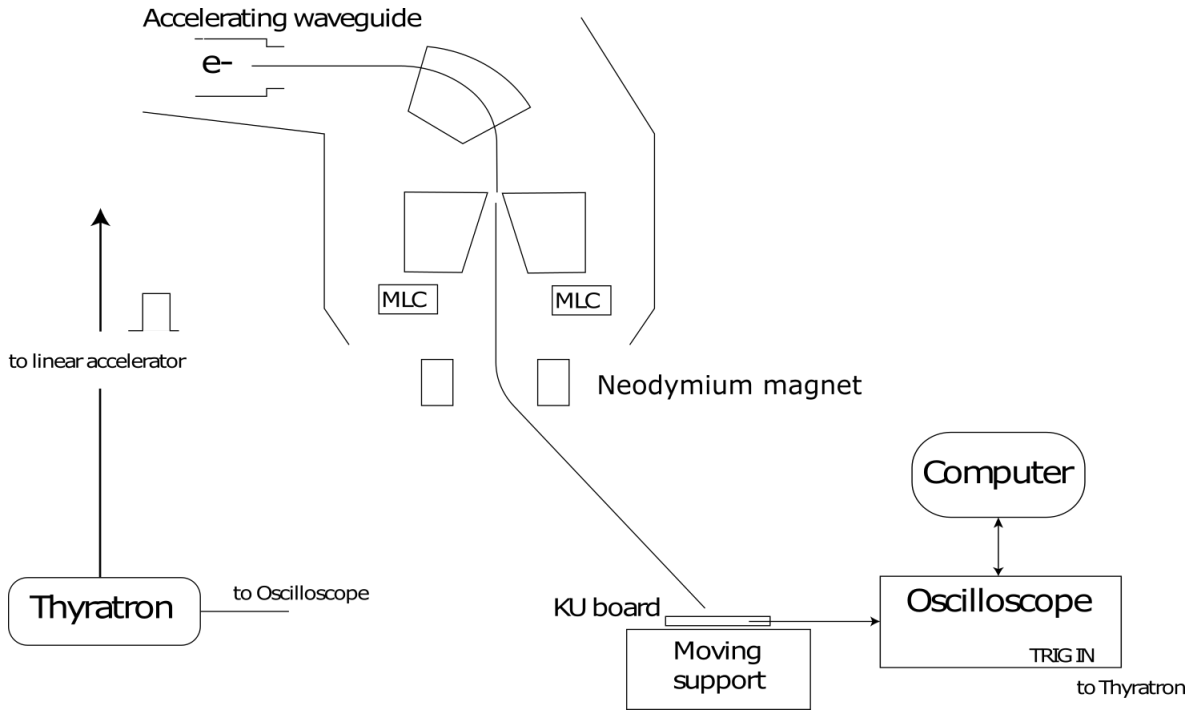

Figure 3.15: Setup used during the studies of the electron beam. At the top, right under the LINAC head, the electron beam is deflected by the Neodymium permanent magnet placed at the exit of the multi-leaf collimator (MLC). Mounted on the horizontal rail of the moving support, the KU board scanned the profile of the beam while the oscilloscope recorded the data. The thyratron provided the trigger to the digitizer in the oscilloscope and the data were recorded on a computer.

3.4 Data analysis and experimental results

This section presents the analysis methodologies and the results obtained studying the data set collected utilizing the facilities at Saint Luke's Hospital. The detector, mounted on the horizontal rail of a remote controlled support, scanned the beam axis to measure the quantity of incident radiation using two independent methods: charge collections and single particle counting. The data were collected using a sampler and digitizer (bandwidth of 1 GHz and a sampling rate 4 GSa/s) and later analysed in three steps:

- the total charge collected per each LINAC pulse is compared to that measured by the medical ion chamber.
- A dedicated algorithm identifies individual charged particles traversing the detector, with a time precision of about 50 ps.
- The precise time discrimination implemented in the previous step is used to investigate the

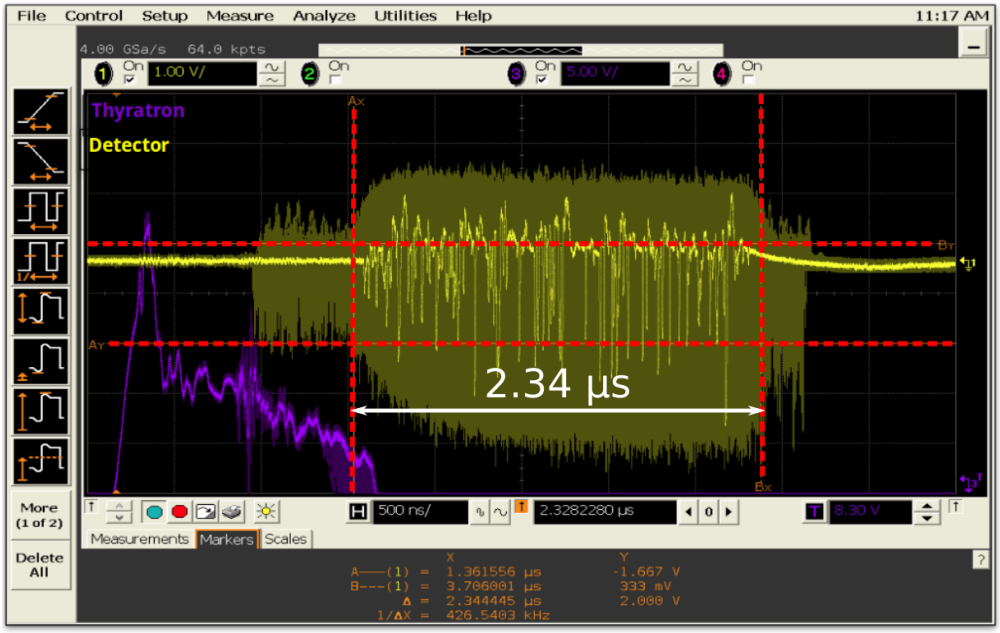

Figure 3.16: The image shows the typical response of the LGAD (yellow) to one LINAC pulse as recorded by the oscilloscope. In the horizontal axis (time), the total duration of the spill is reported between the two red vertical scale-lines: 2.34 μs. The distance between the two red horizontal scale-lines (2 V) give an idea of the maximum amplitude expected. In purple, the signal from the thyratron provides the triggering signal to start the acquisition.

particles	electrons	**scan range**	0 to 25.0cm
energy	6 MeV	**step size**	1 cm
intensity	600 MU/min	**triggers averaged (per data point)**	200
magnetic field size	3x3 cm^2	**lead absorber**	none

Table 3.2: List of the beam proprieties and analysis technical specification. The data were acquired using a 6 MeV electrons beam and without using absorbers to limit the fluence on the sensor.

structure of the LINAC pulse.

The beam and detector specifications used during the tests are summarized in table 3.2.

3.4.1 Charge integration

From Fig. 3.16, one can observe that the electron beam is present from roughly the left-most red marker displayed on the oscilloscope screen. Before analyzing the data, they had to be corrected for DC offsets. This is caused by lower frequency noise and results in a shifting of the signal's baseline by a constant value. This contribution adds to the total amplitude affecting the total integral of the signal. The offset was measured by averaging data from 0.5 to 1.5 μs before the pulse, where

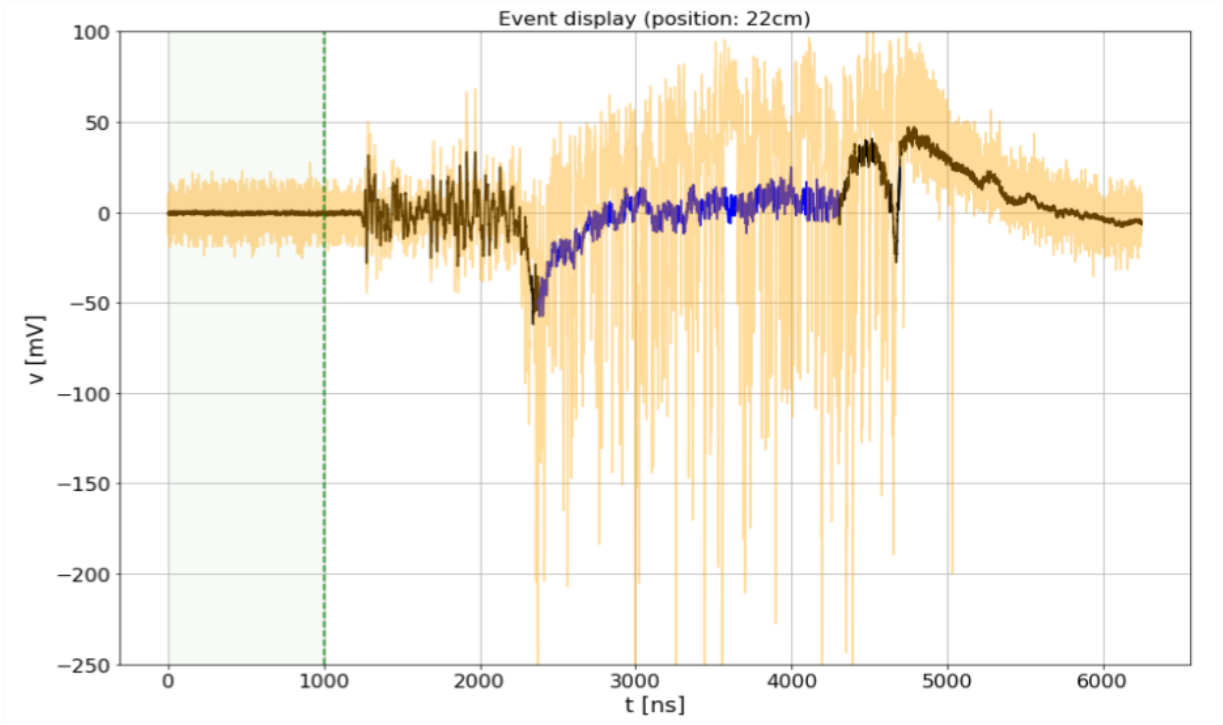

Figure 3.17: Event display of a LINAC pulse (in yellow). Green: the area includes the data points used for quantifying the intrinsic RMS and the DC offset caused by low frequency fluctuations. Black: average of every spill at 22 cm from the beam axis. Blue: the shifting of the baseline due to the charging up of the LGAD is highlighted.

no signal electrons are detected. The RMS of the data in this region defines the intrinsic noise of the measurement, σ_{noise}. In Fig. 3.17 the various contributions are highlighted; these slightly change on an event-by-event basis. The total charge collected during each LINAC pulse was found integrating the signal. To perform the integration, the upper and lower boundaries of the charge have to be carefully decided. As the detector's amplifier is AC coupled and the output has to be with null average, the negative charges collected are then injected back into the pre-amplification stage, creating an 'overshoot' region. Consequently, the absolute minimum and the maximum of the integral are both proportional to the charge and can be used for the measurement.

While moving away from the central beam axis in 1 cm steps, the LGAD recorded 200 LINAC pulses for each position as the ion chamber (described in section 3.3.2) placed at the same location. Figure 3.18 (left) displays the average and RMS of the integrated signal in the LGAD compared to the ion-chamber response at all locations except those on the beam-axis. The linear response (and the corresponding linear fit) points out a good agreement between the two detectors over

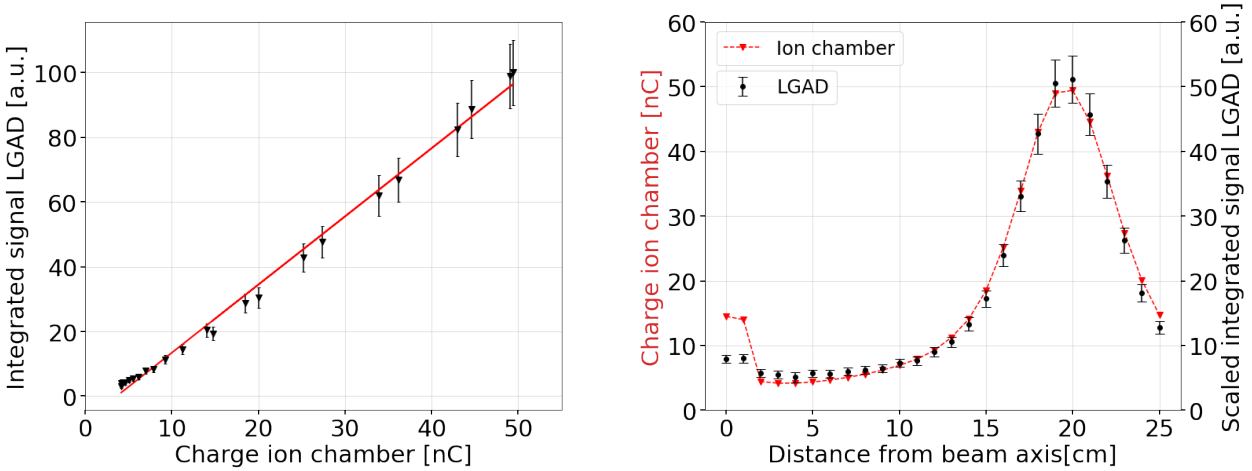

Figure 3.18: The left panel shows the correlation between the charge in the ion chamber and the average integrated signal measured by the LGAD for each LINAC pulse. The linear function the best fits the correlation is depicted in red. In the right panel the charge measured with the ion chamber and the average integrated signal of the LGAD per LINAC pulse as a function of distance from the beam axis are shown. The error bars are calculated using the RMS of the voltage signals obtained over 200 triggers.

most of the position's range. The LGAD gives equivalent results to the ion chamber, but with a time resolution of $3\,\mu$s (single machine pulse), rather than seconds. Later, the results of the fit were used to scale the LGAD response to that of the ion chamber (displayed in the right panel of Fig. 3.18). The figure shows the average and RMS of the integrated charge distribution in the detector compared to the ion chamber as a function of distance from the axis. The comparable charged particle detection efficiencies (region $>= 2$ cm from the beam) is reflected in the devices with broadly similar responses. In this area of the figure, the detectors are in good agreement and minor differences between the two data sets are attributed to small non-linearity in the read-out response (96) as a function of deposited charge.

The dissimilarities in the region ≤ 2 cm occurs under the (undeflected) beam position where the collected radiation is dominated by a large flux of low-energy photons (164). The ion chamber and LGAD display significantly different behaviours attributed to the probability of photo-conversion in the corresponding detectors housings, since neither the LGAD nor the ion chamber are designed to directly detect photons (165). To have a clear and complete understanding of the Si sensor interacting with the LINAC photons, the system would have to be completely constrained by the use of a simulation tool.

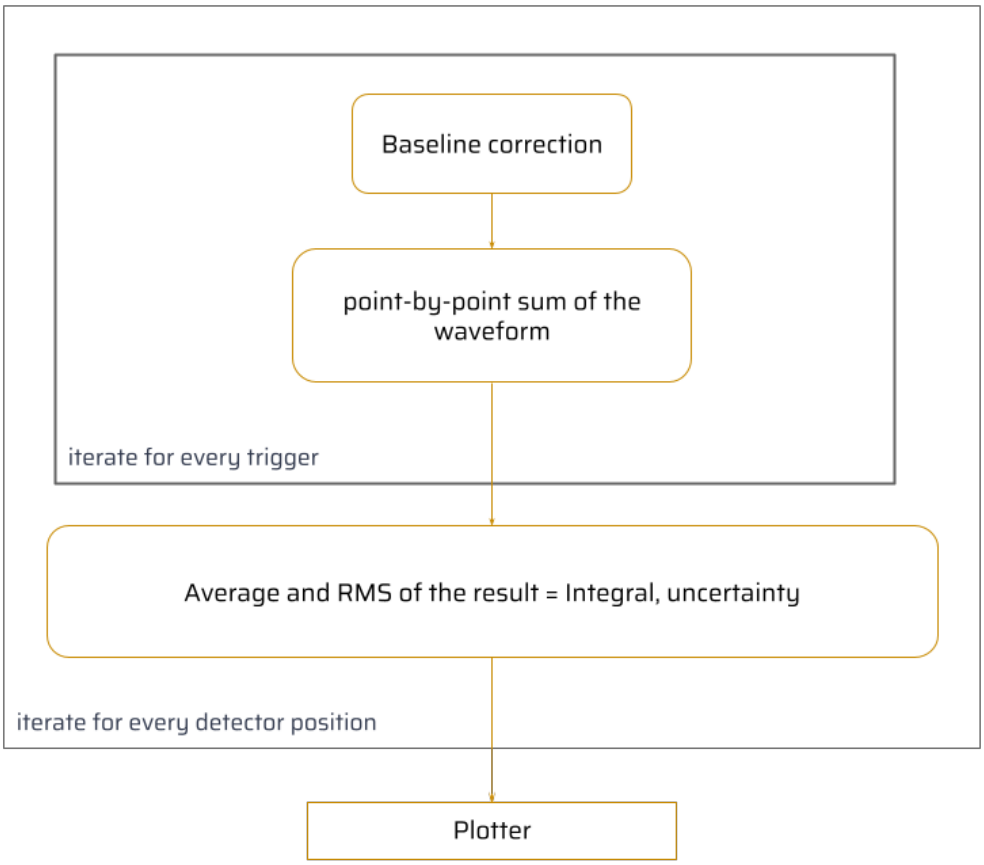

Figure 3.19: The collected charge is estimated adding the amplitude of every samples from the beginning of the particle spill to the end of the trigger (Integral) for each detector position.

The response of the LGAD electronics varies as the number of particle crossing the Si detector (position and LINAC radiation output distribution over time) increases. This effect can be spotted in the RMS fluctuation in Fig. 3.18.A simplified sketch of the charge integration algorithm is displayed in Fig. 3.19

3.4.2 Single particle counting

While the medical ionizing chamber typically needs few seconds to respond and requires several hundred of the LINAC pulses to obtain a measurement, the LGAD data presented in the previous section 3.4.1 are computed after a single pulse. The quick response and low dead time of the Si detector can additionally be exploited to identify each charged particle that traverses the detector. In the magnified display showing the details of a single triggered event (Fig. 3.20), the pulses

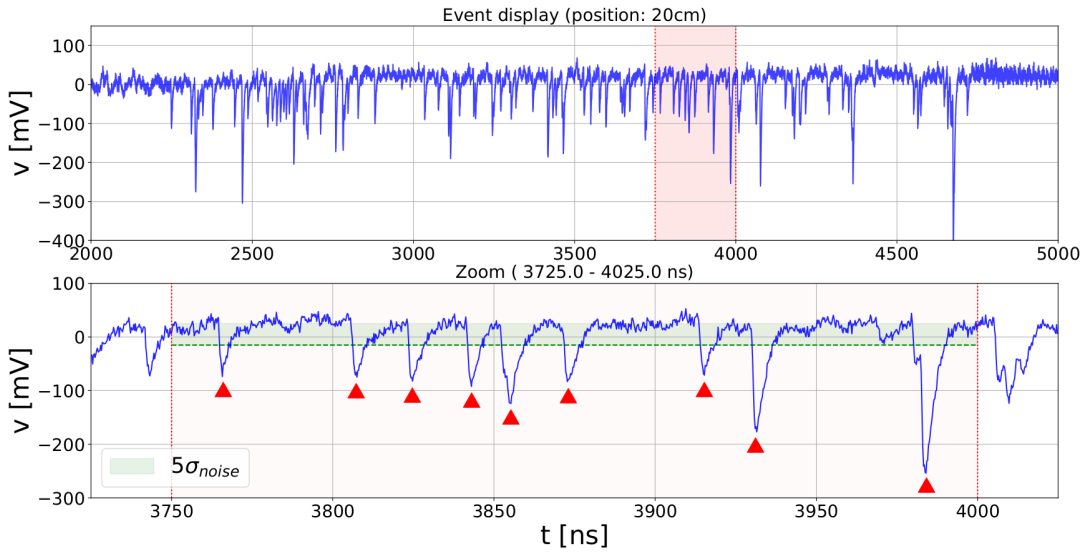

Figure 3.20: Top: section of a typical LGAD signal obtained during one LINAC pulse; the abscissa shows the time elapsed since the trigger. Bottom: zoom on the selected area (highlighted in red) is reported in the bottom panel. Here, the green band corresponds to the width of five times the noise level. The red markers pinpointing isolated excursions from the baseline correspond to candidate charged particles detected by the LGAD and identified by the algorithm.

generated from charged particles are clearly visible and indicated by red markers. At the core of the analysis framework, an algorithm attempts to identify incident particles. The framework, designed such that it could be applied in real-time to give an instantaneous response in a clinical setting, proceeds in the following steps:

1. a low-pass filter processes the data to reduce high-frequency fluctuations coming from electronic noise.

2. The baseline is estimated averaging the samples in the time interval anticipating the signal pulses by 2-4.5 ns. The baseline is used for evaluating the pulses height. This interval was chosen by inspection of the signal pulses (Fig. 3.20). Typical signal rise times are of the order of 1.2 ns (5 samples), after which the signal slowly decays. In order to uniquely identify the pulse's maximum and account for statistical fluctuations, the code defines a baseline starting 8 samples before the putative maximum. The average to calculate the baseline level is performed over ten samples.

3. The information of the baseline is now used to identify candidate peaks greater than $5\sigma_{\text{noise}}$.

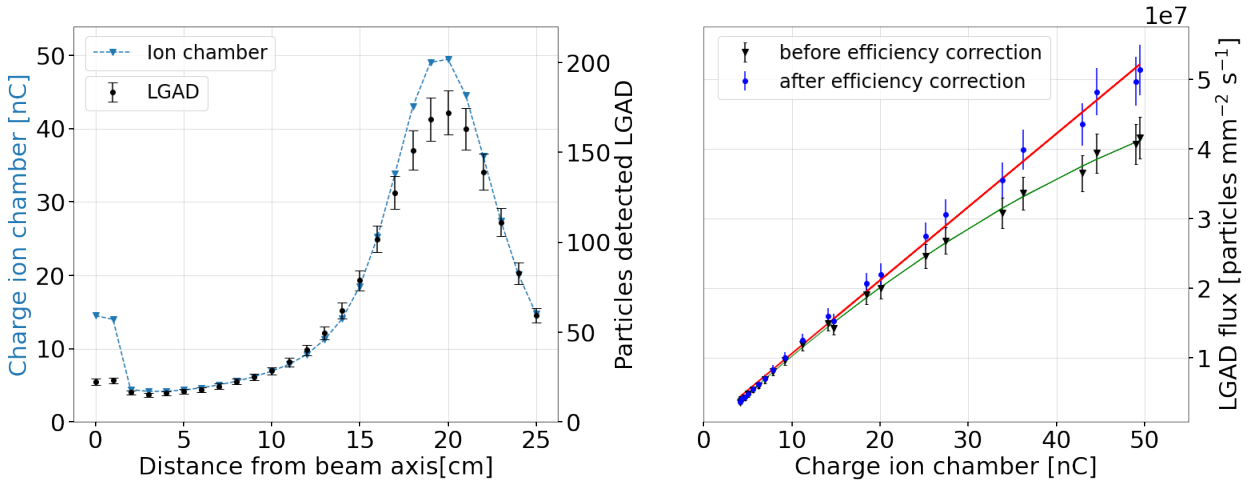

Figure 3.21: Left: comparison between the charge measured by the ion chamber and the average number of particles per pulse measured by the LGAD, as a function of detector position. Right: correlation between the ion chamber and LGAD, before and after an efficiency correction for high fluence rates. The error bars indicate the RMS on the number of particles detected averaging the data collected for 200 LINAC pulses.

4. The candidate peak is required to be the highest sample inside a window of ± 3 ns. This time interval (corresponding to ± 12 samples) is chosen by inspecting isolated signals: it corresponds to the typical time after which the pulses are 50% of their maximum height.

The system collects the time-stamp of an individual particle crossing the detector, T, defined using a 60% CFD (explained in section 1.1.4). As already reported in section 3.3.3, in these operating conditions, the LGAD has a time precision of about 50 ps.

Although the typical high SNR of LGAD allows an efficient particle identification of events isolated in time, when the time spacing between consecutive particles crossing the detector becomes significantly lower than the width of the signal pulse (around 10 ns), the identification efficiency decreases. An ulterior observation of Fig. 3.20 proves that the reconstruction algorithm can fail for overlapping signals (e.g. between 4010-4020 ns). The average number of particles found in a single LINAC cycle as a function of detector position is compared to the ion chamber results in the left panel of Fig. 3.21. Although the shapes of the two curves are similar, at high fluence rates we see an inefficiency due to the intrinsic limit of the algorithm described above in the discrimination of overlapped signals.

By construction, the identification algorithm rejects at least one of the pulses whenever these are closer than 3 ns. Conversely, when peaks are separated by more than 10 ns, the algorithm is

fully efficient. On average, the algorithm fails when consecutive particles pass through the detector within 6.5 ns of each other. The probability of this occurring is described by $\exp(\frac{-6.5}{\tau})$, where τ time between consecutive particles, expressed in ns. This equation defines an efficiency correction. The right panel of Fig. 3.21 illustrates the correspondence between the charge recorded by the ion chamber and the number of particles observed in the LGAD, with and without this efficiency correction. Before the correction, the response can be modelled with a second-order polynomial; after the correction, a linear response is observed. To correct for the detectors geometrical orientation and shape of the active area, an ulterior interpolation had to be implemented. The LGAD data set were in fact subjected to a linear interpolation to be properly compared with the ones of the ionizing chamber. To select the two dependent shift coefficient, the algorithm was designed to scan an array of values and, subsequently, obtain a minimum $\chi 2$ estimation.

The results prove that counting particles with the LGAD gives equivalent information to integrating the charge. However, the new detector operates as a single-quantum detector: while working with fluence-rates smaller than 100 MHz, the detector can resolve single electrons with a time resolution of about 50 ps, corresponding to the precision with which the leading edge can be measured. In Fig. 3.22 the reader can observe a schematic representation of the single particle counting algorithm implemented.

3.4.3 Characterisation of the LINAC beam

The excellent time resolution and linearity of the LGAD allows the study of the dose delivered by the LINAC as a function of time within the single pulses. To study the temporal profile of the beam intensity, the number of particles recorded at all detector positions was summed and plotted as a function of time. As displayed in Fig. 3.23, the fluctuations of the delivered dose observed within the pulses structure scale accordingly with the charged particles flux. The curve approximates the nominal square pulse shown in Fig. 3.10 but the precision of the LGAD allows a sub-structure to be clearly observed. As an additional result, the width of the pulse result to be smaller than nominal at $2.85 \pm 0.01\,\mu$s. Another analysis that was pursued aimed to investigate the train sub-pulses composing thee microsecond LINAC pulse (see Fig. 3.10).

As the medical LINAC operates with a radio-frequency of 2.858 GHz, the sub-pulses (each

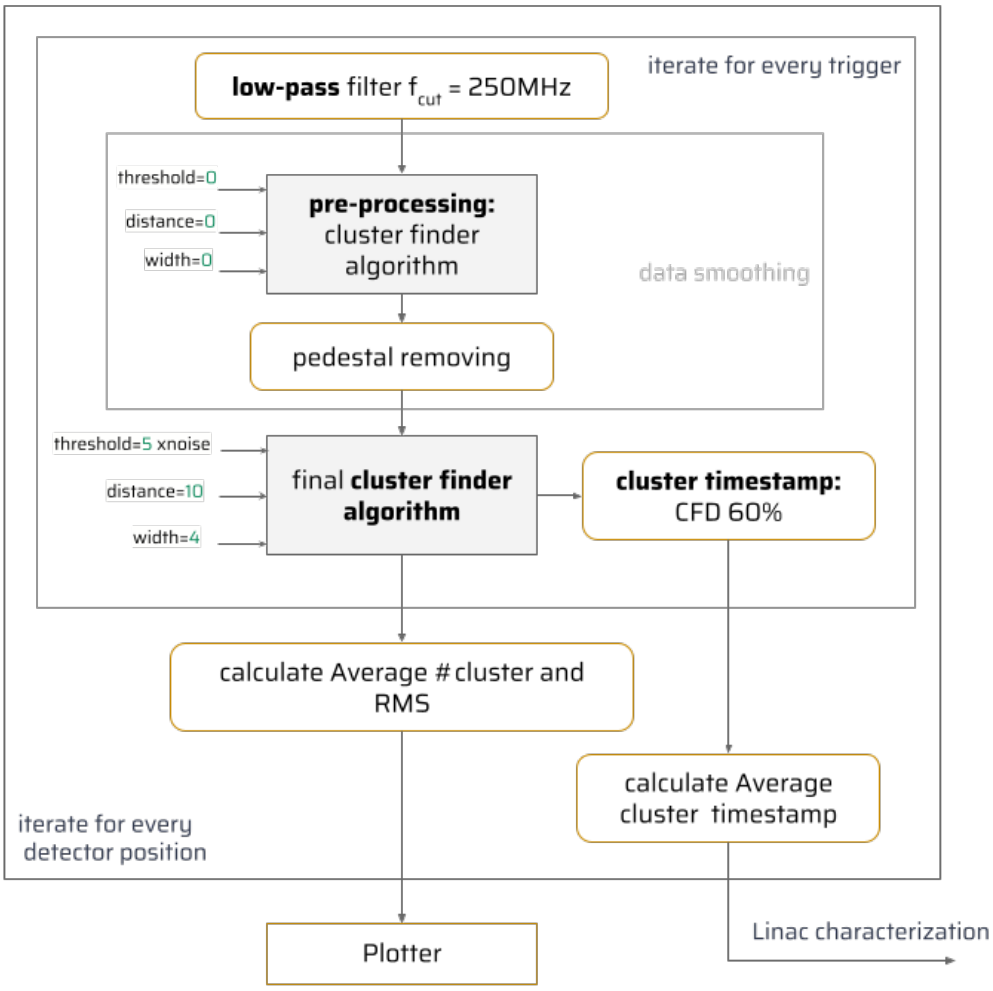

Figure 3.22: Simplified diagram highlighting the crucial point of the single particle counting algorithm.

expected to have a nominal width of 30 ps) have to be separated by 350 ps and, as long as all the other parameters of the machine have a small jitter, the LGAD resolution should be enough (50 ps) to observe their structure. The bottleneck of the measurements comes from the large timing uncertainty of the acquisition trigger, nominally the time between the thyraton trigger signal and the arrival of the LINAC beam (shown as the purple and yellow traces in Fig. 3.16). In the absence of a precise trigger and to reduce potential decoherence over several hundreds of ns, the sub-pulse structure was searched for using the distribution of the difference between the time-stamps for consecutive particles crossing the detector, ΔT, which is shown in Fig. 3.24 (left). It's important noticing that using the difference between consecutive particles, quick variations of the flux de-

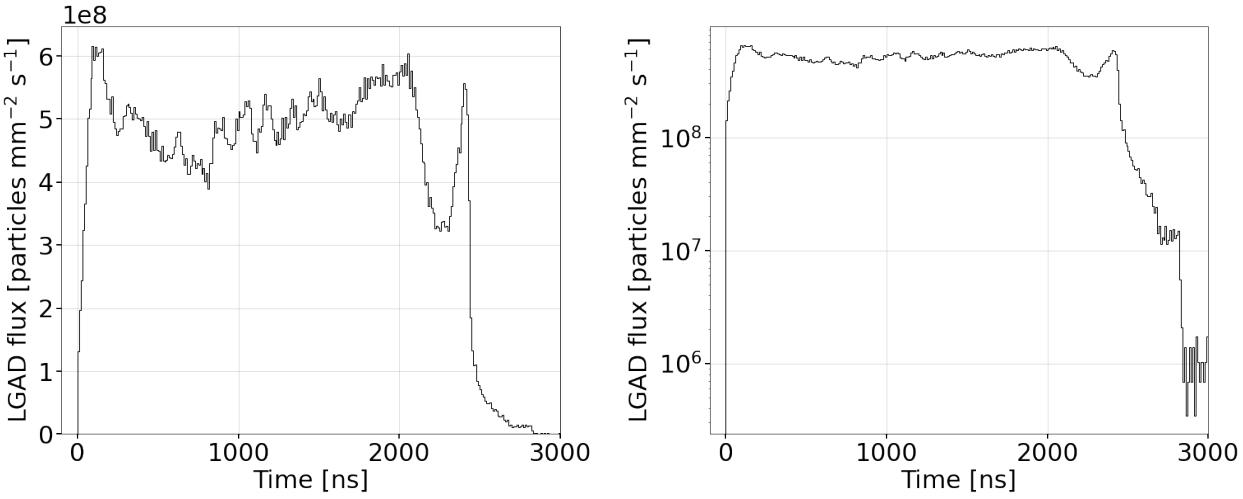

Figure 3.23: Particle fluence-rate recorded and summed over all position expressed as a function of time. In the right panel, the data are presented in log scale.

tected can be identified with more precision.

The distribution of independent, Poisson-distributed events can be described with an exponential $e^{-\frac{t}{\tau}}$, where τ is the mean interval between consecutive detected particles. This shape is subjected to modifications coming from the reconstruction inefficiencies of the particle-finding algorithm. Its response deteriorates for $\Delta T < 10\,\text{ns}$, while the requirement for a local maximum within $\pm 3\,\text{ns}$ implies that no two particles have ΔT below this value. After binning the data in steps of 10 ps, the algorithm computes the modularity in the distribution and calculates the autocorrelation function expressed as:

$$R(\tau) = \frac{1}{N-\tau} \sum_{i=1}^{N-\tau} y_i y_{i+\tau}, \tag{3.7}$$

where y_i is the number of entries in bin i.

The autocorrelation results then in a coarse-grained exponential structure (coming from the shape of the ΔT) superimposed to a fine-grained sinusoidal pattern. After subtracting the exponential trend, the sinusoidal structure becomes evident: Fig. 3.24 (right) shows the autocorrelation as a function of τ. Its periodic structure can be fitted using a modulated sine function with a measured period of $346 \pm 3\,\text{ps}$, consistent with the operating frequency of the LINAC of 2856 MHz. Thus, in addition to observing the large-scale $\sim 3\,\mu$s-wide structure of the LINAC pulses that approximate to square waves, the detector is capable of resolving the individual 350 ps-wide sub-

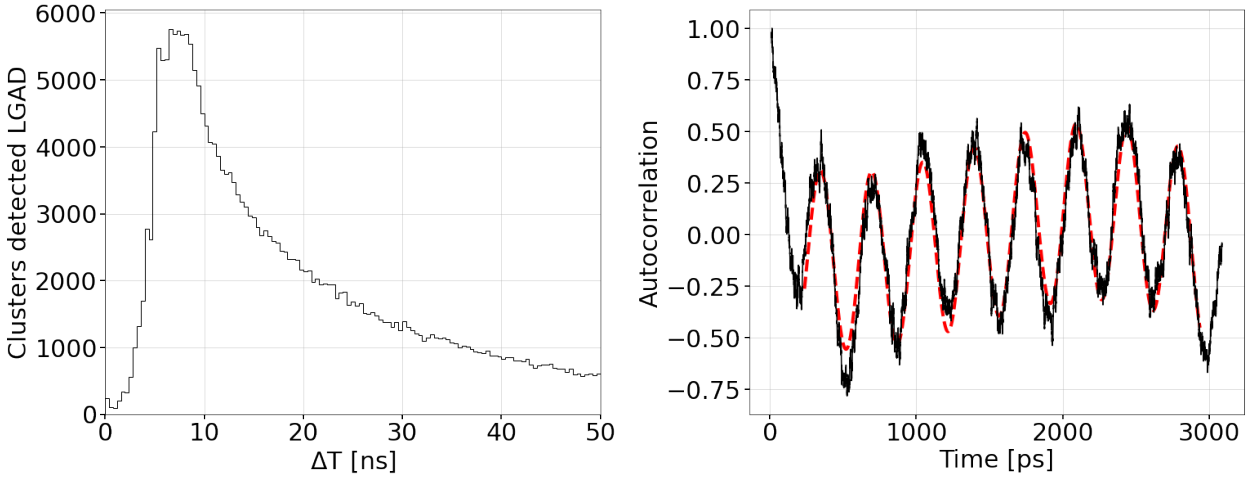

Figure 3.24: Left: Distribution of the time-stamp difference between consecutive particles crossing the detector. Right: autocorrelation fitted results with a modulated sine function.

pulses in the beam.

These tests represent the first proof of concept for the design of dosimetric detectors of new generation. The capabilities of fast integrating devices open the possibility to investigate the temporal structure of the dose delivered by medical accelerator. Small variations over time can be observed with unprecedented accuracy when using single particle detection techniques. At the same time, the typical size of silicon the silicon detectors employed improves the spatial resolution of traditional dosimetric tools, while at the same time reducing the detected rate per channel. The characterization of fast radiation sources is of crucial importance for monitoring the novelties of FLASH radiotherapy machine, where the typical pulses are designed to be contained within few ns.

3.5 Chapter summary

This chapter describes the first use of an LGAD for monitoring the beam profile of a medical LINAC. After an introduction on dosimetry and dosimetric quantities, the chapter provides an overview over the most common accelerating technologies used in medical physics for cancer treatment and diagnostics. The next sections are dedicated to the description of the tests and results obtained at the Saint Luke's hospital in Dublin, Ireland, in collaboration with the UCD. The hospital facility offered the possibility to perform a series of test on a dismissed ELEKTA (161)

LINAC, characterized by an electron pulse repetition frequency of 200 Hz and dose rates output up to 600 MU/min. Each of the 3.2 μs long pulses contains thousands of 30 ps long sub-pulses, separated by 350 ps (frequency of 2.858 GHz).

To monitor the 6 MeV electron beams output by the source, an LGAD sensor designed for HEP experiment was used. The sensor was mounted on a read-out electronic board developed at KU. During the data collection, performed with the use of a fast digitizing oscilloscope, the detector was employed to detect the passage of individual particles, effectively measuring the electrons fluence on the sensing area. At the same time, the analysis of the LGAD response provides an evaluation of the total collected charge. The integrated charge represents a standard dosimetric quantity that served for a comparison with the response of a traditional ionization chamber. Conversely, the study of absorbed radiation using single particle counting at high collected rates (up to 100 MHz) produced unprecedented results. The analysis results proved the possibility to monitor the temporal profile of the beam with a resolution of about 50 ps, highlighting the features of the dose distribution spectrum (otherwise hidden when using traditional charge integration methods). Additionally, the detector single particle resolution allowed to resolve the periodic structure contained within individual LINAC spills. The measured period was measured to be 346 ± 3 ps, consistent with the LINAC's nominal features.

The reported measurements represent a cornerstone for the development of fast dosimetric devices for beam monitoring. In particular, the commissioning of FLASH radiotherapy machine will require in depth studies of the dose delivered prior to their used in clinical treatments. To address the problematic raised by the increased dose-rates, novel fast silicon detectors for dosimetric applications are currently under study.

Chapter 4

Particle Identification in space: the AGILE project

This chapter presents the work that led to the development and first results of the AGILE (Advanced enerGetic Ion eLectron tElescope) detector, which proposes the study of particle and ion abundances using a novel technology for particle identification in space. The low power and compact instrument is built to be encased inside of a CubeSat (166) which constrains the setup to a tight geometric form factor and limits the absorbing material to a few thin layers of active volume. The detector uses a Pulse Signal Discrimination (PSD) method (introduced in section 4.2.3) to label the incident particles. Its novelty resides in the capability of real-time, in-situ identification. The wide range of energies (1 - 100 MeV/nuc) and species (H to Fe) the experiment targets to reconstruct makes it a unique tool for studying the intensities and energy spectra of charged particles originating from solar, distant heliospheric, and galactic sources.

4.1 Scientific motivation

The need for the development of a robust, space-based, real-time instrument for particle identification comes from the lack of high-quality measurements that could advance the understanding of charged particle energization, loss, and transport throughout the heliosphere. Unfortunately, the characterization of solar, magnetospheric, and cosmic ray particles do not pose an easy task. It requires the instrument to be sensitive to a large variety of particles and ion species: the measurement of interplanetary ions is critical to the understanding of Solar Energetic Particles (SEP) and Anomalous Cosmic Rays (ACR) (described in section 4.1.3 and section 4.1.2, respectively). This operation is further complicated by the wide energy spectrum the acceptance of a space-based detector needs to cover. The possibility to unambiguously resolve ion isotopes and achieve a reliable discrimination between electron and protons is of crucial importance for promoting a stronger understanding of the acceleration and transport of charged particles in the inner and remote he-

Science goals	objectives	measurement
Dynamics of the radiation belt	determine the presence characterize electrons in the inner zone	intensities and spectra of $\sim$ 1-10 MeV electrons
	characterize trapped and transient energetic ion populations in the outer zone	intensities and spectra of $\sim$ 2 - 100 MeV/nuc ions (H to Fe)
Study energization, transport and modulation of IP charged particles	study SEP and energetic storm particles (ESP) energization at IP shocks	
	study ACR transport and modulation	
Understand the role of energetic particles in space weather	study proton and ion cutoffs during geo-magnetically disturbed times	

Table 4.1: Overview of AGILE science objectives.

liosphere. Also important for investigating the question of relativistic electron injection (detailed in section 4.1.1) into the inner zone of the magnetosphere, which remains currently an open and controversial topic (45). Table 4.1 summarizes the science goals that will be addressed in the next sections.

4.1.1 The Radiation belt

After being theorized by James Van Allen, the presence of a zone rich of energetic charged particles enclosed by the planets magnetosphere was confirmed in the results collected by Explorer 1 and Explorer 3 in early 1958 (167). In the case of Earth, those particles are generated from the stream of charges released from the upper atmosphere of the Sun (solar wind). They are then trapped by the inner region of Earth's magnetic field, creating two belts extending from an altitude of about 640 to 58,000 km above the surface. Figure 4.1 illustrates a representation of the Van Allen belts surrounding the Earth magnetosphere. Mainly, electrons and protons populate the belts, while the abundance of other species of ions and nuclei are greatly suppressed. In particular, the presence of protons with energies exceeding 100 MeV dominates the inner belt, where

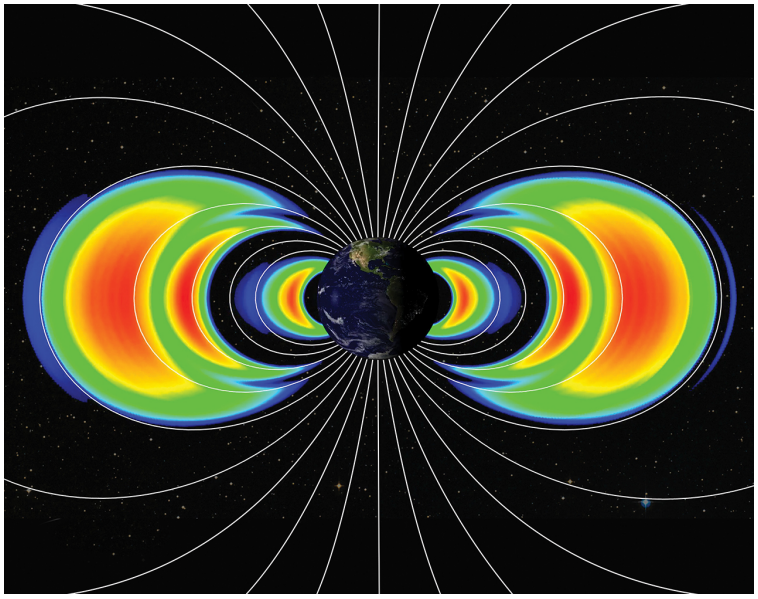

Figure 4.1: Visual representation of the Van Allen belts contained in the Earth's magnetosphere. In this image, one can observe an inner and outer zone as well as a third, transient radiation belt. The latter was discover in 2013 and its presence lasted four weeks, before being destroyed by an interplanetary shock wave originating from the Sun. Image Credits: NASA's Goddard Space Flight Center/Johns Hopkins University, Applied Physics Laboratory.

the more intense magnetic zones constrain their trajectories. The area extends from an altitude of 1,000 km to 12,000 km. Until the 1990s, the data showed high concentrations of electrons with energies that could only reach hundreds of keV. Some studies have attempted to model the presence of relativistic electrons (more than MeV) attributing it to injection mechanism from the outer belts during periods of strong geomagnetic activity (168), while their possible detection was limited by a shorter mean lifetime (less than one year) when moving through the inner zones (169).

Following missions (CRRES (170) in 1992, SAMPEX (171) 1994, POLAR in 1995) have proved that many of the original models describing Earth's radiation belt electrons had to be modified to match such results. Although the launch of NASA's Van Allen Probes mission in 2012 (172) finally provided a reliable instrument for the inner belt electron dynamic studies, the irreducible background coming from the high concentration of protons penetrating the instrumentation shielding produces easily misidentified signatures. Relativistic electrons have remained undetectable until 2015, when the Van Allen Probes provided upper limits on their energy spectra (31). Those intensities are reported in Fig. 4.2, which shows the results obtained during the studies pursued by REPTb. To be considered as a signal event, the experiment requires the incident particles to be

included in its field of vision and to stop in one of the layers present in the Si detector stack. Conversely, the background-like events result from high-energy protons where the trajectory comes from outside the fields of vision or electrons scattered out of the detector stack.

The electron-proton discrimination was explored, motivated by the difference between the measured energy distributions of electrons and protons. The idea of an elusive nature of relativistic electrons in the inner belt is additionally supported by the high-quality measurements of the MagEIS instrument. The data show no measurable intensity greater than 800 KeV (173), indirectly confirming the validity of the upper limits set by the REPT Collaboration (31). The resulting measured fluxes are significantly lower than those predicted by widely accepted theoretical models (AE8 and AE9 (174)). Since the Van Allen Probes have been operating exclusively during times characterized by a low solar activity, the data proved that no significant enhancements of relativistic electrons in the inner belt are expected in the absence of extreme solar wind conditions (175).

The dynamics of the outer belt differs remarkably from the one described for the inner zones. In this region, that extends 13,000 to 60,000 km above the planet surface. The electron radiation belt is mostly produced by the process of inward radial diffusion (176; 177) and by the mechanism of local acceleration (e.g. interaction with plasma waves). The particle abundance is balanced by continuous losses: outward radial diffusion, collisions with the atmospheric particles, losses to the magnetopause. The magnetopause locates the outermost boundaries of a planet magnetosphere, indicating the area of interface between the edges of its magnetic field lines and the front of the solar wind. Inside this toroidal-shaped outer belt the particle abundance constantly varies as it is significantly more exposed to magnetic disturbances.

Its radiation density changes in the presence of geomagnetic storms, energization due to radial transport and high-speed stream (HSS) (178); acceleration of particles caused by the tail of the magnetosphere. Contrarily to the inner belt, the presence of other species of particles in the outer zone is quantifiable. This area is in fact rich of protons and a variety of energetic ions (with a composition similar to the one of the ionosphere); the latter suggests multiple sources of origin for the radiation spectrum. The additional contribution is known to come from high-energy heliospheric particles with sufficient rigidity to penetrate the magnetopause and get trapped in the outer belt. The presence of Anomalous Cosmic Rays (ACRs) will be explained in the next sections 4.1.2. The AGILE project proposes the study of the populations of the two belts.

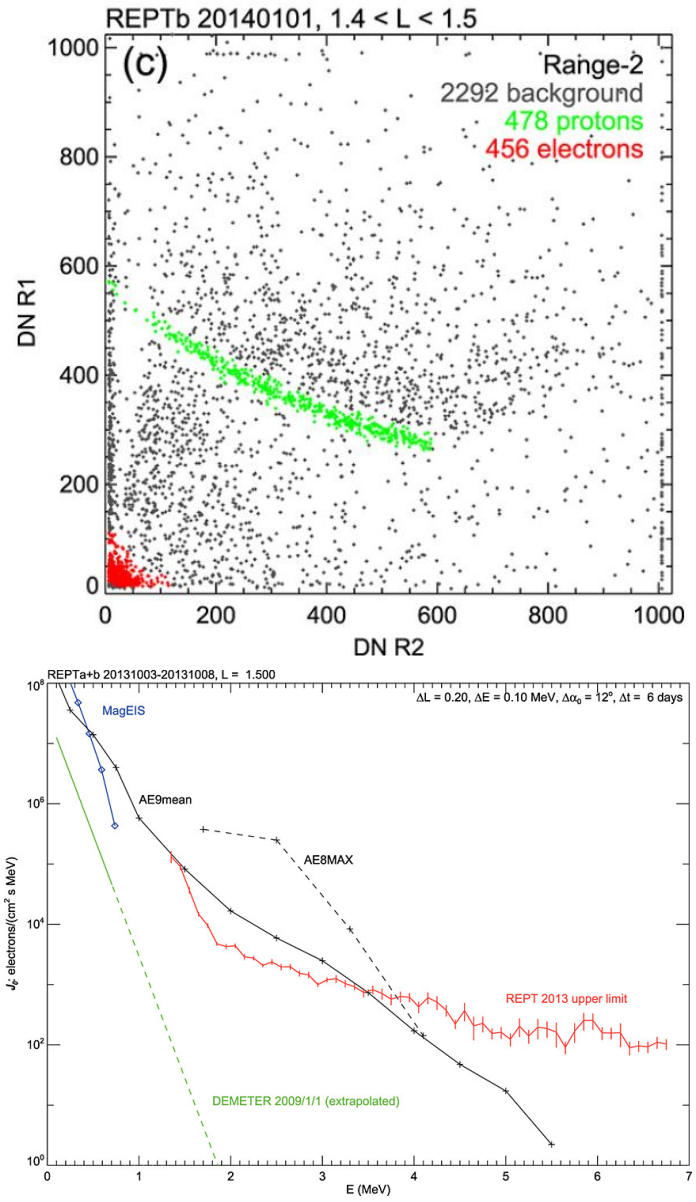

Figure 4.2: Top: results for the pulse height discrimination method used by REPTb to identify electrons-protons in the 1 January 2014 dataset. The ordinate and absiccsa report quantities (DN) proportional to the energy deposed in the R1 and R2 Si detectors (31). Bottom: overlapped plots of the omnidirectional equatorial electron energy spectra in the inner belts. The REPTb data set a new upper limit on the electron intensity, as the data are contaminated by high-energy protons penetrating the instrumentation.

- **Inner radiation belt** Using a robust technique for particle discrimination and energy reconstruction leads to a proper quantification of the inner-belt proton contamination in the data. This helps shedding light onto the dynamics of this zone (179). An accurate identification could unambiguously and unprecedentedly answer the question of the presence of relativis-

tic electrons (>1 MeV) and their behaviour as dictated by the geomagnetic activity. These results would complete prior investigations (180), which have been limited by the proton background. Collaterally, this measurement would help evaluating the damages to instrumentation and satellites caused by deep dielectric discharging due to MeV electrons in the inner belt region.

- **Outer radiation belt** the experiment could contribute to a better understanding of the outer radiation belt electron dynamics, and help examining the nature of their various competing acceleration, transport and loss processes. The range of possible detectable electron energies (1 - 10 MeV) and the instrument identification capabilities would aid in the separation of competing local accelerating mechanisms (solar storm events (181), Coronal mass ejection overlapping and high-speed stream (178)) and quantify their relative contribution to the electrons energization.

4.1.2 Anomalous Cosmic Rays

Anomalous Cosmic Rays (ACRs) contribute to the ion abundance in the heliosphere. This was first observed by Fisk et al. (182), during their studies conducted in 1974. In this measurement, the oxygen-to-carbon (O/C) and helium-to-oxygen (He/O) ratios are computed, and the anomalous results (about 20 in the first case, and approaching the unity in the second) are combined with the preexisting knowledge of the oxygen intensities, increasing with the heliocentric distance. These studies have concluded that the excess of observed ions did not originate on the Sun.

The origin of anomalous cosmic rays is attributed to neutral interstellar particles drifted into the heliosphere. The outward flow of the solar wind allows only neutral particles to enter its front, excluding any thermal interstellar ions. Here, they are ionized by the wind and accelerated by its termination shock up to tens of MeV/nuc (183). This process explains the lower abundance of ions such as C, Mg, Si and Fe in the ACRs composition: due to their relatively low first ionization potential, the interstellar medium's thermal energy is often enough to ionize those elements and, consequently, never reach the termination shock. Due to their singly-charged nature, these atoms can penetrate the Earth's magnetosphere. If their trajectory reaches the residual atmosphere, they can be further stripped off their charges. Therefore, these atoms are trapped in the outer radiation

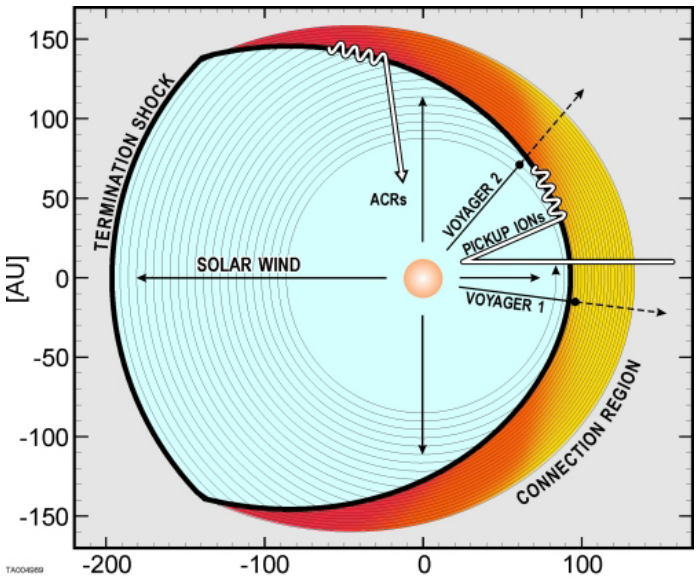

Figure 4.3: The image provides a schematic of the magnetosphere, sectioning through the termination shock at the equator. The sketch includes the path of the ACRs getting trapped in the outer zone of the magnetic lines (32).

belt. A simple visual sketch is provided in Fig. 4.3.

Early direct observation of their composition can be found in (184), where the models of energy spectra of 11 elements (H, He, C, N, O, Ne, Mg, Na, Si, S,Ar) are fitted and compared to the data obtained in the outer heliosphere by the Voyagers 1 (V1) and 2 (V2). In particular, the publication focuses on the neutral density of Ar in the interstellar medium, analyzing the detected quantity of the ionized element and tracing it back to its initial abundance at the location of the termination shock. The results, used to derive the neutral densities of the other ions under studies, highlight the need for additional sources of ACR ions other than interstellar atoms (pickup ions). The composition of ACRs is the source of many astrophysical debates, such as the abundance of interstellar neutral particles or the ionization state of the local interstellar medium.

The AGILE scientific program includes the possibility to perform precise measurements of their abundance in the outer radiation belt. The anomalous ions species trapped by the magnetosphere, deepening the understanding of their dynamics within the solar system (fractionation in the abundances in the heliosheath[1], interplanetary ionization process, and in the injection, acceler-

[1]Locates the zone where the solar wind starts interacting with the interstellar medium. It can be divided into three different regions: the innermost is the termination shock, the outermost heliopause and the area in between the boundaries.

ation, and interplanetary propagation processes). At the same time, accurate particle identification would help in the understanding of hidden properties of the heliosphere as well as the nature of interstellar material.

4.1.3 Solar Energetic Particles

Carrington, during his long lasting studies over the already known Sunspots[2] (185), came across the observation of patches of intensely white lights which he described as 'Singular Appearance seen in the Sun'. The event was later understood to be a solar flare, caused by accelerated charged particles (mainly electrons) in close proximity to Sunspot clusters and interacting with the plasma medium. The effect results in sudden flashes of increased brightness on the Sun surface, detectable in the total solar irradiance spectrum. The radio fade-out occurred in 1936 (as described in (186) and (187)) in correspondence to bright eruptions in the solar chromosphere ultimately explained the phenomenon witnessed by Carrington eight decades earlier: the X-rays generated in solar flares can enhance the ionization density in the Earth's ionosphere which, in turn increases the absorption of radio waves (188).

Flares are thought to be associated with the violent ejection into the heliosphere of plasmas and particles originating from the Sun Corona. These phenomena are formally known as Coronal mass ejections (CMEs). Both effects can result in the production of protons, electrons and ions (He - Fe) showers reaching the Earth with energies between KeV and GeV. These showers are commonly referred to as Solar Energetic Particles (SEPs). These events can be classified in two main categories, based on the acceleration mechanism guiding their trajectory through the interplanetary space: Impulsive and Gradual SEPs. In the first case, the particles are accelerated by solar jets (supposedly created in correspondence of flare events[3]), while the second happens whenever the mass ejection of the Sun Corona move faster then the ambient solar wind. In this case near-Sun CMEs shocks drive strong interplanetary (IP) shock waves.

The scientific community needed decades of studies and experimental results to identify the presence of two competing sources for SEPs (189). The observation on ground level enhancements

[2]Dark areas which are observable on the Sun photosphere. These temporary events highlights zones affected by a high concentration of magnetic field flux that hinders convection.

[3]While historically the flare regions have always been considered the main source of impulsive SEP, modern studies explain how the magnitude of these events can hide additional, correlated phenomena (solar jets) that could better model the particle transportation. The topic will be discussed later, in this section.

(GLEs) displayed that gradual events generally lasted for several days, exhibiting larger radiation fluences and populating a vast range of longitudes. On the contrary, the impulsive (jet-related events) lasted a few hours and were characterized by a smaller flux. Unfortunately, since CMEs and solar flares often happen during the same event, occurring whenever a nearby active region erupts, the precise origin of the remotely accelerated SEPs is highly debated. Additional dissimilarities between the classes of SEPs can be found in their compositions.

4.1.3.1 Gradual SEP

This class of events is proton-rich and usually more gradual in the decay and offset of its effects. Studying their diffusion (described in Eq. 4.1) one can infer that, since the particle transports vary as a power of A/Q (mass and charge), the density of different species populations will be conserved, although their distribution will vary over time (190).

$$n_x(r,t) = \frac{1}{4\pi\Gamma(\varepsilon)} \left(\frac{\varepsilon}{3}\right)^{2\varepsilon-1} \left(\frac{3}{\Lambda_0 v t}\right)^{\varepsilon} exp\left[\frac{-3r^{2-\beta}}{(2-\beta)^2\Lambda_0 v t}\right] \tag{4.1}$$

We can analyze the diffusion of particles belonging to two species X, and Y with velocity v, scattered with mean free path $\Lambda_{X,Y}$ and assuming a power-law dependence on radial position r ($\Lambda_0 r^{\beta}$). Being $\varepsilon = \frac{3}{(2-\beta)}$ and $\beta < 2$, the particles transport can be modeled using equation 4.2 and finally recover the A/Q dependency. The relative abundance of different species of ions can be inferred from:

$$L = \frac{\Lambda_X}{\Lambda_Y} = \left[\frac{A_X/Q_Y}{A_Y/Q_Y}\right]^{\alpha} \tag{4.2}$$

This conservation of the elements species allows to average their abundances over many gradual SEP events and to obtain an estimation of the corresponding abundances on the Sun Corona. Figure 4.4 depicts the intensities of a set of species (C, Ne, Fe) for three gradual SEP events, using different solar longitudes. The increase in intensity of energetic particles (above 0.05 MeV/nuc) due to the passage of an IP shock associated with a gradual SEP is commonly referred to as an energetic storm particle (ESP) event. It is to be noted that the effects of the particle transportation through the IP medium caused by their near-Sun site of acceleration and inner heliosphere is negligible during ESP events. The information carried by the latter is therefore of crucial importance

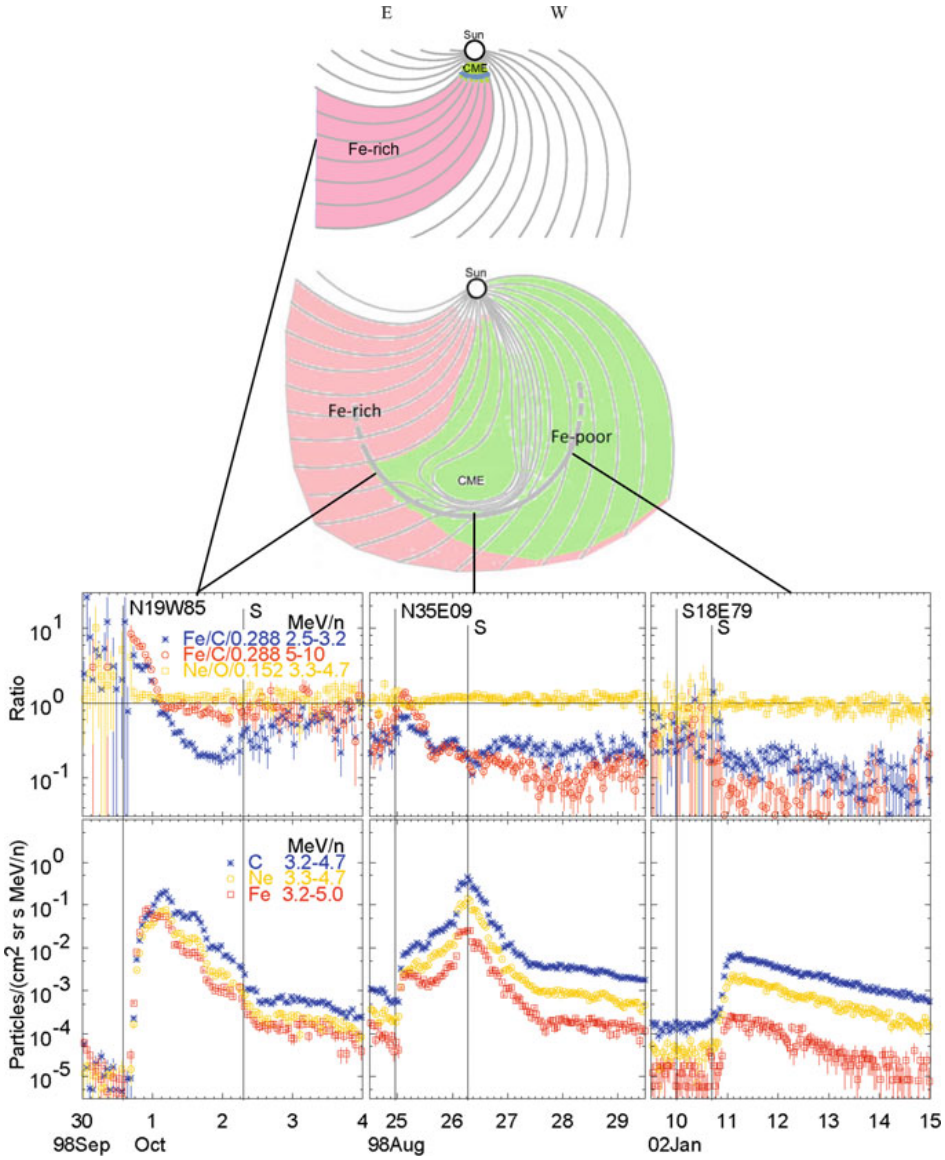

Figure 4.4: The relative abundances of three species (C, Ne, Fe) is plotted as a function of time (33). The initial enhancement in the Fe/O ratio decreases with time as the Fe (higher A/Q) scatters less than the oxygen atoms. The three panels refers to different solar events, which evolution is illustrated in the top section of the image.

in the characterization of the shock properties, the particle source and underlying acceleration mechanisms. Like gradual SEP, more recent studies of ESP (191) highlight an A/Q-dependency in their transport, where its efficiency decreases when accelerating heavy ions. In (34) is also reported that, in the case of high energetic ions (> 10 MeV/nucleon), the ratio of heavy-to-light abundances (Fe/O) lessen with increasing energy. Figure 4.5 summarizes the above mentioned results for the various elements.

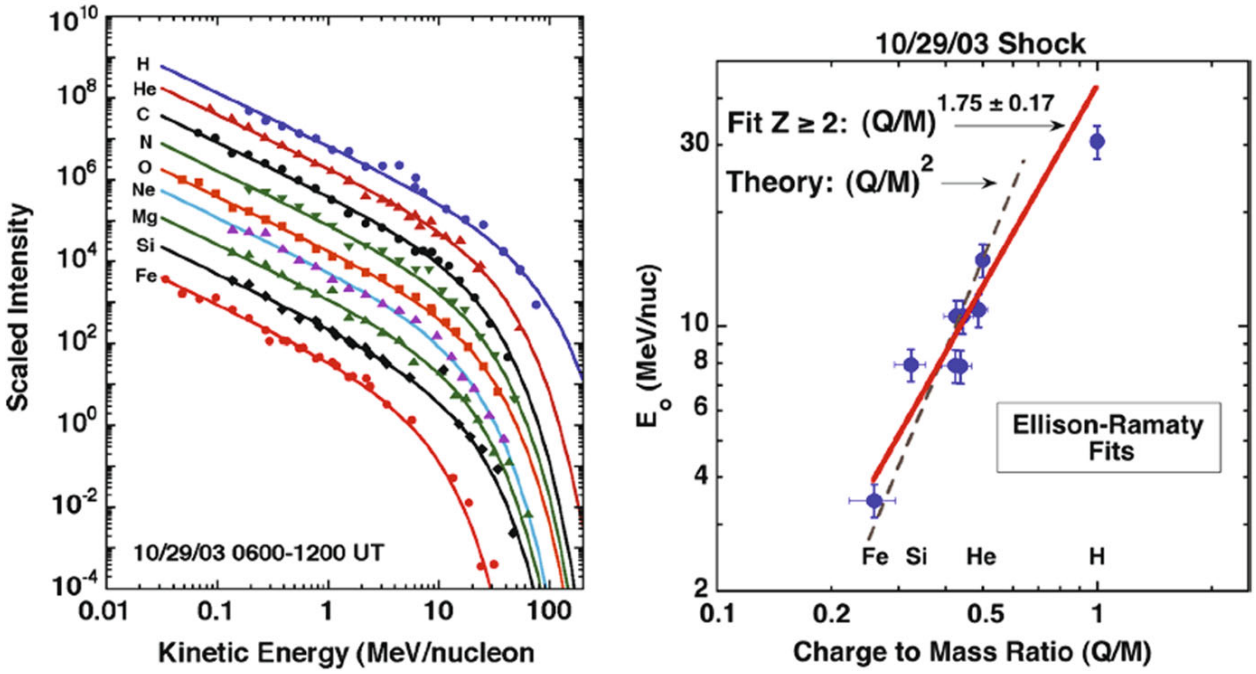

Figure 4.5: The left panel reports the scaled intensity for ions IP detected from ACE and GOES after the shock on October 29, 2003. In the right panel, their energy is plotted as a function of the mass-to-charge ratio and fitted using $\left(\frac{Q}{M}\right)^{1.75}$ for (Z≥2) (34).

4.1.3.2 Impulsive SEP

Early observations of SEPs composition have highlighted the flare-related events to be characterized by higher abundances of accelerated electrons, and by enhanced ^{3}He/^{4}He and Fe/O(C) ratios (192). The first one, in particular, stands out as it presents a 1000-fold increase over the solar wind abundance (^{3}He/^{4}He > 1 in contrast to the expected 5 $\times 10^{-4}$). The same relation can be found for atoms with 76 < Z < 82 when computing their ratio with Oxygen. During flare events, the observation of γ rays and neutrons spectrum gives a picture of the nuclear interaction occurring in the low solar Corona. The results show no evidence of primary produced ^{3}He and the reaction secondaries are often trapped in the flare loops.

This mechanism would then suggests that the ^{3}He acceleration source could be found in the reconnection of jet events which open field lines would allow the plasma to eject the particles in the diverging field (35). While we historically associate impulsive SEP events exclusively with flares, recent studies (193; 194) point out that the particle ejection mechanism needs to happen when the magnetic fields line are open, casting doubts on the correlation between SEPs and neighboring

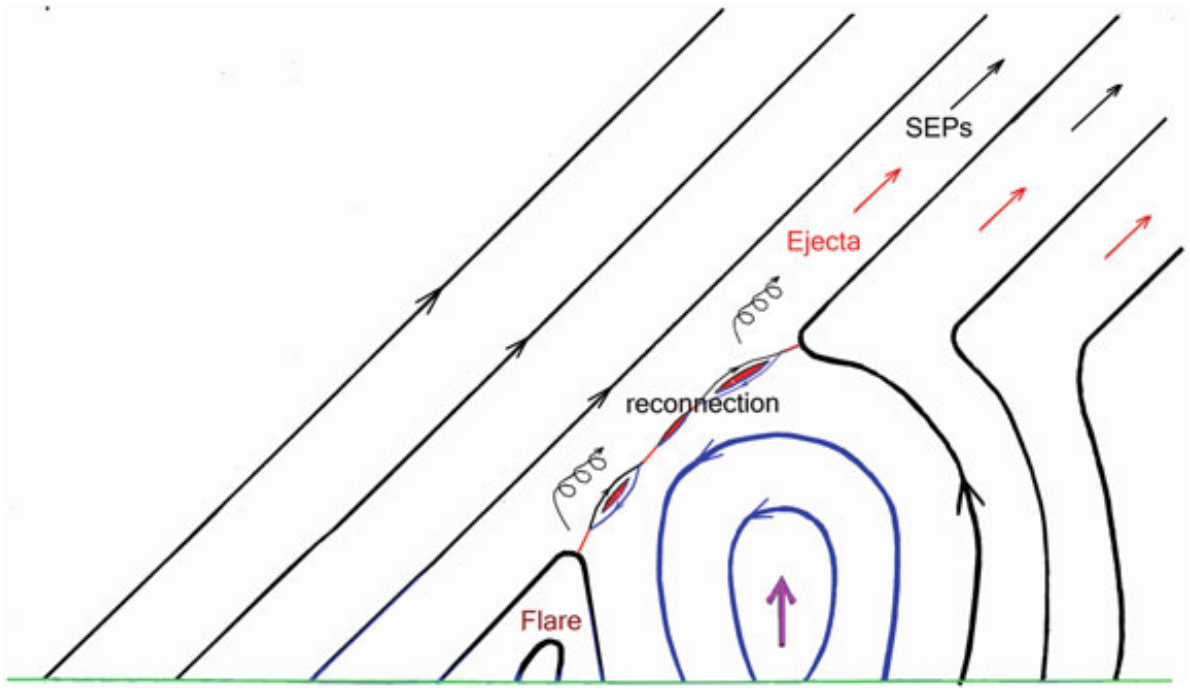

Figure 4.6: Magnetic lines of the Coronal plasma (in blue) reconnecting and producing a jet. Where the lines are open, energetic particles can be ejected.

closed loops (flares). A jet production event is schematized in Fig. 4.6. Additionally, the same results highlight how the steeper ^{3}He abundance enhancements witnessed correspond to narrower, more modest jet reconnections. These events are also characterized by a suppressed He/O and enhanced (Z>50)/O, which advocate for different transportation methods for the two populations. Competing with the theory explained above, previous investigations already accepted transportation models where the acceleration mechanics are explained with resonant wave-particles interactions. As the presence of different mechanisms favoring enhancements of heavy or light ions corresponding to the same event is suspicious, the source of impulsive SEP still represents an unsolved puzzle. The identification capabilities of AGILE allow for a precise investigation of the SEPs dynamics and their composition. The energy range covered by the apparatus opens the possibility to explore the detection and discrimination of ions coming from both types of accelerating events (gradual or impulsive), respectively proton-rich and ^{3}He-rich. The two accelerating mechanisms and the resulting intensities spectrum is detailed in Fig. 4.7. The analysis of their intensities will broaden the knowledge of those mechanisms on the Sun. It highlights important aspects such as relative abundances of elements and isotopes, electron/ion ratios, energy spectra, onset timing,

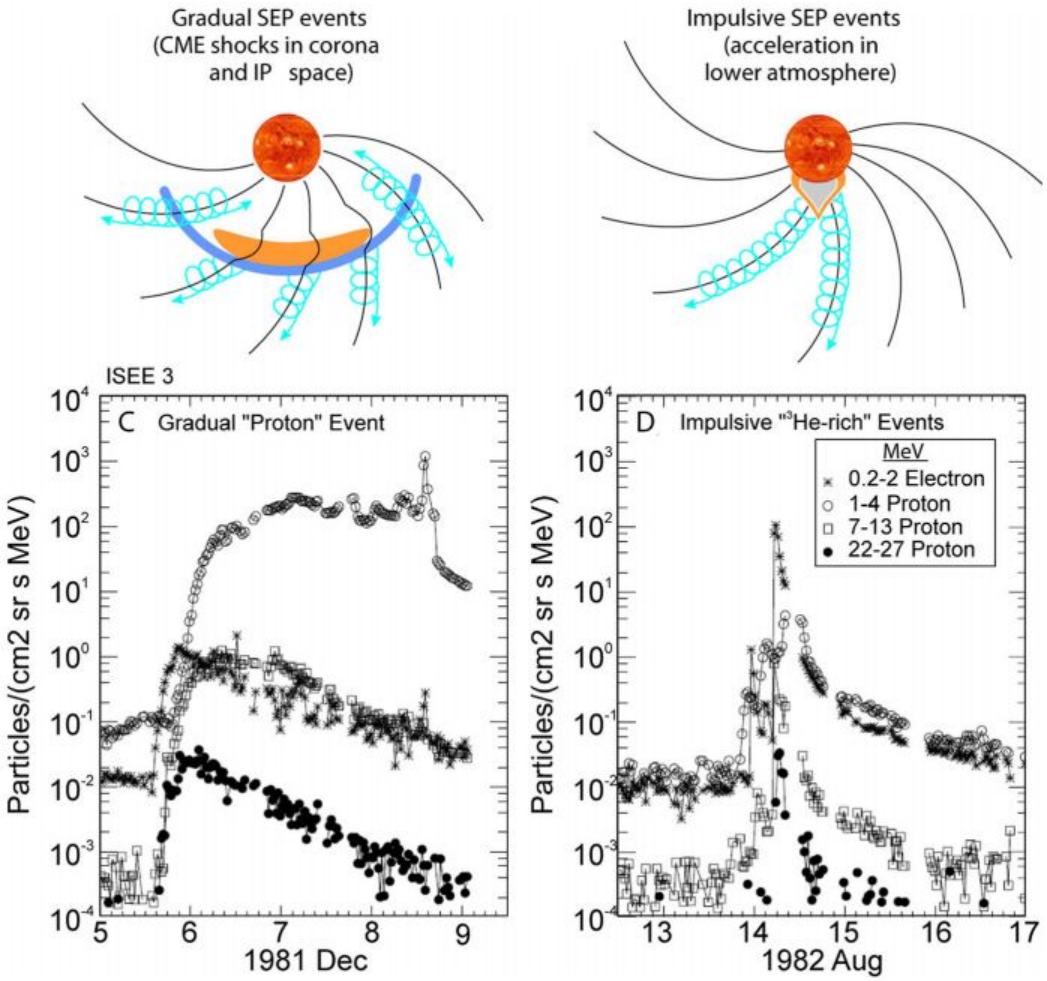

Figure 4.7: Cisual representation of the two type of known SEPs. The fluxes of electrons and protons that overlapped as a function of time is shown in the bottom plots (35).

duration, angular distributions, and their associations with visible solar phenomena. Figure 4.8 provides a simple scheme of how, SEP streaming through the interplanetary field, can be used to map its structure.

4.1.4 Space weather

The mechanism behind the processes responsible for modifying the conditions of the solar system is known as 'space weather'. Indeed, most of the phenomena affecting the Earth and its surrounding space can often be traced back to physical events on the Sun: plasma regions generated during violent solar events propagates through interplanetary space, frequently interacting with

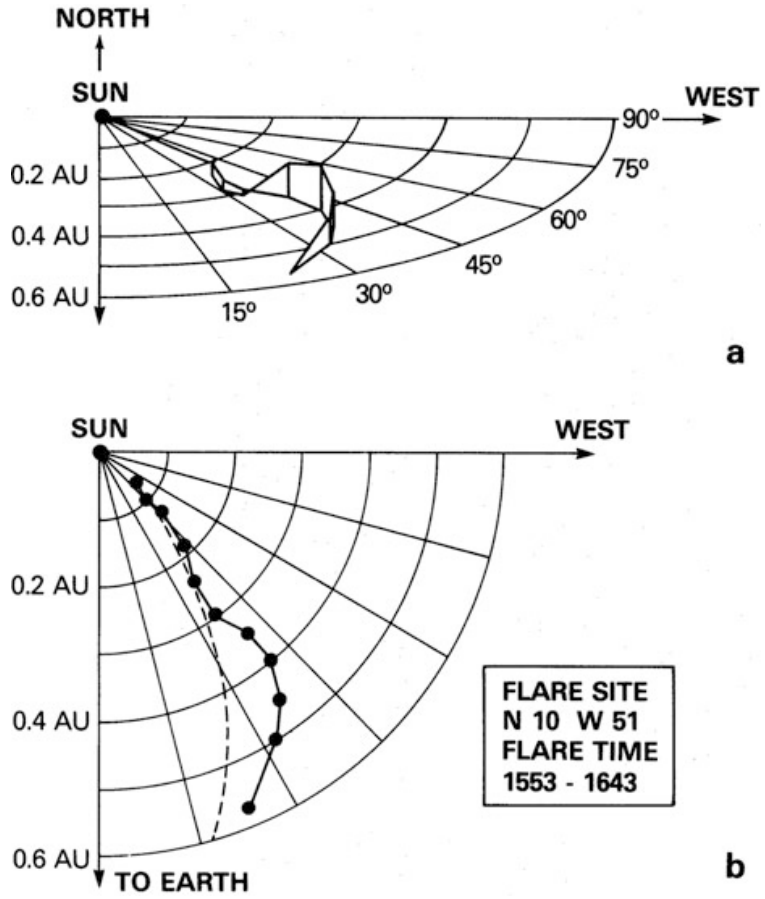

Figure 4.8: Path of the electron population following the ^{3}He ejected by a SEP event: the trajectory can be followed when the direction to the center of the radio signal, and its distance from the Sun it is known (determined by the frequency and models of the electron density vs. radius) (36).

the planet magnetosphere, ionosphere, thermosphere and exosphere. The atmosphere can also be affected, causing repercussion on terrestrial weather. Additionally, the threat triggered by direct and indirect interactions with ionizing, energetic charged particles has been proven to influence human operation on Earth and in space. The energy released during the reconnection of magnetic loops in the Sun Corona (CMEs, jets, flares 4.1.3) caused by heat convection flowing from the Sun outer layers, generates strong open magnetic lines responsible for the transportation of energetic particles outside the heliosphere. The resulting magnetic energy is believed to be the mechanism that superheats the Corona and makes it unstable to the Sun gravitational pull (37).

The expelled material, namely the solar wind, can be projected into interplanetary space with different speed and create zones of low and high pressure. Regions where high-speed streams go into a low-speed stream creating zones of compressed solar wind are called Stream Interac-

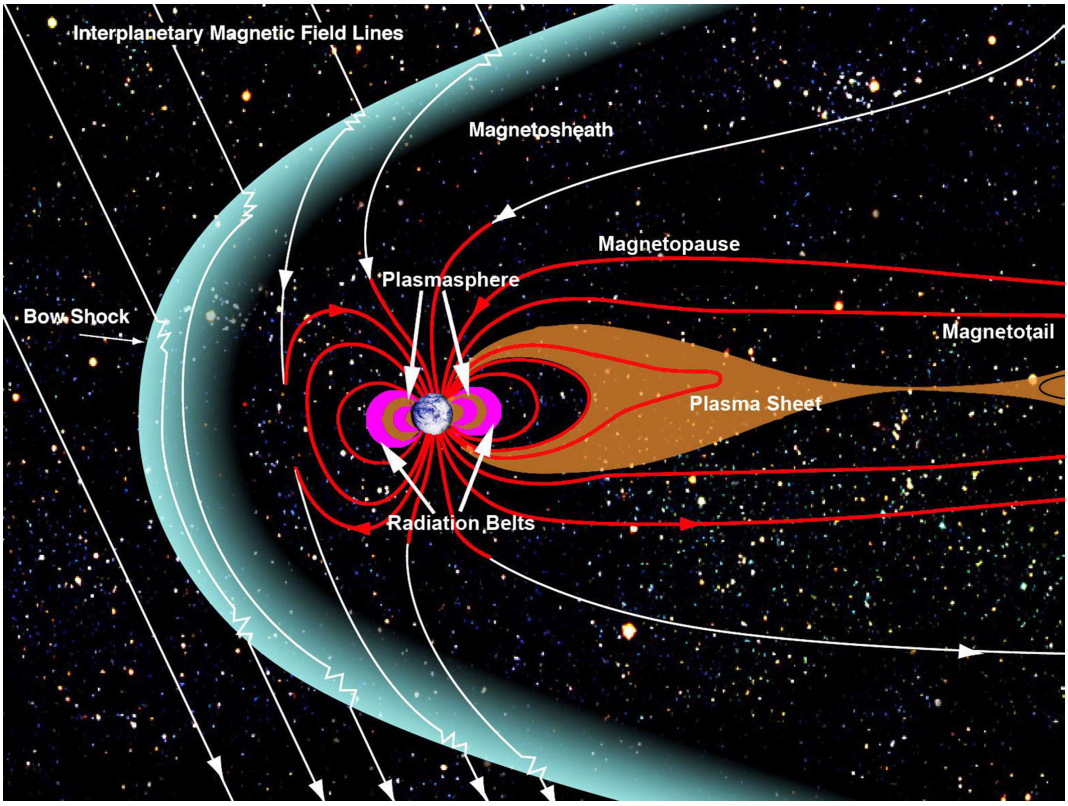

Figure 4.9: Internal structure of the diamagnetic cavity generated from the interaction between the planet magnetic field and the incident solar wind (37). it displays the upstream bow shock formed on the compressed day-side and the stretched out night-side composing the magnetotail. The bow shock encloses the magnetosheat (shocked solar-wind plasma) inside its profile. The reconnection happening in the day-side let some magnetic field lines penetrate the magnetopause.

tion Regions (SIR). These regions are of crucial importance as they regulate the propagation of the ejected material. As illustrated in Fig. 4.9, the resulting plasma cloud travel and interact with the Earth's magnetic field and they can become linked, whenever the latter field lines are compressed (day-side) and stretched out (night-side) creating a diamagnetic cavity around the planet. The plasma, now allowed to enter the magnetosphere, provides energy that is stored in the tail of the magnetosphere, causing instability, reconnection and subsequent release. These efficient energy exchanges from the solar wind into the space environment surrounding Earth are called geomagnetic storms. During a storm, the planet experiences an increase in electric current in its magnetosphere and ionosphere. A large portion of the energy can also be deposited in the atmosphere where the induced electric fields can travel to polar and equatorial latitudes, transporting electrons and ions through magnetic lines (auroral electrojets and ring current). This mechanism

can result in low-frequencies variation of the geomagnetic field and cause geolectric fields through magnetic induction. Geomagnetically-Induced Currents (GICs) are characterized by typical periods of few minutes and can propagate through grid transformers, affecting power lines on Earth.

During large geomagnetic storms, complex interactions between the ionosphere and the thermosphere (which morphology can be drastically affected by the solar wind) can occur. The neutral and ionized components of the two spheres experience frequent collisions and energy exchange allowing the winds to drive plasma transport which, in turn, results in an enhancement in the charge recombination rates. In the medium, electrons and ions oscillate with the propagation of their respective electromagnetic waves depending on their typical frequencies in relation to the plasma one: Electromagnetic waves with frequencies $f < f_{plasma}$ are damped; they cannot move through the plasma and are reflected when entering the plasma from an external interface. If $f > f_{plasma}$ the waves propagate, but at a lower speed. Since during quiet space-weather periods, the ionosphere displays plasma frequencies that varies from few MHz to 20 MHz, the wavelength of radio waves used for telecommunication (satellites,spacecrafts, GPS) has to be accurately calibrated for maximum transmission efficiency. A geomagnetic storm can introduce substantial delay in the communication, modifying the plasma reflection point and disturbing the patterns of communication broadcasting. As already referenced in section 4.1.3, the impact of energetic solar particles in the ionosphere had already been observed from the radio fade-out which occurred in 1936 (186; 187). The extreme ultraviolet (EUV) radiation caused by flares contribute to the ionosphere ionization in the ionosphere (heights greater than 150 km) and can persist for many hours. Additionally, solar flares cause X-rays excess in the deeper atmosphere, affecting the radio-wave absorption (explained in section 4.1.3) and interfering with over-the-horizon communications of civil aviation.

Finally, the effect of intense burst of radiation coming from violent solar event (CMEs, flares, IP shocks) enhances the level of background radiation. The ejected energetic particles follow the interplanetary magnetic field lines which can be subjected to irregularities when the magnetic activity is high. This results in a isotropic scattering (including backs-scattering), increasing the risk of radiation damages to space (and aviation) personal and instrumentation (195; 196).

Among its scientific tasks, AGILE is designed for the studies and observation of space weather effects on human activities in space, furthering our knowledge on ion fluxes, their penetration

to low latitudes and impact human-made technology in low orbit. A practical example of these studies can be found in the weather monitoring for granting maximum safety to the International Space Station (ISS) personal, on-board equipment during intense geomagnetic storms. In addition, precisely identifying incident radiation (particles species and energy) would represent a invaluable tool for absorbed dose estimation. This has the potential of preventing serious radiation hazard to astronauts during extravehicular activity (EVA). Altogether, a better optimization of shielding design and exposure time can serve in future space travel programs.

4.2 Particle ID in space

Generally, the discrimination and subsequent identification of particle (and ion) species entering the acceptance of a detection apparatus require the use of a stack of multiple active layers. The incident object deposits energy along its path, resulting in an output signal which provide crucial information for labeling its identity.

In order to be suitable for launch, a space-borne particle detector is subjected to a series of functional, electric, shock and vibration tests for simulating adverse space conditions and verify its hardware qualification. During the prototyping, scientists face a stringent trade-off between weight, power, and cost in order to maximise the scientific return. The physics requirements guide the project in the choice of the most optimal orbit for operating the instrument which, in turn, constrains its design. A large number of research spacecrafts operates in Low Earth Orbits (LEO), which contrarily to Geosynchronous Orbits (GEO), are contained within the Van Allen Belts (generally below the 1000 km of height). The radiation environment inside the belts remains one of the primary challenges to face.

While mechanical and cost features seem to favor the use of compact, light, and simple detection systems, the best PID performance have been achieved using bulky spectrometers, heavy layers of absorbers and complex telescopes. Few, commonly exploited identification techniques are reported in sections 4.2.1, 4.2.2, and 4.2.3.

4.2.1 $\Delta E - E$ method

Although the amount of possible technologies to be exploited for this task is vast, one of the signatures commonly used for particle identification, both in space and in ground based experiments, is referred to as $\Delta E - E$ (38). This method requires the use of a stack of consecutive detection layers as it relies on the distinction between the stopping power of different species of particles: the initial energy of a particle crossing (at least) the first layer of detection and stopping in one of the following is shared non-uniformly between the crossed detectors. As displayed in Fig. 4.10, to achieve the identification the telescope has to include pairs of thin and thick detectors (where the particle will be likely to stop). The partition of E between the two layers varies dependently on the particle type (197) and the strong correlation between its kinetic energy, charge (Z) and mass (A) provides a unique signature.

The amount of layers required for a complete reconstruction depends on the range of energies and the species of ions and particles to be identified. The lighter and more energetic the incident object is, the more the material is needed to stop its path. Although the method is robust and boasts of dated experimental inheritance, the above mentioned requirements result in the need for bulky, highly power-consuming detector telescopes, which complexity scales directly with the number of layers to be read-out and analyzed.

4.2.2 Time Of Flight - E method

Another, well established method of identification can be achieved using the time needed for a particle to cross two (or more) detectors. The detectros, kept a fixed distance, provide a 'start' and 'stop' signal to the system, consequently allowing to measure the velocity of the incident object. If the latter stops in a following layer of detection, its total kinetic energy can be extracted; the pair of measurements uniquely determines the particle mass.

A classic example of TOF - E identification is described in Fig. 4.11, where the SupraThermal Energetic Particle (STEP) telescope is detailed. During the experiment, particles entering the acceptance could knock off electrons from the Ni aperture foil. The electrons are then accelerated and collected by the Microchannel Plates, which produce the 'start'. The 'stop' is generated by the back-scattering electrons and the energy is measured with the use of the Si detector at the bottom.

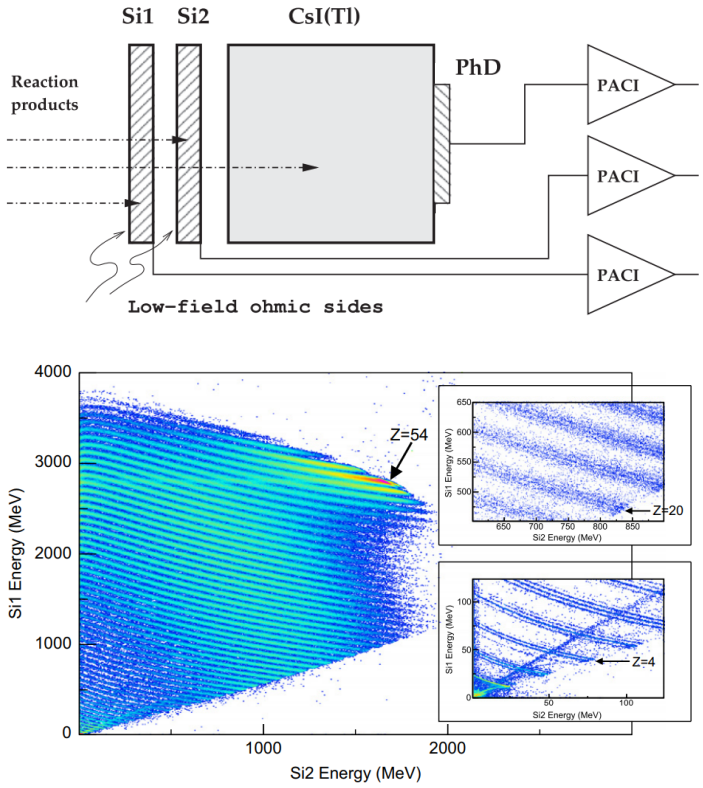

Figure 4.10: Telescope composed by a stack of two silicon detectors (Si1, Si2) and a CsI scintillator is used to identify the incident particle (38). The $\Delta E - E$ correlation between the silicon sensors is expressed in the plot below where : the abscissa gives the energy deposited in Si2, the ordinate that in Si1. The zoomed areas for Z ∼2-6 and 19–23 display the resolution power of the method.

The precision of the measurement can be further increased using detectors with enhanced time resolution providing a TOF information less affected by jitter uncertainties.

4.2.3 Pulse Shape Discrimination

Modern experiments propose to achieve the same identification power provided by the robust $\Delta E - E$ (which functioning is described in section 4.2.1) using Pulse Shape Discrimination (PSD) techniques (198; 199). This method approaches the problem from a different angle since it bases its identification power on the capability to reconstruct the energy loss on each detection layer extracting this information from the shape of the output signals (200). The shape, duration and amplitude of the pulses induced by the passage of the incident particles can be correlated with their energy loss in the active material ($\frac{dE}{dx}(x)$, Bragg curve).

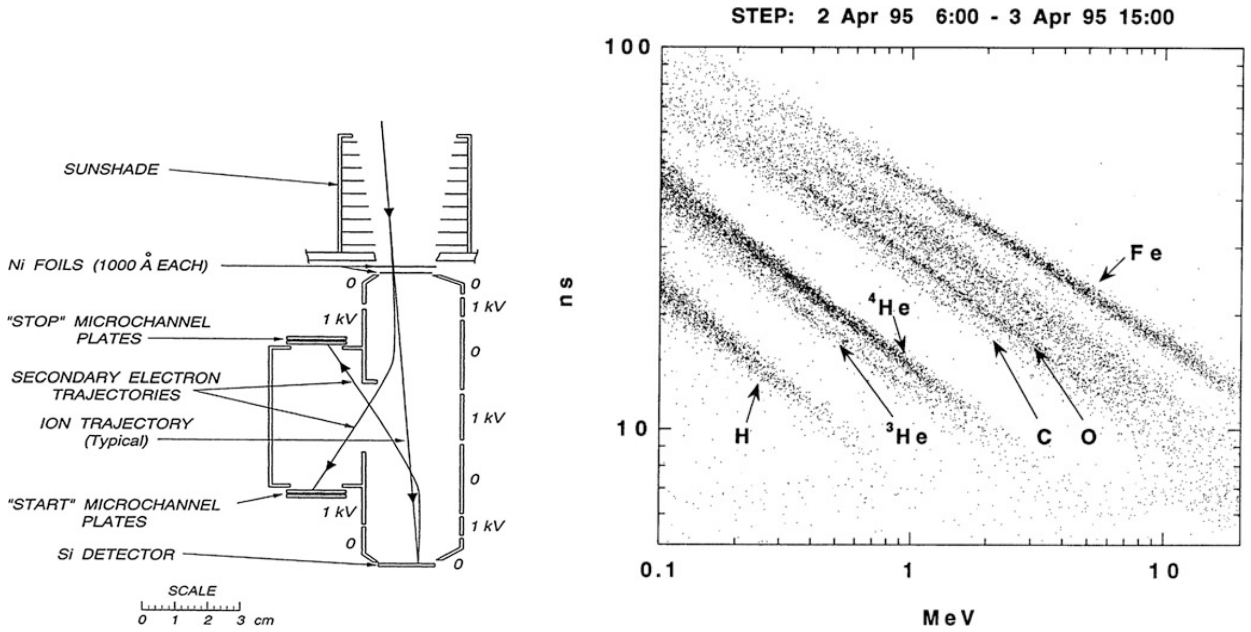

Figure 4.11: Left: STEP telescope for particle identification (39). Right: measurement of time of flight vs. energy for a sample of ions during a small 3 He-rich SEP event (40).

While the minimum requirement for a correct identification is represented by a particle stopping inside a single-detector apparatus, in a multi-layer configuration each one of the sensors in the stack can offer valid independent outputs for particles crossing multiple detection elements. The PSD solves the issues found in the $\Delta E - E$ such as the need for an energy calibration or the amount of needed layers of detection, loosening the hardware request and focusing on the digitizing and post-processing of the wave-forms (201; 202). Figure 4.12 shows the results obtained in the discrimination of a vast range of ions using the PSD approach.

On the other hand, this procedure requires very fast detection systems: PSD-based analysis usually employs the use of thin ($\sim$ few hundreds μm) solid state sensors (e.g. Si sensors) producing current signals typically contained within few tens of ns. The choice (or design) of a fast read-out chain, front end electronics and sampling techniques represents a crucial step in the development of a detecting instrument based on Pulse Shape Discrimination.

4.3 AGILE: The Advanced enerGetic Ion eLectron tElescope

The AGILE (Advanced enerGetic Ion eLectron tElescope) project aims at developping a compact low-cost space-based instrument for detection and identification of particles and ions. This instru-

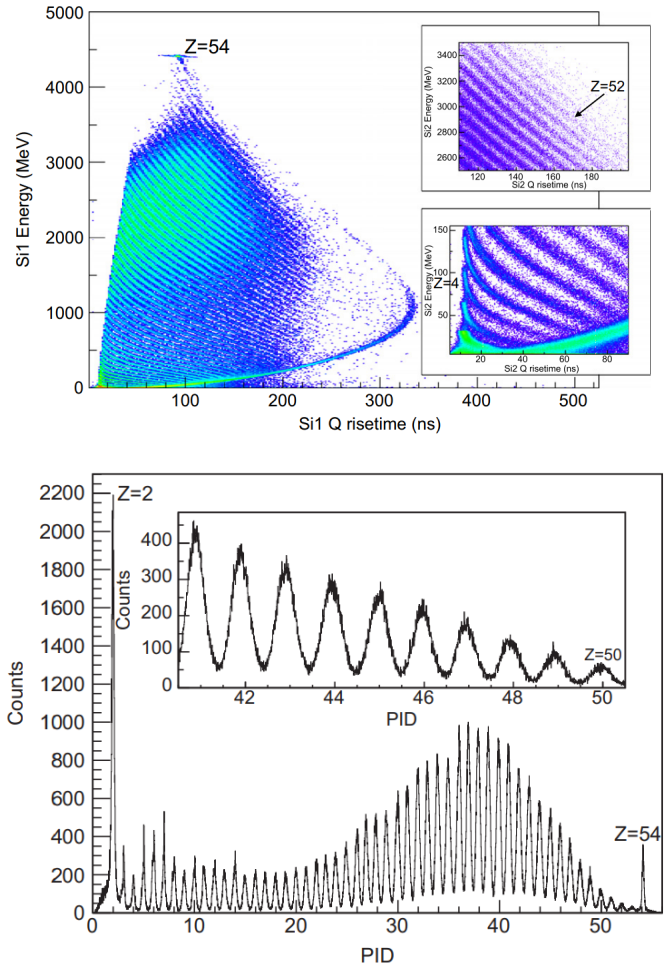

Figure 4.12: The data (acquired with the setup shown in Fig. 4.10) show the resolution capabilities of the PSD method correlating the energy deposited and the resulting signal rise-time in a single layer of detection (above). The linearization of the curve (below) offers a good visual representation of the charge (Z) of the detected ions.

ment targets the reconstruction of a vast variety of elements (from H to Fe) and corresponding energies spanning 1 - 100 MeV/nuc per nucleon (45). The experiment combines the heritage of previous particle telescopes, such as MERIT (Miniaturized Electron pRoton Telescope) onboard CeREs (Compact Radiation belt Explorer) (203), and the expertise of the team in the development of ultra fast silicon detectors and electronics (204) used for particle detectors. As it proposes an in-situ operation, this detector project represents the first attempt for real-time particle identification in space using PSD techniques 4.2.3.

Figure 4.13 presents a sketch of AGILE experimental setup: the active area is represented by a stack of three 300 nm Silicon sensors read-out by a custom-made electronics and digitized by a

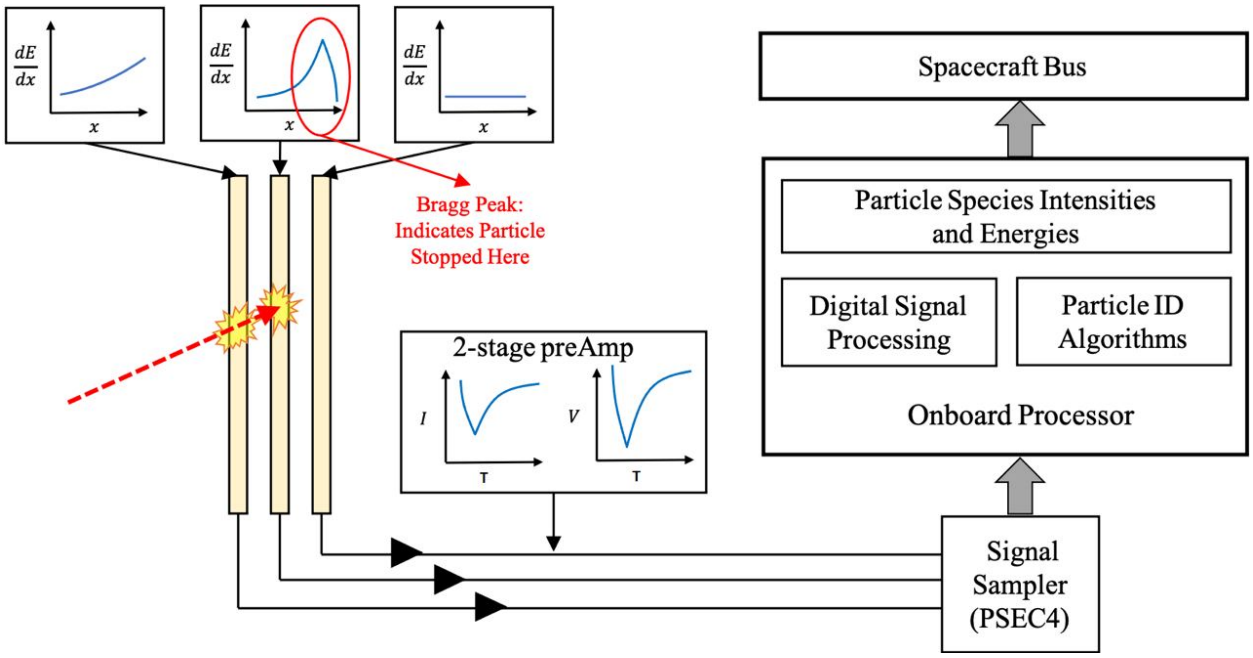

Figure 4.13: Simplified representation of the PSD method as implemented by AGILE: an incident particle passes through the first detection layers, stopping in the last one where we can observe its Bragg peak (41). After being processed by the read-out, the signals are then digitized and their key features reconstructed. To label the particles, the latter are compared with a list of expected inputs.

fast sampler implemented on Application-specific integrated circuits (ASICs). More details on the acquisition chain can be found in the next sections. Following Fig. 4.13, it is possible to outline the chain of actions needed to perform the identification. The three layers of detection output raw signals, later processed and digitized by the front-end. The stopping layer provides the information needed for the species identification. The system uses the amplitude spectrum of the pulse to reconstruct the initial energy. It then correlates its key features to obtain a unique signature and compare them with the ones expected by the simulation.

4.3.1 Form factor, electronics and mechanical design

Following the steps of MERIT, the AGILE instrument will be completely integrated inside a CubeSat. First proposed by Jordi Puig-Suari (166) in 1999 at the California Polytechnic State University, these miniaturized nanosatellites drastically reduced the complications faced during the design of the Orbiting Picosatellite Automatic Launcher (OPAL) at the Stanford University's Space System Development Laboratory (SSDL) and represent one of the most used technologies to educate

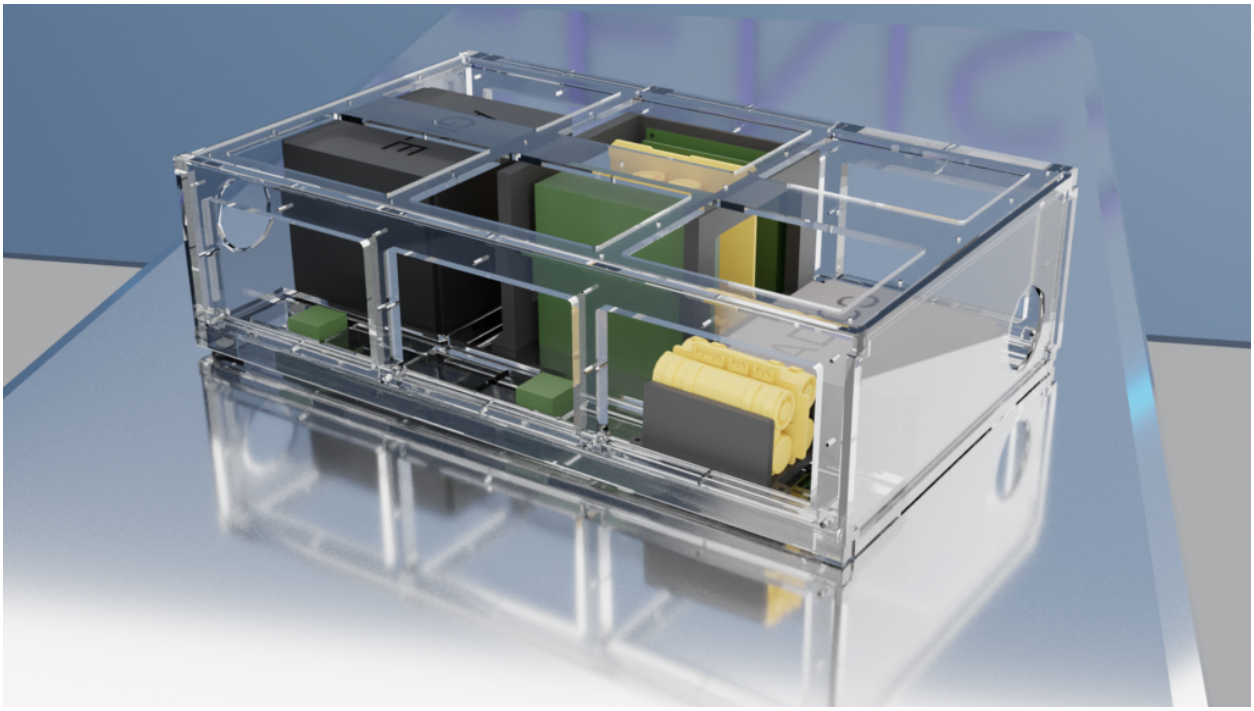

Figure 4.14: Picture of the GenSat-1 model designed by GenSat Engineering (42).

scientists in the development of low-cost platforms for testing and space qualification. CubeSat miniaturized design makes these instruments suitable for launcher–payload interface reducing the space requests as can be launched in multiples exploiting the unused storage of larger vehicles. The size of a CubeSat is compartmentalized in smaller sections called "units" (U) which enclose an effective volume of 1l (10 cm$\times$10 cm$\times$10 cm). Its size can be extended along one axis by stacking units to fit the forms of 0.5U, 1U, 1.5U, 2U, or 3U.

The AGILE project prototyping phase includes the launch of the instrument scheduled for 2022. The detector stack will be deployed in high inclination LEO, where it will orbit with a revolution period of 95 min collecting data for a total of around 35 min per orbit (when orbiting above the poles). Together with the mechanical support and the communication interface, the testing and the satellite operation, the Maryland based GENESIS Engineering (42) company will provide the CubeSat to deploy the AGILE instrument.The GenSat-1 model (in Fig. 4.14) is designed to carry two scientific payloads into polar orbit for data collection in collaboration with the NASA's Goddard Space Flight Center.

The detector layers of AGILE, its front-end, digitizer and power boards (detailed in the next sections) are developed to be contained inside 1U of the GenSat-1. The AGILE mechanical struc-

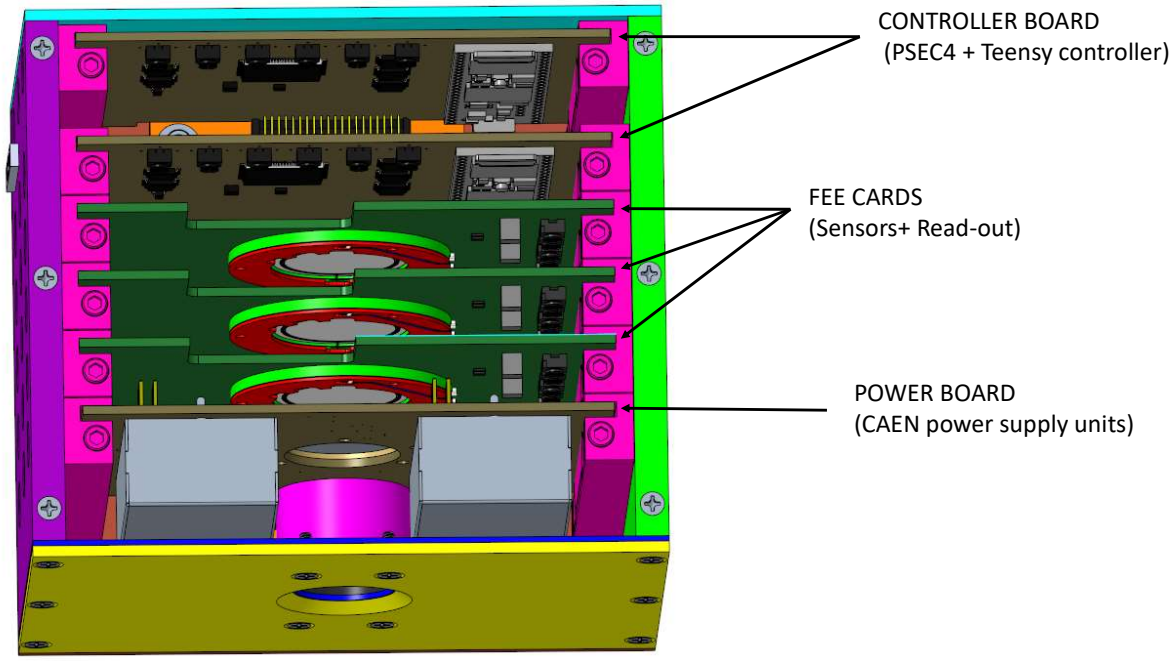

Figure 4.15: 3D render of AGILE instrumental apparatus contained inside the Al enclosure.

ture is composed of a rectangular square box made of an external aluminum enclosure. The structure is completed by a tungsten plate positioned behind its front panel, and a tungsten tube, which bevelled opening determines the instrument acceptance (geometry factor of 0.61 $cm^2 - sr$). In the current design, the detectors face the outside environment through a cutout performed on the power supply board. A 3D render of the AGILE mechanical structure is reported in Fig. 4.15.

The latter provides bias to the Si sensors via the use of two (main + redundant) CAEN A7508N (205) DC-DC components, in charge of stepping the 5 V up to the needed voltages ($\sim$-100 V). While the analog signals move through coaxial cables, the power, as well as the digital signals are routed through the backplane board which connects the instrument to the outside world using a flex connector. Figure 4.16 details the connections between AGILE electronics components.

To read out the analog signals produced by the silicon detectors, set and monitor the voltage levels, transferring data, as well as controlling the instrument's operation mode, AGILE employs

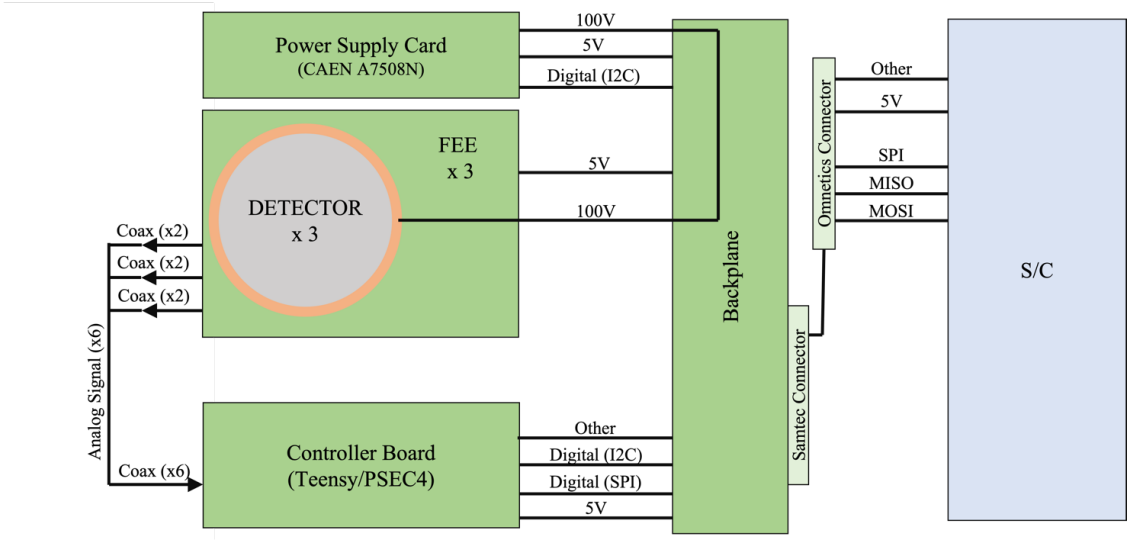

Figure 4.16: Electrical diagram of AGILE signal and power routing inside the GenSat-1 satellite.

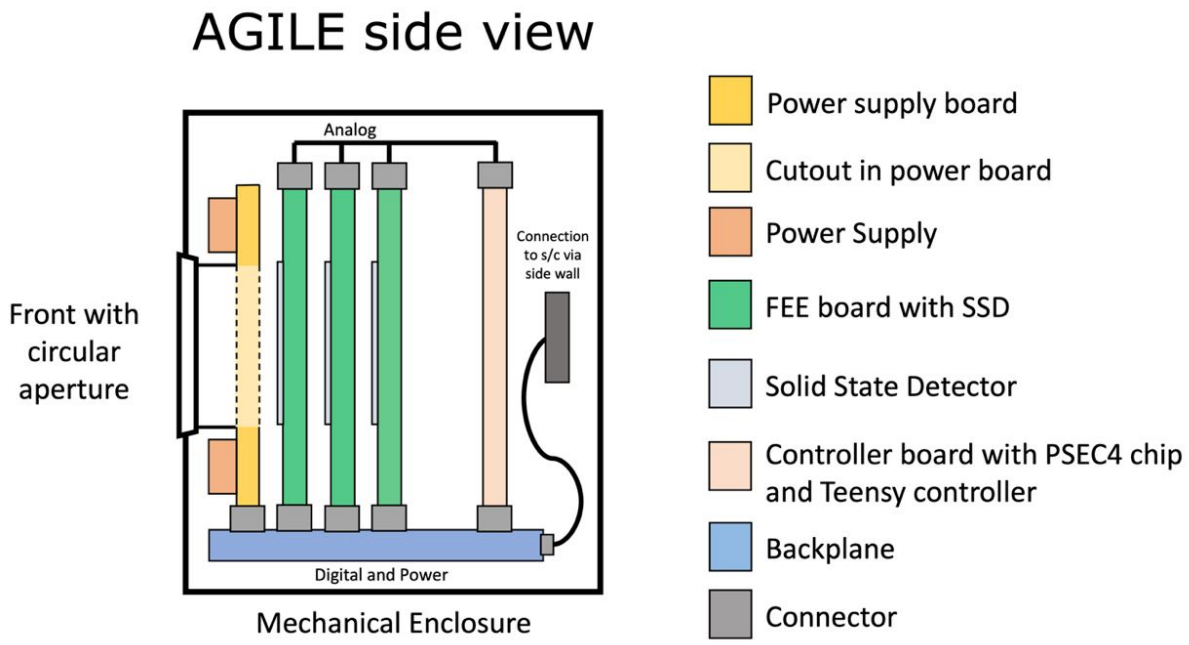

Figure 4.17: Sketch of the AGILE apparatus cross section contained inside the mechanical enclosure (1U) of the GenSat-1.

the combination of a fast digitizer and commercial micro-controller. Together with a Complex Programmable Logic Device (CPLD) for managing the trigger logic, this apparatus is hosted on an additional board (described in section 4.4.4), that concludes the detector stack. A side view of the full instrument is provided in Fig. 4.17.

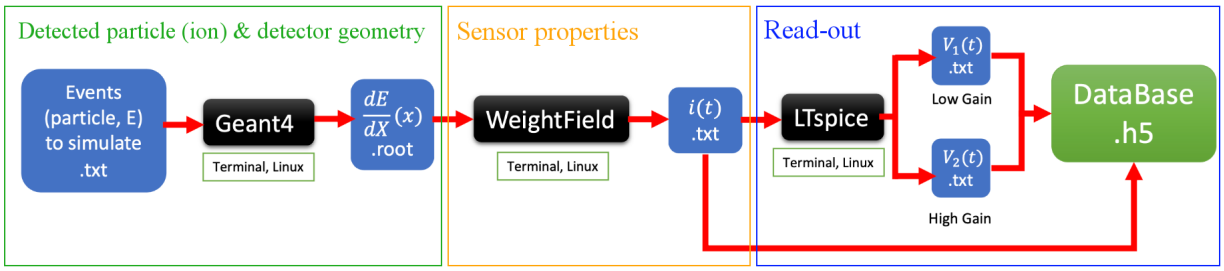

Figure 4.18: Outline of the simulation chain developed for the AGILE project.

4.3.2 AGILE simulation framework

For evaluating the best solution for the detectors to be employed, as well as the read-out and sampling systems to develop, AGILE relies on a simulation framework divided in multiple steps. The process behind the developing of the simulation framework (as described in Fig. 4.18) starts with reproducing the energy deposition profiles in each of AGILE layers. A GEANT4 software (20) provides a reliable environment for building the simulated geometry of the instrument and gives the possibility to generate its nominal response to the passage of particles and ions of any species.

With the use of the GEANT4 framework a selections of the ions investigated by AGILE is produced over the nominal spans of energies (1 to 100 MeV/nuc). Particles entering the detector acceptance loose an amount of energy proportional to their initial energy, their species, and to the amount of material crossed (following the processes discussed in section 1.2.3). As discussed in chapter 1 of this document, the importance of the material, shape and features of detectors active area (sensor) uniquely define its response to the passage of incident radiation. This also determines the design of performing read-out electronics has to be tailored around the choice of a sensor technology.

AGILE opts for the use of silicon sensors. For space applications as well as in particle physics, their use is backed by dated, successful inheritance and user experience. The choice of the sensor dimensions and doping define the features of the free charges released when radiation is absorbed: the silicon thickness (and intensity of the electric field applied) decides their drift time, the doping layers affect the detector radiation resistance, gain, and charge mobility. Since the PSD method (described in section 4.2.3) minimum requirement for proper identification is represented by a particle stopping in one of the detection layers, the amount of material to stop the incoming par-

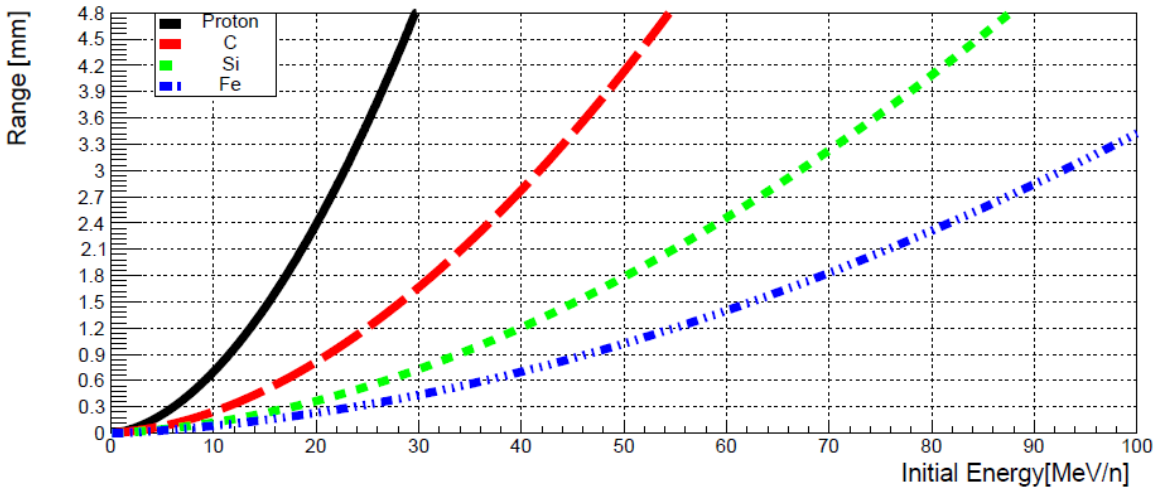

Figure 4.19: Range in silicon (ρ = 2.33 g/cm^3) as a function of energy per nucleon for a set of sample particles and nuclei.

ticles has to be carefully simulated. The simulated results in Fig. 4.19, report the maximum range for a particle with initial energy E crossing a silicon detector active area.

Once the energy losses of ions (and consequently, their range) are simulated, the next step consists in reproducing the detector charge collection and current generation. For that, the Weightfield software (206) inputs information on the energy deposit and outputs the shape and magnitude of the currents generated by the silicon sensors. Contrarily to the cases discussed in chapter 2 and chapter 3, AGILE uses traditional pin diodes, not provided of a gain layer (more information can be found in section 1.2.4). Weightfield2 is a software created ad hoc for the studies of charge collection in silicon and allows for testing different size, doping, and gain configurations.

The data generated have to be processed by a simulated version of the read-out. The full amplification chain was simulated using the LTspice (43) electronics design software. Files containing the information of the detector currents are used to generate the pulses expected to be output by the final read-out. Th reconstructed pulses contain the features that will be used for the implementation of the PSD.

4.4 Design of the AGILE instrument

Guided by the results of the simulation framework of AGILE, the team proceeded in the design and development of the individual detector component. The choice of the optimal sensors properties represents the first milestone for the drafting of an early read-out design. The structure of the amplification chain has to be particularly versatile in order comply with the vast range of energy deposit expected. At the same time, its range of operation are constraint by the limits of the digitizing devices in charge of the data sampling. The performance of the full acquisition chain and the feature of the output signals determines the efficiency of the final particles ID capabilities.

In the next sections We discuss the steps for the design and development of the AGILE instrument, starting from the selection of the preferred features of the silicon sensors.

4.4.1 AGILE detectors

The first crucial step for the development of the instrument is the selection of the detector features. The compact design of AGILE favor the use of thin devices with no absorber volumes in the stack. The use of sensors with reduce thickness also allows to exploit the capabilities of the fast read-out designs already introduced in previous chapters (chapter 2 and chapter 3). Starting from the simulated results on the studies of the energy loss in silicon (introduced in section 4.3.2), We proceeded in evaluating the optimal configuration for AGILE. Figure 4.20 shows the simulation results of the Weightfield software (206) used to predict the sensor response (introduced in section 4.3.2).

An example of the current output is obtained feeding the energy deposition profile of carbon (E = 7.5 Mev/n) nuclei generated with GEANT4, simulating their charge deposition when stopping in a 300 μm thick, p-type, silicon layer. Using a reverse bias of +110 V (depletion voltage $\sim$+60 V) the charges freed during the ionization process reach their saturation velocity drifting toward the electrodes. The right panel of Fig. 4.20 shows that the hole current (in blue) composing part of the total signal is longer than the electrons one, hence defining the total pulse length. For this particular configuration the electron current lasts 8.8 ns while the holes take longer than 13 ns. This difference is dictated by the the two components mobilities ($\mu_{h,e}$), which have a ratio of 1/3 and can be found in Eq. 4.3:

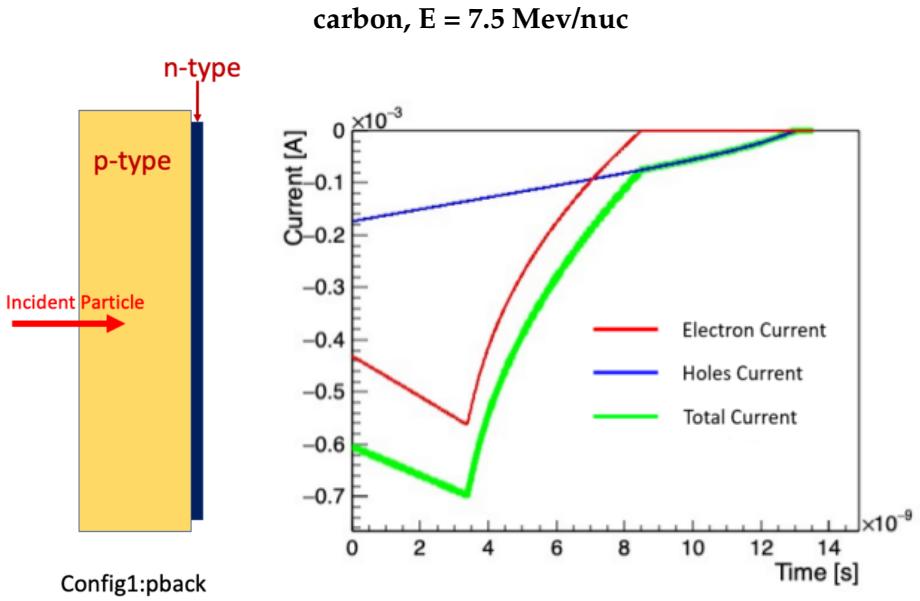

Figure 4.20: Simulation of a carbon nucleus stopping in 300 μm of Si (depletion = +60 V; bias = +110 V). Left panel: simulated detector configuration. Right panel: the red and blue lines represent, respectively, the electron and holes current. The bright green line is the combination of the two currents, hence the total charge moved as a function of time.

$$\frac{\mu_h}{\mu_e} \simeq \frac{450\,cm^2/V\,s}{1350\,cm^2/V\,s} = \frac{1}{3} \quad . \tag{4.3}$$

The energy range of an identifiable ion is not continuous but instead limited by a minimum threshold (the greater Z the higher this energy). If an ion (p-Fe) stopping in a Si layer has an energy lower than this threshold it will stop in the first third portion of the medium. The hole component will then be shorter than the electron one resulting in a total pulse length (charge collection time) defined by the latter. This results in identical collection times (∼8.8 ns for the configuration in Fig. 4.20) for any incident element. Figure 4.21 highlights the minimum pulse duration needed for unique identification, generalizing this behaviour for any incident charged ion (p-Fe) with energy within the acceptance range (bottom panel 4.21);

The use of other configurations of detection, illustrated in Fig. 4.22 were explored during the studies prior to the prototype design. Although different doping typologies correspond to different shapes in the output currents, our studies concluded that the response to incident radiation of simulated p-type and n-type silicon sensors provided similar results in Pulse Shape Discrimina-

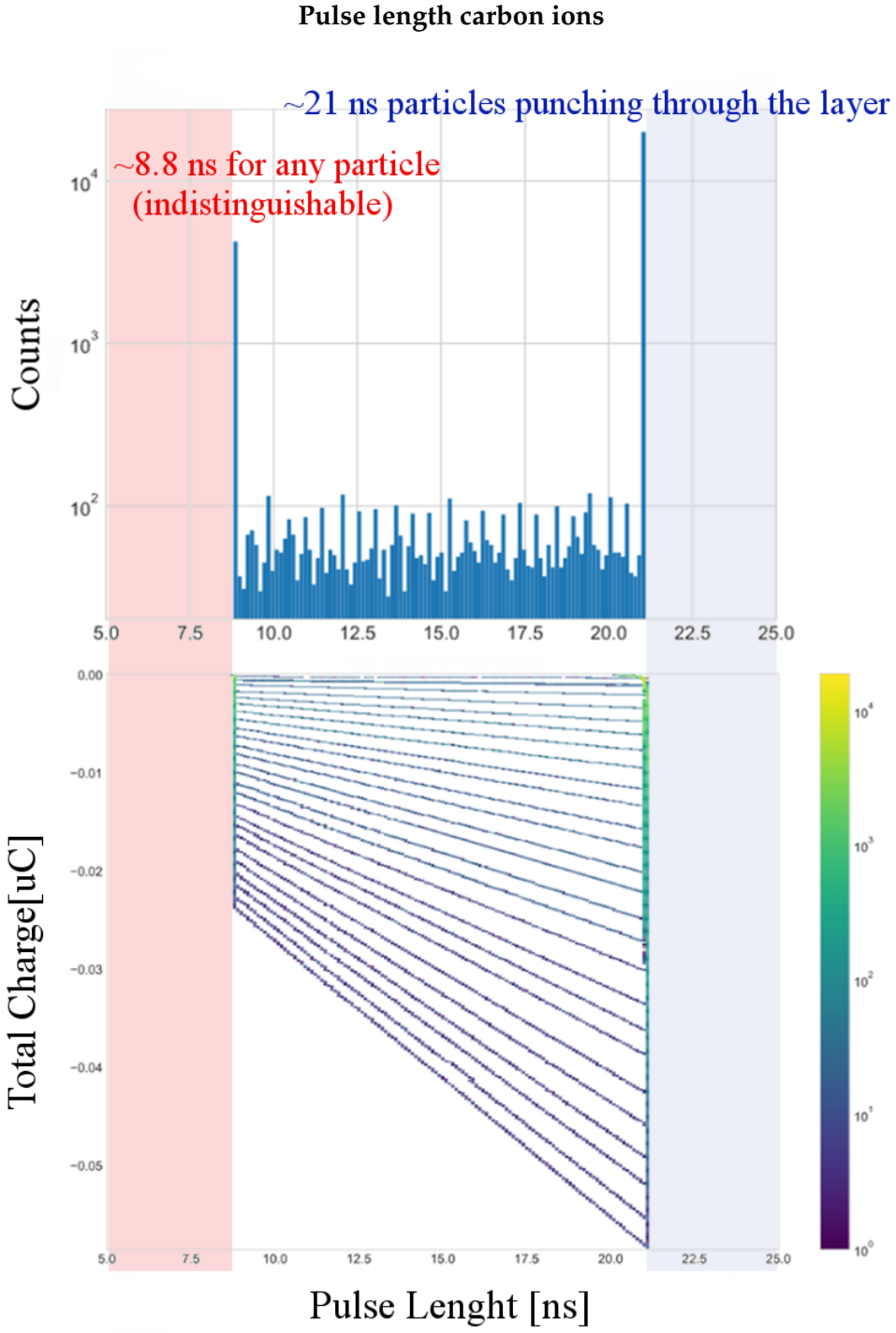

Figure 4.21: Top: histogram of simulated pulse duration for identified carbon nuclei. The hard cut-offs part shows the lower boundary for discrimination (∼8.8 ns) while the overflow bin is populated with entries of nuclei energetic enough to punch through the detection layer. In the bottom plots, the total charge deposited in the silicon is reported as a function of the pulse length. The cut-off effects are then generalized for a gamma of ions and energies.

tion capabilities. More striking differences were observed during the analysis of different detector orientations (207). Prior published results reported evident benefits in the injection of the particles into the rear-side (p-side in Fig. 4.20) of a totally depleted sensor. This method exploits the effect of the rising field profile increasing with the penetration depth (198) which in turn minimizes the plasma-erosion[4] at the Bragg peak. It results in shorter and monotonic current pulses. In this scenario, the freed holes, moving slower than the electrons, have to cover a smaller distance to reach the nearest electrode, introducing minimal modifications in the signal shape and reducing the total collection time. This produces unique correlations between the deposited energies, and the output signal shape.

4.4.2 Design of a double-gain read-out

The possible combinations of ions and associated energies to be uniquely identified by the AGILE instrument represent one of the biggest challenges of the projects. In particular, the amplification chain composing the read-out has to be designed to maintain its performance over the wide spectrum of detectable ions. According to the simulation results, the range of expected amplitudes produced by incoming particles in the Si detector spans almost four orders of magnitude: from 10^{-6} A to 10^{-2} A. Another challenge comes from the stringent size and power consumption constraints imposed by the CubeSat form factor and electric features (which description can be found in section 4.3.1). To deal with these difficulties it was opted for the development of a dual-gain amplification chain, based on low power consumption discrete SMD components. Using this strategy, each detector layer read out by a two-channel board. For the rest of this chapter we refer to these boards as 'FEE card' (Front-End Electronics card). The motivation that drives the design is based on the need of processing every current pulse expected for different particles energy losses, depicted in Fig. 4.23. It is outlined as follows:

- The free charges generated inside the sensor drifts towards the electrodes, inducing a current pulse on the electrodes.
- The pulses are transferred to the pre-amplification stage using bonding wires.

[4]Plasma-erosion indicates the local degradation of materials due to frequent interaction with ionizing plasma.

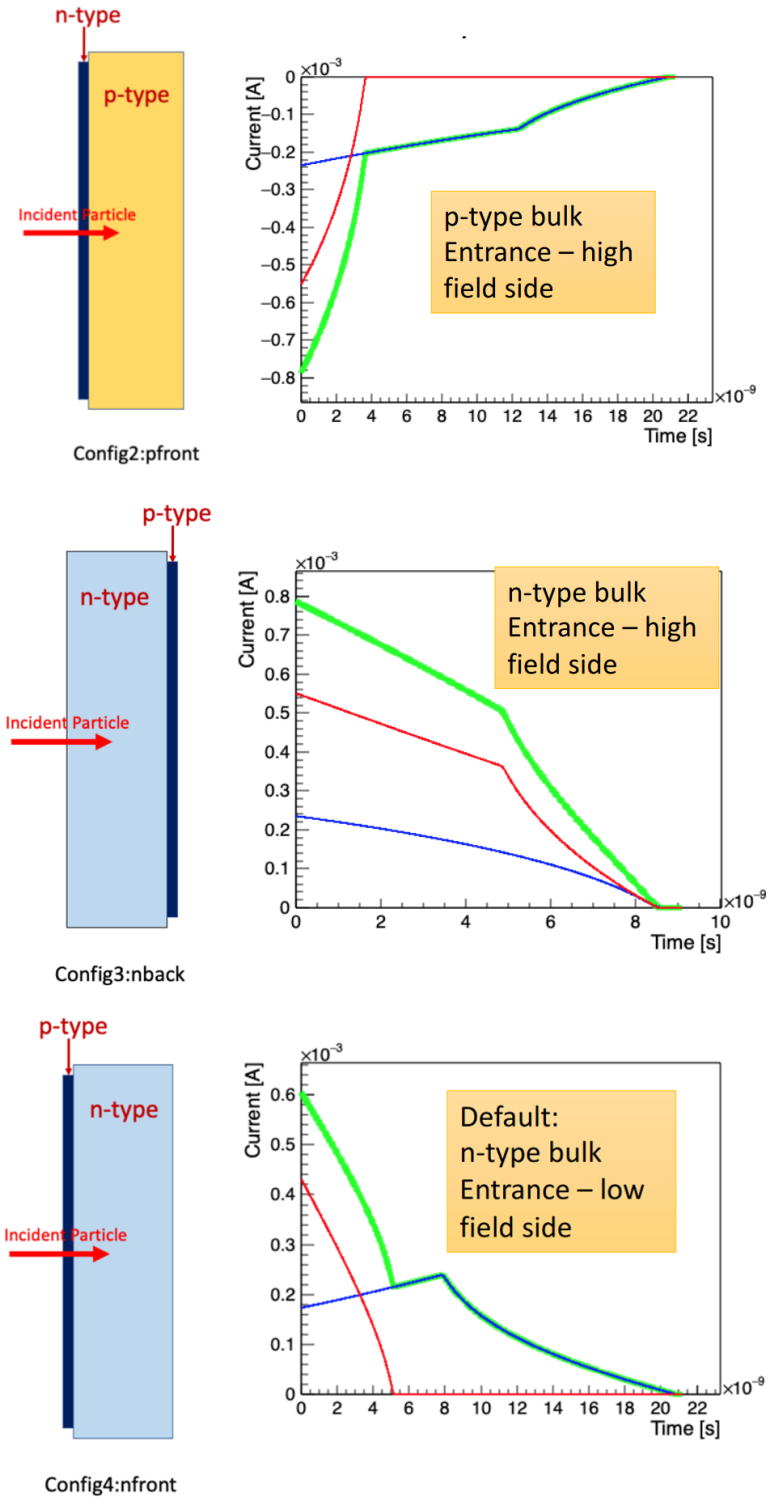

Figure 4.22: Additional possible combinations of detector type and orientation that were studied before selecting a final configuration. Like in Fig. 4.20, the blue line represents the holes current, the red one the electron current and the green one the total one output by the sensor.

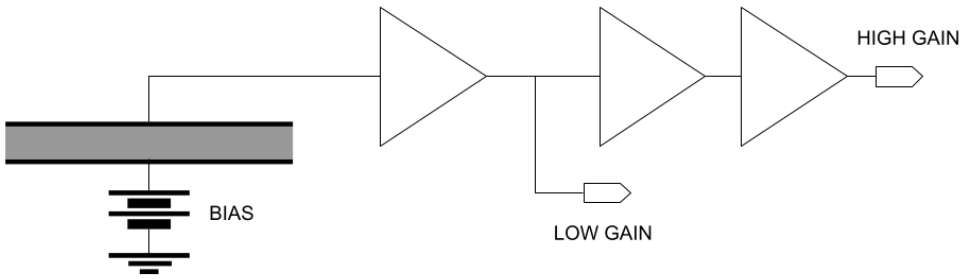

Figure 4.23: Simplified description of the read-out, highlighting the structure of the two amplification lines. To evaluate its performance, the circuit was simulated using LTSpice (43) design and simulation software.

- After being decoupled of its DC components, an Infineon BFP842ESD SiGe bipolar transistor (208) in an common emitter configuration takes care of the first amplification of the signal.
- The signal follows now two different lines. The first line carries the pre-amplified pulse directly to a 50 terminated coaxial output, namely 'Low-gain Output'.
- The second line connects the circuit to two additional common emitter amplifiers (Infineon BFP842ESD SiGe, and Infineon BFP620 silicon bipolar transistor (209) used as a last stage), therefore increasing the signal final amplitude twice before being output by the 'High-gain Output' coaxial connector.

The amplification circuit outputs a response that is tailored to the magnitude of the charge moving inside the silicon, adjusting the amplitude of the produced signal over a wide range of input currents. This expedient allows the cards to always produce voltage outputs with amplitudes in the correct operational range of the digitizing device. The response of the read-out was studied feeding the simulated current generated by the silicon sensors to the LTSpice (43) design and simulation software. The ratio between the High-gain and Low-gain channels provides a better understanding of the circuit's transfer function. The studies were conducted using two different input capacitance, 125 pF and 350 pF (top and bottom panel of Fig. 4.24) to simulate different detector sizes.

As introduced in section 4.4.4, the PSEC4 (210) sampler chip saturates at 800 mV. At the same

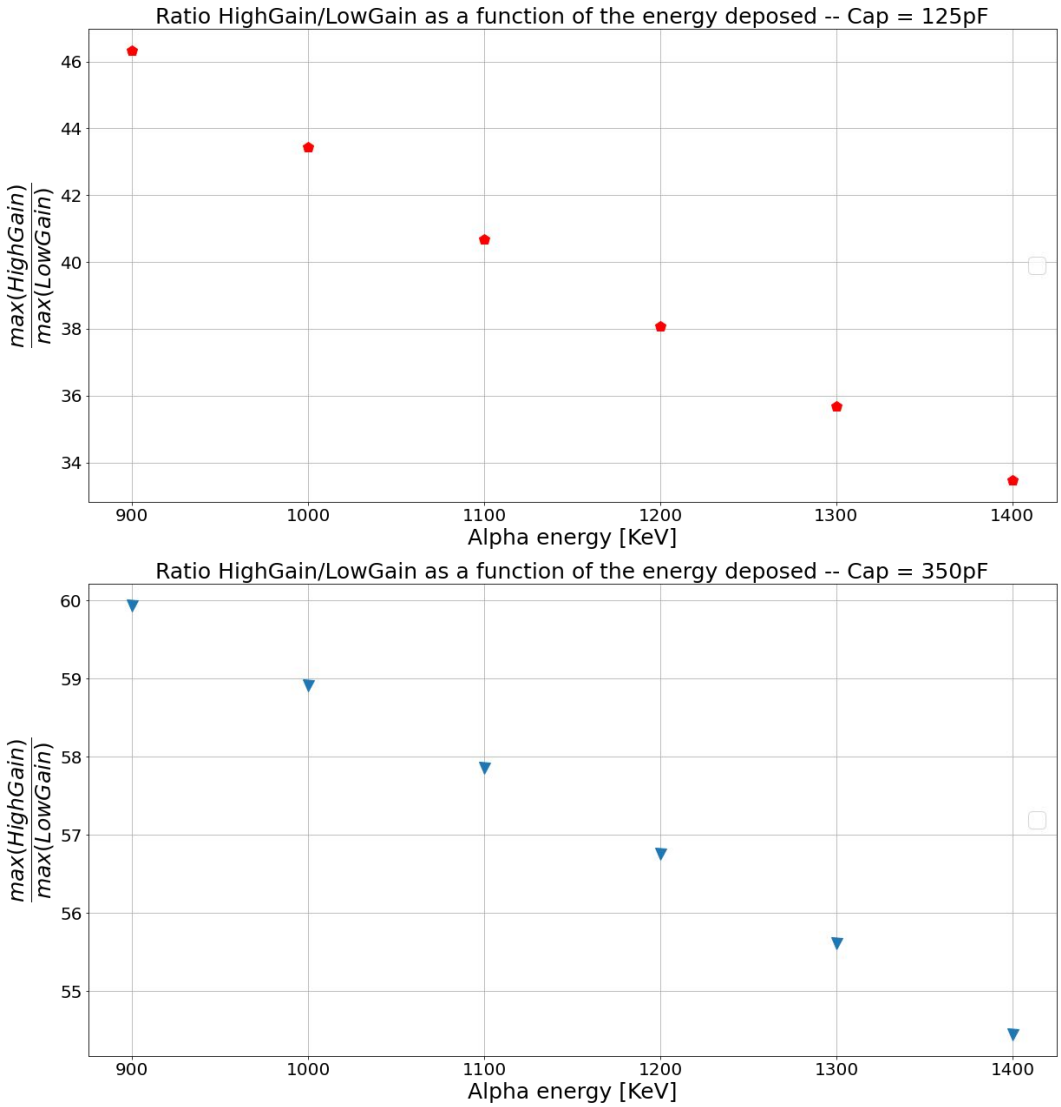

Figure 4.24: Ratios of the signal amplitude produced detecting α-particles as a function of the α energy, and processed by the simulated amplification lines of the dual gain read-out. The curves are used to characterize the response of the high and low-gain, and for later comparison it with real data.

time, signals with amplitude lower than 1 mV cannot be discriminated from the background fluctuations as this value represent the intrinsic noise of the device. The dual-gain design solves the possible saturation issues due to high amount of energy released by stopping heavy particles by processing the latter using a single stage amplification. Conversely, when a current pulse results to be too small to be observed from the low-gain output, the system relies on the study of the high-gain line, where the signal is amplified over three consecutive stages. The pulse shape discrimination method implemented by AGILE requires some important signals feature for identify-

ing incident particles. In particular, the read-out components have been chosen to not represent the bottleneck of the system bandwidth and to react to rapid changes in the input current trend: a sharp rise-time ($\sim$10 ns) allows for a precise reconstruction of the time coordinate, reducing the effect of the jitter and ensuring a reliable identification of the signals.

4.4.3 Power supply board

To power the detectors, the AGILE instrument includes a dedicated PCB hosting two CAEN A7508 (205) power supply CAEN A7508, 1 Ch361 800 V/50 μA High Efficiency HV Power Supply Module. Only one of the two will be used during the flight operations, while the redundant one is supposed to take over in case of critical failure of the main component. To monitor and set the detectors bias voltages, two sets of Digital-to-Analog (DAC) and Analog-to-Digital (ADC) converters carries information in and out of the CAEN A7508. The ADC and DAC modules are controlled by a Teensy micro-controller, described in section 4.4.4. The power supplies perform a DC-DC conversion, in-taking 5V and providing around 100 V to the sensors. In addition, the AGILE instrument exploits the position of the power supply board (depicted in Fig. 4.25) within the stack, to host a a set of two absorbing foils to eliminate the contamination of low-energetic particles (less than 1 MeV) entering the detecting acceptance.

4.4.4 AGILE controller board

The device selected for digitizing and recording the data in the AGILE prototype is a PSEC4 Application-specific integrated circuit (ASIC). At the core of this 6-channel sampler chip a switch-capacitor array (SCA) paired to a threshold-level trigger discriminator samples inputs signals with a depth of 256 sample points. Although the PSEC4 chip has a nominal DC dynamic range of 12 bits, the device intrinsic noise level reduces it to an effective 10.5 bits. The adjustable sampling rate of the PSEC4 (5-15) GS/s is one of the most appealing characteristics of the chip as it allows AGILE to fully reconstruct the rising edge ($\sim$10 ns) of the AC-coupled Si detector pulses. In the first instrument prototype, the sampling rate will be limited to around 7 GS/s. The ASIC sampling rate is imposed by the clock reference fed to the 256-stage voltage-controlled delay line (VCDL). The PSEC4 is also provided with a ramp-compare Analog to Digital Converter (ADC) ran using a

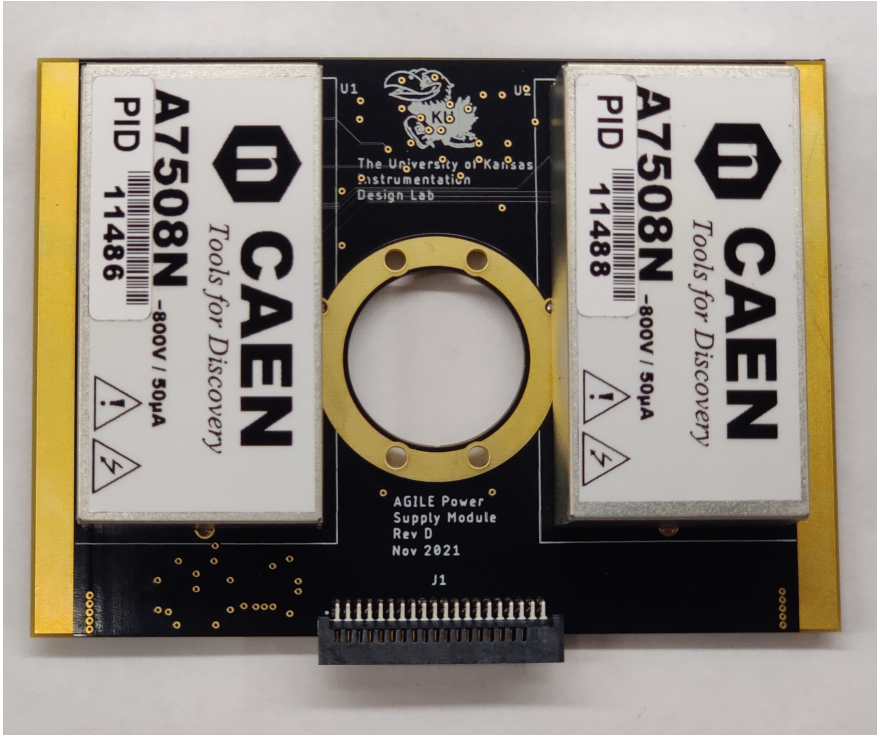

Figure 4.25: Power supply board for AGILE detectors bias voltage distribution. The board hosts one main and one redundant CAEN A7508 units. The input 5 V are converted to around 100 V output to the silicon sensors hosted in the three detection layers.

global analog ramp generator (Wilkinson ADC), ultimately distributing a 1 GHz clock that to each cell of the array. Figure 4.26 provides a simplified sketch of the PSEC4 chip internal architecture.

In standard applications the PSEC4 chip is operated by field-programmable gate arrays (FPGAs) providing timing control, clock generation, readout addressing, data management, and general configurations. The AGILE team decided to instead to use a commercial Teensy 4.1 microcontroller (211), drastically reducing the firmware development time. This controller operates in combination with a LCMXO2-2000ZE-1TG144I FPGA (212) for time sensitive tests to provide the trigger, for the data acquisition and to communicate with the spacecraft via SPI interface. The control and monitoring of the detectors power supplies is also controlled by the Teensy board which uses I^2C interface for setting the bias voltages, monitor the output voltage and current levels, and switching between main and redundant units. The control board's connections routing is sketched in Fig. 4.27. The backplane board interfaces the three FEE cards with the power card and the controller board, and ultimately to the rest of the instrument via a flex or flying lead harness.

All the devices hosted on the control boards are selected to respect the power budget of the

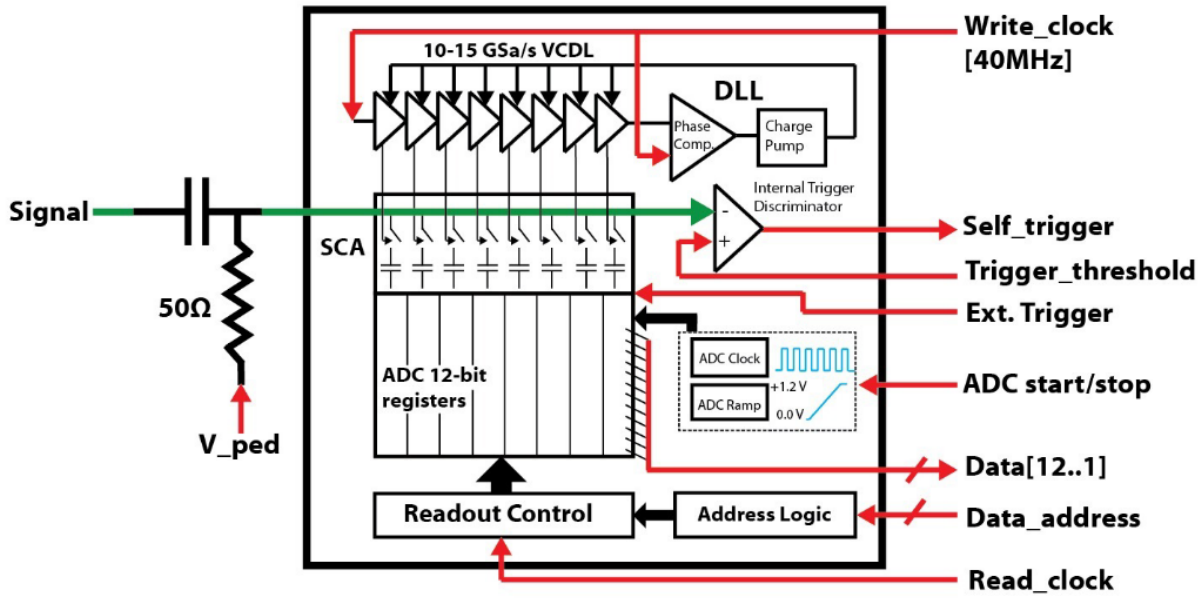

Figure 4.26: Simplified sketch of the PSEC4 internal architecture.

GenSat-1: the PSEC4 chip power requirements at maximum expected trigger rate is of ∼100 mW, the Teensy controller requires 500 mW. The total power consumption of the sampler and controller board is 600 mW.

4.4.5 Simulated particle ID capabilities

When employing particle ID techniques using PSD methodologies, the accuracy of the reconstruction algorithms depends on the choice of unique identifying features for every combination of detected particle, and energy. The shape of collected waveforms contains useful information. For this project, the observed correlation between the decay time and the max amplitude is connected to the ions Z and M values. In particular, when studying the time profile of individual pulses, the rise-time, integration, and decay-time are directly related to the total duration of the charge collection inside the sensor. This information can be used to estimate the depth of the traversed particles before stopping (range) inside the silicon. When fixing the particle's energy, this range differs for particles with different charge and mass, therefore providing a unique signature. These quantities are constrained by the drift time of the free charges inside the medium (as well as the read-out electronics transfer function of the read-out electronics) and represent a reliable discrimination tool only for a subset of possible energies.

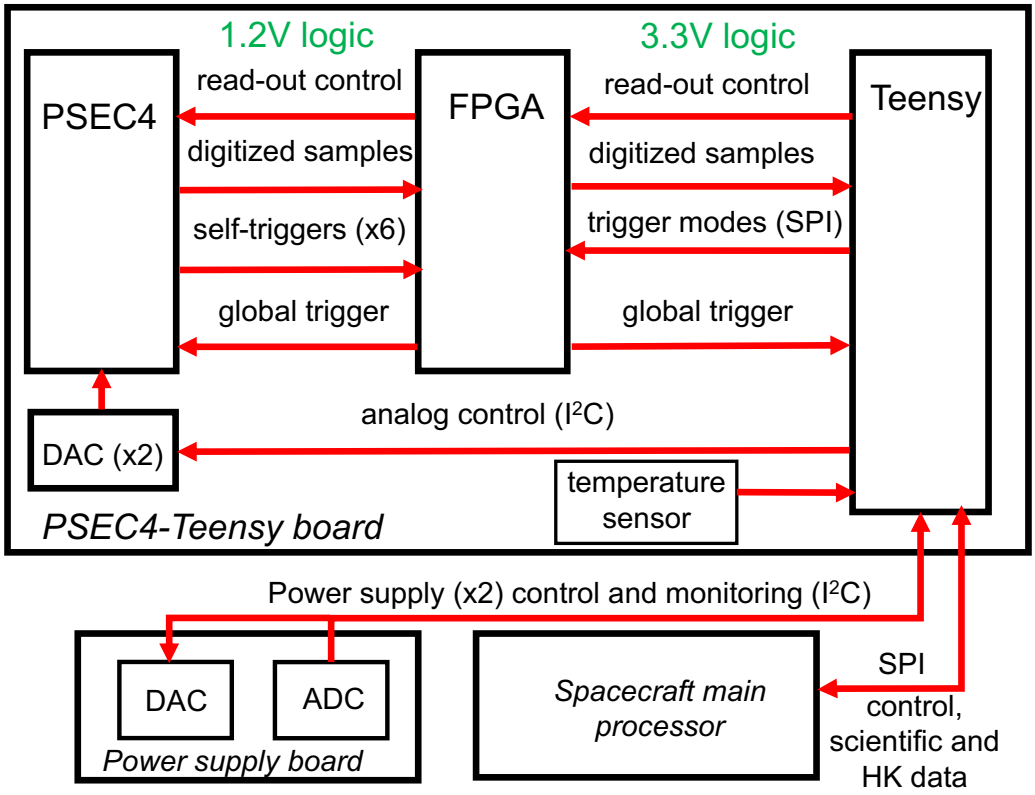

Figure 4.27: Sketch of the connections, input, and output signals between the components of AGILE's control board. After the data digitization, the PSEC returns the digitized sample to the central FPGA. The FPGA is responsible for distributing the global trigger to the digital components on the board as well as setting the trigger modes in the Teensy micro-controller. The Teensy communicates with the power supply board through I^2C interface, and with the spacecraft main processor using SPI protocol.

This partial information can be complemented by the reconstruction of the pulse amplitude, which quantifies the total energy deposited inside the stopping layer. When correlating the pulse amplitude distribution with the time features of the signal, we obtain curves that uniquely identify the incident particles types pinpointing their Z, and M, as well as their initial energy. Figure 4.28 presents the simulation results of the AGILE identification capabilities. The density histogram depicts the maximum amplitude migration as a function of the 90% of the signals decay-time for a multitude of ions (H-Fe) and energies (1-100 MeV/nuc). The use of this particular time signature derives from the read-out circuit technical specification and is the results of optimization procedures performed within the simulation framework.

In the representation of Fig. 4.28 the curves are inclusive of the sole statistical fluctuations of the energy deposition. However, the identification efficiency depends on a number of parameters

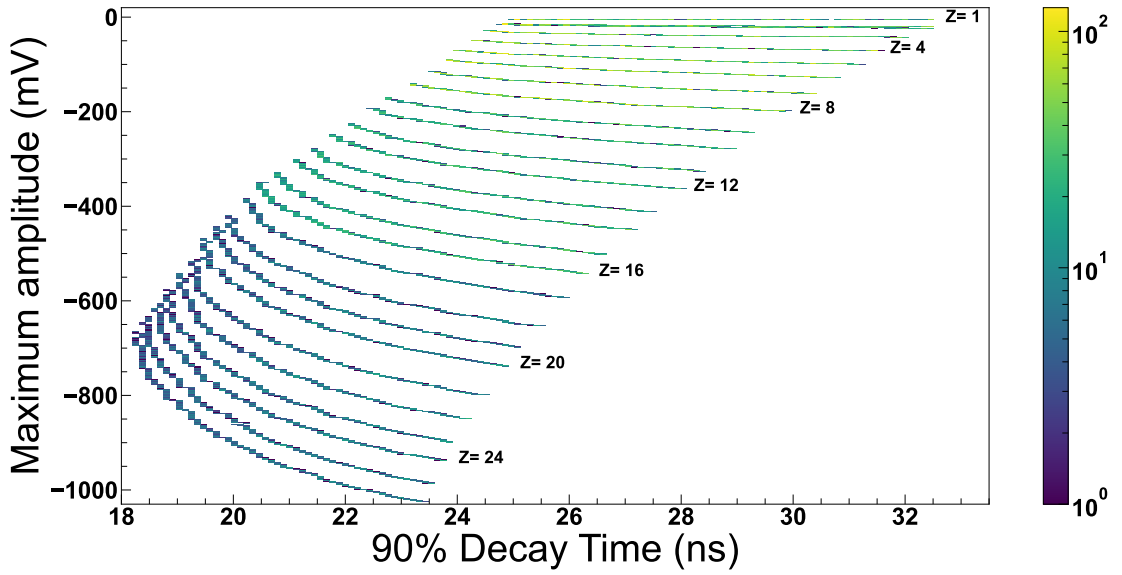

Figure 4.28: The maximum amplitude of the signal generated by ions (H-Fe) stopping in a detector layer are reported as a function of the their decay time at 90% of the peak amplitude value.

and varies according to the particles types, and initial conditions. When including the contribution of the additional sources, the identification bands become larger and, in some cases partially overlap resulting in a drop of identification effectiveness. The noise introduced by the response of the electronic chain modifies the spectrum of the generated signals, while the jitter smears out the resolution of the time measurements. The dynamic range of operation of the read-out electronics is also affected by thermal fluctuations, that can result in subtle drifts of the transistors gain. The comprehensive study of AGILE PSD simulated capabilities, published in (45), lists the contribution of individual uncertainties.

The full simulation results find the main source of uncertainty when considering the detector full field-of-view, and the resulting spread in the direction of incoming particles. When summing all these contributions AGILE demonstrate to fulfill its nominal requirements, providing 100% efficient particle discrimination with an energy resolution of less than 5%. (45) reports in detail the performed studies.

	MSD040	MSD020
Active Area (diameter)	40.00 mm	20.00 mm
Typical Full Depletion (FD)	<60 V	<60 V
Typical Total Leakage current at FD	<5 nA	<10 nA
Total Leakage current (at FD +10V)	<10 nA	<25 nA
Vb @ 10uA	>100 V	>300 V
Typical Vf@ 10mAV	<0.80 V	<0.65 V
Capacitance (FD)	40 pF/cm2	40 pF/cm2

Table 4.2: Technical details of the two Si detectors tested in the choice of AGILE performing sensors.

4.5 Characterization of AGILE read-out

Before the assembly and tests of the telescope electronics chain, and in preparation for a test beam campaign, the performance of the AGILE components were individually evaluated at the University of Kansas laboratory facilities. We will now describe the tests of the individual detector elements, starting from the sensor characterization and selection. While retracing the optimization procedures needed to improve the performance of the FEE cards, this section also provides the results obtained in the preliminary analysis of the detector response to a $\sim$5.5 MeV alpha radiation source (^{241}Am)

4.5.1 Selecting the sensor solution

Two models of silicon detectors produced by Micron Semiconductor Ltd (213) were tested during the prototyping phase of the AGILE apparatus. The vendor was selected thanks to the space inheritance of their productions. Silicon sensors produced by Micron have in fact already been employed in the development of NASA-founded space experiments. This ensures mechanical and electrical stability of the detectors during their launch and data acquisition. Table 4.2 summarizes their technical attributes.

- **MSD040 - p type**

  Two MSD040 - p type, 40 mm diameter circular Si sensors were tested to verify their performance. The components were mounted using epoxy bi-component glue (EPO-TEK EJ2189-LV) (214) to the phase-1 FEE cards described in the next section 4.5.2. Initially the sensors were wire bonded with $\sim$1 cm long aluminum wires to the bias circuit of the FEE cards and

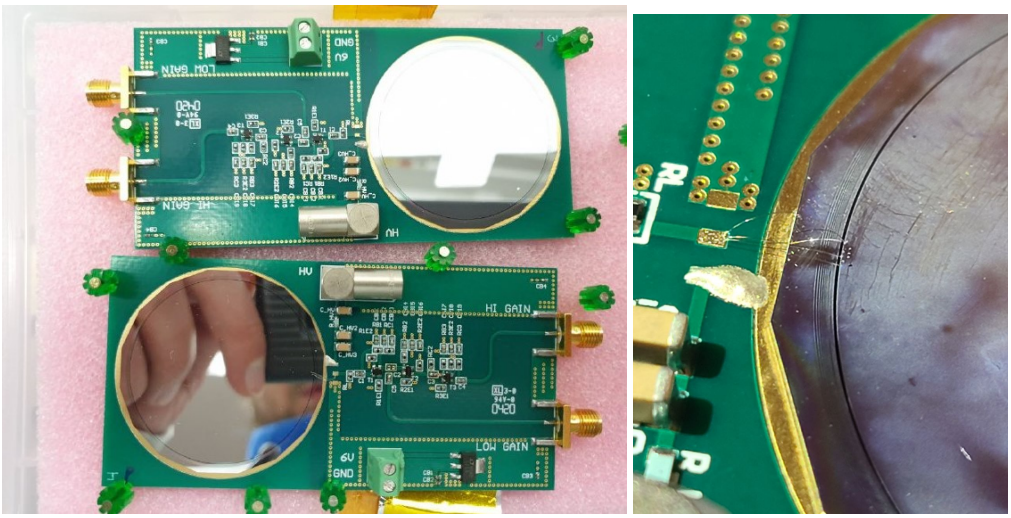

Figure 4.29: Left: picture of the two detectors under analysis, glued and connected to the prototype FEE cards. Right: detail of the wires used to provide a ground reference to the sensor.

powered up using a Keithley 2410 SourceMeter (83). The cards are shown in Fig. 4.29 Using an automatic analysis implemented in Python3 (97) a scan was performed over a range of applied voltages. During the scan, the absorption was measured in real-time with a precision of nA. Figure 4.30 shows early results that point out a behaviour dissimilar from the one predicted by the detectors nominal features. Although the I-V curve of the sensor glued on card#4 (bottom panel of Fig. 4.30) seems to show values consistent with the vendor provided specifications, the current recorded for V < $V_{depletion}$ resulted higher than the nominal one (> 1μA at $\sim$20 V). In contrast, card#3 (top panel) presented clear discrepancies in its current absorption as the I-V curve reaches the compliance level of the Keithley power supply (105μA) before -100 V.

In order to rule out effects of stray superficial currents[5] coming from the interface between the sensors, the epoxy glue, and the bias pad, the two detectors were subjected to a series of cleaning procedures. In order to rule out instabilities of the bias circuit, the bonding wires were initially removed to then undergo an ultrasound cleaning process; the two sensors were treated with different solutions: solely isopropyl alcohol was used for cleaning card#4 while card#3 was submerged in AIMTERGE 520A (215) solder cleaner. To reduce the risk of short circuits or discharges, the latter needed additional cleaning (acetone) after a closer ob-

[5]When subjected to a difference of potential, the conducting components (glue and bias pad) can create fringes of the electric field producing local discharges.

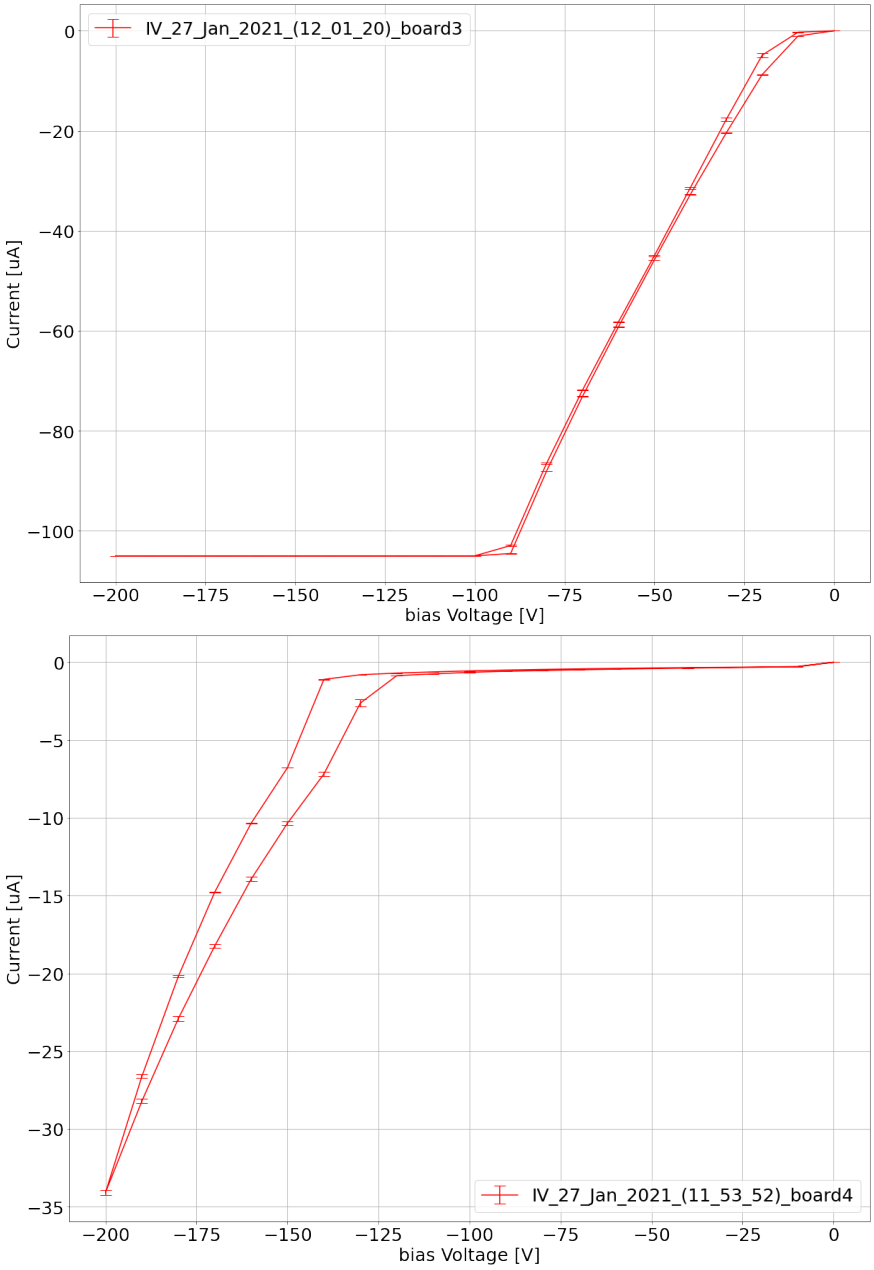

Figure 4.30: Early results of the I-V curve obtained for the two p-type detectors under analysis. Top panel, results obtained with card#3 that presents issues in the current behaviour as it drastically increase, dramatically breaking away from the sensor's nominal features. Card#4 shows a good behaviour for higher bias voltage $V_b > V_{depletion}$ but the absorption results to be high (larger than 1 μA) for lower bias.

servation of the Silicon edges revealed traces of conductive epoxy glue. The I-V curve shown in Fig. 4.31 was collected following the aforementioned procedures and demonstrates the recovered nominal features of the sensor. Following the cleaning process, the current absorbed

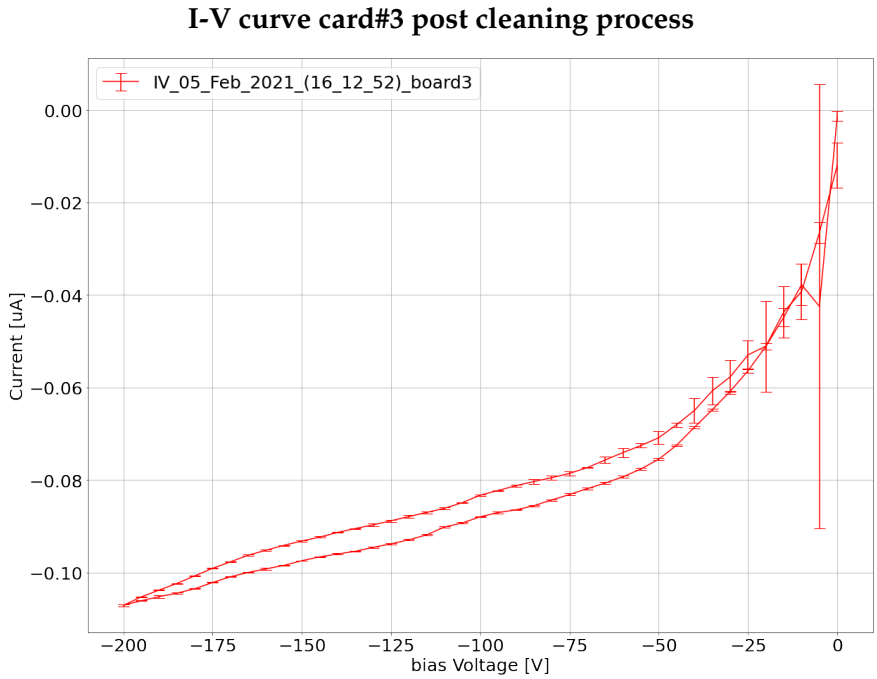

Figure 4.31: I-V curve obtained using the detector bonded on card#3 after the cleaning procedures. The current was recorded using the power supply reading mode (less than 1 nA precision).

by the detector connected on card#4 still presented some instabilities. The sensor was then unglued from the read-out card and the silicon was cleaned using a bath of Toluene[6]. As a result of this cleaning measure the surface of the sensor developed oxidized spots, depicted in Fig. 4.32. Determined to eliminate any eventual effect introduced by the glue, the Si detector was mounted on a different setup where the bias and grounding contact were externally supported (see Fig. 4.33). The readings were still provided by a Keithley source meter. Although the results of Fig. 4.34 indicate the correct functionality of the detector, card#3 was selected for the following steps of data collection.

- **MSD020 - n type**

  The MSD020 sensor differs in comparison to the previous sensors, since it possesses negative doping type and a smaller active area. Changes in the size of the detector result in important modifications of the instrument structure as the geometrical acceptance of the telescope is decided by the minimum solid angle for complete particle reconstruction. A smaller active area results in a smaller solid angle and, consequently, a lower maximum event rate. Gluing

[6]Toluene is a substituted aromatic hydrocarbon. It is sold as a colorless and water-insoluble liquid and is often used in solvents and paint thinners. It was selected for it's ability to act as a solvent with epoxy glues.

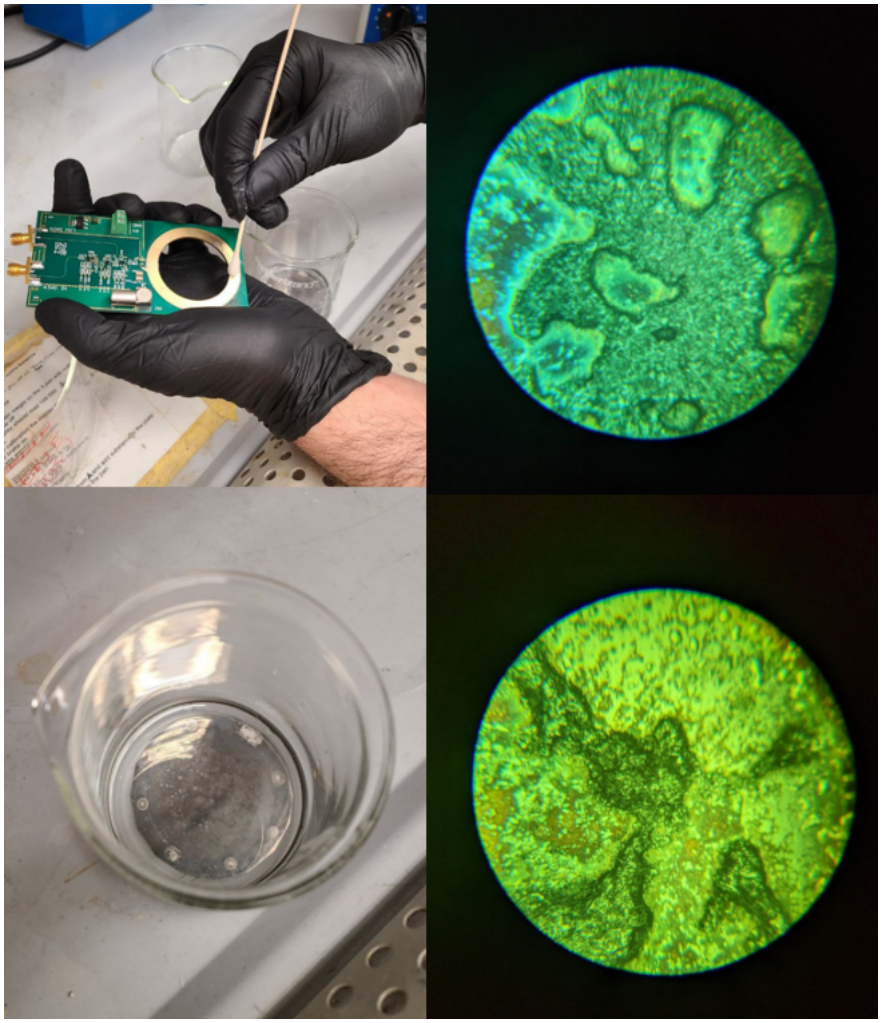

Figure 4.32: The panels on the left (top and bottom) show the two steps procedure of the detector cleaning using Toluene. The panels on the right give an up close view of the oxidized electrodes created from the Toluene bath.

and wire bonding the silicon sensors for space-grade detectors is a complicated procedures requiring dedicated machinery and careful operation. Micron Semiconductor Ltd (213) provides the option of purchasing MSD020 sensors encased in packages with pre-made external HV, guard ring and signal connections, which ease the testing procedures and the detector assembly. The detector is described in Fig. 4.35. A first analysis of the current was performed. The results are described by the plots in Fig. 4.36 and they assessed the MSD020 n-type Si sensor to operate according to nominal technical specifications. Without any additional optimization required, the detector was then bonded to one of the FEE cards.

n-type bulk Si detectors (with particles entering from the bias side of the sensor) are historically

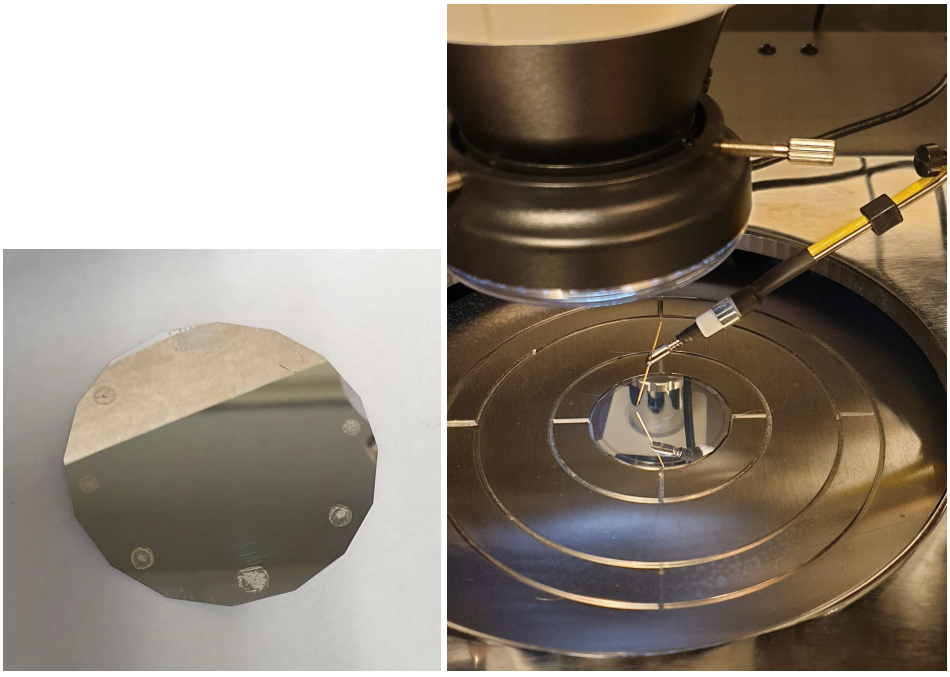

Figure 4.33: left: picture of the silicon detector unglued form card#4; the remnants of the epoxy can be spotted on the metalized surface. Right: the chuck of the probe station (described in a previous chapter 2) provides the bias voltage on the conductive back panel of the sensor. The current is read with the use of tungsten/gold probe.

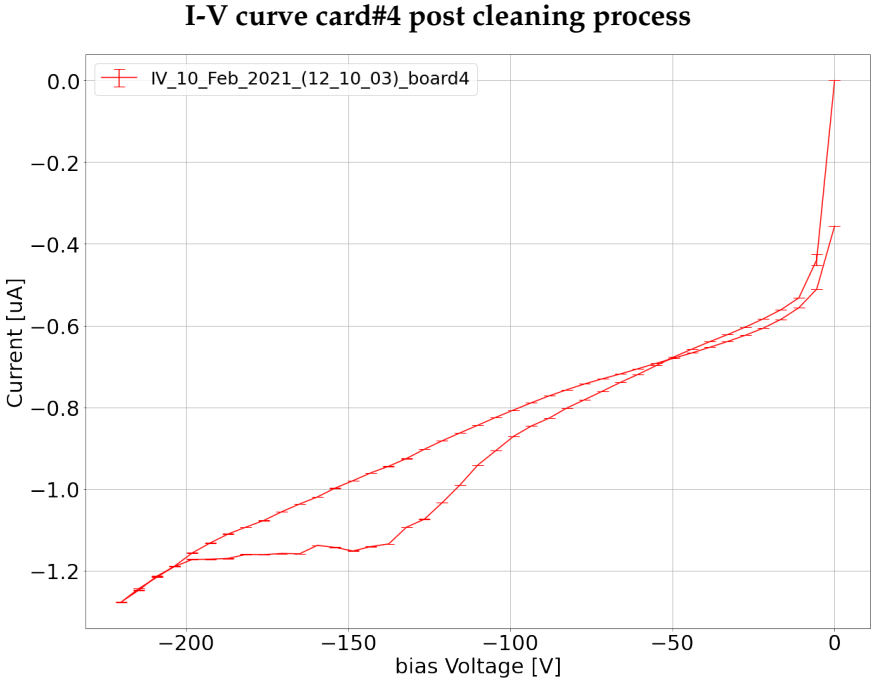

Figure 4.34: After the cleaning process of card#4, the current shows nominal trend as a function of the bias voltage applied.

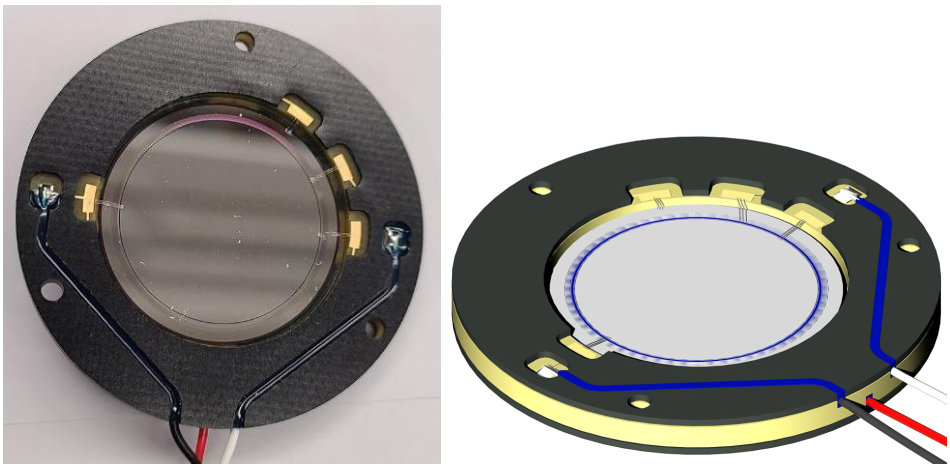

Figure 4.35: 3D render (left) and picture (right) of the MSD020 Si sensor produced by Micron Semiconductor Ltd, encased in the package and provided with external connections: the active front junction (black), the rear ohmic (red), and the guard ring (white).

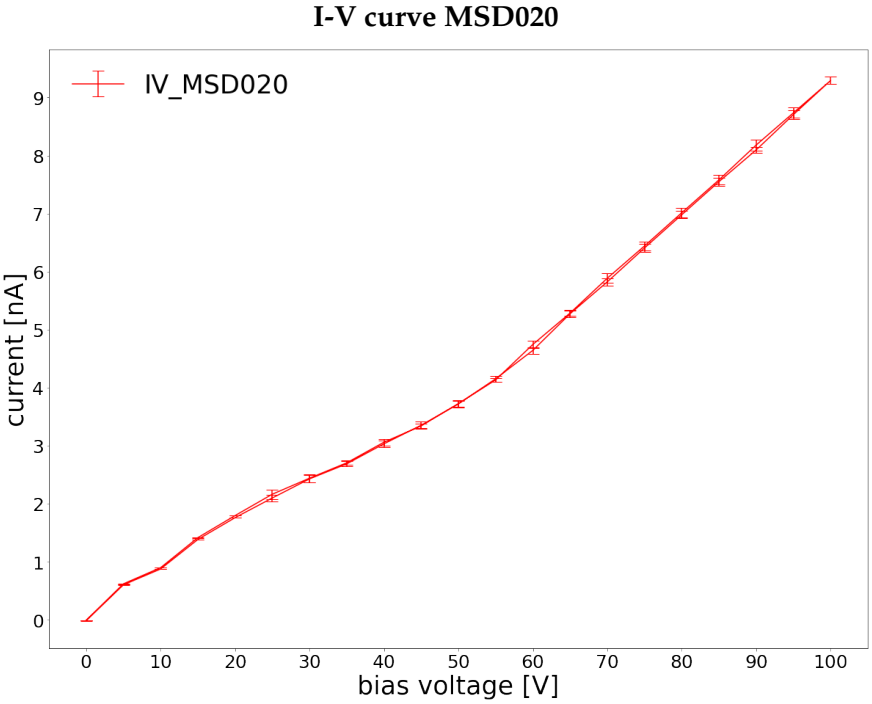

Figure 4.36: The I-V curve of the MSD020 20mm p-type Si sensor validate its correct operation.

the most commonly used for PSD, Config1:pback (as displayed in Fig. 4.20) was the configuration We selected. This configuration uses p-type sensors assembled to receive incident particles from the far side, with respect to the p-n junction. Comparing the simulations, the p-type doping makes for a safer option as the signals qualities remain similar for either particle direction of incidence (pback, pfront of Fig.. 4.20 and Fig. 4.22).

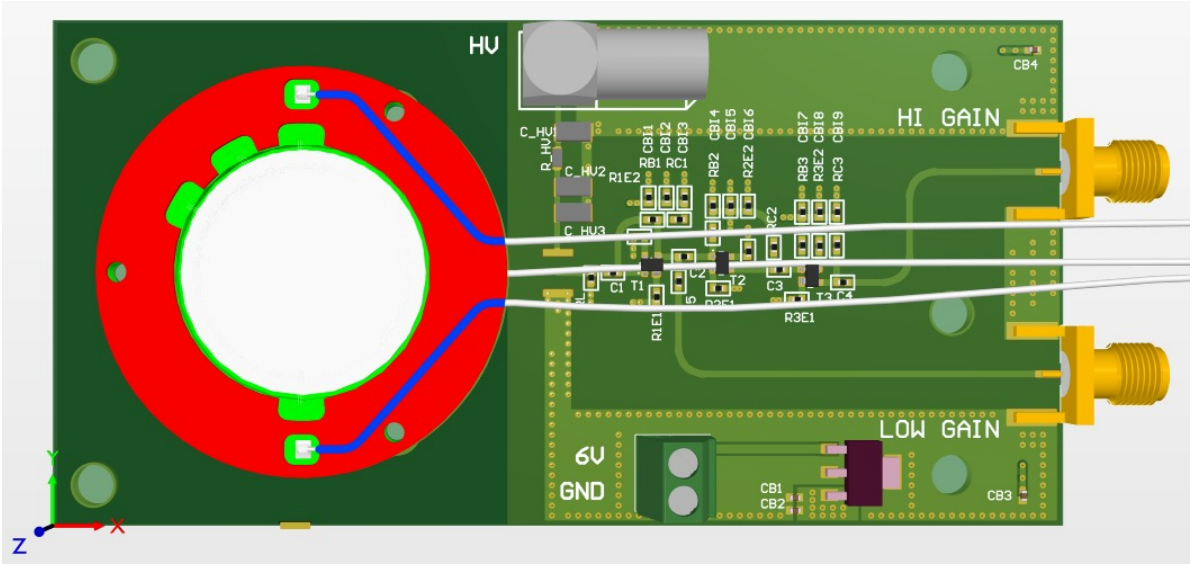

Figure 4.37: 3D render of the v1 FEE-card desinged to test the detectors. The render includes a depiction of the MSD020 provided of front/back planes and guard ring connections and positioned on top of the gold pad.

4.5.2 FEE card preliminary design

A first FEE-card prototype was initially test to validate the functionality of the double-gain readout design (detailed in section 4.4.2) The PCB included an HV pad used to provide the bias voltage to the silicon sensors, as well as the whole amplification chain preceding the sampling devices. A picture of the card and a 3D render of the circuit can be found in Fig. 4.37.

The section of the schematic dedicated to the sensor's polarization is designed to provide stable bias up to few hundred Volts. For polarizing the SiGe BJT transistors and achieving the components correct working point in the various stages of amplification, the circuit uses a 3.3 V line. A voltage regulator working in range up to $\sim$9 V allows to ramp down the voltage to provide the desired values. The FEE-cards developed for the first prototyping phase hosted the MSD020 - n type sensors described in section 4.5.1. Since the circular Si detectors are encased in the plastic package provided by Micron Semiconductor Ltd. (see Fig. 4.35), the sensors can't be glued directly to the golden HV pad. Their backplane is instead connected to the bias circuit using the test wires; their guard-ring and front plane wires are connected, respectively, to the ground line and input of the pre-Amplifier stadium, therefore generating the drifting field inside the Si bulk.

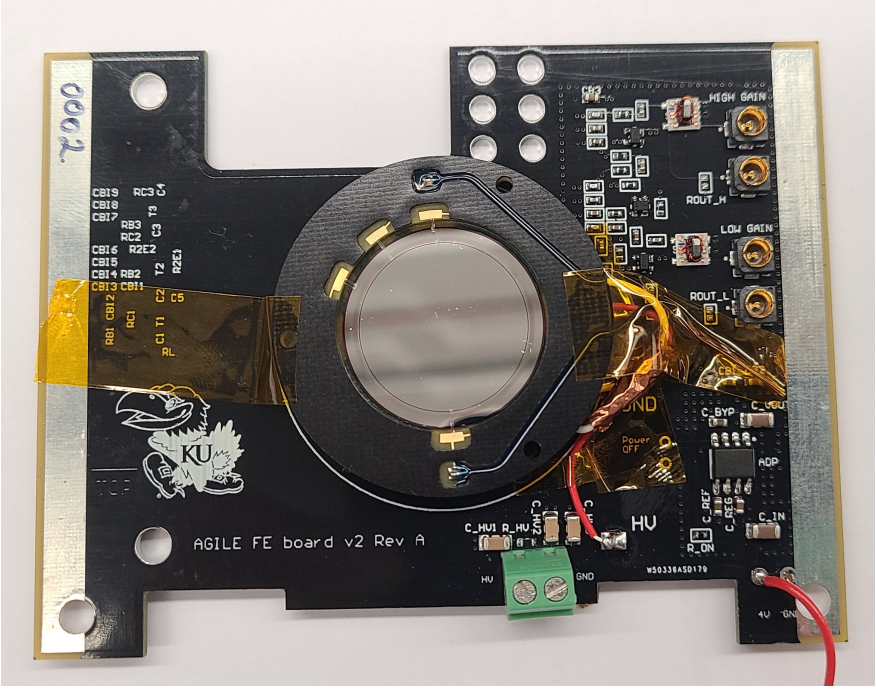

Figure 4.38: Fully assembled AGILE version 2 FEE card, comprised of the dual-gain electronic read-out and silicon sensor.In this prototype the size and shape of the FEE cards are adapted for fitting inside the form factor of the CubeSat. Since the final instrument design expects the presence of a redundant digitizer, in this version each one of the amplification line, high and low-gain, are split in two 50 Ω terminated outputs.

4.5.3 FEE cards: towards a final design

In the production of a new prototypes, the schematic and population of the card were designed to reproduce the final requirements for the AGILE instrument. In particular, the shape and size of the PCB are optimized to fit inside the harness of the CubeSat mock-up (described in section 4.5.4) and facilitate the connection of the detector components. The new FEE cards host a second version of the amplification chain described in section 4.4.2, which differs from the first produced circuit (described in section 4.5.2) only by the choice of the transistor on the last amplification stages. In this updated version, depicted in Fig. 4.38, the sensor occupies the center of the FEE card and the wires connecting the MSD020 4.5.1 are kept close (less than 1 cm) from the grounding and signal bonding pads.

Aside from the board population and slightly optimization of the power distribution, the FEE cards are designed to have similar performance to the previously produced in terms of amplification and noise levels. The standard of the high-bandwidth coaxial output connectors was also

modified (from SMA to MMCX) to comply with the stringent space requirement of the detector stack.

4.5.4 Characterization tests

In order to reproduce the environment of the GenSat-1, the characterization tests were performed enclosing the FEE cards in an aluminum mock-up of the CubeSat payload. A MSD020 4.5.1 silicon sensor was connected to one of the FEE cads and reverse-biased using a Keithley 2410 SourceMeter (83). The amplification stages were powered through the installed voltage regulator which converted the 5 V DC coming from a battery pack or, alternatively, a standard USB connector. The full bandwidth capabilities (4 GHz) Teledyne-LeCroy WaveRunner 640Zi oscilloscope (86) was used to sample the output waveforms with a 13 GSa/s sampling rate over a 300 ns acquisition window.

A ^{241}Am [7] and a ^{90}Sr [8] radiation sources provided the particles to conduct the tests at the KU laboratory. During the tests the detector was operated using a reverse-bias voltage of 60 V, which ensured its full depletion (depletion voltage around 36 V). The threshold level of the digitizer trigger was set to 2 mV. A dedicated algorithm developed with Python3 (97) controls the interface with the oscilloscope. It starts the data acquisition using the segmented mode of the digitizer (oscilloscopes segmented modes are described in section 2.3.1). The number of segmented acquisition can be also controlled.

The algorithm stores data in .h5 files, containing a number of features to perform off-line reconstruction of the waveforms. In particular, the algorithm is capable of recording the oscilloscope `horizontal offset`, `horizontal scale`, `sample number`, `trigger offset`, `time of trigger`, `vertical offset`, and `vertical scale`. These information are processed by the analysis framework. The data is first filtered using a low-pass filter with a cut-off frequency set to 400 MHz. The waveforms are smoothed out of further distortions using a moving average (described in section 1.1.4). The amplitude distribution for the two independent channels, low gain and high gain. The decay time is then measured, using the 90% of the maximum peak amplitude. The analysis framework is design to process the current pulses generated with the LTspice elec-

[7] α-particles with energies 5.486 MeV (85%), 5.443 MeV (13%), and 5.388 MeV (2%).
[8] β radioactive source producing electrons in a continuous spectrum up to 2.3 MeV.

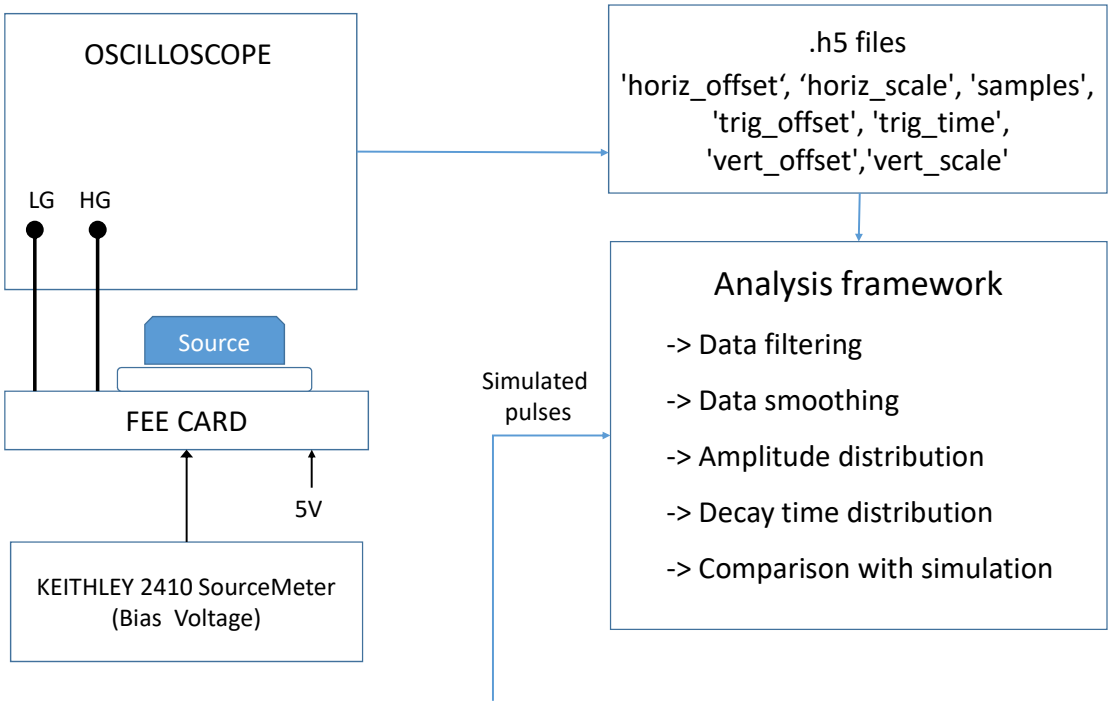

Figure 4.39: Diagram of the full acquisition test used during AGILE FEE card characterization.

tronics simulation software. This expedient enables the direct comparison of the results with the modeled predictions. Figure 4.39 reports a simplified scheme of AGILE characterization setup at the KU laboratories. A first comparison between the simulated and the reconstructed results can be observed in Fig. 4.40 top and bottom panel, which shows overlapped pulses respectively for the Low-gain and High-gain channels.

From these plots, one can observe the low-gain response rising to an average maximum amplitude of around 6 mV with a typical rise times of around 19 ns; at the same time interval the amplitude of the high-gain channel reaches about 470 mV. Both high and low-gain are characterized by long distributions tails due to a slower decay time of around 100 ns. The SNR was calculated to be of $\sim$25 for the low-gain and $\sim$45 for the high-gain. Their amplitude and 90% decay time distribution (chosen as a key feature for the PSD implementation, discussed in section 4.4.5) are better observed in the individual histograms in Fig. 4.41 and Fig. 4.42.

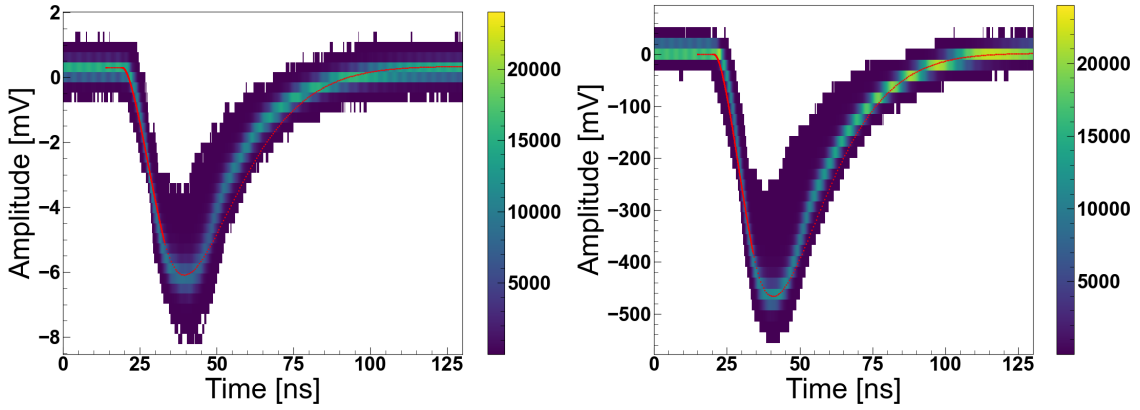

Figure 4.40: ^{241}Am results: Density histograms of the digitized signals sampled by the oscilloscope and reconstructed by the analysis software. The resulting spectrum output by the low-gain (bottom panel), and high-gain (top panel) are overlapped with the simulation results (solid red line). It has to be noted that, for accurate comparison, the high-gain simulation required a scaling factor of 2.2. Plots are extracted from the proceeding submitted to IEEE Transactions on Nuclear Science.

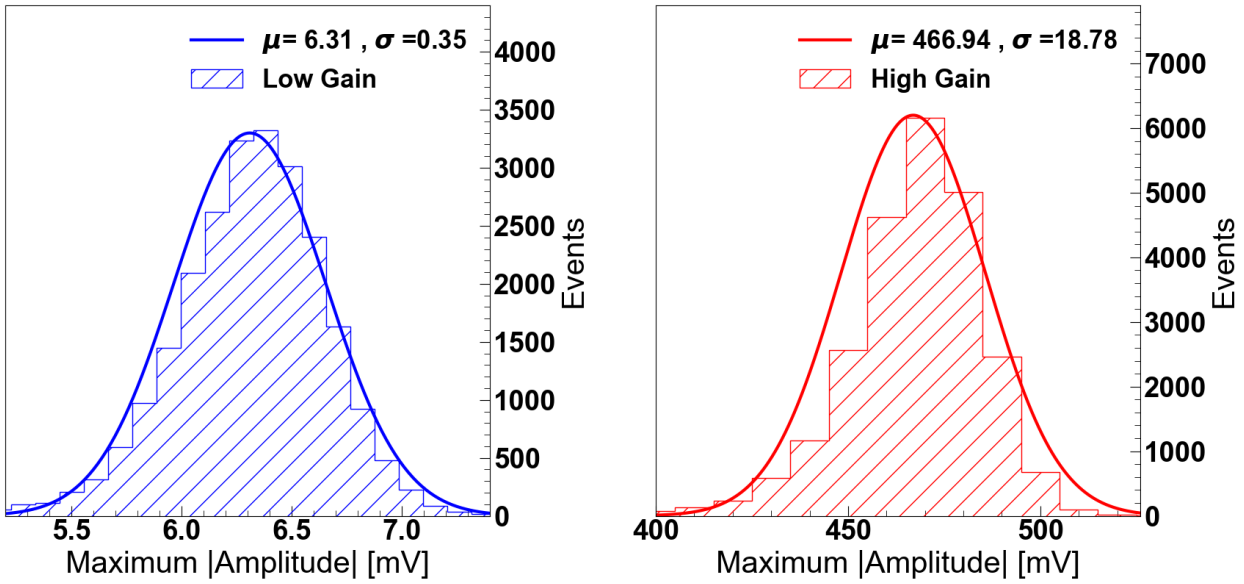

Figure 4.41: ^{241}Am results: Amplitude distribution obtained with both channels of the AGILE FEE card (44).

Fig. 4.43 shows the two variables and their correlations using 2D histograms. As expected, the data collected with the use of a mono energetic α-source distributes in clusters, and can be compared with individual data points in amplitude vs 90% decay time plots obtained from the simulation results (described in section 4.28). The promising agreement found between the collected data and simulated data work as a proof of concept for the PSD strategies implemented by

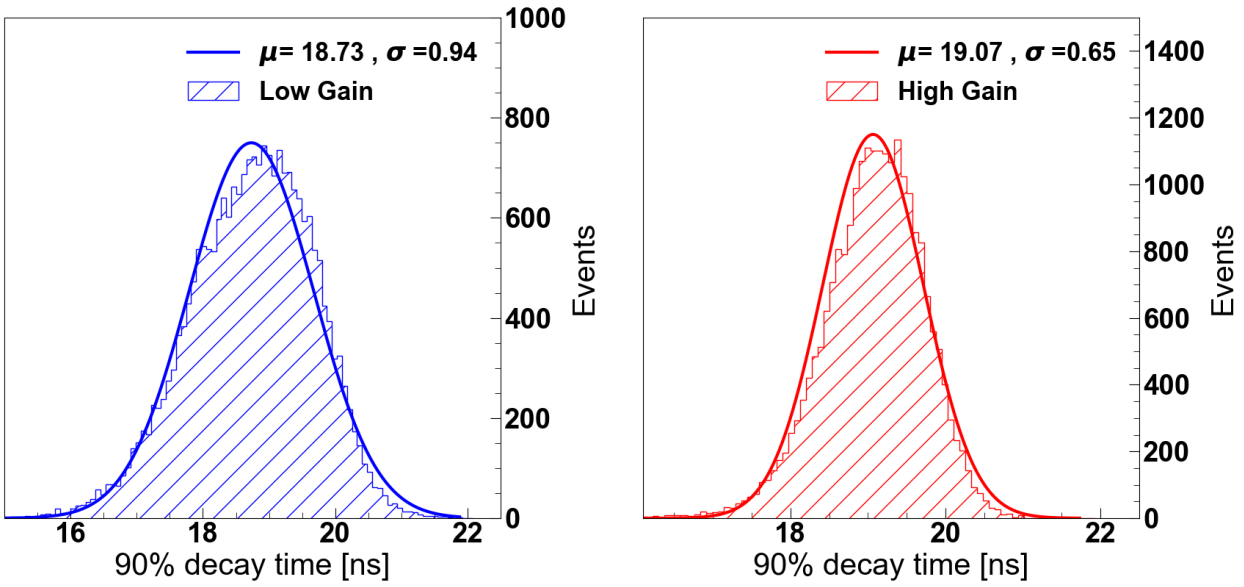

Figure 4.42: ^{241}Am results: 90% decay time distribution obtained with both channels of the AGILE FEE card (44). This value was selected during the comprehensive simulation studies described in (45).

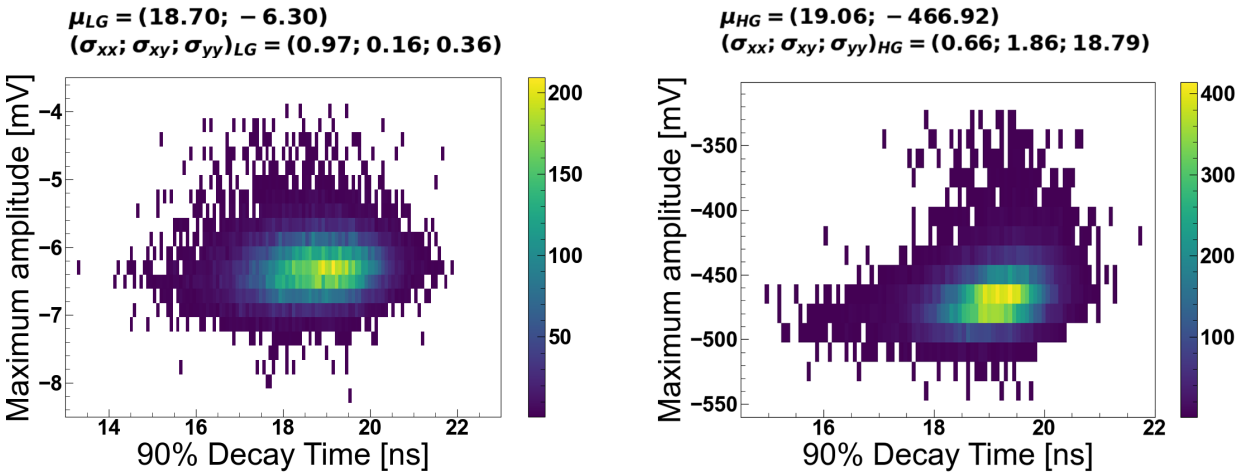

Figure 4.43: ^{241}Am results: Maximum amplitude distribution as a function of the 90% decay time for the low-gain (top panel), and high-gain (bottom panel). The value of the means, their uncertainty, and correlations are expressed on top of the canvases (44).

the AGILE instrument, displaying amplitude resolution of around 5.1% for low-gain, and 3.5% for high-gain measurements with the radiation source utilized. The simulation performed shows a linear correlation between the pulses amplitude the deposited energy. However, energy calibrations will be needed to directly verify the energy resolution of the instrument.

Although the detection of electrons does not represent the first priority for the AGILE pro-

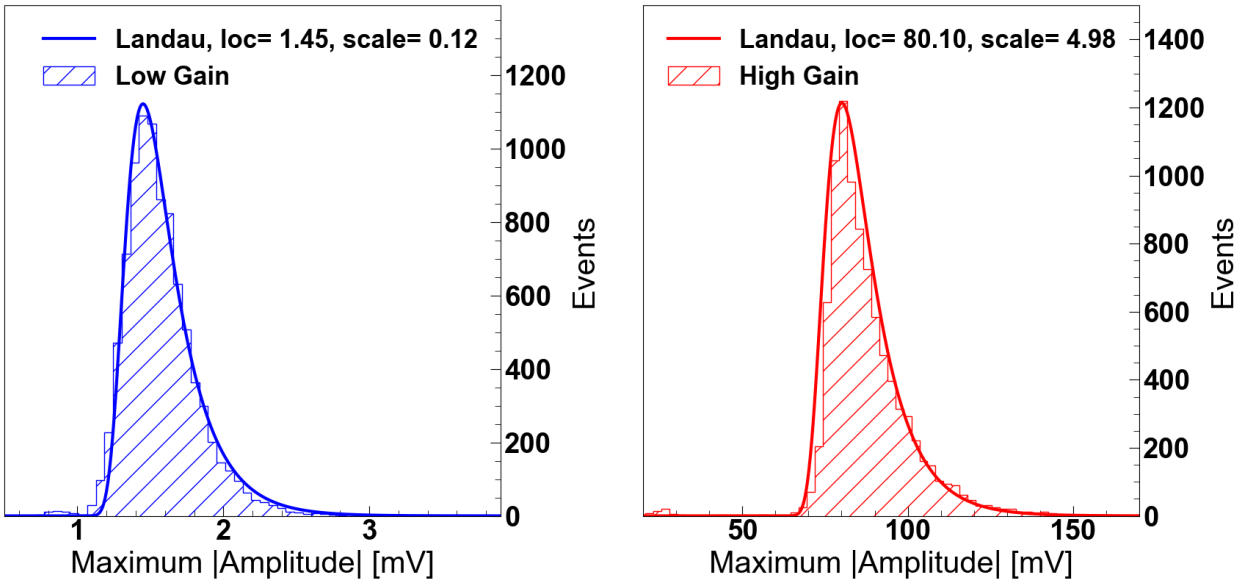

Figure 4.44: Pulse height distribution of the ^{90}Sr source. The typical long tails are characteristics of the Landau energy deposition fluctuations of electrons crossing silicon.

totype, the same studies can be repeated with the use of the ^{90}Sr source and provide additional validity to the method. The histogram of the recorded amplitudes (in Fig. 4.44) are distributed as a Landau (and its convolution with a Gaussian due to the detector resolution effects), which characterize the signature of the electrons energy deposition in silicon.

4.6 Chapter summary

This chapter follows the R&D behind the first prototype of the AGILE detector. The device is a result of the combined effort at KU and NASA Goddard Space Center, representing the first attempt at real-time particle identification in space using a compact stack of silicon sensors. AGILE inherits some of its characteristics from previous timing detectors developed at KU, borrowing similar layout of its read-out electronic chains, as well as digitization and sampling techniques. The instrument, fully designed to be contained inside 1U of a CubeSat, will implement novel pulse discrimination methods for the on-board discrimination of particles in a vast range of energy. These techniques have been thoroughly simulated and compared with pre-existent methods for evaluating the identification performance with elements ranging from H to Fe. The simulation framework also includes the read-out electronic response, mimicking the FEE cards performance variation due to the extreme operation conditions in space. While accounting for the electronic

noise, as well as the intrinsic fluctuation of energy deposition and carrier numbers, the simulated results identify the main source of uncertainty in the angle of particles incidence, when considering the full detection field-of-view (28° of half-angle); the simulated particle identification capabilities of AGILE's PSD will enable the identification of ions with an amplitude resolution less than 5% and particle ID discrimination efficiency up to 100%.

Part of the research work presented in this thesis includes the development of the detector apparatus of the first AGILE prototype. The quality of the sensors was initially tested, prior to the selection of the ones to be installed inside of the instrument. The detectors were populated and assembled at KU and their performance measured using a dedicated acquisition framework. The data were then reconstructed using a customized data analysis algorithm. The characterization of the FEE cards produced promising results when exposing the assembled detectors to radiation sources. The data collected reproduce the expected behaviour of the simulated instrument.

At present, the remaining hardware performance evaluation tests are being carried out at the laboratories at KU. At the same time, AGILE team is collaborating with GENESIS for finalizing the mechanical design and verifying the communications with the GenSat-1. The full detector stack is expected to be installed at a test beam facility for measuring its performance in the detection of different type of ions, prior to its launch.

Summary and Prospects

During this thesis We presented three different projects that utilize timing detection techniques. While embracing different fields of physics, the research work performed found a common thread in the design, development, and characterization of fast silicon detectors. This thesis aims to highlight the versatility of these devices, beginning with an explanation of their use in High Eneregy Physics (HEP) experiments, followed by examples of their implementation in other research fields. Due to their excellent performance, state-of-the-art timing detectors have been employed for developing synergies between particle physics and commercial applications.

We first presented the results obtained from the studies on precise timing detectors, designed to be installed inside the Compact Muon Solenoid (CMS). In preparation for the future Luminosity upgrades of the Large Hadron Collider (LHC), CMS is planning the installation of a new MIP Timing Layer (MTD) (18) to preserve its outstanding reconstruction efficiency. The new timing layer will populate the barrel, and end-cap regions of the experiments, covering a pseudorapidity of $|\eta| < 1.45$ and, $1.6 < |\eta| < 3$ respectively. Low Gain Avalanche Diodes (LGADs) were elected to be installed in the End-cap Timing Layer (ETL). The detectors are required to reconstruct the time of arrival of the collisions decay products with a precision better than 50-60 ps. Due to the extremely harsh radiation environment predicted for this new LHC era, the detectors must ensure stable performance, and $\sim$100% efficiency, up to absorbed doses of $3\times10^{15}\,\mathrm{n}_{eq}/\mathrm{cm}^2$ (corresponding to an integrated luminosity of $1.5\times3000\,\mathrm{fb}^{-1}$).

From 2016, the Collaboration embarked on R&D campaigns for the performance evaluation of the LGADs prior to the final production for the ETL installation. The characterization tests were conducted at the FERMILAB Test Beam Facilities (FTBF), which provided energetic proton beams (120 GeV) with moderate frequencies (53 MHz). The LGADs were produced by three major vendors, Fondazione Bruno Kessler (FBK) (89; 90), Hamamatsu Photonics (HPK) (91), and Centro Nacional de Microelectronica (CNM) (8; 49), all of whom provided samples of different sensors sizes, doping configurations, and overall responses. The data collection required for an installation of

a fast sampling system at the FTBF testing site (93). A custom-made algorithm was designed the integration of the timing measurements with the Data Acquisition System (DAQ), and enabled the combined data acquisition of tracking and timing experimental apparatus. This process included the development of an independent data analysis framework, used to assess the performance of the Devices Under Test (DUTs). From the timing analysis, We observe excellent performance of the tested LGADs. The precision of time of arrival reconstruction met the standard imposed by the ETL nominal requirements for every value of radiation exposure investigated. The timing precision of the detectors spanned from about 30 ps in non-irradiated sensors, to about 50 ps for detectors exposed to the maximum predicted dose (1.5×10^{15} n_{eq}).

The time precision of these detectors is affected by the decreasing of their Signal-to-Noise Ratio (SNR) due to accumulated radiation damages. For this reason, the analysis measures the stability of the detectors gain as a function of the absorbed dose. By construction, for preserving the nominal time precision, the total charge integrated per particle should never be lower than 5 fC. For the ETL sensors, this corresponds to gains exceeding 10. The results show that the charge collection efficiency of irradiated LGADs can be recovered to meet the nominal standard, by increasing the applied bias voltage. The produced data also highlights differences in the response to accumulated radiation for detectors with modified doping configurations. The insertion of carbons in the substrate of FBK sensors seems to work in favor of a better radiation hardness.

The presence of a tracking apparatus at the FTBF site also enabled the study of the spacial features of the detectors. From the spatial distributions of the hits occupancy, one can evince the uniformity and spatial efficiency of the DUTs. Studies of the signal amplitude show little spatial dependency in the integration of the charge over the full active area (about 2% spread in the pulse amplitude). Similarly, the efficiency studies produced satisfactory results for the batches of sensors tested. The hit distribution in pixelated arrays served for investigating the efficiency of the no-gain regions in between adjacent LGADs, and computing the average fill factor of the arrays.

The CMS experiment will benefit from the installation of the MTD in the mitigation of the pile-up events during the High-Luminosity LHC (HL-LHC) operation. The four-dimensional reconstruction coming from the particle tracks and timing information will reduce the number of misidentified vertices, enabling the observation of rare events with increased statistical validity (18). The detectors module of the ETL will take charge of the reconstruction of forward decays.

In addition to the characterization of the LGADs, the KU team is presently collaborating in the quality control of the sensors and read-out modules, using a customized setup assembled at the University laboratories.
LGADs provided of new doping structures are being characterized for evaluating the radiation resistance of new prototypes. The vendors are also investigating the possibility to reduce the ineffective areas between adjacent pixels, while preserving the electrical stability of the arrays. At the same time the CMS Collaboration is progressing towards the development of the ETL read-out and the characterization of the completed detection modules to meet the milestones of the MTD installation schedule. The results presented during this chapter of the thesis were utilized for the drafting of Technical Design Proposal (TDR) of the MTD (18).

Studies on LGADs performance were further expanded in the second project reported in this thesis, by testing their performance for monitoring a medical linear accelerator used for radiotherapy. In this context, a fast silicon detector was used for the reconstruction of individual particle occurrences. Typical clinical machines output spills of radiation (electrons or X-rays) lasting few microsecond within intervals of milliseconds. The dosimetric devices used for measuring the output fluences, often integrate the collected charge over few of the machine cycle. This makes them intrinsically blind to the structure of the beams. The results presented are the product of a Collaboration with the University College of Dublin (UCD) and the St.Luke's hospital of Dublin, Ireland. An LGAD connected to a fast read-out board developed at KU was used to monitor the electrons output of a medical LINear ACcelerator (LINAC) (161) at high deliver fluence. We assembled a setup for the data collection that included a dedicated acquisition system for controlling the operation of a performing digitizer. The features of the detectors allowed the reconstruction of the temporal structure of the machine spills (3.2 μs long) by resolving individual particles. That was achieved thanks to the fast integration time of the detector, equaling a dead-time between consecutive measurements of about 10 ns.

The analysis conducted demonstrates the capabilities of the LGAD in charge integration, comparing the results with the one obtained using a traditional ion chamber. The comparison between the two data sets display a linear correlation. It has to be noted that, while the ion chamber employs multiple machine cycles to collect these results, the fast silicon detector outputs comparable results but with a resolution of 3 μs, and much higher granularity.

The single-particle resolution enabled the possibility to directly measure the delivered fluence by counting individual recorded events. The algorithm developed for the particle counting displays a linear behaviour up to values greater than $\sim$100 MHz, at which the identification efficiency starts decreasing. The algorithm fails in discriminating single events, in correspondence of consecutive particles pass through the detector within 6.5 μs.

The features of the doses delivered were studied with a time precision of about 50 ps. That allowed the first ever experimental observation of a medical LINAC beam substructure. By construction, this is characterized by pulses lasting 30 ps and separated by 350 ps, corresponding to a pulse frequency of about 2.8 GHz. The results of the analysis are in agreement with the nominal features of the machine: the oscillation of the periodical structure of the LINAC were measured to be 346 ± 3 ps.

The measurements reported were published published by Physics in Medicine & Biology (48) and provide a proof of concept for the design of medical detectors based on fast silicon sensors of new generation. LGADs could provide a promising alternative for precise evaluations of the dose in clinical environments. The design of dedicated read-out electronics could allow for drastically reducing the length of the produced signals: pulses ten times shorter would improve by an order of magnitude the detector single-particle resolution capabilities. Moreover, the excellent granularity of these devices is appealing for accurate spatial reconstruction of the beam profile. In order to cover larger areas, that requires a substantial increase in the amount of channels to be read out and digitized. Medical prototypes necessitates for the development of optimized sensors geometry, and dedicated front-end Application-Specific Integrated Circuits (ASICs). Fast detectors attracted the interest of the medical community for applications where rapid responses are required. In particular, the advent of LINAC capable of delivering increased fluences (FLASH radiotherapy (138)) in few ns will require the development of even more performing detectors. The commissioning of these machines for clinical treatments will rely on accurate investigation of their delivered dose profile over time.

In the last project reported in this thesis We presented the use of fast timing techniques for their implementation in particle Identification (particle ID). The AGILE instrument is the result of the combined effort of KU and NASA Goddard Space center and aims to achieve real-time identification of a vast variety of ions (from H to Fe) and energies (1-100 MeV/nuc). For that, the compact

and low power consumption experiment will use Pulse Shape Discrimination (PSD) (197) enabled by fast sampling techniques. In it's first prototyping phase, the instrument will be hosted inside 1 unit of the GENSAT-1 CubeSat (42), scheduled for flight during 2022. A stack of 3 silicon detectors connected to custom-made read-out electronics, and fast sampling devices is currently under development at KU.

The feasibility of the project was first evaluated using a comprehensive simulation framework developed by the team. The optimization of the detector geometry and acceptance, the required sensor features, as well as the amount of absorbing material to be employed were performed using the GEANT4 (20) software. GEANT4 was used in combination with Weightfield2 (206) for generating the expected currents produced by the silicon sensors. The results pointed to the best doping and detector size configuration for AGILE goals: the team selected 300 μm thick p-type silicon sensors for achieving the best PSD performance. To complete the simulation chain, the effects of the read-out on the output pulses have to be taken into account. For accounting for the vast ranges of predicted currents to be processed (from 10^{-6} A to 10^{-2} A), and for complying with the range of operation of the digitizing device downstream, the team opted for the design of a double gain read-out circuit. This provides a dual response with low amplification in cases of large energy deposits in the sensors, and vice versa. Finally, the full simulation was used to investigate the optimal identification features for PSD. using the correlation between the 95% of signal decay time and it's amplitude, AGILE will be able to discriminate ions with an amplitude resolution less than 5% and particle ID discrimination efficiency up to 100% (over an half-angle field-of-view of 28° of half-angle). The simulation results led to the drafting of the publication *'A novel technique for real-time ion identification and energy measurement for in situ space instrumentation'* (45)

The simulation results allowed to move forward with the characterization of the sensors. We evaluated the response of silicon detectors produced by Micron Semiconductor Ltd (213) and selected the ones to be mounted on early prototypes of the Front-End Electronics (FEE cards) cards. This step served as a first characterization of the electronics and in order to assess the best performing detector size. The investigation led to the production of the final FEE prototypes, designed to host silicon sensors with diameters of 20 mm.

The characterization tests of the new FEE cards were conducted at the KU laboratories. Using designed DAQ and analysis framework, the response of the assembled detectors were moni-

tored using radiation sources. The key identification features extracted with the analysis confirming good agreement with the predicted results. These results have been submitted and recently published by IEEE, in the scientific paper '*AGILE Instrument: Advanced Energetic Ion Electron Telescope*' (44).

Presently, the AGILE team is in charge of finalizing the acquisition firmware implemented in the PSEC4 (210) digitizing chip, as well as the data handling using commercial micro-controllers. The GENESIS team is characterizing the handshake between the instrument and the main processor unit. Prior to its launch, the assembled instrument is scheduled to be tested inside the Brookhaven National Laboratory (BNL) testing facilities. The energy calibration will be performed using beams containing most of the ion species predicted for standard operations of the detector in space. This procedures will be needed to correlate the pulse amplitude to the energy deposits and quantify the instrument's energy resolution.

Bibliography

[1] C. Collaboration and T. Mc Cauley, "Collisions recorded by the CMS detector on 14 Oct 2016 during the high pile-up fill," Nov 2016, cMS Collection. [Online]. Available: https://cds.cern.ch/record/2231915

[2] C. Williams, "Particle identification using time of flight," *Journal of Physics G: Nuclear and Particle Physics*, vol. 39, p. 123001, 10 2012. [Online]. Available: https://doi.org/10.1088/0954-3899/39/12/123001

[3] N. Catiglia, "Ultra-fast silicon detector," Public talk, DESY, 2015. [Online]. Available: https://instrumentationseminar.desy.de/sites2009/site_instrumentationseminar/content/e70397/e187805/e196171/UFSD_Cartiglia.pdf

[4] V. Morisbak and F. Ould-Saada, "Search for new physics with atlas at lhc - z' dilepton resonance at high mass," 02 2022. [Online]. Available: https://cds.cern.ch/record/1327635?ln=en

[5] W. Commons. (2007) Pn junction in thermal equilibrium with zero bias voltage applied. [Online]. Available: https://commons.wikimedia.org/wiki/File:Pn-junction-equilibrium-graphs.png

[6] S. Bongu, P. Bisht, T. V. Thu, and A. Sandhu, *Multiple Nonlinear Optical Response of Gold Decorated-Reduced Graphene Oxide-Nanocomposite for Photonic Applications*, 01 2015. [Online]. Available: https://www.researchgate.net/publication/289790915_Multiple_Nonlinear_Optical_Response_of_Gold_Decorated-Reduced_Graphene_Oxide-Nanocomposite_for_Photonic_Applications

[7] M. C. Jiménez-Ramos *et al.*, "Study of ionization charge density-induced gain suppression in lgads," *Sensors*, vol. 22, no. 3, 2022. [Online]. Available: https://www.mdpi.com/1424-8220/22/3/1080

[8] G. Pellegrini *et al.*, "Technology developments and first measurements of low gain avalanche detectors (lgad) for high energy physics applications," *Nuclear Instruments and Methods in Physics Research Section A: Accelerators, Spectrometers, Detectors and Associated Equipment*, vol. 765, pp. 12–16, 2014, hSTD-9 2013 - Proceedings of the 9th International "Hiroshima" Symposium on Development and Application of Semiconductor Tracking Detectors. [Online]. Available: https://www.sciencedirect.com/science/article/pii/S0168900214007128

[9] V. Sola *et al.*, "Ultra-fast silicon detectors for 4d tracking," *Journal of Instrumentation*, vol. 12, no. 02, pp. C02 072–C02 072, feb 2017. [Online]. Available: https://doi.org/10.1088/1748-0221/12/02/c02072

[10] V. Sola et al., "Ultra-fast silicon detectors for 4d tracking," *Journal of Instrumentation*, vol. 12, pp. C02 072–C02 072, 02 2017. [Online]. Available: https://doi.org/10.1088/1748-0221/12/02/C02072

[11] B. Baldassarri, N. Cartiglia, F. Cenna, H. Sadrozinski, and A. Seiden, "Signal formation in irradiated silicon detectors," *Nuclear Instruments and Methods in Physics Research Section A: Accelerators, Spectrometers, Detectors and Associated Equipment*, vol. 845, pp. 20–23, 2017, proceedings of the Vienna Conference on Instrumentation 2016. [Online]. Available: https://www.sciencedirect.com/science/article/pii/S0168900216305514

[12] L. Castillo García, E. L. Gkougkousis, C. Grieco, and S. Grinstein, "Characterization of irradiated boron, carbon-enriched and gallium si-on-si wafer low gain avalanche detectors," *Instruments*, vol. 6, no. 1, p. 2, 2022. [Online]. Available: https://www.mdpi.com/2410-390X/6/1/2/htm

[13] E. Mobs, "The CERN accelerator complex - 2019. Complexe des accélérateurs du CERN - 2019," Jul 2019, general Photo. [Online]. Available: https://cds.cern.ch/record/2684277

[14] T. Sakuma, "Cutaway diagrams of cms detector," in *J. Phys.: Conf. Ser. 513 022032*, no. CMS-OUTREACH-2019-001, 2019. [Online]. Available: http://cds.cern.ch/record/2665537

[15] W. Adam *et al.*, "The cms phase-1 pixel detector upgrade," *Journal of Instrumentation*, vol. 16, no. 02, p. P02027, 2021. [Online]. Available: https://iopscience.iop.org/article/10.1088/1748-0221/16/02/P02027

[16] A. Bartoloni *et al.*, "The cms ecal barrel hv system," *Journal of Instrumentation*, vol. 8, p. C02039, 02 2013. [Online]. Available: https://iopscience.iop.org/article/10.1088/1748-0221/8/02/C02039/meta

[17] J. Molina, C. Warsaw, K. Pozniak, R. Romaniuk, and W. Zabolotny, "Performance of cms hadron calorimeter," *Journal of Instrumentation*, vol. 5, p. T03012, 03 2010. [Online]. Available: https://iopscience.iop.org/article/10.1088/1748-0221/5/03/T03012

[18] J. N. Butler and T. Tabarelli de Fatis, "A MIP Timing Detector for the CMS Phase-2 Upgrade," Tech. Rep. CERN-LHCC-2019-003, CMS-TDR-020, 2019. [Online]. Available: https://cds.cern.ch/record/2667167

[19] "Prospects for HH measurements at the HL-LHC," CERN, Geneva, Tech. Rep., 2018. [Online]. Available: http://cds.cern.ch/record/2652549

[20] S. Agostinelli *et al.*, "Geant4-a simulation toolkit," *Nuclear Instruments and Methods in Physics Research Section A Accelerators Spectrometers Detectors and Associated Equipment*, vol. 506, p. 250, 07 2003. [Online]. Available: https://www.sciencedirect.com/science/article/pii/S0168900203013688

[21] "Nicolo cartiglia ufsd update ctpps october 2015 ufsd," https://indico.cern.ch/event/577879/contributions/2740418/attachments/1575077/2487327/HSTD1--HFWS1.pdf.

[22] N. Minafra *et al.*, "Tests of ultra fast silicon detectors," 21-22 March 2017, lHC Working Group on Forward Physics and Diffraction, CERN. [Online]. Available: https://indico.cern.ch/event/615051/contributions/2513118/attachments/1430949/2542416/UfSiAmplifier_TurinTests.pdf

[23] D. Breton *et al.*, "Measurements of timing resolution of ultra-fast silicon detectors with the sampic waveform digitizer," *Nuclear Instruments and Methods in Physics Research Section A: Accelerators, Spectrometers, Detectors and Associated Equipment*, vol. 835, pp.

51–60, 2016. [Online]. Available: https://www.sciencedirect.com/science/article/pii/S0168900216308373

[24] *Farmer©Ionization Chamber 30013 waterproof*, PTW, 2019/2020. [Online]. Available: https://www.ptwdosimetry.com/fileadmin/user_upload/DETECTORS_Cat_en_16522900_12/blaetterkatalog/index.html#page_12

[25] *Ionization Chambers*. John Wiley Sons, Ltd, 1986, ch. 12, pp. 292–345. [Online]. Available: https://onlinelibrary.wiley.com/doi/abs/10.1002/9783527617135.ch12

[26] M. Garcia-Inza *et al.*, "6mv linac characterization of a mosfet dosimeter fabricated in a cmos process," *Radiation Measurements*, vol. 117, pp. 63–69, 2018. [Online]. Available: https://www.sciencedirect.com/science/article/pii/S1350448718301586

[27] P. N. Shrivastava, "Medical electron accelerators by c. j. karzmark, craig s. nunan, and eiji tanabe," *Medical Physics*, vol. 20, no. 3, pp. 828–828, 1993. [Online]. Available: https://aapm.onlinelibrary.wiley.com/doi/abs/10.1118/1.596995

[28] M.-C. Vozenin, J. Hendry, and C. Limoli, "Biological benefits of ultra-high dose rate flash radiotherapy: Sleeping beauty awoken," *Clinical Oncology*, vol. 31, no. 7, pp. 407–415, 2019. [Online]. Available: https://www.sciencedirect.com/science/article/pii/S0936655519301517

[29] J. D. Wilson, E. M. Hammond, G. S. Higgins, and K. Petersson, "Ultra-high dose rate (flash) radiotherapy: Silver bullet or fool's gold?" *Frontiers in Oncology*, vol. 9, p. 1563, 2020. [Online]. Available: https://www.frontiersin.org/article/10.3389/fonc.2019.01563

[30] T. Mitin and A. L. Zietman, "Promise and pitfalls of heavy-particle therapy," *Journal of Clinical Oncology*, vol. 32, no. 26, pp. 2855–2863, 2014, pMID: 25113772. [Online]. Available: https://doi.org/10.1200/JCO.2014.55.1945

[31] X. Li *et al.*, "Upper limit on the inner radiation belt mev electron intensity," *Journal of Geophysical Research: Space Physics*, vol. 120, no. 2, pp. 1215–1228, 2015. [Online]. Available: https://agupubs.onlinelibrary.wiley.com/doi/abs/10.1002/2014JA020777

[32] V. Florinski *et al.*, "The dynamic heliosphere: Outstanding issues. report of working groups 4 and 6," *Space Science Reviews*, vol. 143, pp. 57–83, 03 2009. [Online]. Available: https://link.springer.com/article/10.1007/s11214-009-9488-7

[33] D. V. Reames, "Element abundances of solar energetic particles and the photosphere, the corona, and the solar wind," *Atoms*, vol. 7, no. 4, 2019. [Online]. Available: https://www.mdpi.com/2218-2004/7/4/104

[34] R. Mewaldt *et al.*, "Solar Energetic Particle Spectral Breaks," in *AGU Spring Meeting Abstracts*, vol. 2008, May 2008, pp. SH41A–10. [Online]. Available: https://aip.scitation.org/doi/abs/10.1063/1.2032701

[35] D. V. Reames, *Impulsive SEP Events (and Flares)*. Cham: Springer International Publishing, 2021, pp. 71–95. [Online]. Available: https://doi.org/10.1007/978-3-030-66402-2_4

[36] ——, "Magnetic topology of impulsive and gradual solar energetic particle events," *The Astrophysical Journal*, vol. 571, no. 1, pp. L63–L66, may 2002. [Online]. Available: https://doi.org/10.1086/341149

[37] M. Hapgood, *Space Weather*, ser. 2399-2891. IOP Publishing, 2017. [Online]. Available: http://dx.doi.org/10.1088/978-0-7503-1372-8

[38] S. Carboni *et al.*, "Particle identification using the ΔE-E technique and pulse shape discrimination with the silicon detectors of the FAZIA project," *Nuclear Instruments and Methods in Physics Research A*, vol. 664, no. 1, pp. 251–263, Feb. 2012. [Online]. Available: https://www.sciencedirect.com/science/article/pii/S0168900211020134?via%3Dihub

[39] D. V. Reames *et al.*, "Energy spectra of ions accelerated in impulsive and gradual solar events," *The Astrophysical Journal*, vol. 483, no. 1, pp. 515–522, jul 1997. [Online]. Available: https://doi.org/10.1086/304229

[40] D. Reames *et al.*, "The energetic particles acceleration, composition, and transport (epact) experiment on the istp/wind spacecraft," vol. 203, 02 1990. [Online]. Available: https://aip.scitation.org/doi/abs/10.1063/1.39137

[41] P. Zyla *et al.*, "Review of Particle Physics," *PTEP*, vol. 2020, no. 8, p. 083C01, 2020.

[42] "GENESIS Engineering," https://genesisesi.com/, accessed: 2021-08-17.

[43] LTspice, "Ltspice." [Online]. Available: https://www.analog.com/en/design-center/design-tools-and-calculators/ltspice-simulator.html

[44] C. Royon *et al.*, "Agile instrument: Advanced energetic ion electron telescope," *IEEE Transactions on Nuclear Science*, vol. 69, no. 4, pp. 811–817, 2022.

[45] F. Gautier *et al.*, "A novel technique for real-time ion identification and energy measurement for in situ space instrumentation," *Nuclear Instruments and Methods in Physics Research Section A: Accelerators, Spectrometers, Detectors and Associated Equipment*, vol. 1012, p. 165599, 2021. [Online]. Available: https://www.sciencedirect.com/science/article/pii/S0168900221005842

[46] T. Isidori, "Diamond detectors for proton Time of Flight in CT-PPS and TOTEM experiments," Jun 2017, presented 26 Jun 2017. [Online]. Available: https://cds.cern.ch/record/2752821

[47] "Technical proposal for a MIP timing detector in the CMS experiment Phase 2 upgrade," CERN, Geneva, Tech. Rep., Dec 2017. [Online]. Available: https://cds.cern.ch/record/2296612

[48] T. Isidori *et al.*, "Performance of a low gain avalanche detector in a medical linac and characterisation of the beam profile," *Physics in Medicine & Biology*, vol. 66, no. 13, p. 135002, jun 2021. [Online]. Available: https://doi.org/10.1088/1361-6560/ac0587

[49] N. Cartiglia *et al.*, "Beam test results of a 16ps timing system based on ultra-fast silicon detectors," *Nuclear Instruments and Methods in Physics Research Section A: Accelerators, Spectrometers, Detectors and Associated Equipment*, vol. 850, pp. 83–88, 2017. [Online]. Available: https://www.sciencedirect.com/science/article/pii/S0168900217300219

[50] C. Beenakker and C. Schonenberger, "Quantum shot noise," *arXiv preprint cond-mat/0605025*, 2006. [Online]. Available: https://arxiv.org/abs/cond-mat/0605025

[51] W. Shockley, "Currents to conductors induced by a moving point charge," *Journal of Applied Physics*, vol. 9, no. 10, pp. 635–636, 1938. [Online]. Available: https://doi.org/10.1063/1.1710367

[52] N. Minafra, "Development of a timing detector for the TOTEM experiment at the LHC," Feb 2016, presented 14 Mar 2016. [Online]. Available: http://cds.cern.ch/record/2139815

[53] F. Herman, "The electronic energy band structure of silicon and germanium," *Proceedings of the IRE*, vol. 43, no. 12, pp. 1703–1732, 1955. [Online]. Available: https://ieeexplore.ieee.org/document/4055356

[54] G. Backenstoss, "Conductivity mobilities of electrons and holes in heavily doped silicon," *Phys. Rev.*, vol. 108, pp. 1416–1419, Dec 1957. [Online]. Available: https://link.aps.org/doi/10.1103/PhysRev.108.1416

[55] N. Moffat, "Low gain avalanche detectors for particle physics and synchrotron applications," Ph.D. dissertation, University of Glasgow, 2020.

[56] P. D. Group *et al.*, "Review of Particle Physics," *Progress of Theoretical and Experimental Physics*, vol. 2020, no. 8, 08 2020, 083C01. [Online]. Available: https://doi.org/10.1093/ptep/ptaa104

[57] K. Shenai, "Introduction to electronics," in *The Electrical Engineering Handbook*, W.-K. CHEN, Ed. Burlington: Academic Press, 2005, p. 83. [Online]. Available: https://www.sciencedirect.com/science/article/pii/B9780121709600500098

[58] W. Riegler, "An application of extensions of the ramo–shockley theorem to signals in silicon sensors," *Nuclear Instruments and Methods in Physics Research Section A: Accelerators, Spectrometers, Detectors and Associated Equipment*, vol. 940, pp. 453–461, 2019. [Online]. Available: https://www.sciencedirect.com/science/article/pii/S0168900219309015

[59] M. Berretti *et al.*, "Test of ultra fast silicon detectors for the totem upgrade project," *JINST*, vol. 12, no. 03, p. P03024, 2017. [Online]. Available: https://iopscience.iop.org/article/10.1088/1748-0221/12/03/P03024

[60] N. Cartiglia *et al.*, "Design optimization of ultra-fast silicon detectors," *Nuclear Instruments and Methods in Physics Research Section A: Accelerators, Spectrometers, Detectors and Associated Equipment*, vol. 796, pp. 141–148, 2015, proceedings of the 10th International Conference on Radiation Effects on Semiconductor Materials Detectors and Devices. [Online]. Available: https://www.sciencedirect.com/science/article/pii/S0168900215004982

[61] H. Photonics, "Characteristics and use of siapd," *Technical Information SD-28*, 2004. [Online]. Available: http://www.hamamatsu.com.cn/UserFiles/DownFile/Related/20130810164103075.pdf

[62] R. Mulargia *et al.*, "Temperature dependence of the response of ultra fast silicon detectors," *Journal of Instrumentation*, vol. 11, no. 12, p. C12013, 2016. [Online]. Available: https://iopscience.iop.org/article/10.1088/1748-0221/11/12/C12013

[63] G. Kramberger *et al.*, "Radiation effects in low gain avalanche detectors after hadron irradiations," *Journal of Instrumentation*, vol. 10, no. 07, pp. P07 006–P07 006, jul 2015. [Online]. Available: https://doi.org/10.1088/1748-0221/10/07/p07006

[64] O. S. Brüning *et al.*, *LHC Design Report*, ser. CERN Yellow Reports: Monographs. Geneva: CERN, 2004. [Online]. Available: http://cds.cern.ch/record/782076

[65] M. Vretenar *et al.*, *Linac4 design report*, ser. CERN Yellow Reports: Monographs. Geneva: CERN, 2020, vol. 6. [Online]. Available: https://cds.cern.ch/record/2736208

[66] "The Proton Synchrotron Booster," Jul 2012. [Online]. Available: https://cds.cern.ch/record/1997372

[67] "The Proton Synchrotron," Jan 2012. [Online]. Available: https://cds.cern.ch/record/1997189

[68] "The Super Proton Synchrotron," Jan 2012. [Online]. Available: https://cds.cern.ch/record/1997188

[69] G. Aad *et al.*, "Observation of a new particle in the search for the standard model higgs boson with the atlas detector at the lhc," *Physics Letters B*, vol. 716, no. 1, pp. 1–29, 2012. [Online]. Available: https://www.sciencedirect.com/science/article/pii/S037026931200857X

[70] V. Klyukhin *et al.*, "Measuring the magnetic flux density in the cms steel yoke," *Journal of superconductivity and novel magnetism*, vol. 26, no. 4, pp. 1307–1311, 2013. [Online]. Available: https://ieeexplore.ieee.org/document/1325165

[71] A. Benaglia, "The CMS ECAL performance with examples," CERN, Geneva, Tech. Rep., Nov 2013. [Online]. Available: https://cds.cern.ch/record/1632384

[72] B. Schmidt, "The high-luminosity upgrade of the LHC: Physics and technology challenges for the accelerator and the experiments," *Journal of Physics: Conference Series*, vol. 706, p. 022002, apr 2016. [Online]. Available: https://doi.org/10.1088/1742-6596/706/2/022002

[73] D. Contardo, M. Klute, J. Mans, L. Silvestris, and J. Butler, "Technical Proposal for the Phase-II Upgrade of the CMS Detector," Geneva, Tech. Rep., Jun 2015, upgrade Project Leader Deputies: Lucia Silvestris (INFN-Bari), Jeremy Mans (University of Minnesota) Additional contacts: Lucia.Silvestris@cern.ch, Jeremy.Mans@cern.ch. [Online]. Available: https://cds.cern.ch/record/2020886

[74] J. Butler *et al.*, "CMS Phase II Upgrade Scope Document," CERN, Geneva, Tech. Rep., Sep 2015. [Online]. Available: https://cds.cern.ch/record/2055167

[75] S. Paoletti, "The CMS Tracker Upgrade for the High Luminosity LHC," CERN, Geneva, Tech. Rep., Nov 2019. [Online]. Available: http://cds.cern.ch/record/2723307

[76] D. Soldi, "Precision calorimetry at high luminosity: the CMS electromagnetic calorimeter from the LHC Run 2 to the HL-LHC," *PoS*, vol. ICHEP2020, p. 782. 6 p, 2021. [Online]. Available: https://cds.cern.ch/record/2784914

[77] C. CMS, "A MIP Timing Detector for the CMS Phase-2 Upgrade," CERN, Geneva, Tech. Rep., Mar 2019. [Online]. Available: https://cds.cern.ch/record/2667167

[78] A. M. Sirunyan *et al.*, "Particle-flow reconstruction and global event description with the CMS detector," *JINST*, vol. 12, no. 10, p. P10003, 2017. [Online]. Available: https://iopscience.iop.org/article/10.1088/1748-0221/12/10/P10003

[79] G. Degrassi, M. Fedele, and P. P. Giardino, "Constraints on the trilinear higgs self coupling from precision observables," *Journal of High Energy Physics*, vol. 2017, no. 4, pp. 1–19, 2017. [Online]. Available: https://link.springer.com/article/10.1007/JHEP04(2017)155

[80] D. Miller and S. Moretti, "Can the trilinear higgs self-coupling be measured at future linear colliders?" *The European Physical Journal C-Particles and Fields*, vol. 13, no. 3, pp. 459–470, 2000. [Online]. Available: https://link.springer.com/article/10.1007/s100520000248

[81] "Thorlab kmts25e, 2022," https://www.thorlabs.com/thorproduct.cfm?partnumber=KMTS25E.

[82] R. Bitter, T. Mohiuddin, and M. Nawrocki, *LabVIEW: Advanced programming techniques*. Crc Press, 2006. [Online]. Available: https://www.researchgate.net/publication/329162844_LabVIEW_Advanced_programming_techniques

[83] *Series 2400 SourceMeter®*, Keithley Instruments, Inc., 2011, rev. K. [Online]. Available: https://download.tek.com/manual/2400S-900-01_K-Sep2011_User.pdf

[84] "Caen dt5533e 4ch power supply, 2022," https://www.caen.it/products/dt5533e/.

[85] "Rohde & schwarz® hmp4000 power supply series, 2022," https://www.rohde-schwarz.com/us/products/test-and-measurement/dc-power-supplies/rs-hmp4000-power-supply-series_63493-47360.html.

[86] *Teledyne-LeCroy WaveRunner 640Zi oscilloscope*, Teledyne, 26 Apr 2021, hdo6kb-ds. [Online]. Available: http://cdn.teledynelecroy.com/files/pdf/hdo6000b-datasheet.pdf

[87] C.-T. Collaboration, "CMS-TOTEM Precision Proton Spectrometer," Tech. Rep. CERN-LHCC-2014-021, TOTEM-TDR-003, CMS-TDR-13, 2014. [Online]. Available: http://cds.cern.ch/record/1753795

[88] "Fermilab official website," http://www.fnal.gov/.

[89] G.-F. Dalla Betta *et al.*, "Design and tcad simulation of double-sided pixelated low gain avalanche detectors," *Nuclear Instruments and Methods in Physics Research Section A: Accelerators, Spectrometers, Detectors and Associated Equipment*, vol. 796, pp. 154–157, 2015, proceedings of the 10th International Conference on Radiation Effects on Semiconductor Materials Detectors and Devices. [Online]. Available: https://www.sciencedirect.com/science/article/pii/S0168900215003551

[90] V. Sola *et al.*, "First fbk production of 50 m ultra-fast silicon detectors," *Nuclear Instruments and Methods in Physics Research Section A: Accelerators, Spectrometers, Detectors and Associated Equipment*, vol. 924, pp. 360–368, 2019, 11th International Hiroshima Symposium on Development and Application of Semiconductor Tracking Detectors. [Online]. Available: https://www.sciencedirect.com/science/article/pii/S0168900218308969

[91] Z. Galloway *et al.*, "Properties of hpk ufsd after neutron irradiation up to 6e15 n/cm2," 2020. [Online]. Available: https://www.sciencedirect.com/science/article/pii/S0168900219306278

[92] A. Ronzhin *et al.*, "Study of the timing performance of micro-channel plate photomultiplier for use as an active layer in a shower maximum detector," *Nuclear Instruments and Methods*

in Physics Research Section A: Accelerators, Spectrometers, Detectors and Associated Equipment, vol. 795, pp. 288–292, 2015. [Online]. Available: https://www.sciencedirect.com/science/article/pii/S0168900215007500

[93] S. Kwan *et al.*, "The pixel tracking telescope at the fermilab test beam facility," *Nuclear Instruments and Methods in Physics Research Section A: Accelerators, Spectrometers, Detectors and Associated Equipment*, vol. 811, pp. 162–169, 2016. [Online]. Available: https://www.sciencedirect.com/science/article/pii/S0168900215015521

[94] "Caen power supplies, 2022," https://www.wiener-d.com/product/mpod-lv-module/.

[95] "Tektronix,dpo7000-series," https://www.tek.com/en/datasheet/dpo7000-series.

[96] N. Minafra *et al.*, "Test of Ultra Fast Silicon Detectors for Picosecond Time Measurements with a New Multipurpose Read-Out Board," *Nucl. Instrum. Meth. A*, vol. 867, p. 88, 2017. [Online]. Available: https://www.sciencedirect.com/science/article/pii/S0168900217304825?via%3Dihub

[97] G. Van Rossum and F. L. Drake, *Python 3 Reference Manual*. Scotts Valley, CA: CreateSpace, 2009. [Online]. Available: https://docs.python.org/3/reference/

[98] "Micross components, 2022," https://www.micross.com/.

[99] "Barcelona detector technologies," https://baretek.eu.com/.

[100] "Saint luke's radiation oncology network website." [Online]. Available: https://www.https://www.friendsofstlukes.ie

[101] J. Greening, "Fundamentals of radiation dosimetry," *Medical Physics Handbooks*, vol. 6, pp. 1–160, 1981.

[102] D. Adlienė and R. Adlytė, "Dosimetry principles, dose measurements, and radiation protection," *Applications of Ionizing Radiation in Materials Processing*, vol. 1, p. 55, 2017. [Online]. Available: http://www.ichtj.waw.pl/ichtj/publ/monogr/sun2017/sun-chapter3.pdf

[103] *Ionizing Radiation*. John Wiley Sons, Ltd, 1986, ch. 1, pp. 1–19. [Online]. Available: https://onlinelibrary.wiley.com/doi/abs/10.1002/9783527617135.ch1

[104] *Quantities for Describing the Interaction of Ionizing Radiation with Matter*. John Wiley Sons, Ltd, 1986, ch. 2, pp. 20–37. [Online]. Available: https://onlinelibrary.wiley.com/doi/abs/10.1002/9783527617135.ch2

[105] H.-G. Menzel, "International commission on radiation units and measurements," *Journal of the ICRU*, vol. 14, no. 2, pp. 1–2, 2014. [Online]. Available: https://journals.sagepub.com/home/cru

[106] F. M. Khan and J. P. Gibbons, *Khan's the physics of radiation therapy*. Lippincott Williams & Wilkins, 2014.

[107] *Gamma- and X-Ray Interactions in Matter*. John Wiley Sons, Ltd, 1986, ch. 7, pp. 124–159. [Online]. Available: https://onlinelibrary.wiley.com/doi/abs/10.1002/9783527617135.ch7

[108] *Charged-Particle Interactions in Matter*. John Wiley Sons, Ltd, 1986, ch. 8, pp. 160–202. [Online]. Available: https://onlinelibrary.wiley.com/doi/abs/10.1002/9783527617135.ch8

[109] S. H. Levitt and F. Khan, "Quality assurance in radiation oncology," *Cancer*, vol. 74, no. S9, pp. 2642–2646, 1994.

[110] R. L. Dixon and K. Ekstrand, "Silicon diode dosimetry," *The International journal of applied radiation and isotopes*, vol. 33, no. 11, pp. 1171–1176, 1982.

[111] N. Stansook *et al.*, "Technical note: Angular dependence of a 2d monolithic silicon diode array for small field dosimetry," *Medical Physics*, vol. 44, no. 8, pp. 4313–4321, 2017. [Online]. Available: https://aapm.onlinelibrary.wiley.com/doi/abs/10.1002/mp.12377

[112] M. Yarahmadi, S. Wegener, and O. A. Sauer, "Energy and field size dependence of a silicon diode designed for small-field dosimetry," *Medical Physics*, vol. 44, no. 5, pp. 1958–1964, 2017. [Online]. Available: https://aapm.onlinelibrary.wiley.com/doi/abs/10.1002/mp.12195

[113] A. Kumar, B. Tiwari, S. Singh, M. Mohan Tripathi, and R. Chaujar, "Radiation analysis of n-channel tgrc-mosfet: An x-ray dosimeter," *IEEE Transactions on Electron Devices*, vol. 65, no. 11, pp. 5014–5020, 2018. [Online]. Available: https://ieeexplore.ieee.org/document/8471105

[114] A. Faigon, I. M. Vazquez, S. Carbonetto, M. G. Inza *et al.*, "Floating gate sensor for in-vivo dosimetry in radiation therapies. design and first characterization." in *Journal of Physics: Conference Series*, vol. 792, no. 1. IOP Publishing, 2017, p. 012057. [Online]. Available: https://iopscience.iop.org/article/10.1088/1742-6596/792/1/012057

[115] K. Cheung, "Intensity modulated radiotherapy: advantages, limitations and future developments," *Biomed Imaging Interv J*, vol. 2, no. 1, p. e19, 2006. [Online]. Available: https://www.ncbi.nlm.nih.gov/pmc/articles/PMC3097603/

[116] S. Ramkumar *et al.*, "An assessment of radiotherapy dosimeters based on cvd grown diamond," *Nuclear Instruments and Methods in Physics Research Section A: Accelerators, Spectrometers, Detectors and Associated Equipment*, vol. 460, no. 2-3, pp. 401–411, 2001. [Online]. Available: https://www.sciencedirect.com/science/article/pii/S0168900200010627

[117] B. Marczewska *et al.*, "A study of radiation dosimeters based on synthetic hpht diamond," *Diamond and related materials*, vol. 16, no. 2, pp. 191–195, 2007. [Online]. Available: https://www.sciencedirect.com/science/article/pii/S0925963506001166?via%3Dihub

[118] M. Bruzzi *et al.*, "Large-area segmented polycrystalline cvd diamond for dose mapping in advanced radiotherapy techniques," in *2016 IEEE Nuclear Science Symposium, Medical Imaging Conference and Room-Temperature Semiconductor Detector Workshop (NSS/MIC/RTSD)*. IEEE, pp. 1–4. [Online]. Available: https://ieeexplore.ieee.org/document/8069394

[119] S. Lam, D. Bradley, and M. U. Khandaker, "Small-field radiotherapy photon beam output evaluation: Detectors reviewed," *Radiation Physics and Chemistry*, vol. 178, p. 108950, 2021. [Online]. Available: https://www.sciencedirect.com/science/article/pii/S0969806X20302450

[120] R. Babic, S. Babic, S. Babic, and N. Babic, "120 years since the discovery of x-rays," *Medicinski pregled*, vol. 69, pp. 323–330, 09 2016. [Online]. Available: https://pubmed.ncbi.nlm.nih.gov/29693857/

[121] A. Assmus, "Early history of x rays," *Beam Line*, vol. 25, no. 2, pp. 10–24, 1995.

[122] H. Coutard, "Principles of x ray therapy of malignant diseases," *The lancet*, vol. 224, no. 5784, pp. 1–8, 1934. [Online]. Available: https://www.sciencedirect.com/science/article/abs/pii/S0140673600900850

[123] S. Gianfaldoni *et al.*, "An overview on radiotherapy: From its history to its current applications in dermatology," *Open Access Macedonian Journal of Medical Sciences*, vol. 5, pp. 521 – 525, 2017. [Online]. Available: https://www.ncbi.nlm.nih.gov/pmc/articles/PMC5535674/

[124] C. Chargari *et al.*, "Brachytherapy: An overview for clinicians," *CA: A Cancer Journal for Clinicians*, vol. 69, no. 5, pp. 386–401, 2019. [Online]. Available: https://acsjournals.onlinelibrary.wiley.com/doi/abs/10.3322/caac.21578

[125] R. G. Dale and B. Jones, "The clinical radiobiology of brachytherapy." *The British journal of radiology*, vol. 71, no. 845, pp. 465–483, 1998. [Online]. Available: https://pubmed.ncbi.nlm.nih.gov/9691890/

[126] P. M. Devlin, *Brachytherapy: applications and techniques*. Springer Publishing Company, 2015.

[127] H. E. Johns and J. R. Cunningham, "The physics of radiology," 1983.

[128] A. B. Fuller, *Ferrites at microwave frequencies*. IET, 1987, no. 23.

[129] C. Davidson, "Transmission-line measurements," in *Transmission Lines for Communications*. Springer, 1989, pp. 92–121.

[130] S. D. Sharma, "Johns and cunningham's the physics of radiology," *Journal of Medical Physics*, vol. 46, no. 2, p. 128, 2021. [Online]. Available: https://www.ncbi.nlm.nih.gov/pmc/articles/PMC8415248/

[131] S. Rosander, M. Sedlaček, O. Wernholm, and H. Babić, "The 50 mev racetrack microtron at the royal institute of technology stockholm," *Nuclear Instruments and Methods in Physics Research*, vol. 204, no. 1, pp. 1–20, 1982. [Online]. Available: https://www.sciencedirect.com/science/article/abs/pii/0167508782900710?via%3Dihub

[132] B. Lin *et al.*, "Flash radiotherapy: History and future," *Frontiers in Oncology*, vol. 11, p. 1890, 2021. [Online]. Available: https://www.frontiersin.org/article/10.3389/fonc.2021.644400

[133] J. Bourhis *et al.*, "Treatment of a first patient with flash-radiotherapy," *Radiotherapy and Oncology*, vol. 139, pp. 18–22, 2019, fLASH radiotherapy International Workshop. [Online]. Available: https://www.sciencedirect.com/science/article/pii/S0167814019329597

[134] M.-C. Vozenin *et al.*, "The advantage of flash radiotherapy confirmed in mini-pig and cat-cancer patients," *Clinical Cancer Research*, vol. 25, no. 1, pp. 35–42, 2019. [Online]. Available: https://clincancerres.aacrjournals.org/content/25/1/35

[135] E. Schüler *et al.*, "Experimental platform for ultra-high dose rate flash irradiation of small animals using a clinical linear accelerator," *International Journal of Radiation Oncology*Biology*Physics*, vol. 97, no. 1, pp. 195–203, 2017. [Online]. Available: https://www.sciencedirect.com/science/article/pii/S0360301616332011

[136] L. M. Smyth *et al.*, "Comparative toxicity of synchrotron and conventional radiation therapy based on total and partial body irradiation in a murine model," *Scientific reports*, vol. 8, no. 1, pp. 1–11, 2018. [Online]. Available: https://www.nature.com/articles/s41598-018-30543-1

[137] A. Patriarca *et al.*, "Experimental set-up for flash proton irradiation of small animals using a clinical system," *International Journal of Radiation Oncology* Biology* Physics*, vol. 102, no. 3, pp. 619–626, 2018. [Online]. Available: https://www.redjournal.org/article/S0360-3016(18)31404-4/fulltext

[138] N. Esplen, M. S. Mendonca, and M. Bazalova-Carter, "Physics and biology of ultrahigh dose-rate (flash) radiotherapy: a topical review," *Physics in Medicine & Biology*, vol. 65, no. 23, p. 23TR03, 2020. [Online]. Available: https://iopscience.iop.org/article/10.1088/1361-6560/abaa28

[139] M. Grotzer, E. Schültke, E. Bräuer-Krisch, and J. Laissue, "Microbeam radiation therapy: Clinical perspectives," *Phys Med*, vol. 31(6), p. 564, 2015. [Online]. Available: https://www.sciencedirect.com/science/article/pii/S1120179715000459

[140] M. Lempart *et al.*, "Modifying a clinical linear accelerator for delivery of ultra-high dose rate irradiation," *Radiother. Oncol.*, vol. 139, p. 40, 2019. [Online]. Available: https://pubmed.ncbi.nlm.nih.gov/30755324/

[141] M. Ashraf *et al.*, "Dosimetry for flash radiotherapy: A review of tools and the role of radioluminescence and cherenkov emission," *Frontiers in Physics*, vol. 8, p. 328, 2020. [Online]. Available: https://www.frontiersin.org/articles/10.3389/fphy.2020.00328/full

[142] S. Alashrah, S. Kandaiya, S. Yong, and S. Cheng, "Characterization of a 2d ionization chamber array for imrt plan verification," *Nucl. Instrum. Meth. A*, vol. 619, no. 1, p. 181, 2010. [Online]. Available: https://www.sciencedirect.com/science/article/pii/S0168900209020774?via%3Dihub

[143] A. Anvari, S. M. R. Aghamiri, S. R. Mahdavi, and P. Alaei, "Statistical analysis on 2d array of ion chamber performance," *Journal of Radiotherapy in Practice*, vol. 14, no. 2, p. 194, 2015. [Online]. Available: https://www.cambridge.org/core/journals/journal-of-radiotherapy-in-practice/article/abs/statistical-analysis-on-2d-array-of-ion-chamber-performance/F52ADB55DDD3E7BDFC6B9B872D54DE3B

[144] A. B. Rosenfeld *et al.*, "Semiconductor dosimetry in modern external-beam radiation therapy," *Physics in Medicine & Biology*, vol. 65, no. 16, p. 16TR01, 2020. [Online]. Available: https://pubmed.ncbi.nlm.nih.gov/32604077/

[145] S. Ahmed, G. Zhang, E. G. Moros, and V. Feygelman, "Comprehensive evaluation of the high-resolution diode array for srs dosimetry," *Journal of Applied Clinical Medical Physics*, vol. 20, no. 10, p. 13, 2019. [Online]. Available: https://aapm.onlinelibrary.wiley.com/doi/10.1002/acm2.12696

[146] E. Bossini, "The Timing System of the TOTEM Experiment," *Instruments*, vol. 2, no. 4, p. 21, 2018. [Online]. Available: https://cds.cern.ch/record/2645090/files/instruments-02-00021.pdf

[147] A. Collaboration, "Technical Proposal: A High-Granularity Timing Detector for the ATLAS Phase-II Upgrade," Tech. Rep. CERN-LHCC-2018-023. LHCC-P-012, 2018. [Online]. Available: https://cds.cern.ch/record/2623663

[148] A. Tremsin and J. Vallerga, "Unique capabilities and applications of microchannel plate (mcp) detectors with medipix/timepix readout," *Radiation Measurements*, vol. 130, p. 106228, 2020. [Online]. Available: https://www.sciencedirect.com/science/article/pii/S1350448719305141?via%3Dihub

[149] S. Procz *et al.*, "X-ray and gamma imaging with medipix and timepix detectors in medical research," *Radiation Measurements*, vol. 127, p. 106104, 2019. [Online]. Available: https://www.sciencedirect.com/science/article/pii/S1350448719300599

[150] S. Manolopoulos *et al.*, "Small field measurements with a novel silicon position sensitive diode array," *Physics in Medicine and Biology*, vol. 54, no. 3, p. 485, 2009. [Online]. Available: https://pubmed.ncbi.nlm.nih.gov/19124947/

[151] A. Bocci *et al.*, "Silicon strip detector for a novel 2d dosimetric method for radiotherapy treatment verification," *Nucl. Instrum. Meth. A*, vol. 673, p. 98, 2012. [Online]. Available: https://www.sciencedirect.com/science/article/pii/S0168900212000526

[152] F. Bisello *et al.*, "Development of silicon monolithic arrays for dosimetry in external beam radiotherapy," *Nucl. Instrum. Meth. A*, vol. 796, p. 85, 2015. [Online]. Available: https://www.sciencedirect.com/science/article/pii/S0168900215005756?via%3Dihub

[153] S. J. Alnaghy *et al.*, "High resolution silicon array detector implementation in an inline mri-linac," *Medical Physics*, vol. 47, no. 4, p. 1920, 2020. [Online]. Available: https://pubmed.ncbi.nlm.nih.gov/31917865/

[154] A. Rosenfeld, M. Silari, and M. Campbell, "The medipix/timepix asic family and its applications," *Radiation Measurements*, vol. 139, p. 106483, 2020. [Online]. Available: https://www.sciencedirect.com/journal/radiation-measurements/special-issue/103SJXSV0C7

[155] M. Moll, "Displacement damage in silicon detectors for high energy physics," *IEEE Transactions on Nuclear Science*, vol. 65, no. 8, p. 1561, 2018. [Online]. Available: https://ieeexplore.ieee.org/document/8331152

[156] M. Ferrero *et al.*, "Radiation resistant lgad design," *Nucl. Instrum. Meth. A*, vol. 919, p. 16, 2019. [Online]. Available: https://www.sciencedirect.com/science/article/pii/S0168900218317741

[157] R. Sadagopan *et al.*, "Characterization and clinical evaluation of a novel imrt quality assurance system," *J Appl Clin Med Phys.*, vol. 10(2), p. 104, 2009. [Online]. Available: https://acsjournals.onlinelibrary.wiley.com/doi/10.1002/1097-0142(19941101)74:9+%3C2642::AID-CNCR2820741810%3E3.0.CO;2-E

[158] V. Favaudon *et al.*, "Time-resolved dosimetry of pulsed electron beams in very high dose-rate, flash irradiation for radiotherapy preclinical studies," *Nucl. Instrum. Meth. A*, vol. 944, p. 162537, 2019. [Online]. Available: https://www.sciencedirect.com/science/article/pii/S0168900219310666

[159] L. Liu, X. Ouyang, J. Zhang, P. Jin, and C. Su, "Properties comparison between nanosecond x-ray detectors of polycrystalline and single-crystal diamond," *Diamond and Related Materials*, vol. 73, p. 248, 2017. [Online]. Available: https://www.sciencedirect.com/science/article/pii/S092596351630231X

[160] R. Ballabriga, M. Campbell, and X. Llopart, "An introduction to the medipix family asics," *Radiation Measurements*, vol. 136, p. 106271, 2020. [Online]. Available: https://www.sciencedirect.com/science/article/pii/S1350448720300354

[161] "Elekta™company website." [Online]. Available: https://www.elekta.com/radiotherapy

[162] L. J. van Battum, W. van der Zee, and H. Huizenga, "Scattered radiation from applicators in clinical electron beams," *Physics in Medicine and Biology*, vol. 48, no. 15, pp. 2493–2507, jul 2003. [Online]. Available: https://doi.org/10.1088/0031-9155/48/15/316

[163] *DSO8104A Infiniium Oscilloscope: 1 GHz, 4 channels*, Agilent, 2009-04-22. [Online]. Available: https://www.keysight.com/us/en/assets/7018-06782/data-sheets/5968-7141.pdf

[164] J. Deng, S. B. Jiang, T. Pawlicki, J. Li, and C.-M. Ma, "Derivation of electron and photon energy spectra from electron beam central axis depth dose curves," *Physics in Medicine and Biology*, vol. 46, no. 5, p. 1429, 2001. [Online]. Available: https://iopscience.iop.org/article/10.1088/0031-9155/46/5/308

[165] C. McKerracher and D. I. Thwaites, "Assessment of new small-field detectors against standard-field detectors for practical stereotactic beam data acquisition," *Physics in Medicine and Biology*, vol. 44, no. 9, p. 2143, 1999. [Online]. Available: https://iopscience.iop.org/article/10.1088/0031-9155/44/9/303

[166] P. Puig-suari, "Development of the standard cubesat deployer and a cubesat class picosatellite," 05 2001. [Online]. Available: https://ieeexplore.ieee.org/document/931726

[167] W. Li and M. Hudson, "Earth's van allen radiation belts: From discovery to the van allen probes era," *Journal of Geophysical Research: Space Physics*, vol. 124, no. 11, pp. 8319–8351, 2019. [Online]. Available: https://agupubs.onlinelibrary.wiley.com/doi/abs/10.1029/2018JA025940

[168] C. O. Bostrom, D. S. Beall, and J. C. Armstrong, "Time history of the inner radiation zone, october 1963 to december 1968," *Journal of Geophysical Research (1896-1977)*, vol. 75, no. 7, pp. 1246–1256, 1970. [Online]. Available: https://agupubs.onlinelibrary.wiley.com/doi/abs/10.1029/JA075i007p01246

[169] C. T. Russell and R. M. Thorne, "Structure of the inner magnetosphere." *Cosmic Electrodyn. 1: 67-89(Apr. 1970).*, 1 1970. [Online]. Available: https://www.osti.gov/biblio/4126239

[170] J. B. Blake, W. A. Kolasinski, R. W. Fillius, and E. G. Mullen, "Injection of electrons and protons with energies of tens of mev into l < 3 on 24 march 1991," *Geophysical Research Letters*, vol. 19, no. 8, pp. 821–824, 1992. [Online]. Available: https://agupubs.onlinelibrary.wiley.com/doi/abs/10.1029/92GL00624

[171] D. N. Baker *et al.*, "Relativistic electron acceleration and decay time scales in the inner and outer radiation belts: Sampex," *Geophysical Research Letters*, vol. 21, no. 6, pp. 409–412, 1994. [Online]. Available: https://agupubs.onlinelibrary.wiley.com/doi/abs/10.1029/93GL03532

[172] N. Fox and J. L. Burch, *The Van allen probes mission*. Springer Science & Business Media, 2014.

[173] J. F. Fennell *et al.*, "Van allen probes show that the inner radiation zone contains no mev electrons: Ect/mageis data," *Geophysical Research Letters*, vol. 42, no. 5, pp. 1283–1289, 2015. [Online]. Available: https://agupubs.onlinelibrary.wiley.com/doi/abs/10.1002/2014GL062874

[174] G. P. Ginet *et al.*, *AE9, AP9 and SPM: New Models for Specifying the Trapped Energetic Particle and Space Plasma Environment*. Boston, MA: Springer US, 2014, pp. 579–615. [Online]. Available: https://doi.org/10.1007/978-1-4899-7433-4_18

[175] S. G. Claudepierre *et al.*, "The hidden dynamics of relativistic electrons (0.7–1.5 mev) in the inner zone and slot region," *Journal of Geophysical Research: Space Physics*, vol. 122, no. 3, pp. 3127–3144, 2017. [Online]. Available: https://agupubs.onlinelibrary.wiley.com/doi/abs/10.1002/2016JA023719

[176] L. A. Frank, "Inward radial diffusion of electrons of greater than 1.6 million electron volts in the outer radiation zone," *Journal of Geophysical Research (1896-1977)*, vol. 70, no. 15, pp. 3533–3540, 1965. [Online]. Available: https://agupubs.onlinelibrary.wiley.com/doi/abs/10.1029/JZ070i015p03533

[177] Q. Ma *et al.*, "Modeling inward diffusion and slow decay of energetic electrons in the earth's outer radiation belt," *Geophysical Research Letters*, vol. 42, no. 4, pp. 987–995, 2015. [Online]. Available: https://agupubs.onlinelibrary.wiley.com/doi/abs/10.1002/2014GL062977

[178] S. G. Kanekal *et al.*, "Relativistic electron response to the combined magnetospheric impact of a coronal mass ejection overlapping with a high-speed stream: Van allen probes observations," *Journal of Geophysical Research: Space Physics*, vol. 120, no. 9, pp. 7629–7641, 2015. [Online]. Available: https://agupubs.onlinelibrary.wiley.com/doi/abs/10.1002/2015JA021395

[179] *Proc. 23rd World Summit on Exploring the Dark Side of the Universe (EDSU2020 March 9–13, 2020, Guadeloupe Islands)*, 2020. [Online]. Available: https://kuscholarworks.ku.edu/handle/1808/30804

[180] D. L. Turner *et al.*, "Investigating the source of near-relativistic and relativistic electrons in earth's inner radiation belt," *Journal of Geophysical Research: Space Physics*, vol. 122, no. 1, pp. 695–710, 2017. [Online]. Available: https://agupubs.onlinelibrary.wiley.com/doi/abs/10.1002/2016JA023600

[181] D. N. Baker *et al.*, "Highly relativistic radiation belt electron acceleration, transport, and loss: Large solar storm events of march and june 2015," *Journal of Geophysical Research: Space Physics*, vol. 121, no. 7, pp. 6647–6660, 2016. [Online]. Available: https://agupubs.onlinelibrary.wiley.com/doi/abs/10.1002/2016JA022502

[182] L. A. Fisk, B. Kozlovsky, and R. Ramaty, "An Interpretation of the Observed Oxygen and Nitrogen Enhancements in Low-Energy Cosmic Rays," , vol. 190, p. L35, May 1974. [Online]. Available: https://ui.adsabs.harvard.edu/abs/1974ApJ...190L..35F/abstract

[183] M. E. Pesses, J. R. Jokipii, and D. Eichler, "Cosmic ray drift, shock wave acceleration, and the anomalous component of cosmic rays," , vol. 246, pp. L85–L88, Jun. 1981. [Online]. Available: https://ui.adsabs.harvard.edu/abs/1981ApJ...246L..85P/abstract

[184] A. C. Cummings, E. C. Stone, and C. D. Steenberg, "Composition of anomalous cosmic rays and other heliospheric ions," *The Astrophysical Journal*, vol. 578, no. 1, pp. 194–210, oct 2002. [Online]. Available: https://doi.org/10.1086/342427

[185] H. Schwabe and H. Schwabe Herrn, "Sonnen — beobachtungen im jahre 1843," *Astronomische Nachrichten*, vol. 21, no. 15, pp. 234–235, 1844. [Online]. Available: https://onlinelibrary.wiley.com/doi/abs/10.1002/asna.18440211505

[186] J. A. Fleming, "Notes on radio fade-out of august 25, 1936," *Terrestrial Magnetism and Atmospheric Electricity*, vol. 41, no. 4, pp. 404–406, 1936. [Online]. Available: https://agupubs.onlinelibrary.wiley.com/doi/abs/10.1029/TE041i004p00404

[187] J. Bartels, "Solar eruptions and their ionospheric effects—a classical observation and its new interpretation," *Terrestrial Magnetism and Atmospheric Electricity*, vol. 42, no. 3, pp. 235–239, 1937. [Online]. Available: https://agupubs.onlinelibrary.wiley.com/doi/abs/10.1029/TE042i003p00235

[188] M. Desai and J. Giacalone, "Large gradual solar energetic particle events," *Living Reviews in Solar Physics*, vol. 13, 09 2016. [Online]. Available: https://link.springer.com/article/10.1007/s41116-016-0002-5

[189] S. W. Kahler, E. Hildner, and M. A. I. Van Hollebeke, "Promt solar proton events and coronal mass ejections." , vol. 57, no. 2, pp. 429–443, Apr. 1978. [Online]. Available: https://link.springer.com/article/10.1007/BF00160116

[190] D. V. Reames, *Gradual SEP Events*. Cham: Springer International Publishing, 2021, pp. 97–133. [Online]. Available: https://doi.org/10.1007/978-3-030-66402-2_5

[191] M. I. Desai *et al.*, "Spectral properties of heavy ions associated with the passage of interplanetary shocks at 1 AU," *The Astrophysical Journal*, vol. 611, no. 2, pp. 1156–1174, aug 2004. [Online]. Available: https://doi.org/10.1086/422211

[192] H. V. Cane, R. E. McGuire, and T. T. von Rosenvinge, "Two Classes of Solar Energetic Particle Events Associated with Impulsive and Long-Duration Soft X-Ray Flares," , vol. 301, p. 448, Feb. 1986. [Online]. Available: https://ui.adsabs.harvard.edu/abs/1986ApJ...301..448C/abstract

[193] R. Bučík *et al.*, "Temperature in solar sources of 3he-rich solar energetic particles and relation to ion abundances," *The Astrophysical Journal*, vol. 908, no. 2, p. 243, feb 2021. [Online]. Available: https://doi.org/10.3847/1538-4357/abd62d

[194] R. Bučík, "3he-rich solar energetic particles: Solar sources," *Space Science Reviews*, vol. 216, no. 2, Mar 2020. [Online]. Available: http://dx.doi.org/10.1007/s11214-020-00650-5

[195] R. Schwenn, "Space Weather: The Solar Perspective," *Living Reviews in Solar Physics*, vol. 3, no. 1, p. 2, Aug. 2006.

[196] R. A. Leske, R. A. Mewaldt, E. C. Stone, and T. T. von Rosenvinge, "Observations of geomagnetic cutoff variations during solar energetic particle events and implications for the radiation environment at the space station," *Journal of Geophysical Research: Space Physics*, vol. 106, no. A12, pp. 30 011–30 022, 2001. [Online]. Available: https://agupubs.onlinelibrary.wiley.com/doi/abs/10.1029/2000JA000212

[197] S. Barlini *et al.*, "New digital techniques applied to a and z identification using pulse shape discrimination of silicon detector current signals," *Nuclear Instruments and Methods in Physics Research Section A: Accelerators, Spectrometers, Detectors and Associated Equipment*, vol. 600, no. 3, pp. 644–650, 2009. [Online]. Available: https://www.sciencedirect.com/science/article/pii/S0168900209000023

[198] M. Mutterer *et al.*, "Breakthrough in pulse-shape based particle identification with silicon detectors," *IEEE Transactions on Nuclear Science*, vol. 47, no. 3, pp. 756–759, 2000. [Online]. Available: https://ieeexplore.ieee.org/document/856510

[199] C. Ammerlaan, R. Rumphorst, and L. Koerts, "Particle identification by pulse shape discrimination in the p-i-n type semiconductor detector," *Nuclear Instruments and Methods*, vol. 22, pp. 189–200, 1963. [Online]. Available: https://www.sciencedirect.com/science/article/pii/0029554X63902489

[200] G. Pausch *et al.*, "Application of the pulse-shape technique to proton-alpha discrimination in si-detector arrays," *Nuclear Instruments and Methods in Physics Research Section A: Accelerators, Spectrometers, Detectors and Associated Equipment*, vol. 365, no. 1, pp. 176–184, 1995. [Online]. Available: https://www.sciencedirect.com/science/article/pii/0168900295004882

[201] H. Hamrita *et al.*, "Charge and current-sensitive preamplifiers for pulse shape discrimination techniques with silicon detectors," *Nuclear Instruments and Methods in Physics Research A*, vol. 531, no. 3, pp. 607–615, Oct. 2004.

[202] L. Bardelli, G. Poggi, M. Bini, G. Pasquali, and N. Taccetti, "Application of digital sampling techniques to a "single chip telescope" for isotopic particle identification," *Nuclear Physics A*, vol. 746, pp. 272–276, 2004, proceedings of the Sixth International Conference on Radioactive Nuclear Beams (RNB6). [Online]. Available: https://www.sciencedirect.com/science/article/pii/S0375947404009820

[203] S. G. Kanekal *et al.*, "The merit onboard the ceres: A novel instrument to study energetic particles in the earth's radiation belts," *Journal of Geophysical Research: Space Physics*, vol. 124, no. 7, pp. 5734–5760, 2019. [Online]. Available: https://agupubs.onlinelibrary.wiley.com/doi/abs/10.1029/2018JA026304

[204] N. Minafra *et al.*, "Test of ultra fast silicon detectors for picosecond time measurements with a new multipurpose read-out board," *Nuclear Instruments and Methods in Physics Research Section A: Accelerators, Spectrometers, Detectors and Associated Equipment*, vol. 867, 04 2017. [Online]. Available: https://www.sciencedirect.com/science/article/pii/S0168900217304825?via%3Dihub

[205] *CAEN A7508, 1 Ch 800 V/50 µA High Efficiency HV Power Supply Module (5V in)*, CAEN, 29 May 2017, rev. 1. [Online]. Available: https://www.caen.it/products/a7508/

[206] "Weightfield2." [Online]. Available: http://personalpages.to.infn.it/~cartigli/Weightfield2/Main.html

[207] N. Neindre *et al.*, "Comparison of charged particle identification using pulse shape discrimination and ee methods between front and rear side injection in silicon detectors," *Nuclear Instruments and Methods in Physics Research Section A: Accelerators, Spectrometers, Detectors and Associated Equipment*, vol. 701, p. 145–152, 11 2013. [Online]. Available:

https://www.researchgate.net/publication/257024727_Comparison_of_charged_particle_identification_using_pulse_shape_discrimination_and_DE-E_methods_between_front_and_rear_side_injection_in_silicon_detectors

[208] *BFP842ESD SiGe:C NPN RF bipolar transistor*, Infineon, September 2018, v2.0. [Online]. Available: https://www.infineon.com/dgdl/Infineon-BFP842ESD-DS-v02_00-EN.pdf?fileId=5546d46265f064ff01663896cf294ebc

[209] *BFP620 Surface mount high linearity silicon NPN RF bipolar transistor*, Infineon, 2019-01-25, revision 2.0. [Online]. Available: https://www.infineon.com/dgdl/Infineon-BFP620-DS-v02_00-EN.pdf?fileId=5546d462689a790c01690f0396db3924#:~:text=The%20BFP620%20is%20a%20RF,wide%20range%20of%20wireless%20applications.

[210] E. Oberla *et al.*, "A 15gsa/s, 1.5ghz bandwidth waveform digitizing asic," *Nuclear Instruments and Methods in Physics Research Section A: Accelerators, Spectrometers, Detectors and Associated Equipment*, vol. 735, pp. 452–461, 2014. [Online]. Available: https://www.sciencedirect.com/science/article/pii/S016890021301276X?via%3Dihub

[211] PJRC, "Teensy 4.1 development board," accessed on: 2021-08-17. [Online]. Available: https://www.pjrc.com/store/teensy41.html

[212] *LCMXO2-2000ZE-1TG144I)*, Lattice Semiconductor Corporation, March 2017, version 3.3. [Online]. Available: https://www.digikey.com/en/products/detail/lattice-semiconductor-corporation/LCMXO2-2000ZE-1TG144I/2785503

[213] "Micron Semiconductor Ltd," https://www.micron.com/, accessed: 2021-08-01.

[214] *EPO-TEK® EJ2189-LV*, EPOXY TECHNOLOGY, February 2021, rev. XI. [Online]. Available: https://www.epotek.com/docs/en/Datasheet/EJ2189-LV.pdf

[215] *AIMTERGE 250A*, AIM Globall Solder Solutions. [Online]. Available: https://aimsolder.com/sites/default/files/aimterge_520a_tds.pdf